UNIVERSITY OF BIRMINGHAM

The influence of sphingosine-1-phosphate receptor 2 in determining the invasive behaviour of oral squamous carcinoma cell lines using 2 and 3D models

By
Adjabhak Wongviriya

A thesis submitted to the University of Birmingham for the degree of
DOCTOR OF PHILOSOPHY

School of Dentistry
College of Medical and Dental Sciences
The University of Birmingham
March 2023

Abstract

Introduction: The sphingosine-1-phosphate receptor 2 (S1PR2) has been shown to influence several cellular activities, including growth and motility. Epidermal growth factor (EGF) is well-known for its ability to regulate the proliferation and motility of various cell types. In previous studies, the activation of S1PR2 suppressed tumour propagation in various cell types; however in oral squamous cell carcinoma (OSCC) lines, it stimulated migration and invasion. Since a single study may not be enough to clarify the function of S1PR2 and the overlapping functions between S1PR2 and EGF, the present study investigated the influence of EGF and S1PR2 in proliferation, migration and invasion in three OSCC lines (H357, H400 and H413) as well as potential crosstalk between EGF/ EGF receptors and S1P/S1PR2 pathways.

Material and methods: Proliferation in response to EGF and S1PR2 treatments was determined using growth curves and the BrdU assay. Migration was studied using scratch wound and transwell assays, whilst matrix invasion was investigated using a transwell assay and a multicellular tumour spheroid (MCTS) model. EGF production was determined using an enzyme-linked immunosorbent assay (ELISA) and gene expression levels were determined using reverse transcriptase-polymerase chain reaction (RT-PCR) analyses.

Results: While cultures treated with 1 ng/ml EGF promoted the proliferation of H357 and H413 and inhibited H400 cells, 20 ng/ml EGF inhibited the growth of all three OSCC lines. Inhibition of S1PR2 with the known antagonist JTE013 decreased proliferation but stimulation with the agonist CYM5478 did not increase proliferation. EGF at 1 and 20 ng/ml induced migration and invasion of all three OSCC lines with the concentrations applied. S1PR2 inhibition reduced migration and invasion of these lines. The reverse effect on migration and invasion was identified when S1PR2 was stimulated except for H357 and H413 in scratch wound assays and for H400 in transwell assays. S1PR2 also suppressed EGF's induction of

migration and invasion. Neither the inhibition nor stimulation of SIPR2 affected EGF production, however EGF stimulation was found to upregulate *sphingosine kinase 1* (*SPHK1*), an enzyme that generates S1P.

Conclusions:

The three OSCC lines exhibited different characteristics of proliferation, migration, invasion and gene expression. EGF regulated OSCC proliferation to differing degrees, depending on the concentration and cell line, but it promoted migration and invasion according to concentration. The inhibition of S1PR2 suppressed proliferation, migration and invasion of the three OSCC lines and also the EGF-induced migration and invasion effect. This implied that S1P/S1PR2 may exert control on EGF/ EGF receptors in regulating the motility of the three OSCC lines. EGF/EGF receptors also demonstrated crosstalk with the S1P/S1PR2 axis by increasing the expression of *SPHK1*, which potentially increases S1P production. This information about the role of S1PR2 in regulating growth, migration and invasion and how it involves EGF/EGF receptors may lead to promising new treatments for OSCC patients by potentially preventing or reducing metastasis.

Acknowledgements

Firstly, I would like to acknowledge the support given to me by the senior staff in the Faculty of Dentistry, Naresuan University, especially in the department of Oral diagnosis, which included encouraging me to apply for a PhD. I would also like to thank the Faculty of Dentistry for supporting my scholarship throughout the four years of this study. Studying at the University of Birmingham was a memorable opportunity that opened up my world, teaching me lessons not only in relation to a particular academic topic but also in life.

Secondly, I would like to express my appreciation to my family for cheering me up and giving me the strength to challenge myself. I want to thank my sister, Pinnara Wongviriya, for helping to manage my financial documents and for coming to visit me in the UK. Also, I would like to thank Mevisa Smith and Nana for always receiving my call when I was lonely.

Third, I would like to thank all of the involved lab technicians for always being there and for teaching me how to perform the experiments required, as well as helping me solve any problems. Special thanks go to my friends in Thailand and the School of Dentistry in the University of Birmingham for emotionally supporting me, especially Witchayut Sasimonthon, Jitpisute Chunthorng Orn, Ngamjit Kongsupon, Bongkot Mahayotsanan, and Nakaret Kano who helped read my thesis and always cheered me up with delicious food.

Lastly, I would like to sincerely express my gratitude to my supervisors, Professor Gabriel Landini, Dr Richard Shelton, Professor Michael Milward, and Professor Paul Cooper for their help advising me on my PhD research project as well as for supporting me throughout my PhD. Your guidance has helped me to accomplish another level of achievement.

Contents

Abstract **2**
Acknowledgements **4**
Contents **5**
List of abbreviations **9**
List of figures **14**
List of tables **20**
List of appendix tables **21**
Chapter 1: Introduction **23**
1.1 Oral mucosa 24
1.1.1 Cell junctions *24*
1.1.2 Motile unit of epithelial cells *27*
1.1.3 Process of epithelial cell contraction *28*
1.2 Oral squamous cell carcinoma (OSCC) 30
1.3 Cancer invasion 31
1.3.1 Epithelial-mesenchymal transition (EMT) *31*
1.3.2 Migration of epithelial cells *33*
1.4 Epidermal growth factor (EGF) 36
1.5 Sphingosine-1-phosphate (S1P) 38
1.5.1 Rho GTPases *40*
1.5.2 S1P/S1PR2 signalling and tumour invasion *42*
1.6 Cancer invasion and the application of cell culture models *in vitro* 43
1.7 Overall aims 47
1.8 Overall objectives 47
Chapter 2: Materials and methods **48**
2.1 Cell culture 49
2.1.1 Subcultures of OSCC cells *49*
2.1.2 Cell counting *50*
2.2 Reagent preparation and treatments 50
2.3 Determination of cell proliferation 52
2.3.1 Growth curves and doubling times *52*
2.3.2 BrdU proliferation assay *52*
2.4 Migration assays 53
2.4.1 Scratch wound assay *55*

2.4.2 Transwell migration assay.....57
2.5 Determination of invasion.....60
2.5.1 Transwell invasion assay.....60
2.5.2 Multicellular tumour spheroid (MCTS) assay.....61
2.6 Reverse Transcription-Polymerase Chain Reaction (RT-PCR).....69
2.6.1 Semi-quantitative reverse transcriptase-polymerase chain reaction (sqRT-PCR).....69
2.6.2 Real-time polymerase chain reaction (Real-time PCR).....75
2.7 Rac1 G-LISA activation assay.....78
2.7.1 Reagent preparation.....79
2.7.2 Lysate collection and total protein quantification.....79
2.7.3 G-LISA procedure.....80
2.7.4 Data Analysis.....81
2.8 Enzyme-linked immunosorbent assay (ELISA).....81
2.8.1 Antibody and standard preparation.....81
2.8.2 Plate preparation.....82
2.8.3 Assay procedure.....82
2.9 Statistical analysis.....85
Chapter 3: Investigation of proliferation, migration and invasion in OSCC lines.....86
3.1 Aims.....87
3.2 Objectives.....87
3.3 Growth curves and doubling times.....87
3.4 BrdU assay.....87
3.5 Scratch wound assay.....90
3.6 Transwell migration assay.....90
3.7 Transwell invasion assay.....93
3.8 Multicellular spheroid analysis.....93
3.8.1 The effect of matrix stiffness on invasion.....96
3.8.2 The potential effect of proliferation on matrix invasion.....114
3.9 Conclusion.....125
Chapter 4: Effects of epidermal growth factor on proliferation, migration, invasion and gene expression in OSCC lines.....127
4.1 Aims.....128
4.2 Objectives.....128
4.3 *EGFR* expression and EGF production.....128
4.4 Growth curve and doubling time analysis.....130

4.5 BrdU assay 133
4.6 Scratch wound migration assay 133
4.7 Transwell migration assay 137
4.8 Transwell invasion assay 139
4.9 Multicellular tumour spheroid 141
4.9.1 Analysis of the number of clusters 141
4.9.2 Analysis of the maximum invading distance 144
4.9.3 Analysis of the circularity of the main cluster 146
4.9.4 Analysis of the fractal dimension of the main cluster 146
4.9.5 Analysis of the maximum diameter of the main cluster (MDMC) 149
4.10 The effect of EGF on epithelial mesenchymal transition (EMT) events 149
4.11 The effect of EGF on *Rac1* expression and Rac1 activity 152
4.12 Conclusion 155
Chapter 5: Effects of S1PR2 on proliferation, migration, invasion and gene expression in OSCC lines 156
5.1 Aims 157
5.2 Objectives 157
5.3 The expression of *S1PR*s 158
5.4 Growth curves and doubling times 158
5.5 BrdU assay 161
5.6 Scratch wound migration assay 163
5.7 Transwell migration assay 165
5.8 Transwell invasion assay 165
5.9 Multicellular tumour spheroids (MCTS) 168
5.9.1 Analysis of the number of clusters 168
5.9.2 Analysis of the maximum invading distance 171
5.9.3 Analysis of the circularity and fractal dimension of the main cluster 171
5.9.4 Analysis of the maximum diameter of the main cluster (MDMC) 174
5.10 Matrix metalloproteinase production 174
5.11 Sphingosine kinases expression 178
5.12 Conclusion 180
Chapter 6: The crosstalk between EGF/EGFR and S1P/S1PR2 in controlling migration and invasion of OSCC lines 181
6.1 Aims 182
6.2 Objectives 182

6.3 Scratch wound migration assay 182
6.4 Transwell migration assay 184
6.5 Transwell invasion assay 186
6.6 Multicellular tumour spheroids 188
6.6.1 Analysis of the number of clusters 188
6.6.2 Analysis of the maximum invading distance 191
6.6.3 Analysis of the circularity of the main cluster 194
6.6.4 Analysis of the fractal dimension of the main cluster 196
6.6.5 Analysis of the maximum diameter of the main cluster (MDMC) 196
6.7 Matrix metalloproteinases expression 199
6.8 Effects of EGF/EGF receptors and S1P/S1PR2 on Rac1 activity 202
6.9 Determination of crosstalk between S1P/S1PR2 and EGF/EGF receptors 202
6.10 Conclusion 204
Chapter 7: Discussion 207
7.1 *EGF*, *EGFR* and *S1PR*s expression 208
7.2 Cell proliferation 209
7.2.1 Comparison of proliferative profiles 210
7.2.2 The effect of EGF on cell proliferation 211
7.2.3 The effect of S1PR2 on cell proliferation 213
7.3 Determination of migration and invasion 215
7.3.1 Comparison of migratory and invasive profiles between the three OSCC lines 215
7.3.2 Generation of a protocol for the MCTS model 215
7.3.3 The effect of matrix stiffness on invasion characteristics 218
7.3.4 The relationship between the proliferation and invasion 222
7.3.5 The effect of EGF on migration and invasion 223
7.3.6 The effect of S1PR2 on OSCC migration and invasion 225
7.3.7 The effect of S1PR2 on EGF-induced migration and invasion 230
7.4 The effect of EGF and S1PR2 on Rac1 activity 231
7.5 Crosstalk between EGF/EGF receptors and S1P/S1PR2 pathways 233
7.6 Limitations of this study 235
7.7 Potential future studies and applications 237
Chapter 8: Conclusions 240
Appendix 242
References 255

List of abbreviations

2D	Two-dimensional
3D	Three-dimensional
ABC transporter	AATP-binding cassette transporter
ADP	Adenosine diphosphate
Akt	Protein kinase B
Arp2/3	Actin-related protein 2/3
Arf6	ADP-ribosylation factor 6
Asef	Rho guanine nucleotide exchange factor 4
ATP	Adenosine triphosphate
BCIP	5-bromo-4-chloro-3-indolyl-phosphate
BP180	Collagen type XVII / Bullous pemphigoid antigen 180
BP230	Bullous pemphigoid antigen 230
BrdU	Bromodeoxyuridine
CCM	Collective cell migration
Cdc42	Cell division control protein 42 homolog
cDNA	complementary DNA
dH_2O	Distilled water
DMEM	Dulbecco's modified Eagle's medium/nutrient mixture
DMSO	Dimethyl sulfoxide

DNase I	Deoxyribonuclease I
DOI	Depth of invasion
ECM	Extracellular matrix
EGF	Epidermal growth factor
EGFR	Epidermal growth factor receptor
ELC	Essential light chain
ELISA	Enzyme-linked immunosorbent assay
EMT	Epithelial-mesenchymal transition
ERK	Extracellular signal-regulated kinase
FBS	Foetal bovine serum
GAPs	GTPase activating proteins
GDIs	Guanine nucleotide dissociation inhibitors
GDP	Guanosine diphosphate
GEFs	Guanine exchange factors
GTP	Guanosine triphosphate
HB-EGF	Heparin-binding EGF-like growth factor
HNSCC	Head and neck squamous cell carcinoma
HRP	Horseradish peroxidase conjugate
IRSp53	Insulin receptor tyrosine kinase substrate p53
JAMs	Junctional adhesion molecules

LIMK	LIM kinase
MCTSs	Multicellular tumour spheroids
MDMC	Maximum diameter of the main cluster
MEK	Mitogen-activated protein kinase
MMPs	Matrix metalloproteinases
MT1-MMP	Membrane type 1 matrix metalloproteinase
MTS	Dimethylthiazol-carboxymethoxyphenyl-sulfophenil tetrazolium
NBT	4-nitro blue tetrazolium chloride
NM-II	Non-muscle myosin type II
OSCC	Oral squamous cell carcinomas
O_2	Oxygen
PAAG	Polyacrylamide hydrogel
PAK	p21-activated kinase
PBS	Phosphate buffered saline
PDGF	Platelet-derived growth factor
Pi	Phosphate
PI3K	Phosphoinositide 3-kinase
PPN	Percentage of Ki67 positive nuclei
Rac1	Ras-related C3 botulinum toxin substrate 1
RhoA	Ras homolog family member A

RLC	Regulatory light chain
RT-PCR	Reverse transcription-polymerase chain reaction
S1P	Sphingosine-1-phosphate
S1PR	Sphingosine-1-phosphate receptor
SCC	Squamous cell carcinomas
SGPL	Sphingosine-1-phosphate lyase
SGPP	Sphingosine-1-phosphate phosphatase
SMA	Smooth-muscle actin
SMase	Sphingomyelinase
SPHK	Sphingosine kinase
SPNS2	Sphingolipid transporter 2
sqRT-PCR	Semi-quantitative reverse transcriptase polymerase chain reaction
STAT3	Signal transducer and activator of transcription 3
TAZ	Transcriptional coactivator with PDZ-binding motif
TGF-α	Transforming growth factor-alpha
TGF-β	Transforming growth factor-beta
TIAM1	TIAM Rac1 associated GEF 1
TNF-α	Tumour necrosis factor-alpha
ULA	Ultra-low attachment
VAV2	VAV guanine nucleotide exchange factor 2

VEGF	Vascular endothelial growth factor
WAVE	WASP-family verprolin-homologous
YAP	Yes-associated protein
Zeb1	Zinc finger E-box binding homeobox 1

List of figures

Figure 1. Diagram depicting different epithelial cell junctions. **25**

Figure 2. Steps of actomyosin contraction in epithelial cells. **29**

Figure 3. Collective migration of epithelial cells. **35**

Figure 4. Sphingosine rheostat. **39**

Figure 5. Diagram depicting the regulation of Rho GTPases. **41**

Figure 6. Comparison between the 2D culture and MCTS model. **45**

Figure 7. Representative images of BrdU staining in an untreated H357 cultures. **54**

Figure 8. Scratch wound assay determining migration. **56**

Figure 9. Example image of transwell migration assay captured using fluorescence microscopy. **59**

Figure 10. Three methods of tumour spheroid generation. **63**

Figure 11. The process of transferring, embedding and culturing tumour spheroids in the collagen matrix. **65**

Figure 12. Example showing the importance of spheroid's positioning (untreated H413 spheroids embedded in 3 mg/ml collagen for one day). **67**

Figure 13. Plate setups for real-time PCR. **77**

Figure 14. Examples of standard curves obtained with the ELISA. **84**

Figure 15. Proliferation of H357, H400 and H413 cells was determined by examining the growth curves and doubling times over 14 days of culture. **88**

Figure 16. Proliferation determined using the BrdU assay. **89**

Figure 17. Scratch wound migration assay in H357, H400 and H413 cultures at 12, 18 and 24 h. **91**

Figure 18. Transwell migration assay of H357, H400 and H413 cells. **92**

Figure 19. Transwell invasion assay of H357, H400 and H413 cultures. **94**

Figure 20. Selection of methods for generating MCTS. **95**

Figure 21. The requirement for FBS during spheroid generation step. **95**

Figure 22. Representative images of MCTS of H357, H400 and H413 cells. **97**

Figure 23. The number of clusters of invading spheroids embedded in 0.5, 1.5 and 3 mg/ml collagen matrices, two days of incubation (growth-inhibited dataset). **100**

Figure 24. Comparison of the number of clusters in three OSCC lines, two days of observation (growth-inhibited dataset). **102**

Figure 25. The maximum invading distance of spheroids embedded in 0.5, 1.5 and 3 mg/ml collagen matrices, two days of incubation (growth-inhibited dataset). **103**

Figure 26. Comparison of the maximum invading distance in three OSCC lines, two days of observation (growth-inhibited dataset). **105**

Figure 27. The circularity of invading spheroids embedded in 0.5, 1.5 and 3 mg/ml collagen matrices, two days of incubation (growth-inhibited dataset). **107**

Figure 28. Comparison of the circularity of the main cluster in three OSCC lines, two days of observation (growth-inhibited dataset). **108**

Figure 29. The fractal dimension of invading spheroids embedded in 0.5, 1.5 and 3 mg/ml collagen matrices, two days of incubation (growth-inhibited dataset). **109**

Figure 30. Comparison of the fractal dimension of the main cluster of spheroids in three OSCC lines (growth-inhibited dataset). **111**

Figure 31. The MDMC of invading spheroids embedded in 0.5, 1.5 and 3 mg/ml collagen matrices, two days of incubation (growth-inhibited dataset). **112**

Figure 32. Comparison of MDMC of in three OSCC lines. **113**

Figure 33. Representative images captured using confocal microscopy of spheroids embedded in the three collagen concentrations (0.5, 1.5 and 3 mg/ml) without mitomycin C treatment. **115**

Figure 34. The number of clusters identified from invading spheroids of H357, H400 and H413 cells without proliferation inhibition (no mitomycin C treatment). **116**

Figure 35. The maximum invading distance of the spheroids embedded in three collagen concentrations without mitomycin C treatment. **118**

Figure 36. The circularity changes for the spheroids embedded in three collagen concentrations without mitomycin C treatment. **120**

Figure 37. Fractal dimensions for the spheroids without mitomycin C treatment after two days of culture. **122**

Figure 38. Comparison of the MDMC for spheroids embedded in three collagen concentrations without proliferation inhibition (no mitomycin C treatment). **124**

Figure 39. Baseline *EGFR* gene expression and EGF protein expression. **129**

Figure 40. The effect of EGF on proliferation of H357, H400 and H413 cells determined using the growth curves and doubling times. **131**

Figure 41. Representative images of H400 cells captured using phase contrast microscopy on day 14 of culture..... **132**

Figure 42. The effect of EGF on proliferation of three OSCC lines determined using BrdU assay. **134**

Figure 43. The effect of EGF on migration was determined using the scratch wound migration assay at three timepoints: 12, 18 and 24 h..... **135**

Figure 44. Transwell migration assay determining the effect of EGF on migration of H357, H400 and H413. ..... **138**

Figure 45. The effect of EGF on invasion was determined using the transwell invasion assay. ... **140**

Figure 46. The effect of EGF on invasion was determined using the MCTS assay..... **142**

Figure 47. Comparison of the number of clusters following 1 and 20 ng/ml EGF treatments. **143**

Figure 48. The effect of 1 and 20 ng/ml EGF on the maximum invading distance of the three OSCC lines. **145**

Figure 49. Comparison of the main cluster's circularity following 1 and 20 ng/ml EGF treatments. **147**

Figure 50. Fractal dimension of the three OSCC lines when treated with 1 and 20 ng/ml EGF. .. **148**

Figure 51. The MDMC of the three OSCC lines was increased by the 1 ng/ml and 20 ng/ml EGF treatments. **150**

Figure 52. The effect of EGF on EMT marker expression was determined using two PCR analyses. **151**

Figure 53. The effect of EGF on *Rac1* gene expression and Rac1 activity. **154**

Figure 54. The expression of *S1PR1-5* was determined using sqRT-PCR analysis. **159**

Figure 55. The effect of S1PR2 on proliferation of H357, H400 and H413 cell lines determined using growth curves and doubling times. **160**

Figure 56. Effects of S1PR2 on proliferation using a BrdU assay on H357, H400 and H413 cells. **162**

Figure 57. The scratch wound migration assay was used to determine the effect of S1PR2 on the migration of three OSCC line.. ..... **164**

Figure 58. Effects of stimulation and inhibition of S1PR2 on the migration of H357, H400 and H413 cells using a transwell assay. **166**

Figure 59. Transwell assay of H357, H400 and H413 cells, determining the role of S1PR2 on invasion. **167**

Figure 60. Effects of S1PR2 on invasion determined using MCTS assay. **169**

Figure 61. Number of clusters generated for each of the cell lines following either S1PR2 inhibition or stimulation. **170**

Figure 62. The maximum invading distance of three OSCC lines following S1PR2 inhibition and stimulation. **172**

Figure 63. The effects of S1PR2 on the circularity of the main clusters of three OSCC lines..... **173**

Figure 64. The effects of S1PR2 on the fractal dimension of the main clusters of H357, H400 and H413 spheroid cultures. **175**

Figure 65. Effects of S1PR2 on the MDMC of invading spheroids of H357, H400 and H413 cell lines. **176**

Figure 66. The effect of S1PR2 on *MMP2* and *MMP9* expression determined using real time-PCR analysis, 48 h of incubation. **177**

Figure 67. The regulation of *SPHK1* and *SPHK2* gene expression by S1PR2 using real-time PCR analysis, 48 h of incubation. **179**

Figure 68. Scratch wound migration assay of the three OSCC lines to investigate the effect of S1PR2 on EGF-induced migration. **183**

Figure 69. The effect of S1PR2 on EGF-induced migration for the three OSSC lines as determined using a transwell migration assay. **185**

Figure 70. Transwell invasion assay used to determine the effect of S1PR2 on EGF-induced invasion **187**

Figure 71. The effects of S1PR2 on EGF-induced invasion determined using a MCTS assay. **189**

Figure 72. Effects of S1PR2 on EGF-induced increase in the number of clusters of three OSCC lines. **190**

Figure 73. Effects of S1PR2 on EGF-induced maximum invading distance for H357, H400 and H413 spheroids. **192**

Figure 74. Effects of S1PR2 on EGF-reduced circularity for H357, H400 and H413 ..... **195**

Figure 75. Effects of S1PR2 on EGF-induced complexity of the invading spheroid as determined by the fractal dimension of the boundaries. **197**

Figure 76. Effects of S1PR2 on EGF-induced MDMC in the three OSCC lines. **198**

Figure 77. Real time-PCR analysis determining the effect of S1PR2 on EGF-induced *MMP2* and *MMP9* expression. **200**

Figure 78. G-LISA analysis determining Rac1 activity of three OSCC lines following either EGF or S1PR2 treatments. **203**

Figure 79. ELISA, determining the effect of S1PR2 on EGF and TGF-β1 production **205**

Figure 80. Real time-PCR analysis determining the effect of 1 ng/ml and 20 ng/ml EGF on *SPHK1* and *SPHK2* expression. **206**

Figure 81. Proposed crosstalk model between EGF and S1PR2 in H357, H400 and H413 cells. **236**

List of tables

Table I. Details of primer assays for sqRT-PCR analysis **72**

Table II. Details of primers for real-time PCR analysis **76**

Table III. Linear regression analysis showing the relationship between invading parameters and incubation duration (day) in the growth inhibited dataset **98**

Table IV. The effect of S1PR2 on cellular motility and MMP production **227**

List of appendix tables

Appendix table I. The number of clusters of the three OSCC lines embedded in the three collagen concentrations, with proliferation inhibition **243**

Appendix table II. The maximum invading distance of the three OSCC lines embedded in the three collagen concentrations, with proliferation inhibition **243**

Appendix table III. The circularity of three OSCC lines embedded in three collagen concentrations, with proliferation inhibition **244**

Appendix table IV. The fractal dimensions of the three OSCC line spheroids embedded in the three collagen concentrations, with proliferation inhibition **244**

Appendix table V. The MDMC of the three OSCC lines embedded in the three collagen concentrations, with proliferation inhibition **245**

Appendix table VI. The number of clusters identified for the three OSCC lines embedded in three collagen concentrations, without proliferation inhibition **245**

Appendix table VII. The maximum invading distance for the three OSCC lines embedded in three collagen concentrations, without proliferation inhibition **246**

Appendix table VIII. The circularity for spheroid cultures for the three OSCC lines embedded in three collagen concentrations, without proliferation inhibition **246**

Appendix table IX. The fractal dimension for spheroids for the three OSCC lines embedded in three collagen concentrations, without proliferation inhibition **247**

Appendix table X. The MDMC of the three OSCC lines embedded in three collagen concentrations without proliferation inhibition, without proliferation inhibition **247**

Appendix table XI. The effect of EGF treatment on the number of clusters in the three OSCC lines **248**

Appendix table XII. The effect of EGF on the maximum invading distance in the three OSCC lines **248**

Appendix table XIII. The effect of EGF on the circularity of the three OSCC lines **249**

Appendix table XIV. The effect of EGF on the fractal dimension of the three OSCC lines **249**

Appendix table XV. The effect of EGF on the MDMC in the three OSCC lines **249**

Appendix table XVI. The effect of S1PR2 on the number of clusters of the three OSCC lines ... **250**

Appendix table XVII. The effect of S1PR2 on the maximum invading distance (μm) of three OSCC lines **250**

Appendix table XVIII. The effect of S1PR2 on the circularity of three OSCC lines. **251**

Appendix table XIX. The effect of S1PR2 on the mean fractal dimension of spheroids for the three OSCC lines. **251**

Appendix table XX. The effect of S1PR2 on the MDMC (μm) for the three OSCC lines **252**

Appendix table XXI. The effect of S1PR2 on EGF-increased the number of clusters of three OSCC lines **252**

Appendix table XXII. The effect of S1PR2 on EGF-increased the maximum invading distance (μm) of three OSCC lines **252**

Appendix table XXIII. The effect of S1PR2 on EGF-decreased the circularity of the main cluster of three OSCC lines **253**

Appendix table XXIV. The effect of S1PR2 on EGF-increased the fractal dimension of the main cluster of three OSCC lines **253**

Appendix table XXV. The effect of S1PR2 on EGF-increased the MDMC (μm) of three OSCC lines **254**

Chapter 1: Introduction

1.1 Oral mucosa

The oral cavity is lined by a mucous membrane called the oral mucosa. Its functions are to protect the underlying tissue from external stimuli, to lubricate and to sense and regulate temperature (Kumar, 2014, Hand & Frank, 2015). The oral mucosa is composed of three layers: the oral epithelium, basement membrane and connective tissue. The oral epithelium is the outermost structure of the oral mucosa (Kumar, 2014) which in physiological conditions, comprises epithelial cells that adhere as a multicellular stratified layer sheet to the basement membrane. To maintain this architecture, keratinocytes exhibit cell junctions to attach to the neighbouring cells as well as to the basement membrane. There are three major types of cell junctions: gap junctions, tight junctions and adhesive junctions (**Figure 1**) (Nanci, 2017).

1.1.1 Cell junctions

Gap junctions (communicating junctions) allow small molecules up to 1.2 nm in diameter and electric current to permeate through (Kierszenbaum & Tres, 2019) and are formed by two connexons (a channel consisting of six integral membrane proteins named connexin) between adjacent cells (Kawamoto *et al.*, 1984, Goodenough & Paul, 2009).

Tight junctions, so-called *zonula occludens*, are located at the most apical part of the epithelial cells (Kawamoto *et al.*, 1984) and have two main functions: to determine cell polarity and to prevent permeability of some substances such as diffused lipids and protein (van Meer *et al.*, 1986, Kumar, 2014, Zihni *et al.*, 2016). Each tight junction is mainly composed of proteins occludin and claudin which connect with the intracellular domain of the junction and link to internal actin fibres (detailed in **section 1.1.2**) that encircle cells.

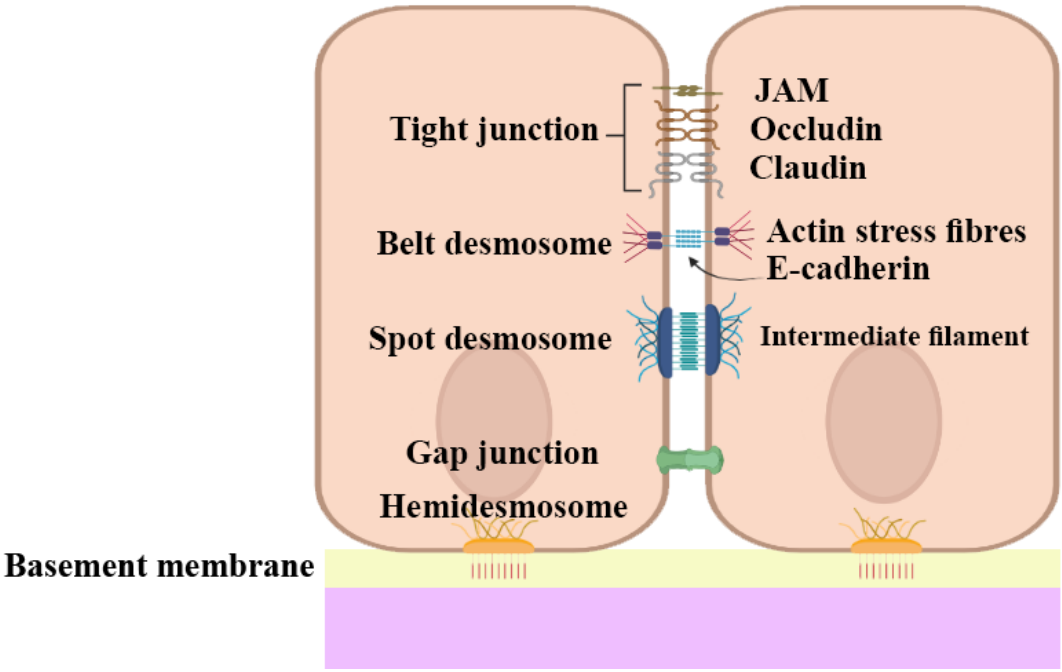

Figure 1. Diagram depicting different epithelial cell junctions. Tight junctions are composed of junctional adhesion molecules (JAMs), occludins and claudins. Adhesive junctions are divided into belt and spot desmosomes. Belt desmosomes consist of E-cadherin which binds to catenin proteins and actin filaments, also encircling cells like the belt. Spot desmosomes are composed of desmoglein and desmocollin (desmosomal cadherins) which link with tonofilaments via a cytoplasmic plaque. Gap junction, composed of six connexins. Hemidesmosomes are junctions that attach cells to the basement membrane. (Created with BioRender.com)

Adhesive junctions locate basal to the tight junctions and are classified according to the type of connection into two subtypes including those linking cell-to-cell (zonula adherens and macula adherens) and those attaching cell-to-matrix (hemidesmosome) (Kawamoto *et al.*, 1984, Nanci, 2017, Kierszenbaum & Tres, 2019).

Zonula adherens (belt-desmosomes) function to stabilise cell-cell adhesion, as well as regulating the actin cytoskeleton, intracellular signalling and transcriptional regulation (Hartsock & Nelson, 2008). Each junction is composed of a transmembrane domain and cytoplasmic plaque. The transmembrane domain of zonula adherens junctions consists of two homophilic E-cadherin proteins which connect to the cytoplasmic plaque that attaches to actin filaments via catenin proteins (Canel *et al.*, 2013, Groeger & Meyle, 2019). From these structural arrangements, it encircle cells in a belt-like manner, similar to tight junctions (Hartsock & Nelson, 2008).

Macula adherens (spot-desmosomes more commonly termed desmosomes) are spot-like junctions that provide strength and rigidity to the epithelium. Each junction comprises a transmembrane protein and desmosomal cadherins (Kottke *et al.*, 2006). The extracellular component binds to those of neighbouring cells, while the intracellular component connects to a cytoplasmic plaque that attaches to keratin filaments (Garrod & Chidgey, 2008).

Hemidesmosomes locate at the basal part of epithelial cells, providing attachment to the basement membrane. Each junction is composed of a cytoplasmic plate which on one side connects to intracellular tonofilaments, a type of intermediate filament, and the other connects to the transmembrane plaque. This plaque divides into two layers, inner and outer plaques, which attaches with the basal lamina of the basement membrane via transmembrane adhesion molecules which include plectin, bullous pemphigoid antigen 230 (BP230), collagen type XVII (BP180), integrin$\alpha_6\beta_4$ and laminin 5. With support from anchoring filaments which interact

with laminin 5, hemidesmosomes stably attach the basement membrane and upper dermis (Kawamoto *et al.*, 1984, Walko *et al.*, 2015, Nanci, 2017).

1.1.2 Motile unit of epithelial cells

Typically, postnatal eukaryotic epithelial cells do not migrate although this can occur during pathological events, such as wound healing and cancer invasion (Lamouille *et al.*, 2014). The ability of epithelial cells to adhere, migrate and resist deformation depends on an ability to generate forces opposing the surrounding extracellular matrix (ECM) and linking the cytoskeleton with the ECM to maintain tensional homeostasis and control of tissue function (Kassianidou & Kumar, 2015).

Stress fibres are the major contractile structure in many animal cell types (Tojkander *et al.*, 2012) which play an essential role in the morphogenesis, migration and mechanosensing of non-muscle cells (Burridge & Wittchen, 2013). Stress fibres are usually relatively thicker and stable in non-motile cells, such as epithelial cells, but are thinner and dynamic (more actin assembly and organising) in highly motile cells (Hotulainen & Lappalainen, 2006, Tojkander *et al.*, 2012). These fibres are composed of approximately 10-30 bundles of actin filaments (Burridge & Wittchen, 2013) conjoined in a polarised manner by crosslinking proteins such as α-actinin and zyxin. With the aid of non-muscle myosin type II (NM-II), cells can maintain isometric tension by generating contractile forces and transmitting those through cellular adhesions to the ECM (Kassianidou & Kumar, 2015).

NM-II is another structure that functions in combination with stress fibres to provide cellular organisation, polymerisation and cell contraction (Komatsu & Ikebe, 2007). NM-II molecules are bipolar and consist of two major parts: a heavy chain and a light chain. The heavy chain is divided into a globular head, neck and tail regions. The globular head can attach to actin and adenosine triphosphate (ATP). The neck has two types of light chain, namely the regulatory

light chain (RLC) and the essential light chain (ELC) and this region can rotate enabling the globular head to bind to actin filaments as well as providing the stroke force that propels actin filaments (Heissler & Sellers, 2015). The tail region forms a spiral contractile unit, NM-IIs arrange as anti-parallel homodimers into a hexamer with the globular head of each molecule attached to actin filaments (Kassianidou & Kumar, 2015).

While the actinomyosin system drives locomotion, the migrated cells require a counterbalance to stabilise the cell body. The structure that plays a role in this is cytokeratin (Yoon & Leube, 2019). These molecules are intermediate filaments containing keratin proteins that are involved in cellular activities, such as the wound healing process and cancer metastasis (Paladini *et al.*, 1996, Knösel *et al.*, 2006, Tanaka *et al.*, 2020). Intermediate filaments are also understood to be involved in cell movement because of spanning the entire cytoplasm and being present in various forms, ranging from soluble-filament precursors to filamentous networks. In stable epithelia, keratins remain in the form of thick bundles and have a low turnover rate, while, in invading cancers, the cells lose cell-cell contact and the stability of the hemidesmosomes decreases whilst keratin cycling has been found to increase at the leading edge of cells (Windoffer *et al.*, 2011).

1.1.3 Process of epithelial cell contraction

Epithelial cells generate tension forces through the contractile units in an ATP-dependent manner. In the presence of ATP, NM-II exists in a straight conformation and does not bind to actin (**Figure 2A**) however, dephosphorylation from ATP to adenosine diphosphate (ADP) and phosphate (Pi) releases the binding site of the globular head of NM-II (Vicente-Manzanares *et al.*, 2009). NM-II then changes conformation by rotating its neck and bending the globular head toward the barbed end of the actin filaments (Kassianidou & Kumar, 2015) (**Figure 2B**).

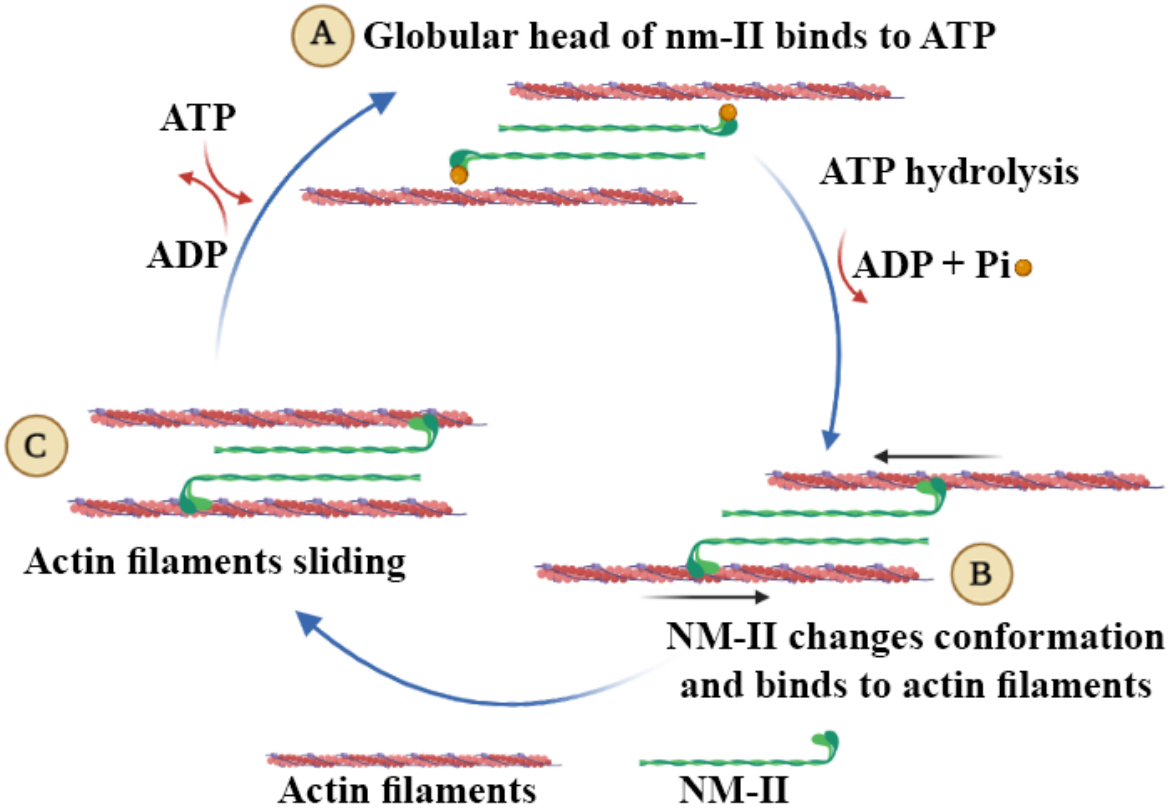

Figure 2. Steps of actomyosin contraction in epithelial cells. **A)** In the phosphorylated stage, the globular head of NM-II does not bind to the actin filaments. **B)** Hydrolysis of ATP changes the NM-II's conformation, allowing it to bind with the actin filaments. **C)** Head of NM-II rotates towards the centre of the actin filaments, resulting in actin filament sliding (contraction). When ADP is released from the NM-II, the ATP is allowed to bind to the globular head of NM-II, which reverts to the A) stage. (Created with BioRender.com).

As Pi is released, the head of NM-II rotates towards the centre of actin filaments, which further drags the attached actin filament, resulting in the actomyosin filaments forming bundles and shortening of the contractile unit (**Figure 2C**). Finally, ADP is released from NM-II, allowing the ATP to reattach and restart the cycle (Brito & Sousa, 2020) (**Figure 2A**). The contraction provided by the stress fibres generates tension across the cell, allowing the epithelial cells to anchor to the ECM. Conversely, the contraction of the actin stress fibres that link with cell junctions (adhesion belts) can induce deformation of the cell membrane and leads to cell migration (Cooper, 2013).

1.2 Oral squamous cell carcinoma (OSCC)

Oral cancer is a global health problem. For example, in 2020, 744,994 new cases were diagnosed globally, and oral cancer was reported as a cause of death in 364,339 cases (World Cancer Research Fund International, 2022). About 90% of cancers in the oral cavity are oral squamous cell carcinomas (OSCC) (Montero & Patel, 2015) originating from the oral epithelium, which has a high turnover rate and consequently this increases the probability of replication errors occurring during cell division (Brad *et al.*, 2009a, Holly *et al.*, 2013).

The best way to increase the survival rate for OSCC patients is early diagnosis. However, diagnosis is often delayed because the initial presentation of the cancer goes unnoticed. It has been reported that about 60% of OSCC cases were first diagnosed at stage III or stage IV and this late diagnosis is understood to reduce the five-year survival rate to 10% - 40% (Seoane-Romero *et al.*, 2012).

Cancers can cause death via uncontrolled proliferation (Gupta & Sivasankari, 2017) and tumour cell migration (leading to local invasion and distant metastasis) (Clark & Vignjevic, 2015). Since cancer cells have a high division rate and can spread to organs with a high blood perfusion, such as liver, bones and brain (Obenauf & Massagué, 2015), this can cause organ

failure and death (Cedervall *et al.*, 2016). The major cause of death in cancer patients is related to metastasis, therefore it is an important prognostic factor for staging and determining survival rates (Ganjre *et al.*, 2017).

1.3 Cancer invasion

A key aspect of improving OSCC patient outcomes is the ability to reduce or prevent tumour metastasis (Veiseh *et al.*, 2011). Invasion is a term used to describe the penetration of transformed cells into the surrounding structures and it is the first step of cancer metastasis (Guan, 2015). Some cancer cells can migrate into the vasculature resulting in transportation to other organs, causing secondary tumours (Clark & Vignjevic, 2015).

During invasion and metastasis, epithelial cancer cells can undergo epithelial-mesenchymal transition (EMT) which results in an alteration of the epithelial phenotype into a more mesenchymal-like state. It is understood that EMT and migration are parallel processes since cancerous cells also need plasticity, changing from non-motile epithelial cells into mesenchymal-like cells, which are more migratory (Ganjre *et al.*, 2017).

1.3.1 Epithelial-mesenchymal transition (EMT)

EMT is a biological process involving several cellular events and can occur in both physiological and pathological situations. The process is typically categorised into three types, (EMT types I - III) (Kalluri & Weinberg, 2009).

EMT type I occurs during embryonic development. The primitive epithelium transforms into primary mesenchymal cells during the implantation and gastrulation periods of embryo development. EMT type II is reported to occur during wound healing and fibrosis where it has been proposed that epithelial cells differentiate into fibroblast-like cells, while EMT type III occurs in malignant tumour propagation (Kalluri & Weinberg, 2009). Recent studies have

indicated that this type of EMT is a mechanism required for metastasis, turning non-motile epithelial cells into motile mesenchymal-like cells (Kalluri & Weinberg, 2009, Krisanaprakornkit & Iamaroon, 2012, Abdulkareem *et al.*, 2018). The hallmarks of type III EMT are the loss of epithelial cell adhesion and the breaching of the basement membrane and the ECM through the upregulation of relevant *matrix metalloproteinases* (*MMPs*) (Krisanaprakornkit & Iamaroon, 2012).

During the EMT process, various types of cancer have been shown to downregulate epithelial markers including *E-cadherin*, *β-catenin*, *desmoplakin*, *cytokeratins*, *claudins* and *occludins* while upregulating several mesenchymal markers (Krisanaprakornkit & Iamaroon, 2012). These markers include *vimentin* (the major intermediate filament expressed in non-muscular mesenchymal cells (Satelli & Li, 2011)), *N-cadherin* (an adhesion molecule associated with increased cell motility and tumour invasiveness (Cherng *et al.*, 2008)) and *smooth-muscle actin* (*SMA*) (the actin isoform which plays a vital role in fibrogenesis (Cherng *et al.*, 2008)).

E-cadherin is a key protein that plays a role in maintaining stratified epithelial integrity (Canel *et al.*, 2013). It is a component of zonula adherens junction which has a role in connecting epithelial cells and providing cellular polarity. The downregulation of this protein expression affects epithelial integrity, resulting in a more mesenchymal-like phenotype and an increased motility of tumour cells (Bravo-Cordero *et al.*, 2012).

Besides cell-cell de-adhesion, in some types of locomotion, such as mesenchymal migration and collective cell migration (CCM), transformed cells have to breach the basement membrane to penetrate the underlying connective tissue, where MMPs play a pivotal role (Gupta & Sivasankari, 2017). In tumours, MMPs facilitate invasion by degrading the extracellular matrix, enabling a mechanical alteration that promotes proliferative and invasive responses (Dangi-Garimella *et al.*, 2010). However, studies revealed that only some cells at the tumour

front underwent EMT, indicating the transient nature of EMT and variations within a single tumour (Krisanaprakornkit & Iamaroon, 2012).

1.3.2 Migration of epithelial cells

To invade the underlying tissue, it is essential that transformed cells have the ability to migrate. There are two modes of migration that have been described: single cell migration and CCM (Ganjre *et al.*, 2017) and interestingly cancer cells can switch between the two types of behaviour (Clark & Vignjevic, 2015). For example, when the leader cells in CCM produce an excessive traction force toward the migratory site that outweighs the forces of attachment to the surrounding cells, the leader cells can detach and migrate as single cells (Zegers & Friedl, 2014).

Single cell migration is characterised by the loss of cell-cell adhesion. This type of migration has been suggested to occur in two ways, specifically amoeboid movement and mesenchymal movement (Parri & Chiarugi, 2010, Clark & Vignjevic, 2015). During amoeboid movement, cells produce short protrusions (membrane 'blebbing') while remaining rounded during migration. Conversely, during mesenchymal movement cells elongate into a spindle shape and generate new focal adhesions with the substrate to migrate (Clark & Vignjevic, 2015). Mesenchymal movement starts when transformed cells extend lamellipodia or invadopodia with intracellular actin polymerisation, forming a branching filamentous network. Meanwhile, integrins at the invadopodia sites interact with ECM ligands creating new focal adhesions. Subsequently, cells secrete proteolytic enzymes that degrade old focal contacts with the ECM, creating a path for migration. The cell body then contracts and the trailing edge detaches from the ECM, causing the cell to move forward, where the adhesive force is strongest (Parri & Chiarugi, 2010).

CCM is a mode of migration that maintains cell-cell adhesion. The group of cells migrate as either sheets, strands, tubes, or clusters (Parri & Chiarugi, 2010, Clark & Vignjevic, 2015). As a consequence, it appears that this mode of locomotion facilitates the survival of tumour cells after metastasis by firstly providing wider chemotactic sensitivity and reducing random traction forces produced by cells which subsequently enhances the directionality of migration. These help the cell cluster to reach the blood and lymphatic circulation efficiently (Malet-Engra *et al.*, 2015). Secondly, CCM provides a greater diversity of cells within the invasive population, increasing the possibility of dragging cancer stem cells alongside the other invading cells which may facilitate further proliferation at secondary sites (Clark & Vignjevic, 2015).

Previous studies have reported that the migration of epithelial cancer cells occurs as CCM rather than as single cells (Clark & Vignjevic, 2015). As described earlier, epithelial tumours undergo EMT but can maintain CCM as most EMT processes appear to be transient and possibly incomplete, therefore tumour sheets are likely to contain heterogeneous populations with both epithelial- and mesenchymal-like phenotypes (Theveneau & Mayor, 2013).

CCM is, in principle, similar to mesenchymal migration but instead of exhibiting a front-rear polarity, the cells become organised into 'leader' and 'follower' cells (**Figure 3A**). Leader cells extend pseudopodia in the direction of invasion, forming β1-integrin-mediated focal adhesions and engaging in the upregulation of membrane type 1 matrix metalloproteinase (MT1-MMP) to cleave ECM embedded collagen fibres. This creates a micro-track/path for the follower cells while the rear and lateral edge of the leader cells maintain cell-cell adhesions with the follower cells (Parri & Chiarugi, 2010).

It has been proposed that leader cells maintain strong contractility along the apical junction complex which comprises a tight junction and adhesive junction to stabilise the cellular contacts.

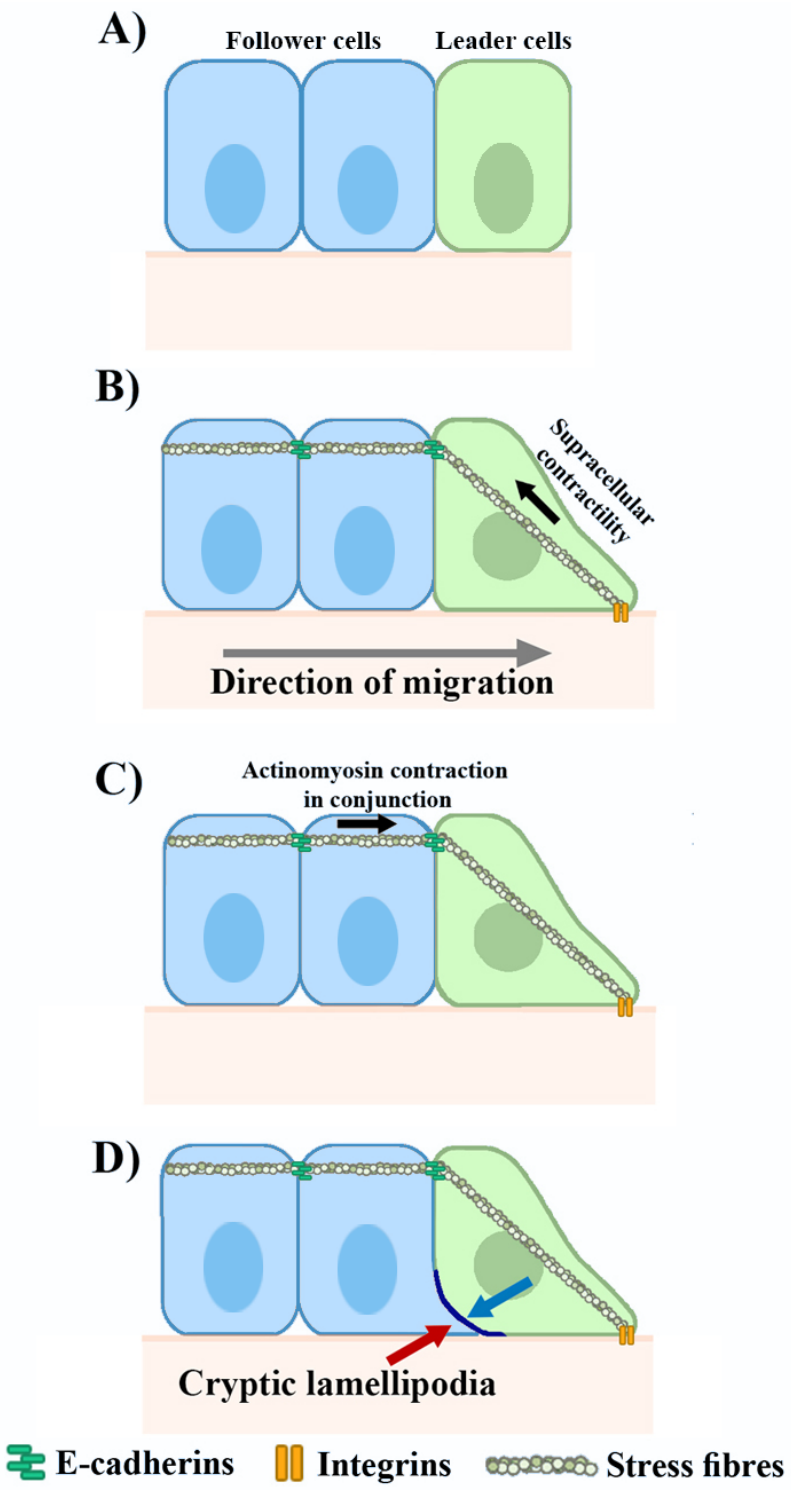

Figure 3. Collective migration of epithelial cells. **A)** Sheet of transformed cells can adopt a front-rear polarity, with leader (green cells) and follower cells (blue cells). **B)** The leader cells extend protrusions and adhere to ECM. The actinomyosin contraction in the leader cells provides a mechano-coupling force and transduce via the stress fibres (black arrow) to follower cells. **C)** The follower cells linked to the leader cells via cell junctions generate actinomyosin contractility (black arrow). **D)** The rear pole of the leader cells moves forward, causing a crypt (blue arrow) which drags the lateral and basal portions of the follower cells forward, resulting in cryptic lamellipodia (red arrow).

At the same time, the inner portion of the migrating group appears to retain low tensile stress, which helps the sheet of migrated cells maintain the mechanocoupling and actinomyosin contraction along the apical cell junctions (Zegers & Friedl, 2014). After the extension of the protrusion region with lamellipodia and invadopodia, the actinomyosin filaments contract in the leader cells, extending longitudinally from the protrusion to the adherens junctions that attach to the follower cells. The contractile force caused by the leader cells is understood to be transmitted to the follower cells (called supracellular contractility) (**Figure 3B**) (Zegers & Friedl, 2014). At the rear pole of the leader cells, force from the supracellular contractility provided by the leader cells and force from the cell-cell adhesions within the follower cells (**Figure 3C**) are proposed to determine the cellular locomotion. Once the supracellular contractility force of the leader cells has been exerted, the basal part of the rear pole of the leader cells moves forward in the direction of migration and the generated mechano-coupling force drags the follower cells in the same direction. As a consequence of this traction force, the lateral and basal portions of the follower cells extend protrusions termed 'cryptic lamellipodia' towards the migratory site (**Figure 3D**) which create new attachments to the basement substance and exert traction force on the following cells that also migrate (Zegers & Friedl, 2014). Invasion is understood to be driven through the regulation of actin dynamics, therefore any signals controlling actin dynamics have the potential to influence invasion. Two well-established molecules contributing to actin cytoskeletal reorientation are epidermal growth factor (EGF) (Li *et al.*, 2009, Gandy *et al.*, 2013) and sphingosine-1-phosphate (S1P) (Lepley *et al.*, 2005, Adada *et al.*, 2015).

1.4 Epidermal growth factor (EGF)

Human EGF is a 6 kDa protein consisting of 53 amino acids (Negahdari *et al.*, 2016) which can bind to four EGF receptor subtypes: epidermal growth factor receptor (EGFR or HER1),

HER2-4 (Voldborg *et al.*, 1997). The epidermal growth factor receptor (EGFR also known as ErbB1/HER1) is part of a family of receptor tyrosine kinases which is classified as an oncogene (Kimura *et al.*, 2016), a mutated form of proto-oncogene (gene, the activation of which following a mutation can turn normal cells to cancerous cells) (Ross, 1998). Its overexpression relates to poor prognosis in many cancer studies (Ribeiro *et al.*, 2014, Kimura *et al.*, 2016). Many cancers such as breast, prostate, pulmonary system, bladder and head and neck have been reported to involve EGFR dysregulation (Oliveira *et al.*, 2006) either by gene mutations or gene amplification. In OSCC, the majority of EGFR dysregulation is caused by amplification, while gene mutations are not common (Ribeiro *et al.*, 2014, Kimura *et al.*, 2016). Since approximately 75% - 90% of OSCC patients exhibit EGFR overexpression (Lu *et al.*, 2001, Kimura *et al.*, 2016, Islam *et al.*, 2017), this is postulated to be an underlying key to the malignant phenotype of OSCC and has become a target for treatment in OSCC patients (Kimura *et al.*, 2016).

EGFR has three domains: an extracellular domain, a transmembrane domain and an intracellular domain. The extracellular domain is a receptor where soluble ligands can bind including EGF, transforming growth factor-alpha (TGF-α), amphiregulin, epigen, epiregulin and heparin-binding EGF-like growth factor (HB-EGF) (Wieduwilt & Moasser, 2008). When EGF is bound to EGFR, the extracellular domain of the receptor provides homo-dimerization with other EGFR molecule and activates the intracellular domain via tyrosine kinase, causing the activation of a downstream signalling pathway that controls cellular activities such as proliferation, differentiation, apoptosis inhibition, migration and invasion (Voldborg *et al.*, 1997, Wieduwilt & Moasser, 2008, Wee & Wang, 2017).

Many mechanisms explaining how EGF promotes migration and invasion have been proposed (Patel *et al.*, 2007, Gandy *et al.*, 2013, Islam *et al.*, 2017, Ohnishi *et al.*, 2017). One mechanism is through the regulation of Rho GTPases (Kurokawa *et al.*, 2004, Dise *et al.*, 2008, Li *et al.*,

2009, Hu *et al.*, 2012) (discussed later in **section 1.5.1**) which are the same downstream molecules activated by S1P (Lepley *et al.*, 2005, Malchinkhuu *et al.*, 2008, Takashima *et al.*, 2008, Du *et al.*, 2010).

1.5 Sphingosine-1-phosphate (S1P)

S1P is a lipid mediator which plays a role in controlling physiological and pathological cellular processes, including proliferation, apoptosis, migration and angiogenesis (Greenspon *et al.*, 2009, Du *et al.*, 2010, Patmanathan *et al.*, 2016). Since S1P affects various cellular activities, the amount of this molecule is precisely regulated by producing and degrading enzymes. The balance between the production and degradation of S1P is called the 'sphingosine rheostat' (Newton *et al.*, 2015). S1P is derived from the metabolism of sphingomyelin within the cytoplasm (**Figure 4A**). Generally, sphingomyelin, the membrane-bound precursor, is converted into ceramide by sphingomyelinase (SMase) when the epithelial cells receive apoptotic stimuli (Slattum & Rosenblatt, 2014, Gudipaty & Rosenblatt, 2017). Ceramide is converted into sphingosine by ceramidase (**Figure 4B**), after which sphingosine is phosphorylated by both sphingosine kinase 1 and -2 (SPHK1 and SPHK2) to form S1P (**Figure 4C**). The S1P molecule can be dephosphorylated by sphingosine-1-phosphate phosphatases (SGPP1 and SGPP2) and reversibly converted to sphingosine (**Figure 4D**) and it can also be irreversibly degraded by sphingosine-1-phosphate lyase (SGPL) (**Figure 4E**) (Newton *et al.*, 2015).

After S1P has been formed, it is transported to the intercellular space (**Figure 4F**) and binds to its own receptors and neighbouring cell receptors (**Figure 4G**). There are five receptor subtypes named sphingosine-1-phosphate receptor 1 to 5 (S1PR1 to 5) and S1PR1 to -3 are ubiquitously expressed in most cell types. S1PR4 expression is restricted to lymphoid tissues, whereas S1PR5 is expressed mainly in the brain, skin and natural killer cells (Blaho & Hla, 2014).

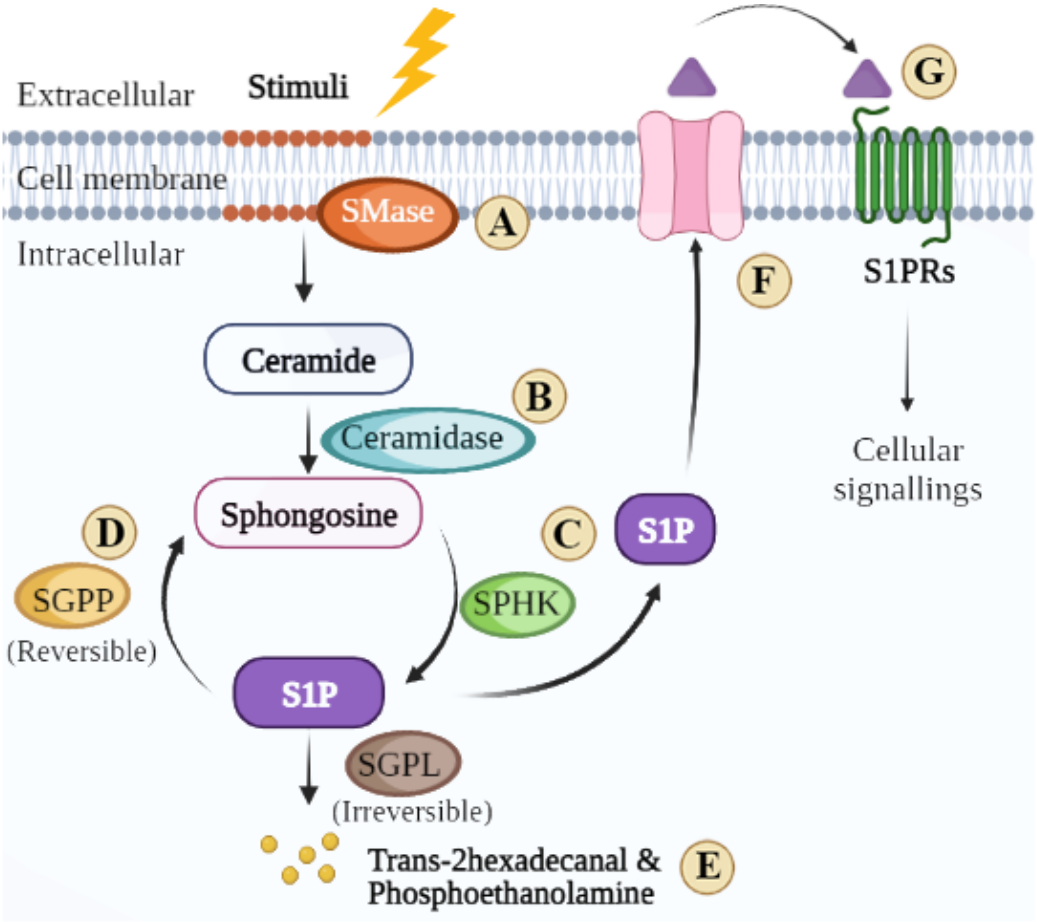

Figure 4. Sphingosine rheostat. **A)** When receiving external stimuli, SMase converts sphingomyelin into ceramide. **B)** Ceramidase further converts ceramide into sphingosine. **C)** Sphingosine is converted into S1P by SPHK1 and SPHK2 **D)** S1P is reversibly reverted to sphingosine by SGPP1 and SGPP2. **E)** S1P is irreversibly degraded to trans-2hexadecanal and phosphoethanolamine by SGPL. **F)** Produced S1P was exported via transporters, *e.g.* sphingolipid transporter 2, AATP-binding cassette transporter (ABC transporter), into the intercellular space. **G)** S1P binds to five subtypes of S1PR and generates cellular signalling. (Created with BioRender.com).

Depending on the cell type, S1PRs couple with various types of G protein which cause the activation of diverse signalling pathways (Adada *et al.*, 2013, Nema *et al.*, 2016). Several studies have revealed that in some biological processes, more than one S1PR subtype functions in concert with each of the others (Tanimoto *et al.*, 2004, Young & Van Brocklyn, 2007). Among the five subtypes, the activation of S1PR2 has been linked to the regulation of cancer biology, especially motility (Lepley *et al.*, 2005, Takuwa *et al.*, 2011, Patmanathan *et al.*, 2016, Pang *et al.*, 2020). When stimulated with S1P, S1PR2 can bind to GαI, GαQ and Gα12/13, consequently activating Rho GTPases and providing movement through cytoskeletal dynamic changes (Adada *et al.*, 2013, Nema *et al.*, 2016).

1.5.1 Rho GTPases

Rho GTPases are a subfamily of enzymes within the Ras superfamily which help to link the upstream signal to the effector structures. Each member of this subfamily is about 21-25 kDa and share a similar common G-domain core responsible for nucleotide exchange (Parri & Chiarugi, 2010, Murali & Rajalingam, 2014). When upstream signalling has been received, the Rho GTPase translocates from the cytosol towards the plasma membrane where it is activated by guanine exchange factors (GEFs), turning inactive guanosine diphosphate (GDP)-bound into its active guanosine triphosphate (GTP)-bound form (**Figure 5A**) (Parri & Chiarugi, 2010, Zegers & Friedl, 2014). As an antagonist of GEFs, Rho GTPase is inactivated by GTPase activating proteins (GAPs), regulatory proteins that hydrolyse GTP into GDP (**Figure 5B**). Moreover, Rho GTPase can be inhibited by guanine nucleotide dissociation inhibitors (GDIs) which bind to GDP-bound Rho GTPases that are sequestered within the cytosol, preventing phosphorylation at the plasma membrane (**Figure 5C**) (Parri & Chiarugi, 2010, Murali & Rajalingam, 2014, Zegers & Friedl, 2014).

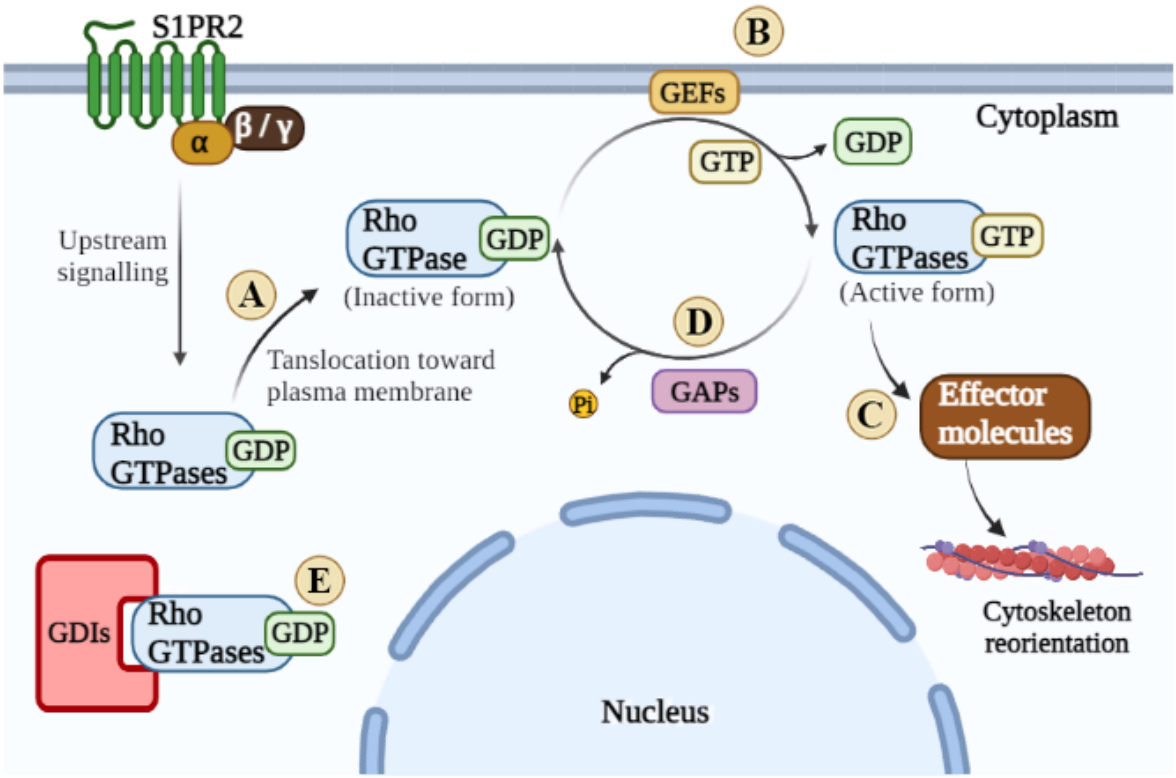

Figure 5. Diagram depicting the regulation of Rho GTPases. **A)** When receiving upstream signalling, Rho GTPases translocate toward the plasma membrane and **B)** are activated by GEFs, switching from a GDP-bound form to ATP-bound. **C)** Active Rho GTPases further stimulate downstream effector molecules. **D)** Rho GTPases are reversibly inactivated by GAPs. **E)** GDIs bind to GDP-bound Rho GTPases within cytosol, preventing them from being activated. (Created with BioRender.com).

Active Rho GTPases further regulate specific effector's molecules, causing the modulation of cellular activities (**Figure 5D**). The Rho family consists of 20 proteins divided into eight sub-groups, but one of the best characterised to date is Ras-related C3 botulinum toxin substrate 1 (Rac1).

The principal function of Rac1 protein is contributing to cytoskeletal reorganisation although in cancer, it stimulates actin polymerisation, causing the lamellipodial extension of the leading edge in mesenchymal movement (Kurokawa *et al.*, 2004, Murali & Rajalingam, 2014) and in CCM (Zegers & Friedl, 2014). Rac1 can bind to the insulin receptor tyrosine kinase substrate p53 (IRSp53) (Miki *et al.*, 2000), a scaffolding molecule that connects with WASP-family verprolin-homologous (WAVE) proteins/actin-related protein 2/3 (Arp2/3) complex. The activation of this axis results in actin branching initiation (Mullins *et al.*, 1998). Rac1 also regulates the turnover of actin filament at lamellipodia by binding to p21-activated kinase (PAK). This binding causes phosphorylation of Lim kinase (LIMK) and cofilin, subsequently resulting in the suppression of actin-severing activity (Arber *et al.*, 1998, Gorovoy *et al.*, 2005, Delorme *et al.*, 2007).

1.5.2 S1P/S1PR2 signalling and tumour invasion

S1PR2 reportedly controls cytoskeletal conformation and may regulate the invasiveness of tumours (Slattum & Rosenblatt, 2014). Indeed, the majority of studies underline a tumour suppressive role for S1PR2 where its activation reduces proliferation, migration, invasion and metastasis (Lepley *et al.*, 2005, Du *et al.*, 2010, Asghar *et al.*, 2018, Pang *et al.*, 2020, Petti *et al.*, 2020). While the role of S1PR2 in various types of cancer have been studied, the role of S1PR2 in OSCC is still poorly understood (Nema *et al.*, 2016). In a study of oesophageal adenocarcinoma, the inhibition of S1PR2 appeared to reduce S1P or transforming growth factor-beta (TGF-β)-induced migration and invasion (Miller *et al.*, 2008). Similarly, a study

using OSCC cells demonstrated that the sphingosine rheostat was dysregulated and that the inhibition of S1PR2 reduced S1P-induced migration and invasion (Patmanathan *et al.*, 2016). This finding contradicted other studies reporting that S1PR2 activation attenuated cellular motility (Arikawa *et al.*, 2003, Du *et al.*, 2010, Price *et al.*, 2015, Pang *et al.*, 2020) and that S1PR2 was not involved in cellular motility (Kim *et al.*, 2011, Petti *et al.*, 2020), implying that S1PR2 function is cell type specific.

1.6 Cancer invasion and the application of cell culture models *in vitro*

Due to the importance of cancer cell invasion in metastasis, there have been attempts to create an accurate, measurable set of indices for staging, grading, and prognosis. Staging system is based on the clinical features including tumour size, lymph node involvement and metastasis. It is divided into four stages, stage 4 being the most severe (Brad *et al.*, 2009b, Epstein & Elad, 2015). In contrast, the grading system is based on histopathological features, dividing into three grades, including well-, moderated- and poorly- differentiated. Variables such as invasion pattern, tumour thickness, degree of keratinisation, nuclear pleomorphism, lymphatic response and mitotic rate were used to grade each tumour. The more resemble the parent tissue, the lower grade (less severe) the tumour is (Brad *et al.*, 2009b).

Various other types of gradings have been proposed, which include the analysis of histological features such as the depth of invasion (DOI), invasion index and Bryne's grading system (Wagner *et al.*, 2017). Scoring systems have been also used to classify qualities or amounts, however, in histopathology, these are often based on some observational and to some degree subjective, determination by pathologists. Scores often lack reproducibility (Li *et al.*, 2015) due to being mostly based on individual perception which have been shown to show inter- and intra- observer variability (Landini & Rippin, 1996, Abu Eid & Landini, 2005). In addition, many of the proposed classifications are modifications of previously defined scoring systems.

It is, therefore, difficult to standardise results by comparing different studies and this further constrains the ability to analyse large datasets (Pentenero *et al.*, 2005, Jenei *et al.*, 2011, Wagner *et al.*, 2017). Due to these limitations, more recent studies have attempted to address some of these problems by applying automated methods and algorithms for the analysis of histological images (Landini & Rippin, 1996, Berens *et al.*, 2015, Vinci *et al.*, 2015).

In terms of experimental approaches, two-dimensional (2D) *in vitro* models are relatively easy to interpret and convenient to implement but cannot easily demonstrate fully the *in vivo* invasion process. Two-dimensional cultures constrain the cells grown on a flat substrate, which forces the cells to be aligned artificially (**Figure 6A**). This condition also increases the area of cell-media exchange and enhances nutrition and oxygenation, subsequently resulting in the alteration of molecular signals (Alemany-Ribes & Semino, 2014). Moreover, monolayer cell cultures cannot establish the architectural structure of solid tumours or the drug interactions because anti-cancer agents are able to penetrate the targeted cells evenly (Alemany-Ribes & Semino, 2014). Therefore an interest in developing *in vitro* culture methods that better represent the properties of solid tumours has arisen (Alemany-Ribes & Semino, 2014, Sant & Johnston, 2017).

Multicellular tumour spheroids (MCTSs) represent a cell culture method where cells aggregate into round clusters (Costa *et al.*, 2016, Sant & Johnston, 2017) first developed by Moscona and Moscona (1952). It was reported that the cell suspensions of chicken chondrogenic cells aggregated into tissue-like structures that restored the original characteristic of the tissue.

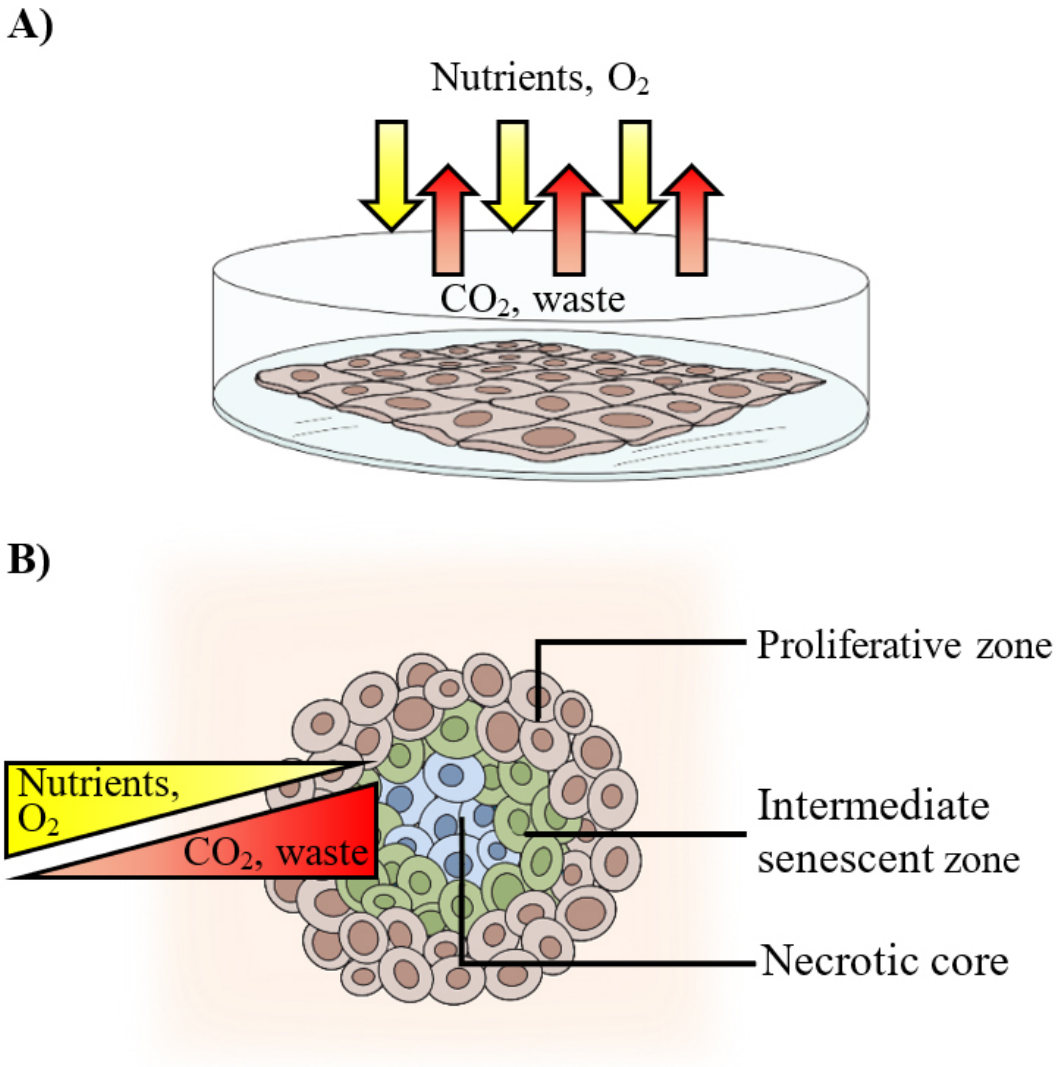

Figure 6. Comparison between the 2D culture and MCTS model. **A)** Cells cultured as monolayers are driven to spread on a flat substrate. This arrangement provides cells with the ability to evenly receive nutrients, oxygen (O_2) and treatments as well as exchange the waste product with the culture media. **B)** MCTSs typically organise into three zones: proliferative zone, intermediate senescent zone and necrotic core. This architecture provides a gradient when exchanging nutrients, O_2 and waste products with the culture media, resulting in limited penetration of pharmacological treatments.

Spheroid shape and multiple layers created a structural conformation that enabled a better understanding, for example, of the penetration and distribution of drugs. These approaches have been used extensively in pharmacology and drug discovery research. Depending on size, tumour spheroids organise into three zones that mimic solid tumours: an external proliferating zone, an intermediate senescent zone and an internal necrotic area (**Figure 6B**) (Zanoni *et al.*, 2016, Däster *et al.*, 2017). Gene expression is affected by the three-dimensional (3D) cellular organisation characteristics of these micro-tissues (Costa *et al.*, 2016) and it has been reported that gene expression within spheroids is comparable with that observed in solid tumours *in vivo* (Costa *et al.*, 2016). Due to these advantages, there has been an increase in research using spheroid cultures to better mimic real tumour conditions as well as reducing the use of animal models (Alemany-Ribes & Semino, 2014, Sant & Johnston, 2017). Apart from the mimicry of structure, MCTS can be used to explore how cells grow and invade the matrix (Lam *et al.*, 2014, Vinci *et al.*, 2015, Liu *et al.*, 2020). Moreover, although histological cross-sections are widely used in invasion analysis, these need to be prepared orthogonal to the tissue surface to represent tissue architecture accurately, which is difficult to standardise in practice (Smith-Zagone & Schwartz, 2005). With spheroids however, this limitation can be eliminated since a spherical specimen sectioned through its centre guarantees a cross-section throughout all concentric layers (Alemany-Ribes & Semino, 2014, Sant & Johnston, 2017).

It becomes clear that 2D culture models are useful in preliminary investigations of tumour behaviour however these are likely to result in substantial differences when compared with what occurs in a 3D solid tumour. Although there are several reports on the function of S1PR2 in the migration and invasion of several tumours, its role in OSCC remains unclear and therefore needs to be investigated.

1.7 Overall aims

This study aimed to investigate how tissue invasion in three OSCC cell lines namely H357, H400 and H413 was influenced by EGF and S1PR2 in both 2D and 3D cultures as well as gaining insight into any any possible crosstalk between EGF/EGF receptors and S1P/S1PR2 in the control of migration and invasion.

1.8 Overall objectives

a) To develop a suitable protocol of 3D MCTS assay for H357, H400 and H413 cells
b) To determine the effects of EGF on proliferation, migration, invasion and gene expression of the three OSCC lines
c) To determine the effects of S1PR2 on proliferation, migration, invasion and gene expression of the three OSCC lines
d) To determine the crosstalk between EGF/EGF receptors and S1P/S1PR2 that might affect the control of motility of the three OSCC lines

Chapter 2: Materials and methods

2.1 Cell culture

Three human OSCC lines were used in this study: H357 (ECACC 06092004), H400 (ECACC 06092006) and H413 (ECACC 0609200) (Prime *et al.*, 1994, Prime *et al.*, 2004). The H357 line was derived from a stage I carcinoma of the tongue of a 74year-old male patient. The H400 line was derived from the alveolar process stage II carcinoma of a 55-year-old female patient. H413 was derived from a buccal mucosa stage II carcinoma of a 53-year-old female patient.

The cell lines used in these experiments were regularly tested for mycoplasma infection. The cells were maintained in Dulbecco's modified Eagle's medium/nutrient mixture F-12 Ham, 1:1 mixture (DMEM) (SAFC Biosciences, UK). Complete DMEM was made by supplementing to a final concentration of 0.25 μg/ml hydrocortisone (Sigma, UK), 2 mM L-glutamine (Sigma, UK) and Penicillin-Streptomycin solution (Sigma, UK): 98 units/ml of penicillin solution and 98 μg/ml streptomycin. Before use, 10% foetal bovine serum (FBS) (Biosera, UK) was added to the supplemented DMEM.

The cell lines were obtained from liquid nitrogen storage and defrosted in warm water (~37°C). Cell suspensions were transferred into centrifuge tubes (Corning, UK), and 1 ml of media containing 10% FBS (equal amount with cell suspension) and centrifuged at 1000 rpm for 3 min to form a cell pellet. The supernatant was aspirated and cells were resuspended in DMEM containing 10% FBS, before seeding into T75 flasks (Thermo Fisher Scientific, UK) and incubating in an Heracell^{TM} 150i CO_2 humidified incubator (Thermo Fisher Scientific, UK) at 37°C in an atmosphere of 5% CO_2. Media were changed every second day and checked for visible signs of contamination daily.

2.1.1 Subcultures of OSCC cells

Cultures underwent subculturing after visually reaching about 70-80% confluence. Spent medium was aspirated and the cultures were washed twice with phosphate buffered saline (PBS) (Sigma-

Aldrich, UK), then treated with 0.05% trypsin-EDTA solution (Sigma, UK) (1 ml for T25 and 3 ml for T75 flasks) and incubated in a humidified incubator for 8 min and checked using a phase contrast microscopy (Primo Vert, Zeiss, Germany) to ensure cell detachment. The trypsinisation reaction was neutralised with an equal volume of medium containing 10% FBS. Cell suspensions were then transferred into a centrifuge tube (Corning, UK) and centrifuged at 1000 rpm for 3 min to form a cell pellet before removal of the supernatant and resuspension with fresh medium.

2.1.2 Cell counting

To determine the number of viable cells, a trypan blue assay was performed. Equal volumes of cell suspension and 0.4% trypan blue (Sigma, UK) were mixed and incubated for 10 min in the humidified incubator, allowing any cells with damaged membranes (used here to indicate non-viability) to uptake the dye. Trypan blue-cell suspensions were mixed using a pipette and 10 µl used to determine cell number by counting four primary squares of an improved Neubauer haemocytometer using a phase contrast microscopy (Primo Vert, Zeiss, Germany). This allowed cell suspension concentration to be calculated. For subsequent flask seeding concentrations of 0.5 x 10^6 cells in 5 ml for T25 flasks and 1.5 x 10^6 cells in 10 ml for T75 flasks was used.

2.2 Reagent preparation and treatments

Based on previous published work, this study analysed the cellular and molecular effect of two concentrations of EGF, *e.g.* 1 ng/ml (representing a low dose) and 20 ng/ml (representing a high dose) (Kawamoto *et al.*, 1984, Cowley *et al.*, 1986, Kamata *et al.*, 1986, Prime *et al.*, 1994). The EGF solution was prepared by dissolving human recombinant EGF powder (Gibco, UK) in distilled water (dH_2O) to create the stock solution at a concentration of 100 µg/ ml. The stock solution was sterilised using a 0.22 µm-filter and was kept at -20^oC. The working solution

was prepared by freshly diluting in the supplemented DMEM to either 1 ng/ml (representing a low concentration) or 20 ng/ml (representing a high concentration) EGF.

The S1PR2 treatment agents, consisted of a solution of JTE013, a S1PR2 antagonist compound and CYM5478, a S1PR2 agonist compound. The reagent JTE013 (1 -[1,3-dimethyl-4-(2-methyl ethyl)-1H-pyrazolo[3,4-*b*]pyridine-6-yl]-4-(3,5-dichloro-4-pyridinyl)-semicarbazide) (Tocris Bioscience, UK) is a S1PR2 antagonist (Blankenbach *et al.*, 2016). According to the manufacturer's information, this reagent could inhibit the binding of S1P to human S1PR2 with an IC_{50} value of 17.6 nM. However, at a concentration of 10 μM, JTE013 exhibits 4.2% inhibition of S1PR3 but does not inhibit S1PR1. Moreover, JTE013 at a concentration of 10 μM was reported in a study on human breast cancer cells to inhibit S1PR4 as well, although the product sheet did not indicate so (Long *et al.*, 2010). However, there is no evidence on the effects of concentration on the selectivity of JTE013 in OSCC. The reagent CYM5478, 1-[2-[2,5-dimethyl-1-(phenylmethyl)-1H-pyrrol-3-yl]-2-oxoethyl]-5-(trifluoromethyl)-2(1H)-pyridinone is a selective S1PR2 agonist (Herr *et al.*, 2016). According to the manufacturer's information, it is selective for S1PR2 over the other four subtypes.

This study used JTE013 and CYM5478 at concentrations of 10 μM following the methods used in previous studies of smooth muscle cells (Osada *et al.*, 2002), hepatocytes (Ikeda *et al.*, 2003) and rat and mouse basilar artery cells (Salomone *et al.*, 2008). A previous study reported that JTE013 and CYM5478 at 5 μM affected migration and invasion of OSCC (Patmanathan *et al.*, 2016). However, in preliminary tests 5 μM JTE013 and CYM5478 did not cause significant differences in migration, whereas 10 μM, the concentration used for the experiments reported here did show migration differences.

The cells were treated with EGF, JTE013, CYM5478 or combination of EGF and JTE013 or CYM5478. The details of the treatments are specified in the results sections.

2.3 Determination of cell proliferation

To determine the proliferation rates of the cell lines, two types of assays were performed. Growth curves provided an indication of the doubling time and the bromodeoxyuridine (BrdU) assay was used to obtain the proportion of the proliferating cells.

2.3.1 Growth curves and doubling times

Cell suspensions of each of the three lines were diluted to a concentration of 5,000 cells/ml. Two millilitres were plated into each well of a 6-well plate (Thermo Scientific, UK) and cultured with DMEM with 10% FBS, DMEM with 10% FBS containing either EGF treatments or S1PR2 treatments. Fresh media were replenished every second day. The number of viable cells in each group was counted following trypsinisation on days 2, 4, 6, 8, 10, 12 and 14 and growth curves plotted. The doubling time (T_d) was determined from the gradient of the growth curve in the log phase of the plots, using the equation below,

$$Td = \frac{ln2}{K}$$

where K is the growth rate expressed as the fractional increase or decrease. The untreated group was used as the normal control. The experiment was carried out using three biological replicates from independent experiments.

2.3.2 BrdU proliferation assay

5-Bromo-2'-deoxy-uridine Labeling and Detection Kit II obtained from (Roche, Germany) uses immunohistochemistry for detecting BrdU incorporated into nuclear DNA.

Single cell suspensions generated from the three cell lines of H357, H400 and H413 in DMEM containing 0.1% FBS were diluted to a concentration of $2.5x10^4$ cells/ml. One millilitre of each cell suspension was added to a 24-well plate and incubated in the humidified incubator for 24 h to allow

cell attachment. Subsequently, the media were replaced with 1 ml of FBS-free DMEM and FBS-free DMEM containing either EGF or S1PR2 treatments and incubated for 48 h.

After this, the old media were removed and cells were incubated with medium containing the BrdU labelling reagent in the humidified incubator for 60 min. Cultures were then washed three times with PBS and fixed with ethanol (30 ml 50 mM glycine in 70 ml absolute ethanol) at -20ºC for 20 min. Cultures were washed three times with buffer and incubated with 1:10 dilution of anti-BrdU antibodies in incubation buffer for 30 min at 37°C. Cultures were then washed three times and incubated with 1:10 dilution of anti-mouse Ig-AP in PBS for 30 min. Cultures were washed three times with PBS and incubated with colour substrate solution (mixture of 13 µl 4-nitro blue tetrazolium chloride (NBT) -solution and 10 µl 5-bromo-4-chloro-3-indolyl-phosphate (BCIP) -solution in 3 ml substrate buffer) at room temperature (~25ºC). then washed with PBS twice. Since the nuclei of BrdU-negative cells were difficult to visualise, these were stained with DAPI (Abcam, UK) (**Figure 7A-B**). The untreated group was used as the normal control, while the negative control group was prepared by treating cells with water (the solvent of the stock BrdU solution) during the BrdU staining step, so the newly synthesised DNA of this group would not be stained in blue (**Figure 7**). Cultures were visualised using bright field and fluorescence microscopy (Nikon Eclipse TE300, Japan) equipped with a digital camera (Nikon D5100, Japan). The resolution of the image was determined using a stage micrometre (Graticules, UK). For images captured using the X20 objective lens, the resolution was 1 pixel = 0.12 µm. Finally, 1,000 BrdU positive cells from three individual experiments were counted manually. The data was presented as percentages.

2.4 Migration assays

To investigate the migration of three OSCC lines, the study performed two assays including scratch wound assay and transwell migration assay.

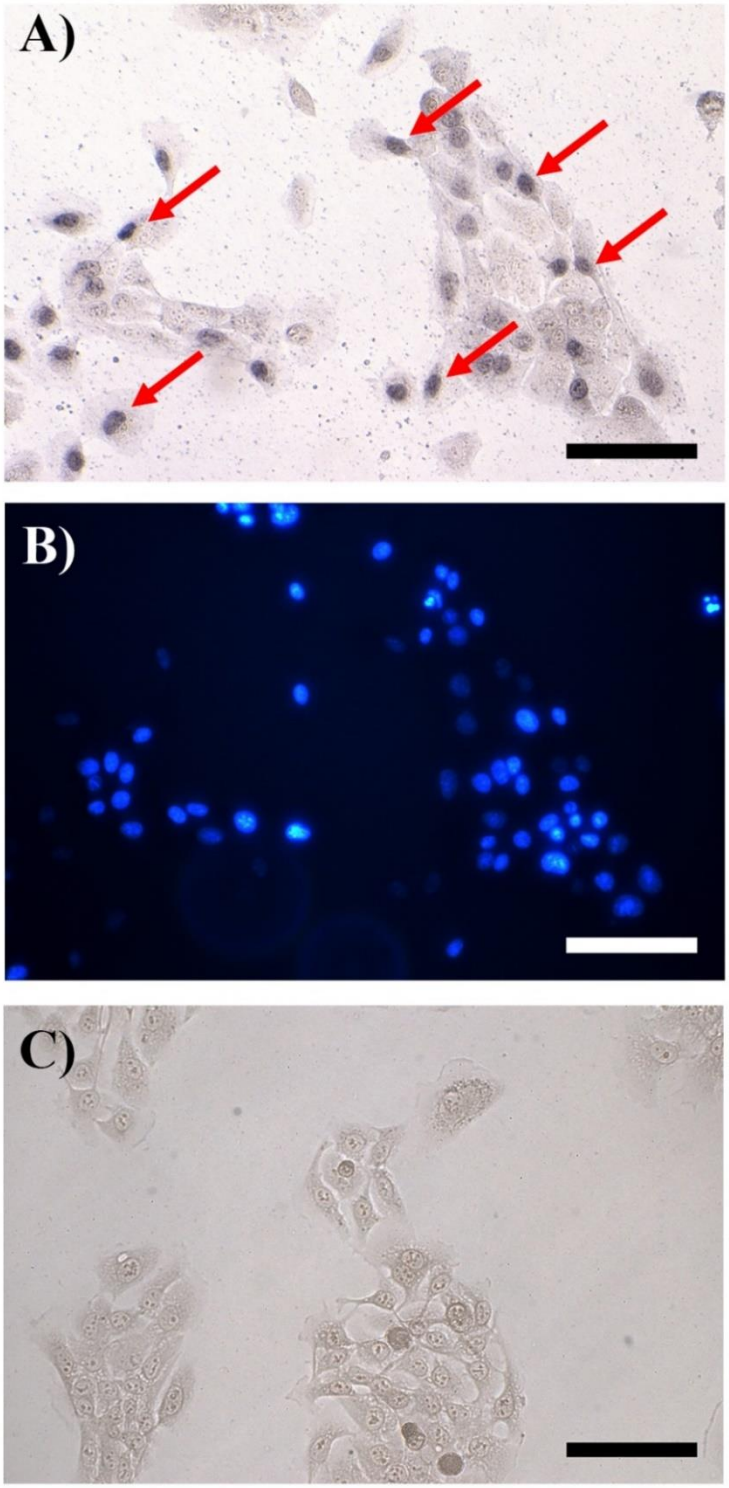

Figure 7. Representative images of BrdU staining in an untreated H357 culture. **A)** Red arrows indicate dark blue nuclei of proliferating cells. **B)** To visualise all nuclei, the cultures were stained with DAPI. Image of the same area in A) captured using fluorescence microscopy. **C)** In the negative control, cells were treated with the water (solvent of BrdU solution) in the BrdU staining step. This is to show how the BrdU negative cells would appear. Cells in this group did not exhibit dark staining in the nucleus in the negative control. (Scale bar = 50 µm; X20 objective lens).

2.4.1 Scratch wound assay

The scratch wound assay is an *in vitro* method to evaluate the ability of cells to migrate over time by assessing how the cells at the edge of a scratch wound move across the generated gap in monolayer culture (Liang *et al.*, 2007). Migration is determined by comparing the gap area or width from images captured at different culture time points (Grada *et al.*, 2017). Six-well plates were prepared by drawing (with a fine point marker) two horizontal reference lines on the underside of the plates to ensure that images were captured from the same location at each time point (**Figure 8A**). Single cell suspensions of OSCC lines were prepared at a concentration of 0.3 x 10^6 cells/ml. One millilitre of cell suspension was seeded into the 6-well plates and incubated in the humidified incubator. Media were replenished every second day until cultures were 100% confluent. Since proliferation increased cell number, with the limitation of space, cells at the border of the wound tended to be pushed towards the wound gap and influenced the migratory data. For this reason, cultures were washed twice with PBS and incubated with 1 ml FBS-free DMEM containing 8 µg/ml mitomycin C (Merck, UK) in the humidified incubator for 2 h to inhibit cell proliferation, before performing the scratch process.

After mitomycin C treatment, the culture scratch wound was performed using a sterile 200 µl-pipette tip, guided with a ruler to create a straight line across the centre of each well, perpendicular to the reference lines. Cultures were washed with PBS three times to remove any debris and the remaining media containing mitomycin C. One millilitre of the FBS-free media (control) and FBS-free media containing either EGF or S1PR2 treatments was added to the appropriate wells. The wounds were visualised using phase-contrast microscopy (Nikon Eclipse TE300, Japan). Images were captured captured using a digital camera (Nikon D5100, Japan) (resolution of image captured with X4 objective lens: 1 pixel = 0.58 µm, determined with a stage micrometre) and data files were saved in '.NEF' format.

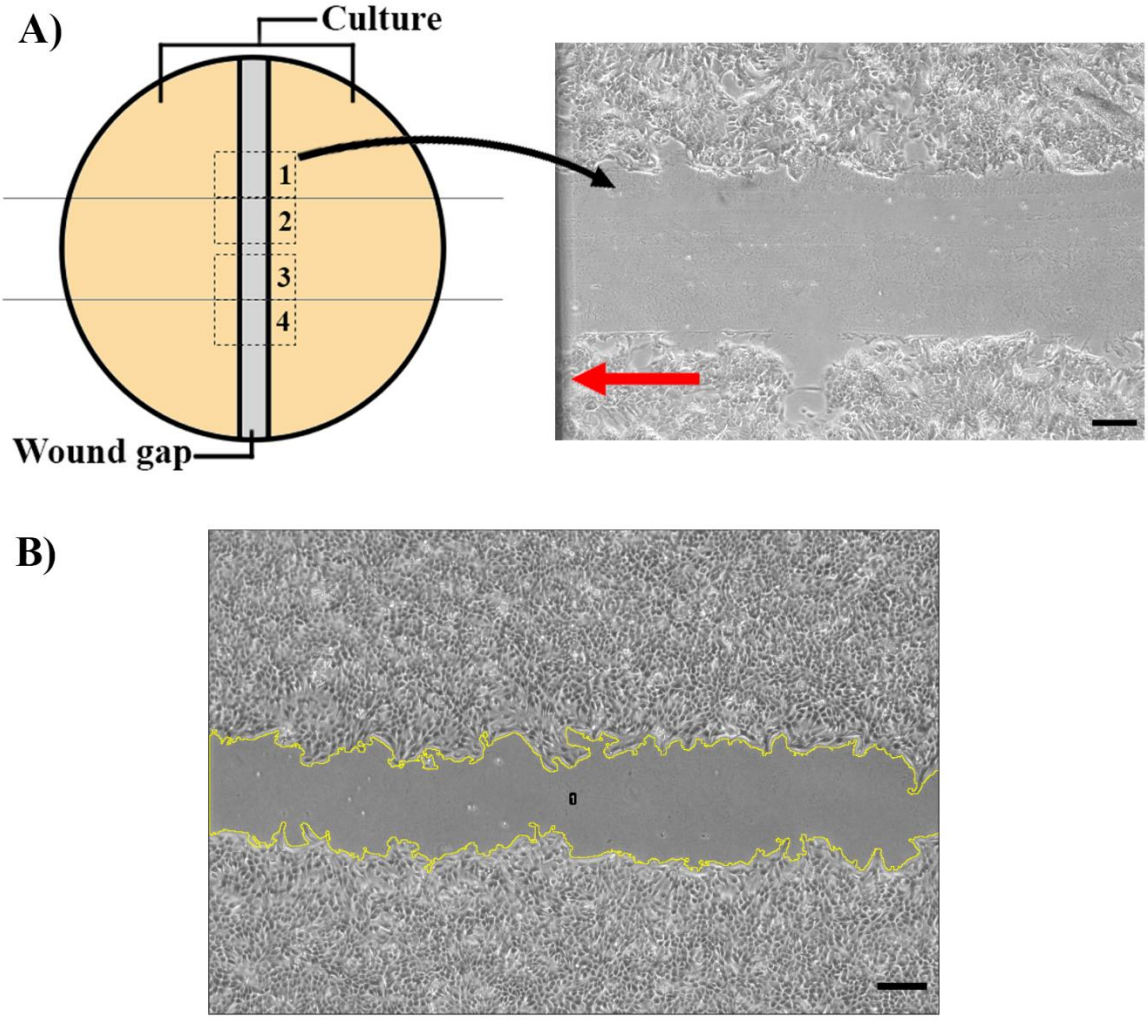

Figure 8. Scratch wound assay determining migration. Two horizontal lines drawn at the bottom of the well were used as reference lines for taking images. Dashed-line boxes represent areas where images were captured (left). In the example image of untreated H357 (8 h of incubation) before being cropped, the red arrow points to the reference line (right). **B)** Example of the MRI_Wound_Healing_Tool plugin detection (in yellow) of the margins of the scratch wound image of untreated H400 captured using phase contrast microscopy. (Scale bar = 200 μm; X4 objective lens).

Four images were captured from four areas along the scratch gap (above and below the reference lines) at 0, 12, 18 and 24 h (samples were returned to the incubator during these time points) and three biological replicates were performed from independent experiments. All images were captured to include the reference lines to ensure that the same areas were imaged at the different time points.

Images were analysed using ImageJ (v1.52r) (Rasband, 1997) and the DCRaw Reader plugin was used to open the NEF file data (Coffin, 2008). All images were captured so the scratched lines were aligned horizontally and cropped to a size of 1100.18 x 700.63 µm and then converted to 8-bit greyscale. Gap areas were measured using the MRI_Wound_Healing_Tool plugin written by Volker Baecker (Fenu *et al.*, 2019) which enabled measurement of the area between the margins of the scratch wound (**Figure 8B**). The parameters used set in the plugin were as follows: variance filter radius = 10; threshold = 50; radius open = 4; and minimum size of the particle = 10,000. The percentage wound closure was calculated according to the formula (Grada *et al.*, 2017):

$$Percentwoundclosure = \left(\frac{Area(t0) - Area(tn)}{Area(t0)}\right) x100$$

where Area (T_0) is the initial gap area (in μm^2) and Area (T_n) is gap area at time n (in μm^2).

2.4.2 Transwell migration assay

The transwell migration assay is another technique used to determine cell migration rate in response to various chemo-attractants (Justus *et al.*, 2014) based on the observation of the movement of single cells through a filter membrane towards a chamber which has a high concentration of chemoattractants.

H357, H400 and H413 cells were grown in T75 flasks until approximately 90% confluent. Then, cultures were washed twice with PBS and incubated in 5 ml of media containing mitomycin C (Merck, UK) at 8 µg/ml concentration in the humidified incubator for 2 h. Cultures were washed twice with PBS and single cell suspensions were generated by trypsinising and diluted in FBS-free media to a concentration of 8.0 x10^5 cells/ml.

The transwell inserts used in this experiment had 8µm-pore size membranes (Greiner bio-one, UK) and were placed in the 6-well plates to create an upper and a lower chamber. Either EGF or S1PR2 treatments were added to cell suspensions. Then, 1.5 ml of each cell suspension were added to the upper chamber of the inserts. Equal amounts of media containing 10% FBS was added into the lower chamber to create the gradient between the upper and the lower chambers and incubated in the humidified incubator for 24 h.

After incubation, tissue culture inserts were washed twice with PBS and non-migrated cells on the upper surface of the insert membrane were removed using cotton-tipped applicators (Thermo Fisher Scientific, UK). The tissue culture inserts were carefully immersed into the glass beaker containing PBS to remove cell debris. This step was undertaken twice to ensure that non-migrated cells were completely removed since the remaining cells on the upper surface of the membrane could be seen using the microscopy (**Figure 9A**). Tissue culture inserts now contained only migrated cells on the lower surface of the filter membrane and these were stained with Calcein AM (Thermo Fisher Scientific, UK). The Calcein AM solution (Invitrogen, UK) was prepared by diluting Calcein AM stock solution in PBS to give a final concentration of 2 µM Calcein AM. One millilitre of the Calcein AM solution was added to the lower chamber of the 6-well plates where tissue culture inserts were located. The 6-well plates were covered with aluminium foil to prevent bleaching from exposure to light and incubated at room temperature for 30 min.

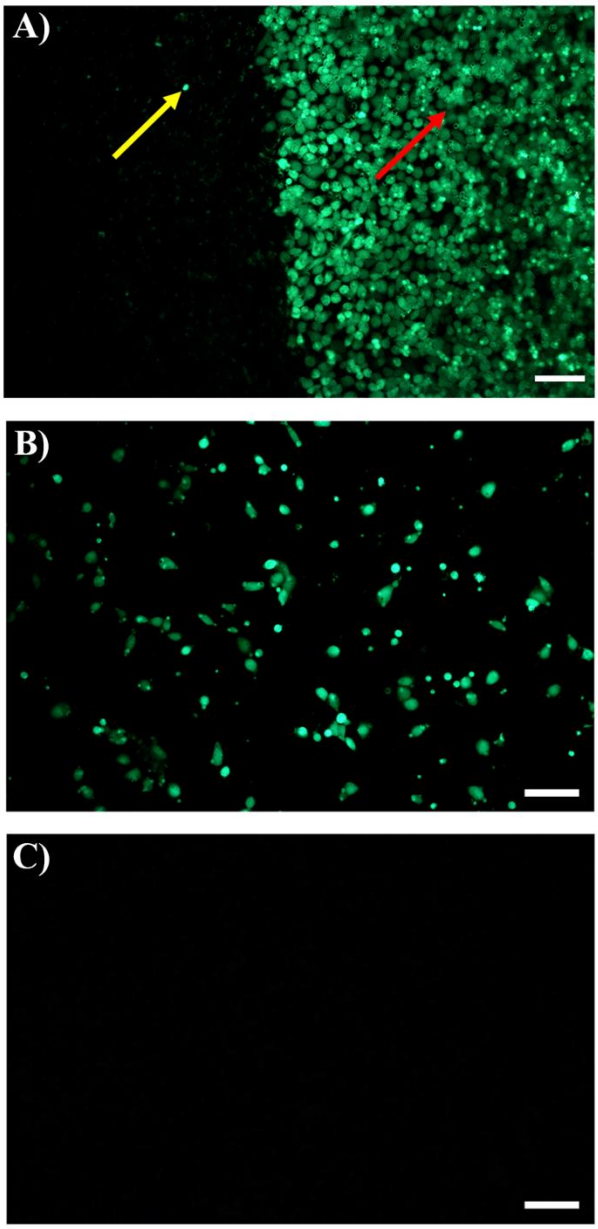

Figure 9. Example image of transwell migration assay captured using fluorescence microscopy. **A)** The interference of non-removed cells on the upper side of the transwell membrane (example of untreated H413). The left side of the image corresponds with the the upper part of the membrane where cells were removed. Only a few stained cells remained on that side (yellow arrow). The right side of the image corresponds with the area where cells on the upper side of the membrane were not removed (red arrow). When not removed, stained cells covered the entire membrane and it was not possible to detect migrated cells. **B)** Cells attracted by 10% FBS media were stained with calcein AM. **C)** Negative control well where the lower chamber contained FBS-free media showed no obvious cells stained with calcein AM. (Scale bar = 100 µm; X10 objective lens).

Then, the insert membranes were cut using a scalpel blade no. 12 (Swann-Morton, UK) and placed in a new 6-well plate. One millilitre of PBS was added to each well to prevent cell drying.

Migratory cell membranes were visualised with a fluorescence microscopy (Nikon Eclipse TE300, Japan**).** The Calcein AM stain was excited at a wavelength of 490 nm (**Figure 9B**). The untreated group was the normal control, while the group in the lower chamber without addition of 10% FBS was the negative control (**Figure 9C**). Images were captured with a DSLR camera (Nikon, Japan) connected to the microscopy and saved as '.NEF' files. Ten images were captured (resolution of image captured at X10 objective lens: 1 pixel = 0.24 μm) per group and cell counts were performed from images manually. The experiment was undertaken using three biological replicates from independent experiments.

2.5 Determination of invasion

Invasion in cancer is defined as the penetration of cancer cells into the surrounding tissues. In epithelial neoplasms, to invade through the connective tissue, cells must modify their shape and interact with the ECM. Several assays can be used to determine invasion, such as the transwell invasion assay (Kramer *et al.*, 2013), the Platypus invasion assay (Hulkower & Herber, 2011) and 3D cell tracking (Pijuan *et al.*, 2019). Each of these assays provide different information and all have some limitations; in this thesis, the transwell invasion and multicellular tumour spheroid (MCTS) assays were used as each can overcome limitations of the others.

2.5.1 Transwell invasion assay

The transwell invasion assay is a variation of the transwell migration assay where ECM is added to the tissue culture insert before introducing the cell suspension. Cells therefore, guided

by a chemoattractant gradient, invade through the ECM before penetrating the transwell membrane (Justus *et al.*, 2014). Transwell inserts with 8µm pores membrane (Greiner bio-one, UK) were positioned in the 24-well plates and 30 µl 0.5 mg/ml rat tail collagen type I matrix (Cultrex, UK)

were applied to the upper surface of the insert membrane (the preparation of the collagen matrix is described in **section 2.5.2.2**). The cultures were incubated in the humidified incubator for 1 h to allow the collagen gel to set. The three OSCC lines were treated with 5 ml of 8 µg/ml mitomycin C (Merck, UK) for 2 h to inhibit proliferation. Cell suspensions were created from monolayer cultures and were diluted to a concentration of 5.0 x 10^4 cells/ml. Five hundred microlitres of diluted cell suspensions were added with either EGF or S1PR2 treatments before transferring to the collagen-coated tissue culture inserts. Five hundred microlitres of DMEM containing 20% FBS were added to the lower insert chamber to create a chemoattractive gradient between the upper and the lower chambers The group in the lower chamber without addition of 20% FBS was considered as the negative control. The cultures were then incubated in the humidified incubator for 48 h. Following this, collagen and non-migrated cells present in the upper chamber were removed and the staining and image capturing procedures were undertaken as described in **section 2.4.2**. Cell counts were performed manually and the experiment was undertaken using three biological replicates from independent experiments.

2.5.2 Multicellular tumour spheroid (MCTS) assay

To perform the MCTS assay, the procedure was divided into four steps including the generation of the spheroid, collagen matrix preparation, the embedding of the spheroids and spheroid shape analysis.

2.5.2.1 Generation of MCTSs

The experiment began with the selection of the spheroid generation method, out of three common approaches: hanging drop, liquid-overlay and ultra-low attachment (ULA)-plates. For hanging drop method, single cell suspensions of H357, H400 and H413 were produced from monolayer cultures and diluted to a concentration of 1.67 x 10^4 cells/ml. To create a humidified environment to prevent dehydration of the hanging drops, 5 ml PBS was added to 9-cm petri dishes (Thermo Fisher Scientific, UK). Droplets were generated by transferring 30 µl of each cell suspension to the inner surface of the lid, providing approximately 500 cells per spheroid. The lid was then gently inverted and placed over the culture dish which contained 5 ml PBS. The hanging-drop cultures were placed in a humidified incubator for one day to allow cell aggregation (Berens *et al.*, 2015) (**Figure 10A**). For the liquid-overlay method, 2% W/V cell-culture-grade agar (Sigma-Aldrich, UK) was added into a 96-well plate (Thermo Fisher Scientific, UK) and left to set. Then, 150 µl of cell suspension (3.33 x 10^3 cells/ml) was added into a prepared well plate and incubated for 24 h (**Figure 10B**). For the ULA-microplate method, 150 µl of cell suspension (3.33 x 10^3 cells/ml) was added into each well (Perkin Elmer, UK) and incubated and observed daily using phase contrast microscopy for four days (**Figure 10C**).

2.5.2.2 Collagen matrix preparation

Collagen hydrogel was prepared by mixing rat-tail collagen type I (Cultrex, UK) with X10 DMEM (Sigma-Aldrich, UK), DMEM (Biosera, UK) and dH_2O on ice to fabricate a range of concentrations of rat-tail collagen matrix including 0.5, 1.5 and 3 mg/ml. The pH of the collagen matrix was adjusted to 7.4 by adding 1M NaOH solution (Sigma-Aldrich, UK) and 7.5% W/V $NaHCO_3$ solution (Sigma-Aldrich, UK).

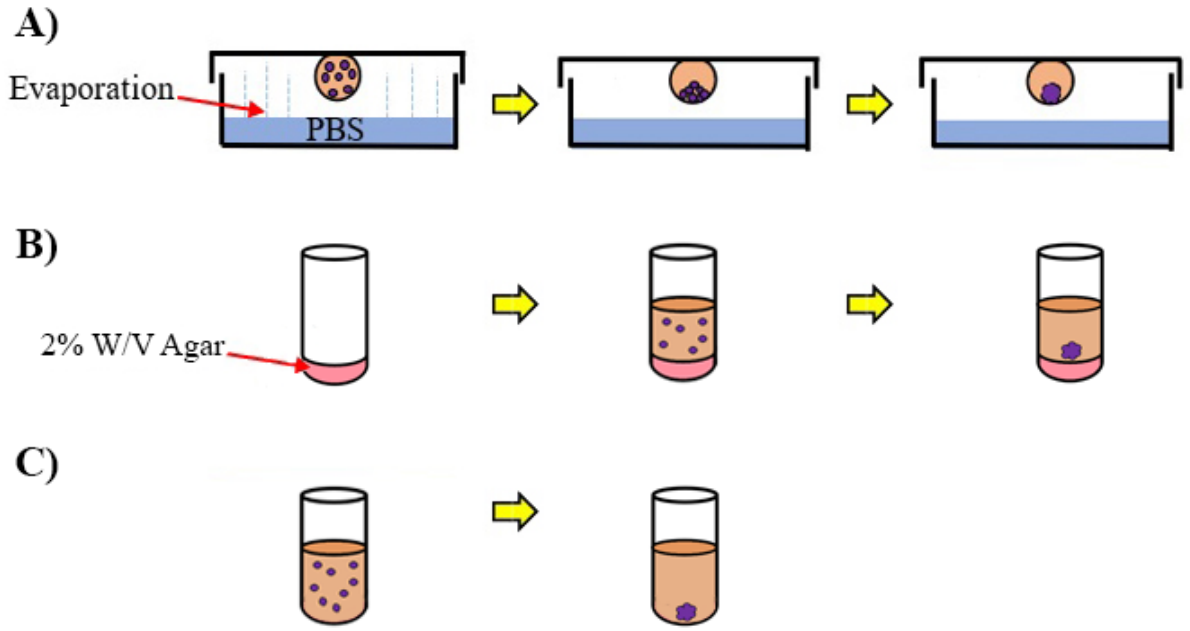

Figure 10. Three methods of tumour spheroid generation. **A)** In the hanging drop method, 30 µl of cell suspension containing approximately 500 cells was hung on the inner surface of the petri dish lid for one day to allow spheroid formation. **B)** In the liquid-overlay method, the bottom of each well was coated with agar to prevent cell attachment, before adding cell suspension (500 cells per 150 µl) and incubating the culture for one day. **C)** In the ULA-microplate method, a cell suspension (500 cells per 150 µl) was added into each well and incubated for four days. The images (left to right) show the dispersed cells growing into tumour spheroid structures.

2.5.2.3 Transferring and embedding tumour spheroids into the collagen matrix

After a spheroid was formed, PBS was removed from the bottom of the petri-dish and the petri-dish was carefully inverted. Spheroid morphology was observed using phase contrast microscopy (Primo Vert, Zeiss, Germany). Then, the petri-dish was inverted to the original position and left for at least 15 min to allow the spheroid in the droplet to descend by gravity to the bottom of the droplet. The transferring process was done in the upside-down position as shown in **Figure 11A**.

Sixty microlitres of plain collagen mixtures were seeded on the base of the 48-well plate to prevent the spheroid from contacting the plate. The tumour spheroid was transferred into the newly mixed collagen matrix. Then, 280 µl of collagen matrix containing tumour spheroid was transferred into the 48-well plate. Finally, 60 µl of collagen matrix were prepared and overlaid the spheroid (**Figure 11B**). This was undertaken to avoid the tendency of cells to spread along the surface (Liu *et al.*, 2020) and the loss of the spherical morphology (**Figure 12**).

Samples were incubated in the humidified incubator for 20 min to allow gel formation**.** Calcein AM (Thermo Fisher Scientific, UK) was added into media without FBS at a ratio of 0.1 µl Calcein AM stock solution per 1 ml of DMEM. Two hundred microlitres were added to each well. Samples were incubated in the humidified incubator for 30 min. In the experiments with media containing 1 ng/ml EGF; 20 ng/ml EGF; 10 µM JTE013 or 10 µM CYM5478 (chapters 4, 5 and 6), the concentrations prepared were three times higher than required, to compensate for the dilution that would occur when the reagents penetrated the collagen matrix (Vinci *et al.*, 2015). For this experiment, replenishment of media was not performed because the tumour observation was carried out within two days. Tumour spheroids were visualised using confocal microscopy (Zeiss LSM 700, Germany) equipped with a photomultiplier (Zeiss LSM T-PMT, Germany) **(**resolution of image captured using a X10 objective lens was 1 pixel = 1.52 µm).

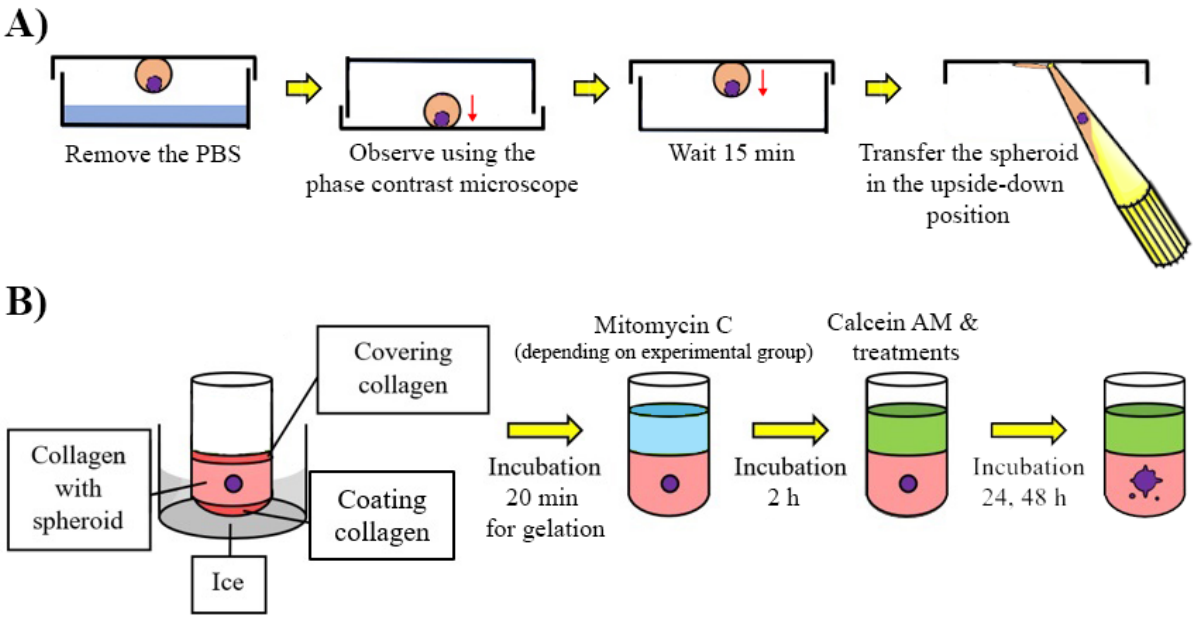

Figure 11. The process of transferring, embedding and culturing tumour spheroids in the collagen matrix. **A)** After cells were aggregated, the spheroid was observed using phase contrast microscopy. The plate was left still for 15 min after being turned over back to the original position. Aspiration was done in the upside-down position (left to right). **B)** There were three collagen layers in the experimental setup: the coating layer, the collagen containing the spheroid and the covering collagen. After the collagen set, the growth-inhibited group was treated with mitomycin C for 2 h. Samples were incubated in media containing calcein AM for 30 min and incubated with the relevant treatments depending on the experimental group (EGF, S1PR2 antagonist, S1PR2 agonist, or the combination of EGF and S1PR2) 48 h. Images were captured on the embedding day (0), day 1 and day 2 (left to right).

Images of the middle plane of the spheroid were captured at 0, 24 and 48 h after being embedded. In the example image of the spheroid partially reverted when touched to the well (**Figure 12**), H413 spheroids were mixed with 3 mg/ml collagen matrix and transferred into the mounted capillary tube. Spheroids were stained with calcein AM (Thermo Scientific, UK) for 30 min, captured using light-sheet fluorescence microscopy (Leica SP8, Germany, resolution 1 pixel = 0.36 μm.) and reconstructed using 3D view function.

2.5.2.4 Spheroid shape characterisation

Five parameters were used to describe the invasion features of the spheroids: number of clusters, the maximum invading distance, circularity, fractal dimension and the maximum diameter of the main cluster. The 'number of clusters' represented the number of tumour fragments that detached into the matrix which could be seen as an indication of infiltration as opposed to expansive or cohesive growth. The 'maximum invading distance' was the distance travelled by detached cells invading the collagen matrix. The 'circularity' of the main cluster was a morphological parameter describing how the largest cell cluster approached a circle while the fractal dimension (again of the main cluster) represented the degree of complexity of the boundary of the largest cluster. The circularity of irregular objects is a size-dependent parameter as it is calculated according to the formula below (Russ J.C. & R.T., 2000):

$$Circularity = \frac{4\pi Area}{Perimeter^2}$$

Where Area = the area of the main cluster of the spheroid and Perimeter = the length of the cluster boundary.

The 'fractal dimension' differs from circularity in that it is size-independent and its value is computed using the following formula (Mandelbrot, 1967):

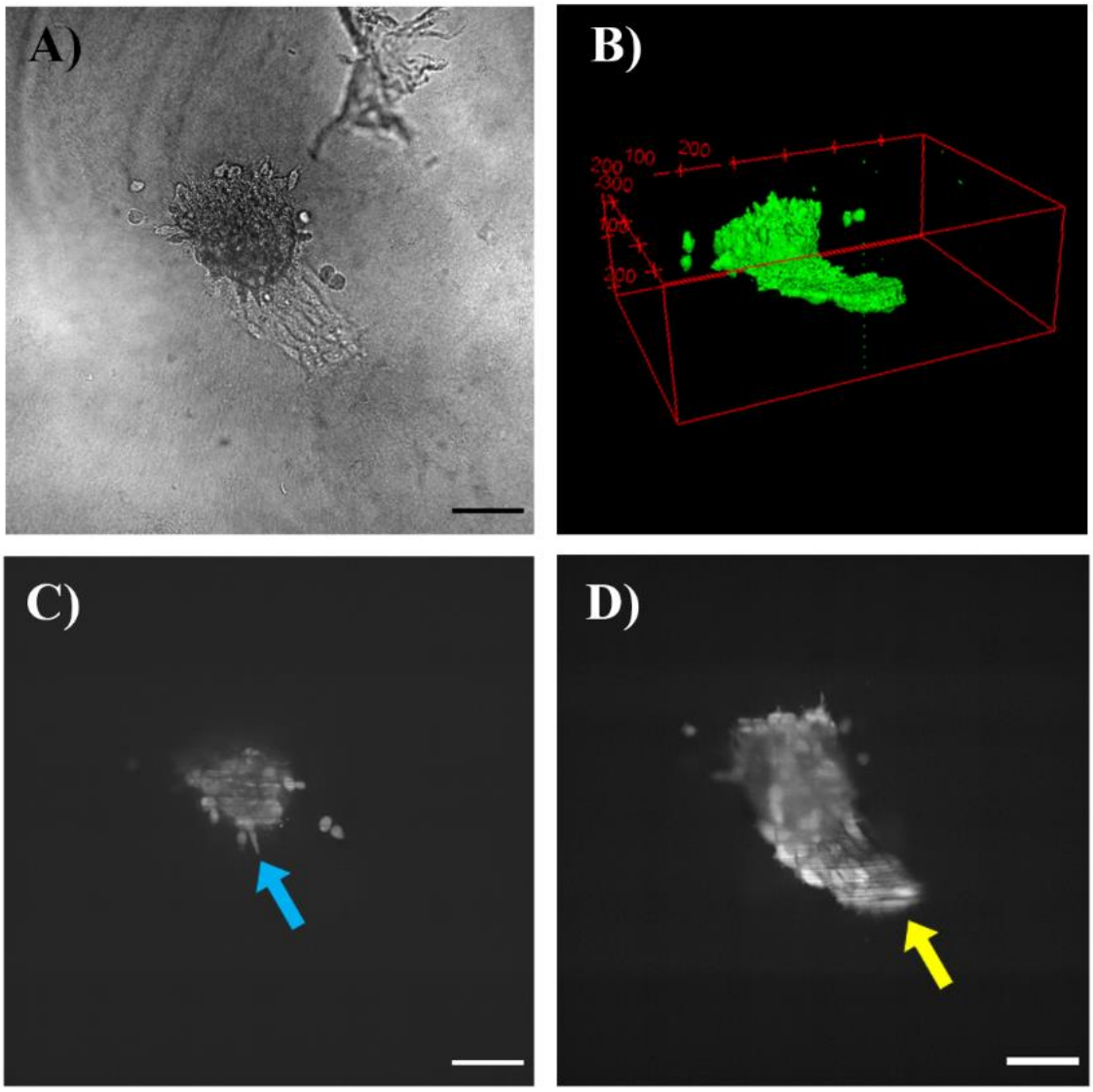

Figure 12. Example showing the importance of spheroid's positioning (untreated H413 spheroids embedded in 3 mg/ml collagen for one day). **A)** In this bright-field image, it is hard to distinguish between cells invading the collagen matrix and those spreading as a monolayer. **B)** 3D construction of the same spheroid shows that it is spreading along the well bottom. **C)** Image of the spheroid (the upper part) showing cells extending spike-like protrusions (blue arrow) into the matrix. **D)** In the lower part of the spheroid that touched the well, cells spread along the plate, adopting a polygonal morphology (yellow arrow). (Scale bars represent 100 μm; images were captured using a light-sheet fluorescence microscopy (Leica SP8, Germany, resolution 1 pixel = 0.36 m).

$$D = \lim_{s>0} \frac{\log(N(S))}{\log 1/S}$$

Where N(s) = number of square boxes intersected by the image, S = side length of the boxes and D = fractal dimension, which for images of closed boundaries on the plane has values $1 \leqslant D \leqslant 2$.The two parameters define different aspects of the morphology of the tumour's border.

The analysis was as follows: a folder of renamed images was opened as a stack in ImageJ software (Rasband, 1997). Areas occupied by cells were segmented using Li's thresholding method (Li & Lee, 1993). Then, the result was processed by filling holes in the thresholded result followed by a morphological opening (minimum filter followed by maximum filter of radius = 1 pixel), and a binary reconstruction to remove artifacts that disappear after 3 morphological erosions). A stack of the segmented images was saved for further calculation of the number of cell clusters and invading distance using the Particles8 plugin (Landini, 2021). For invading distance, the stack was processed with the BinaryFilterReconstruct plugin (performing three erosions followed by a Binary Reconstruction). Finally, the largest distance between two points of visible cells was computed using the Convex Hull Plus plugin (Landini, 2021).

To analyse the morphology of the main cluster, smaller particles were eliminated from the image, keeping the largest particle of each image. The maximum diameter of the main cluster (MDMC or Feret diameter of the spheroid), the largest distance between any two points in the spheroid) and the circularity of spheroids were calculated using the Particles8 plugin. The fractal dimension was computed from the boundaries of the segmented spheroids (using the Find Edges and Skeletonize commands) before applying the Fractal Box Count function using boxes of 4, 6, 8, 12, 16, 32, 64 pixels.

2.6 Reverse Transcription-Polymerase Chain Reaction (RT-PCR)

RT-PCR is a highly sensitive and specific method for analysing RNA transcripts. It is based on reverse transcribing mRNA to complementary DNA (cDNA), then amplifying the cDNA template to detectable levels and quantifying the relative or absolute gene expression levels within and between sample groups (Walker *et al.*, 2002). Two types of reverse transcription polymerase chain reaction (RT-PCR) were used in this study, including: semi-quantitative (sqRT-PCR) and real-time polymerase chain reaction (real-time PCR). The methods are described as follows.

2.6.1 Semi-quantitative reverse transcriptase-polymerase chain reaction (sqRT-PCR)

The first method performed was sqRT-PCR. This method involves multiple individual steps including, cell culture preparation, total RNA extraction, RNA quantification, reverse transcription of total RNA, sqRT-PCR amplification reaction and electrophoresis.

2.6.1.1 Cell culture preparation for the harvest of total RNA

H357, H400 and H413 cells were cultured in a T25 flask with DMEM supplemented with 10% FBS until reaching approximately 80% confluence. Cells were treated with either EGF (1 ng/ml and 20 ng/ml), S1PR2 antagonist or S1PR2 agonist for 4 h (sqRT-PCR) and for 48 h (real-time PCR). Cultures were washed with PBS at room temperature to remove any remaining media that could interfere with the cell lysis process.

Total RNA was extracted from the OSCC cultures using the RNeasy kit (Qiagen, UK), as described below. After washing with PBS, 350 µl of Buffer RLT were added to the cultures and pipetted to ensure that the lysis buffer covered all areas.

2.6.1.2 RNA purification

After RNA was extracted using the RNeasy kit, an on-column DNase I digest (Merck, UK) was used to purify the RNA by removing the DNA. The lysates were transferred into an Eppendorf tube and an equal volume of 70% ethanol added to enable precipitation of RNA and were mixed by pipetting. Then, lysate samples were transferred into RNeasy spin columns assembled in 2 ml-collection tubes and centrifuged at 10,000 rpm for 30 sec and the flow-through was discarded.

Three hundred and fifty microlitres of Buffer RW1 were added to the samples and centrifuged at 10,000 rpm for 30 sec. The flow-through was discarded and the spin column remained in the original collection tube. DNA was lysed by adding 80 µl deoxyribonuclease I (DNase I) mixture (10 µl DNAse I and 70 µl digest buffer) into the column and incubated at room temperature for 15 min. After the DNA was digested, 350 µl buffer RW1 was added and centrifuged at 10,000 rpm for 30 sec and the flow-through was discarded and 500 µl of Buffer RPE was added to the columns and centrifuged at 10,000 rpm for 30 sec, before discarding the flow-through.

Five hundred microlitres of Buffer RPE was added to the sample and centrifuged at 10,000 rpm for 2 min and the flow-through discarded. The column was placed into a new 1 ml-collection tube and centrifuged at 13,200 rpm for 1 min before replacing the spin columns assembled in 1.5 ml-collection tubes. Samples were solubilised with 30 µl of RNase free water and centrifuged at 10,000 rpm for 1 min to elute the RNA.

2.6.1.3 RNA quantification

After extraction, RNA was quantified using a Genova Nano micro-volume spectrophotometer (Jenway, UK). First, 1 µl RNase-free water was transferred to a clean lower 'read head' to obtain the value of the base line absorbance. Then, after wiping the lower read head with ethanol alcohol, 1 µl of RNA sample was transferred to the lower read head. Spectrophotometer

readings indicated as the amount of RNA (µg/ml) and the purity (260/280). This process was repeated for each sample and average values used in calculations for downstream analyses.

2.6.1.4 Reverse transcription of total RNA

RNA was used to generate cDNA by reverse transcription using the Tetro kit (SLS, UK). A final volume of 12 µl reaction mix for each sample consisted of 2 µg of RNA, 1 µl of oligo (dt)18, 1 µl of 10 mM dNTP, 4 µl of 5X RT buffer, 1 µl of RNase inhibitor and 1 µl of reverse transcriptase (200 mg/ml). Samples were incubated in a thermal cycler (Eppendorf, Germany) at 45°C for 30 min and the reaction terminated at 85°C for 5 min. Obtained cDNA was diluted in 30 µl of RNase free water.

2.6.1.5 Semi-quantitative RT-PCR amplification reaction

The REDTaq (Merck, UK) system was used to perform a polymerase chain reaction. Primers were purchased from Invitrogen (UK). The primer sequences used for sqRT-PCR were derived from the NCBI database (https://www.ncbi.nlm.nih.gov/tools/primer-blast/) (**Table I**). The amplification reaction included 2 µl of forward and reverse primer (10 µM), 9.5 µl of RNase free water, 12.5 µl of REDTaq probe (Merck, UK), and 1 µl of cDNA (approximately 200 ng). The final PCR volume was 25 µl. The amplification of the target gene sequences was cycled under the following conditions: denaturation step at 94°C for 5 min; annealing step at 94°C for 20 sec, 60°C for 20 sec and 72°C for 20 sec; and extension step at 72°C for 10 min, respectively. The amplification process was performed using three biological replicates in a separate experiment for each gene.

Table I. Details of primer assays for sqRT-PCR analysis

Gene name	Supplier	NCBI Access number	Sequence (from 5' to 3')	Melting temp. (°C)	Products base pair (bp)
Homo sapiens glyceraldehyde-3-phosphate dehydrogenase	Invitrogen	NM_001256799.3	**F:** TCTAGACGGCAGGTCAGGTCC	63	598
			R: CCACCCATGGCAAATTCCATG	60	
Homo sapiens sphingosine-1-phosphate receptor 1	Merck	NM_001400.5	**F:** GCCCAGTGGTTTCTGCGGGAA	74	341
			R: ACCAAGGAGTAGATCCTGCAGTA	62	
Homo sapiens sphingosine-1-phosphate receptor 2	Invitrogen	NM_173556.5	**F:** ACCAAGGAGTAGATCCTGCAGTA	60	577
			R: GCAACAGAGGATGACGATGA	57	
Homo sapiens sphingosine-1-phosphate receptor 3	Merck	NM_005226.4	**F:** CTCAGGGAGGGCAGTATGTTC	64	336
			R: GGACTTGACCAGGAAGTAGATGCG	68	
Homo sapiens sphingosine-1-phosphate receptor 4	Merck	NM_003775.4	**F:** TCCAGCCTTCTGCCCCTCTAC	68	306
			R: CAGGGCCAGGATCCAGTCCAT	71	
Homo sapiens sphingosine-1-phosphate receptor 5	Merck	NM_001166215.2	**F:** GCCGGTGAGCGAGGTCATCGT	74	552
			R: TAGGCCTTGGCGTAGAGCGG	70	

Table I. Details of primer assays for sqRT-PCR analysis (continued)

Gene name	Supplier	NCBI Access number	Sequence (from 5' to 3')	Melting temp. (°C)	Products base pair (bp)
Homo sapiens epidermal growth factor	Merck	NM_001963.6	**F:** TAGGCATTAGCCATGGTGCC	60	342
			R: TCAAGTCATCCTCCCATCACC	59	
Homo sapiens epidermal growth factor receptor	Merck	NM_001346900.2	**F:** AGAAAGGCAGCCACCAAATTAGCC	66	304
			R: TTCCTGGCTAGTCGGTGTAAACGT	66	
Homo sapiens Rac family small GTPase1	Invitrogen	NM_018890.4	**F:** TGATGCAGGCCATCAAGTGT	59	287
			R: ATCGGCAATCGGCTTGTCTT	60	
Homo sapiens matrix metallopeptidase 9	Invitrogen	NM_004994.3	**F:** TTCGACGGGAAGGACGGGCT	65	470
			R: ACCGTCGAGTCAGCTCGGGT	65	
Homo sapiens Cadherin1	Invitrogen	NM_001317185.2	**F:** CAAGTGCCTGCTTTTGATGA	56	339
			R: GCTTGAACTGCCGAAAAATC	56	
Homo sapiens Vimentin	Merck	NM_003380.5	**F:** AGTTTTTCAGGAGCGCAAGA	58	195
			R: TTGGTTGGATACTTGCTGGA	56	

2.6.1.6 Electrophoresis

The PCR products were subjected to electrophoresis in 1.5% agarose gel to visualise the amplified product. The agarose gel was prepared by adding 0.9 mg of agarose powder (Bioline, UK) to 60 ml of 1X TAE (Severn Biotech, UK) buffer in a conical flask. The mixture was heated using a microwave oven (800 Watts) for 1 min and was swirled to allow the powder to melt and combine evenly before being re-heated again in the microwave for 30 sec.

After the agarose was completely solubilised, 3 µl of SYBR Gold (Invitrogen, USA) were added and swirled evenly in running water to reduce the gel temperature. The agarose solution was then poured into an electrophoresis tray and combs were then inserted into the tray to create wells for sample loading. The agarose solution was cooled at room temperature for 30 min to allow gelation and once set, the well forming combs were removed.

When the DNA amplification process was concluded, loading dye was prepared using REDTaq® ReadyMix™ PCR Reaction Mix (Merck, UK) by making a mixture of 12.5 µl of REDtaq, 1 µl of obtained cDNA and 9.5 µl of RNase-free water. Then, 5 µl of loading dye prepared from each cDNA sample was loaded into each well of the gel. Three microlitres of GeneRuler 1kb DNA ladder (Thermo Scientific, UK) were included as a reference to determine the size of the amplicon. Electrophoresis was performed at room temperature at 120 V for 30 min to separate the PCR products.

2.6.1.7 Electrophoresis band visualisation and relative intensity calculation

The amplified bands were visualised using the G:BOX Syngene image analyser (Syngene, UK) and were captured using the Genesnap software version 7.12.06 (Syngene, UK). The band intensity from each experimental group was determined and compared using the GeneTools analysis software version 4.3.8 (Syngene, UK). The experiment was performed using three biological replicates from independent experiments.

2.6.2 Real-time polymerase chain reaction (Real-time PCR)

Real-time PCR differs from sqRT-PCR in that it allows the researchers to observe amplifying data at the present time. In this experiment, culture was treated with either EGF or S1PR2 treatments for 48 h, however the RNA quantification process was the same as described in sqRT-PCR (**section 2.6.2.1-4**).

2.6.2.1 Determination of primer efficiency

The efficiency of primers was determined from the generation rate of the PCR amplicon. Ten microlitres of each cDNA sample were pooled into a stock mixture termed 'mixture 100%'. This mixture was diluted in RNase-free water to 50%, 10%, 1% and 0.1%. Pure RNase-free water was used as a 0% mixture. One microlitre of each mixture was transferred to a well of a LightCycler® 480 Multiwell Plate 96 (Roche, Switzerland) on ice. The primer sequences for RT-PCR were derived from sequences within the NCBI database (**Table II**). One microlitre of both forward and reverse primers were combined with 100 µl of LightCycler® 480 SYBR Green I Master (Roche, Switzerland) and 76 µl of RNase-free water. Nine microlitres of reaction mix solutions were transferred to each well (**Figure 13A**) and centrifuged at 4^{o}C for 3 min. The amplification process was performed using a LightCycler 480 Instrument II (Roche, Switzerland) with 5 min of initial denaturation at 95°C followed by 46 cycles of amplification. Each cycle consisted of denaturation at 95°C for 10 sec, annealing at 60°C for 15 sec and elongation at 72°C for 10 sec. The efficiency of the primers was calculated from the standard curve plotted from the amplified products.

Table II. Details of primers for real-time PCR analysis

Gene name	**Supplier**	**Access number of NCBI**	**Sequence (from 5' to 3')**	**Melting temp. (°C)**	**Products base pair (bp)**
Homo sapiens glyceraldehyde-3-phosphate dehydrogenase	Merck	NM_001357943.2	**F:** TCGACAGTCAGCCGCATCTT	61	104
			R: GCCCAATACGACCAAATCC	56	
Homo sapiens hypoxanthine phosphoribosyltransferase 1	Invitrogen	NM_000194.3	**F:** GACCAGTCAACAGGGGACAT	59	195
			R: AACACTTCGTGGGGTCCTTTTC	61	
Homo sapiens tyrosine 3-monooxygenase/tryptophan 5-monooxygenase activation protein zeta	Invitrogen	NM_001135699.2	**F:** ACTTTTGGTACATTGTGGCTTCAA	59	94
			R: CCGCCAGGACAAACCAGTAT	60	
Homo sapiens beta-2-microglobulin	Invitrogen	NM_004048.4	**F:** ACCCCCACTGAAAAAGATGA	56	114
			R: ATCTTCAAACCTCCATGATG	52	
Homo sapiens matrix metallopeptidase 2	Merck	NM_004530.6	**F:** CATCATCAAGTTCCCCGGC	58	119
			R: TGTCCTTCAGCACAAACAGG	58	
Homo sapiens matrix metallopeptidase 9	Merck	NM_004994.3	**F:** CCTGGAGACCTGAGAACCAA	58	105
			R: AGATTTCGACTCTCCACGCA	59	
Homo sapiens sphingosine kinase 1	Merck	NM_001142601.2	**F:** GCTGCGAAGTTGAGCGAAAA	60	380
			R: CCCGCTGGATCCATAACCTC	59	
Homo sapiens sphingosine kinase 2	Merck	NM_001204159.3	**F:** CTAGTCGGGGCATCTGGAAA	59	150
			R: CTCACTGTCCTGGCCTGAC	59	

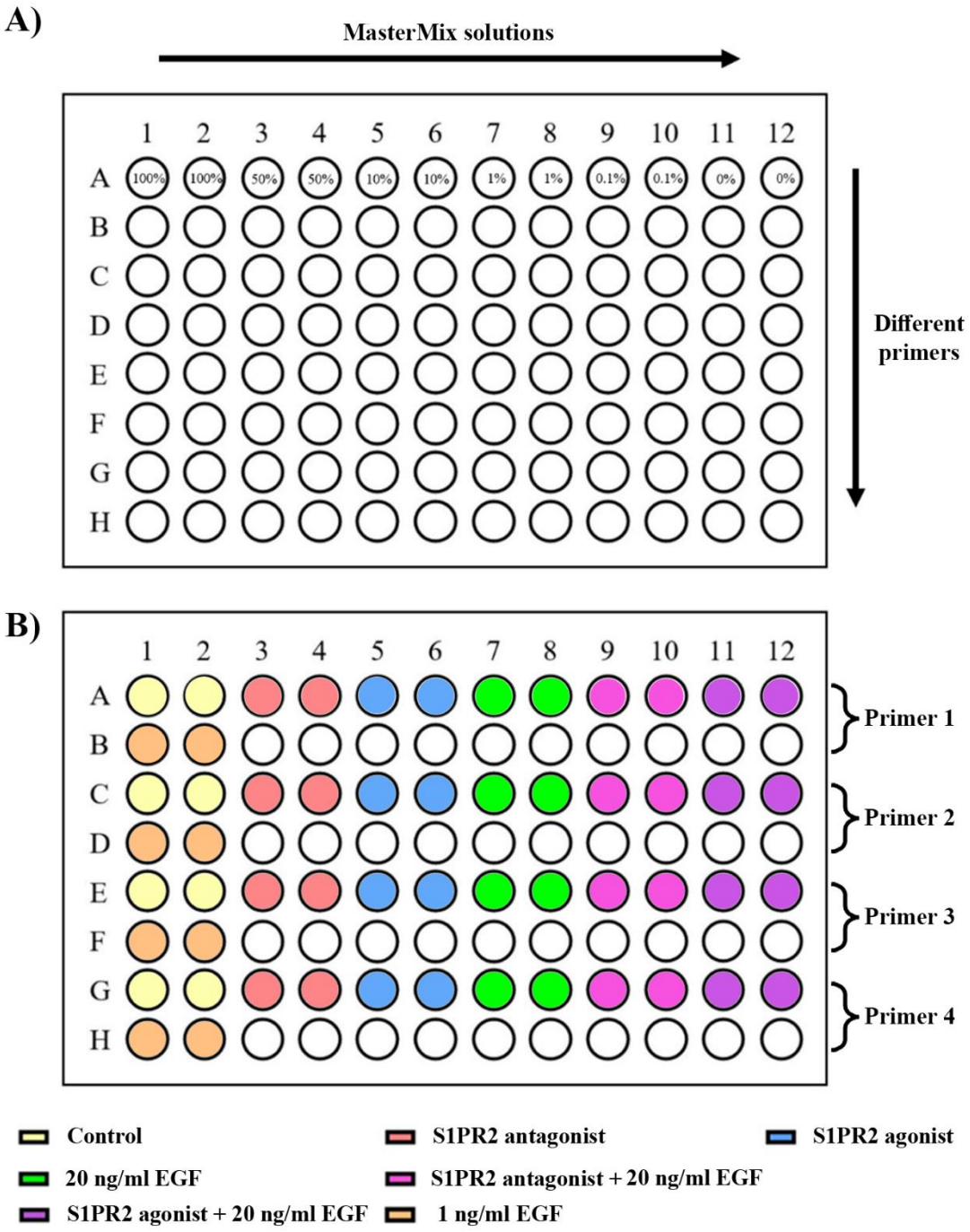

Figure 13. Plate setups for real-time PCR. **A)** Plate setup for primer efficiencies step. Components were added to a 96-well PCR plate. Nine microlitres of the MasterMix solution of each primer were added in each row, while 1 µl of each sample was added in each column. In each row, from left to right, five primer concentrations, including 100%, 50%, 10%, 1%, 0.1% and 0%, were added into each well, while each column varied the primer of each gene. Samples were analysed in duplicate and averages were derived. **B)** Plate setup for amplification step. Each sample was added into the well from left to right (two wells per sample). MasterMix solution of each primer was added from top to bottom.

Only primers with an efficiency range from 1.8 to 2.2 were used in the study (according to manufacturer's instructions, PCR efficiency is approximately 2).

2.6.2.2 Real-time PCR amplification

The Master mix solution containing each primer and cDNA of samples were added into wells of a 96-well plate in order as shown in **Figure 13B**.The amplifying process was performed as described in **section 2.6.2.1**. Primers with the lowest standard deviation in crossing point values between samples were used as reference housekeeping genes for the OSCC lines as they represented the most stable housekeeping gene (lowest variation between samples) (Kozera & Rapacz, 2013). Therefore, the calculated relative fold change would not be affected by the discrepancy of this gene expression. The amplification was performed on the target genes. Relative fold changes in relation to the housekeeping gene were calculated. The experiment was performed in three biological replicates from independent experiments where each experiment was the average of two technical replicates.

2.7 Rac1 G-LISA activation assay

Rac1 is a type of RhoGTPase which is activated by switching from binding to GDP to bind with GTP (Liang *et al.*, 2021). Traditionally, activation of Rac1 can be measured using a pull-down assay which detects the amount of RhoGTPase which binds with GTP. However, this assay is time consuming, needs large amounts of total cellular protein and the number of samples per assay are limited. The G-LISA Rac1 activation assay Biochem Kit (Cytoskeleton, USA) uses a RhoGTP-binding protein-coated 96-well plate to capture the active RhoGTPases. The bound active Rac1 was detected with a Rac1 specific antibody and luminescence. The level of activation of Rac1 was determined by comparing the luminescence readings from treated samples and the control.

2.7.1 Reagent preparation

Anti-Rac1 and the secondary antibodies - horseradish peroxidase conjugate (HRP) were dissolved in 40 µl and 80 µl of PBS, respectively. Cell lysis buffer, binding buffer, wash buffer and antibody dilution buffer were reconstituted in 100 ml, 8 ml, 100 ml and 15 ml of sterile dH_2O, respectively. The protease inhibitor cocktail was reconstituted in 1 ml DMSO (Sigma, UK).

2.7.2 Lysate collection and total protein quantification

Three OSCC lines were cultured in T25 flasks until reaching approximately 50% confluence. To inactivate Rac1 activity, cultures were serum-starved with 0.5% FBS media for one day and FBS-free media for another day. This study consisted of six groups including: 1) control, 2) treatment with 10 µM S1PR2 antagonist, 3) treatment with 10 µM S1PR2 agonist, 4) treatment with 20 ng/ml EGF, 5) treatment with 10 µM S1PR2 antagonist and 20 ng/ml EGF and 6) treatment with 10 µM S1PR2 agonist and 20 ng/ml EGF. For the groups inhibiting or stimulating S1PR2, cultures were incubated in 5 ml FBS-free media containing either 10 µM JTE013 or 10 µM CYM5478 in the humidified incubator for 15 min, respectively (15 min was selected because the maximum activation of Rac1 ranges from 30 sec to 30 min, and then decreases to the baseline level). For groups with EGF stimulation, used media were replaced with fresh media containing 20 ng/ml EGF for 2 min.

Cultures were placed on ice, and after the used media were aspirated, were washed with ice-cold PBS. Since excess PBS could affect dilution, the culture flasks were tilted while placing on ice for 1 more min before re-aspirating. Cells were lysed by adding 160 µl of ice-cold cell lysis buffer. Total lysates were transferred into 1.5 ml Eppendorf tubes and centrifuged at 13,200 rpm, 4^{o}C for 2 min.

For each sample twenty microlitres of lysate were transferred into spectrophotometer cuvettes and 1 ml of protein assay reagent added and incubated for 1 min at room temperature. Twenty microlitres of lysis buffer mixed with 1 ml of Precision Red™ advanced protein assay reagent was set as a blank reference. The absorbance of samples was read at a wavelength of 600 nm. The concentration

of total protein was calculated according to manufacturer's instructions by multiplying the absorbance by 5 to obtain the protein concentration in mg/ml. The rest of the lysate was diluted with lysis buffer to a concentration of 0.3 mg/ml before snap-freezing and storing at -70ºC.

2.7.3 G-LISA procedure

The blank sample (negative control) was prepared by mixing 60 µl of lysis buffer with an equal amount of binding buffer in a microcentrifuge which was placed on ice. The positive control was prepared by mixing 24 µl freshly reconstituted Rac1 control protein with 36 µl lysis buffer and 60 µl binding buffer. Lysate samples were thawed at room temperature and quickly placed on ice. Sixty microlitres of diluted lysates were mixed with 60 µl binding buffer. Then, strips of the Rac1 affinity plate were assembled with a strip holder and placed on ice. One hundred microlitres of ice-cold water were added into each well of the strips to dissolve the lyophilized Rac1-GTP binding powder also containing buffering and stabilisation components. This process was to link the Rac1-GTP binding protein to the bottom of the well. Water in the well-plates was removed by inverting the plate and tapping onto paper towels 5-7 times. Fifty microlitres of blank, positive control and samples were quickly transferred to the wells, covered with the lid and placed on the R100/TW Rotatest Shaker (Luckham, USA) at 4°C for 30 min. Meanwhile, anti-Rac1 primary antibody was diluted to 1:250 with antibody dilution buffer.

After shaking, samples were washed with washing buffer twice at room temperature. Two hundred microlitres of antigen presenting buffer were added into each well and incubated at room temperature for 2 min. Antigen presenting buffer was removed and samples were washed with washing buffer three times. Fifty microlitres of diluted anti-Rac1 antibody was added to each well and the plate was placed on the R100/TW Rotatest Shaker (Luckham, USA) at room temperature for 45 min. The secondary HRP horseradish peroxidase labelled antibody was diluted to 1:200 with antibody dilution buffer.

After shaking, samples were washed with washing buffer three times at room temperature followed by thorough removal of the wash buffer. Fifty microlitres of diluted secondary HRP labelled antibody was added to each well and shaken on the R100/TW Rotatest Shaker (Luckham, USA) at room temperature for 45 min. The HRP detection reagent was prepared by mixing equal amounts of HRP reagent A and B. Subsequently, this was agitated for 45 min and the secondary HRP labelled antibody was removed. Samples were then washed with washing buffer three times before adding with 50 µl of prepared HRP detection reagent. Luminescence was measured using a Spark® multimode microplate reader (Tecan, Switzerland) within 3 min. The settings of the microplate reader were: shaking 5 sec, room temperature, integration time = 100 ms).

2.7.4 Data Analysis

The data from each group (duplicate wells) were averaged. To avoid high background readings, only data with a ratio of positive control: blank which was between 3 to 5 was used (as indicated by the manufacturer's instructions). Background luminescence of the blank sample was subtracted from the luminescence of each sample. Results are presented as normalised data to the control.

2.8 Enzyme-linked immunosorbent assay (ELISA)

This study used ELISA to measure the amount of EGF and TGF-β1 which are the growth factors that are reported to bind with EGFR and promote invasion (Voldborg *et al.*, 1997, Joo *et al.*, 2008).

2.8.1 Antibody and standard preparation

Human EGF and human TGF-beta 1 DuoSet ELISA kits were purchased from R&D systems (Quantikine ELISA, USA) to assay EGF and TGF-β1 levels. Stock solutions of the capture antibodies were prepared by reconstituting with 0.5 ml of PBS. Working solutions of capture

antibodies were freshly prepared by diluting the stock solutions in the reagent diluent 2 to 2 µg/ml while the detection antibodies were reconstituted to stock solutions with 1 ml of reagent diluent 2. Working solutions of detection antibodies were prepared by diluting the stock solution in reagent diluent to 50 ng/ml (just before use). The standard was reconstituted with 0.5 ml of reagent diluent 2 before performing 2 fold serial dilution 7 times, providing 8 concentrations of EGF and TGF-β1 (including blank). Streptavidin-HRP was 1:40 diluted in reagent diluent to a working concentration before use.

2.8.2 Plate preparation

One hundred microlitres of the working capture antibody solutions were transferred to 96-well plates, covered with an adhesive strip and incubated overnight at 4^{o}C. These plates were washed with wash buffer using an automatic microplate washer (Biotek ELX50, USA) three times. Water in the well-plates was removed by inverting them onto paper towels and gently tapped. Each well was blocked with 300 µl of 5% Tween 20 (Thermo Scientific, UK) in PBS and incubated at room temperature for 1 h before washing with wash buffer as previously described.

2.8.3 Assay procedure

H357, H400 and H413 cells were cultured in T25 flasks until they reached 50% confluence. Used media were replaced with FBS-free media containing either 10 µM S1PR2 antagonist or S1PR2 agonist for 48 h. Media used to incubate the culture were collected and centrifuged at 1,000 rpm for 3 min. Supernatants were collected in 1.5 ml Eppendorf and stored at -80^{o}C. To activate latent TGF-β1 to immunoreactive TGF-β1, supernatants were mixed with 1 M HCl (Sigma-Aldrich, UK) and incubated at room temperature for 10 min. The acidity of samples was then neutralised by adding 1.2 M NaOH (Sigma-Aldrich, UK) containing 0.5 M HEPES (Sigma-Aldrich, UK).

Prepared 96-well plates were loaded with either supernatants or the prepared standard and covered with an adhesive strip before incubating for 2 h at room temperature. Samples were washed three times, supplemented with 50 ng/ml human EGF or TGF-β1 detection antibody solution and incubated for 2 h at room temperature. The washing process was performed before supplementing each well with diluted Streptavidin-HRP. Samples were covered and incubated for 20 min at room temperature without exposure to light. The substrate solution was freshly prepared by mixing colour reagents A and B before use. Samples were washed three times, then added with substrate solution and incubated at room temperature for 20 min without exposure to the light. The reaction was stopped by adding stop solution to each well. The optical density of samples was immediately read at 450 nm and 570 nm (for wavelength correction) using a Spark® multimode microplate reader (Tecan, Switzerland). The blanks (negative control) were subtracted from the samples and standards. Standard curves were plotted for the mean absorbance of each standard (Y-axis) and the log concentration of the standard (X-axis) (**Figure 14**). Concentrations of EGF and TGF-β1 were calculated from the linear regression equation obtained from the standard curves. For TGF-β1, concentrations obtained were multiplied by 1.4 to compensate for the dilution by the activation solution.

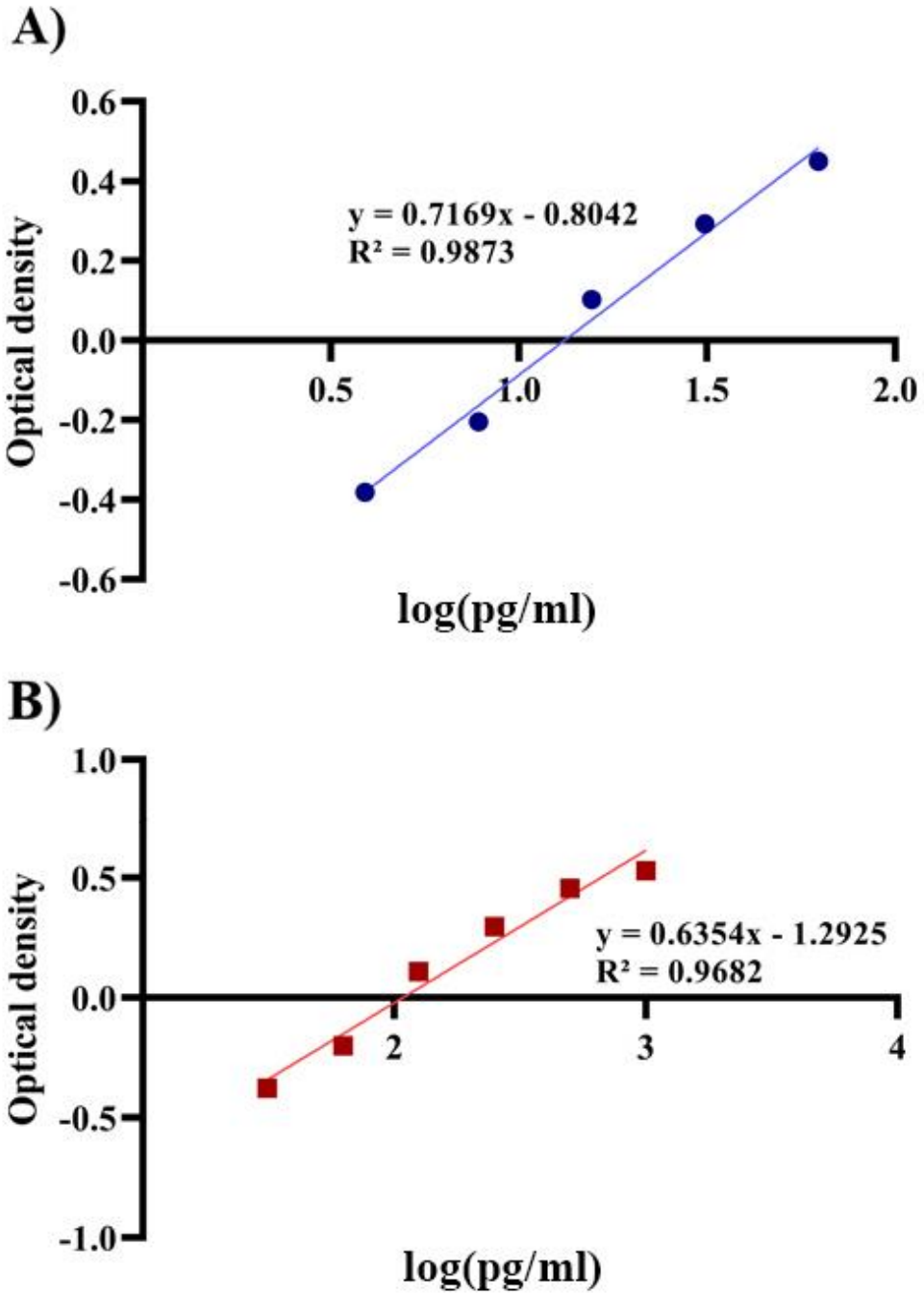

Figure 14. Examples of standard curves obtained with the ELISA. Graphs represent the optical density at the log of amount of growth factor (pg/ml). Linear regression equations of the graph were used to convert the optical density of samples to concentration in pg/ml. **A)** standard curve for EGF and **B)** standard curve for TGF- β1. Experiments were performed in triplicate.

2.9 Statistical analysis

Data of each experimental group were analysed using statistical software GraphPad Prism (Version 9.0.0, USA). The normality tests of experiments with a sample size lower than 30 was performed using the Shapiro-Wilk test. In contrast, the normality tests of experiments with a sample size of 30 or higher were performed using the Kolmogorov-Smirnov test. Multiple comparisons were performed using One-way ANOVA test followed by *post-hoc* Tukey tests. For the MCTS assay, which had both time and treatments as variables, multiple comparisons were performed using Two-way ANOVA. The correlation between variables was determined using linear regression analysis. Probability (p) values lower than 0.05 were considered statistically significant.

Chapter 3: Results

Investigation of proliferation, migration and invasion in OSCC lines

3.1 Aims

This chapter presents the proliferative, migratory and invasive profiles of the three OSCC lines, H357, H400 and H413, as well as the development of a protocol for the MCTS model for determining invasion in further experiments.

3.2 Objectives

a) To determine proliferation, migration and invasion of H357, H400 and H413 cells

b) To develop a protocol for the MCTS model

3.3 Growth curves and doubling times

To determine the growth of H357, H400 and H413, cell counts were performed for up to 14 days**.** The doubling time of H357 (1.9 ± 0.1 days) was significantly higher than that of H400 (1.3 ± 0.1 days) and H413 cells (1.3 ± 0.1 days) ($p<0.01$, One-way ANOVA), implying that H357 grew more slowly than H400 and H413 cells. Although the counts for H413 were higher than those of H400 (from day 4 onwards) the differences in the doubling time between H400 and H413 cells were not statistically significant (**Figure 15**).

3.4 BrdU assay

The percentage of BrdU positive cells (shown in **Figure 16**) in H357 cells was 15.5 ± 8.4. This value was significantly lower than that of H400 (23.1 ± 3.3), ($p<0.05$, One-way ANOVA) and H413 (22.3 ± 1.1), ($p<0.05$, One-way ANOVA). While the percentage of BrdU positive cells in H400 cultures was slightly higher than in H413 cultures, this difference was not statistically significant.

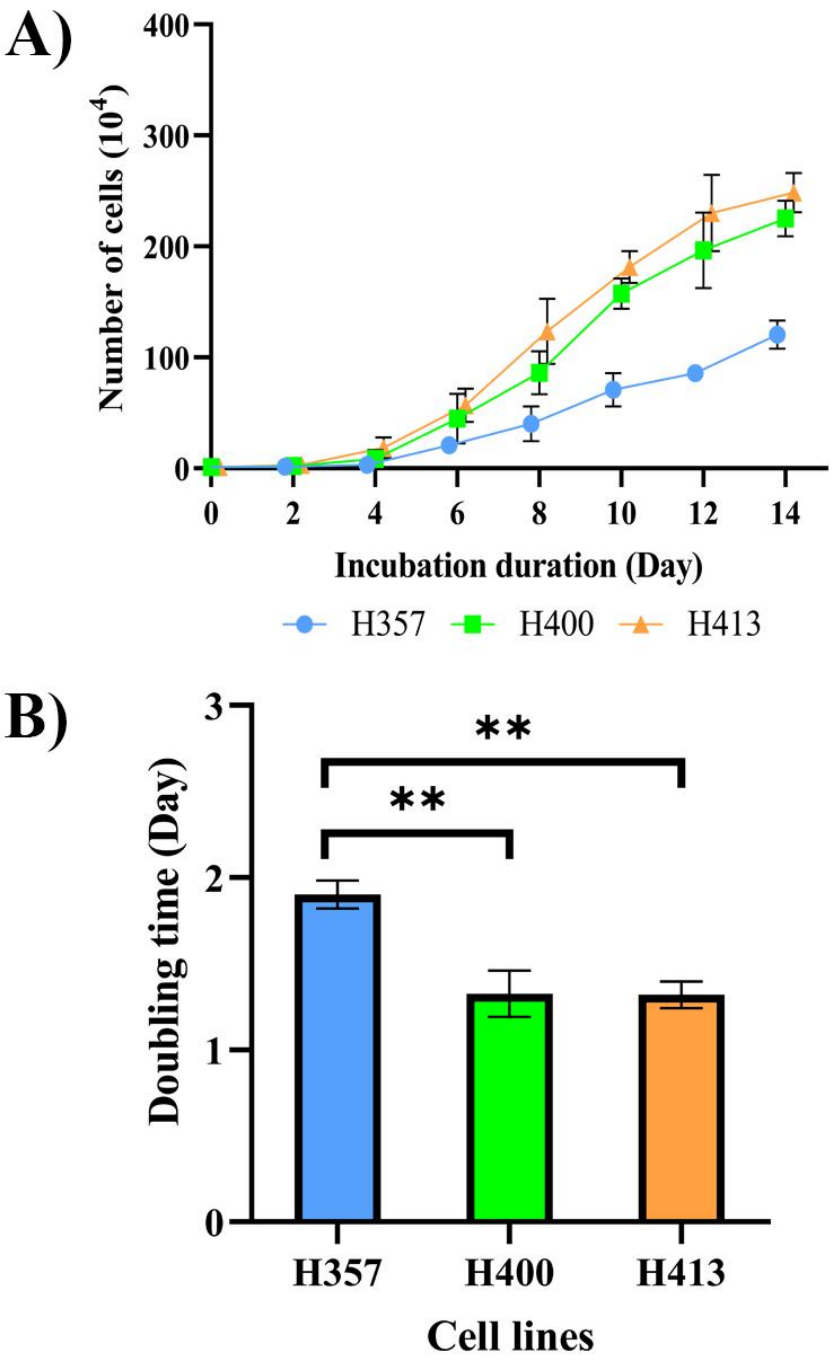

Figure 15. Proliferation of H357, H400 and H413 cells was determined by examining the growth curves and doubling times over 14 days of culture. Cell suspensions of each line were seeded at 1.0x 10^4 cells/well and cultured with DMEM containing 10% FBS. **A)** The gradient of H357's growth curve was flatter than of H400 and H413. **B)** H357 had a higher doubling time than H400 and H413 cells although there was no statistical difference in doubling time between H400 and H413 cells. (Three biological replicates from independent experiments; Points on the line graphs have been jittered to prevent overlapping; One-way ANOVA followed by *post-hoc* Tukey tests, ** = p-value < 0.01, data presented as mean ± 1 SD).

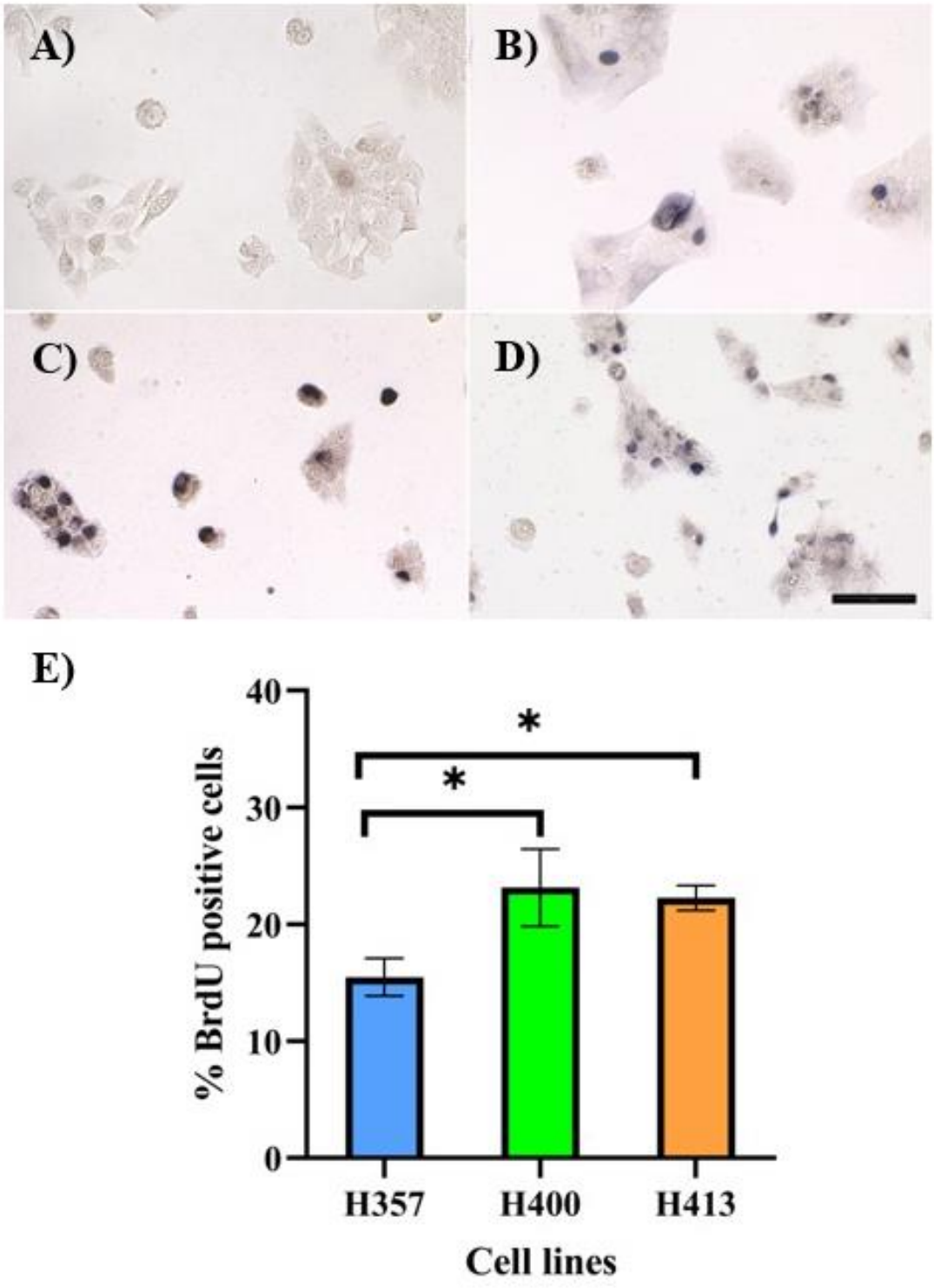

Figure 16. Proliferation determined using the BrdU assay. **A-D)** Representative images captured using phase contrast microscopy. **A)** Negative control which cells were treated with the water (solvent of BrdU solution) in BrdU staining step. **B)** H357 cells. **C)** H400 cells. **D)** H413 cells. **E)** The percentage of BrdU positive cells (nuclei stained in blue) in H357 cells was significantly lower than in H400 and H413 cultures, implying a lower proliferation rate. (Scale bar shown represents 50 μm; X20 objective lens; three biological replicates from independent experiments, N = 1,000 cells; One-way ANOVA followed by *post-hoc* Tukey tests, * = p-value < 0.05, data presented as mean ± 1 SD).

3.5 Scratch wound assay

The percentage wound closure at 12, 18 and 24 h for H357, H400 and H413 cells are shown in **Figure 17**. At 12 h, the percentage wound closure for H357 (12.1 ± 2.4) was half that of H400 (24.2 ± 4.8) cells ($p<0.01$, One-way ANOVA). The percentage wound closure for H357 was also lower than that of H413 cells (16.0 ± 1.8), but the difference was not statistically significant. H400 cells also migrated more rapidly than H413 cells by 1.5 fold ($p<0.01$, One-way ANOVA). At 18 h, the percentage wound closure in H357 cultures increased to 14.5 ± 8.5. This percentage was half the value for that of H400 cells (32.0 ± 6.1), ($p<0.05$, One-way ANOVA) but was not statistically different from H413 cells (22. ± 2.5). Again, H400 cells had a higher wound closure rate than H413 cells by 1.5 fold ($p<0.05$, One-way ANOVA). At 24 h, the percentage wound closure of H357 cells increased to 18.3 ± 11.4, which was less than half the value of H400 cells (39.0 ± 4.5), ($p<0.1$, One-way ANOVA) and also lower than in H413 cells (26.3 ± 5.5), ($p<0.05$, One-way ANOVA). At this time point, although H400 showed a higher percentage wound closure than H413, the difference was not statistically significant.

3.6 Transwell migration assay

The transwell migration assay was used to compare the migratory properties of the three cell lines. **Figure 18A** illustrates the negative control where the lower chamber did not contain 10% FBS. **Figures 18B-D** show migrated cells stained with calcein AM after incubation for 24 h. Out of the three OSCC lines, H400 cultures had the highest number of migrated cells per field of view (111 ± 27 cells). This number was significantly higher than H357 (25 ± 7 cells) by 4.4 fold ($p<0.01$, One-way ANOVA) and H413 cultures (38 ± 6 cells) by 2.9 fold ($p<0.01$, One-way ANOVA). Although H413 demonstrated more migrated cells than H357, the difference was not statistically significant (**Figure 18E**).

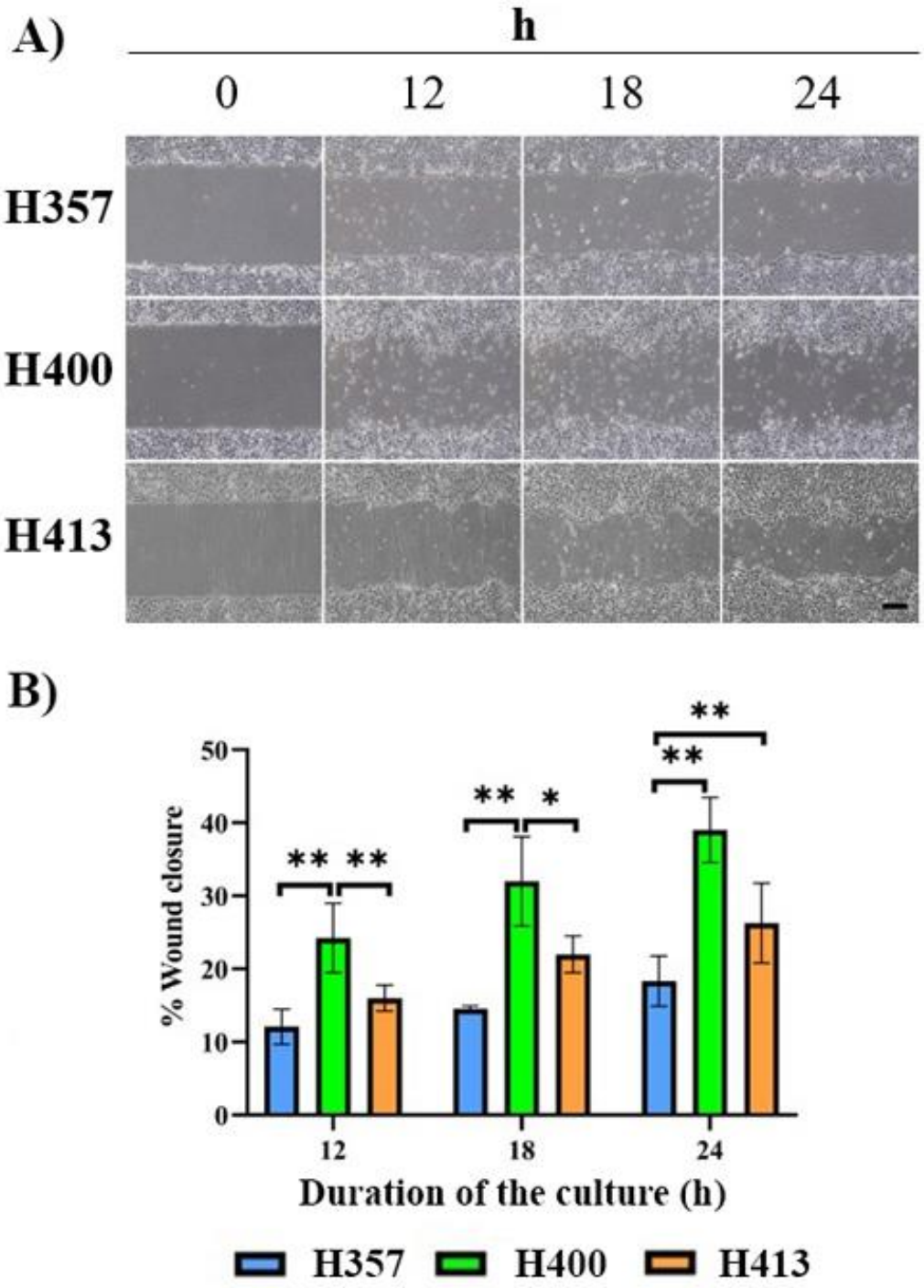

Figure 17. Scratch wound migration assay in H357, H400 and H413 cultures at 12, 18 and 24 h. **A)** Images of cultures captured using phase contrast microscopy showing wound closure over times. **B)** The percentage wound closure in the figure indicates that H357 cells exhibited the slowest wound closure rate across all time points assayed, followed by H413 and H400 cells, respectively. (Scale bar shown represents 200 µm; X4 objective lens; Three biological replicates from independent experiments were performed with N=4 for each experiment; One-way ANOVA followed by *post-hoc* Tukey test, * = p-value < 0.05 and ** = p-value < 0.01, data presented as mean ± 1 SD).

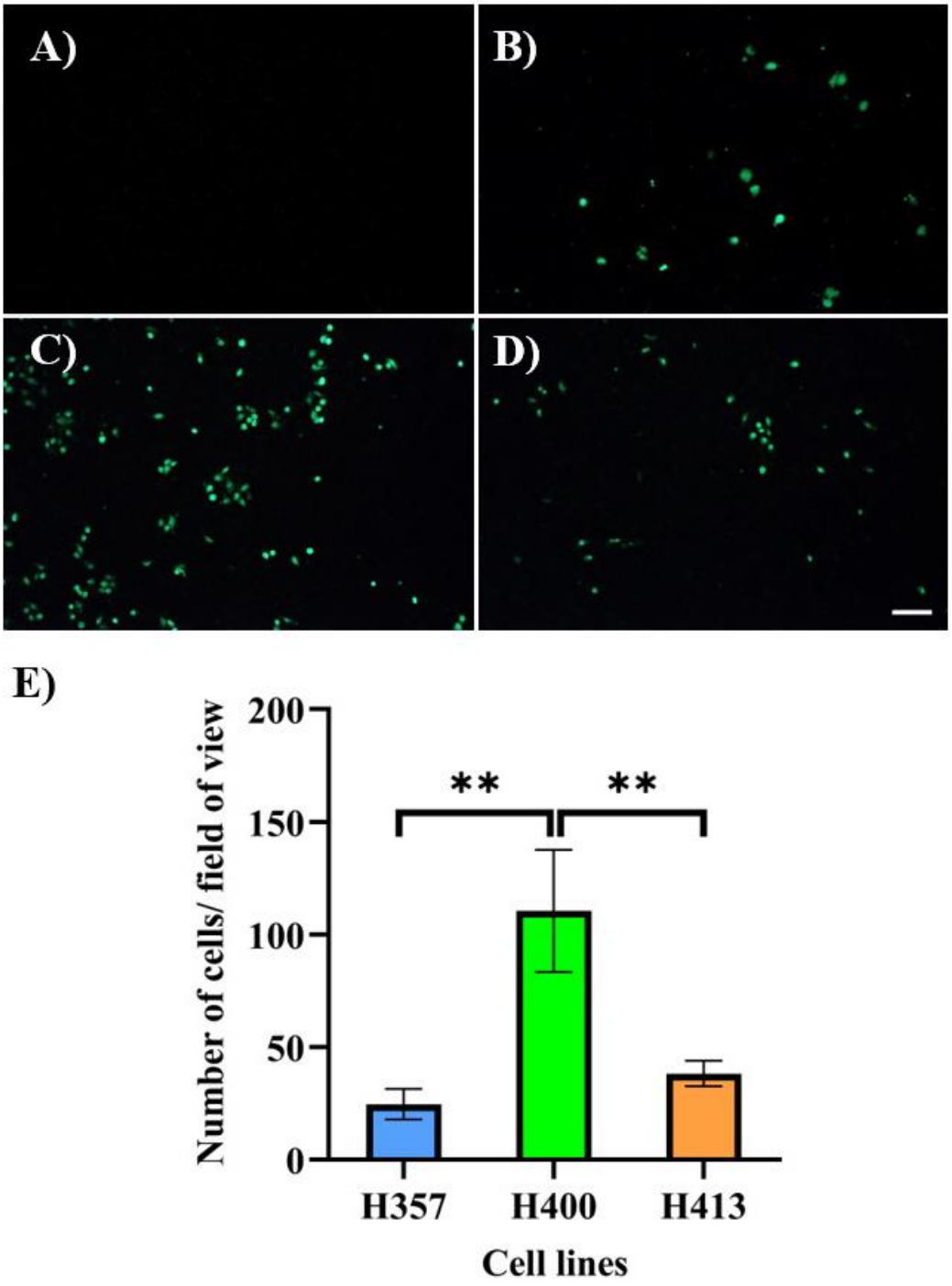

Figure 18. Transwell migration assay of H357, H400 and H413 cells. Representative images were captured using a fluorescence microscopy. Cells were stained with calcein AM. **A)** Negative control well where the lower chamber contained FBS-free media showed no obvious cells stained with calcein AM. **B)** H357. **C)** H400. **D)** H413. **E)** The number of migrated cells per field of view for H400 was higher than for H357 and H413 cells. (Scale bar shown represents 100 µm; X10 objective lens; Three biological replicates from independent experiments were performed with N=10 for each experiment; One-way ANOVA followed by *post-hoc* Tukey test, ** = p-value < 0.01, data presented as mean ± 1 SD).

3.7 Transwell invasion assay

The transwell invasion assay data for H357, H400 and H413 cells after being incubated for 48 h are shown in **Figure 19**. H357 cultures had an average of 8 ± 2 cells per field of view. This was significantly lower than that for H400 (24 ± 3 cells), (3.0 fold, $p<0.01$, One-way ANOVA) and H413 cultures (19 ± 6 cells), (1.3 fold, $p<0.05$, One-way ANOVA). The difference between H400 and H413 cultures was not statistically significant.

3.8 Multicellular spheroid analysis

Another approach used for determining the invasive profile of H357, H400 and H413 cell lines was the MCTS model. The hanging-drop method used was able to generate single spheroids within one day (**Figure 20A**). The liquid-overlay method also generated a single spheroid but only after 4 days of incubation. According to the image, the spheroids from this technique exhibited more loosely attached cells at the outer surface of the spheroid than with the hanging-drop method (**Figure 20B**). These cells were easily detached when transferring spheroids. In comparison, the ULA-microplate method generated multiple spheroids of various sizes after 4 days incubation, however visibly it appeared that numerous cells failed to aggregate into the main spheroid (**Figure 20C**).

Since the hanging-drop method provided similar sized spheroids within one day of culture, this method was used for subsequent experiments. However, the effects of continuous proliferation need to be considered when investigating invasion. This study attempted to minimise cell growth by reducing the FBS supplements during spheroid generation and two experimental groups were designed to investigate those effects: 1) a group in which cell suspension was created in media supplemented with 10% FBS and 2) a group without the FBS supplement.

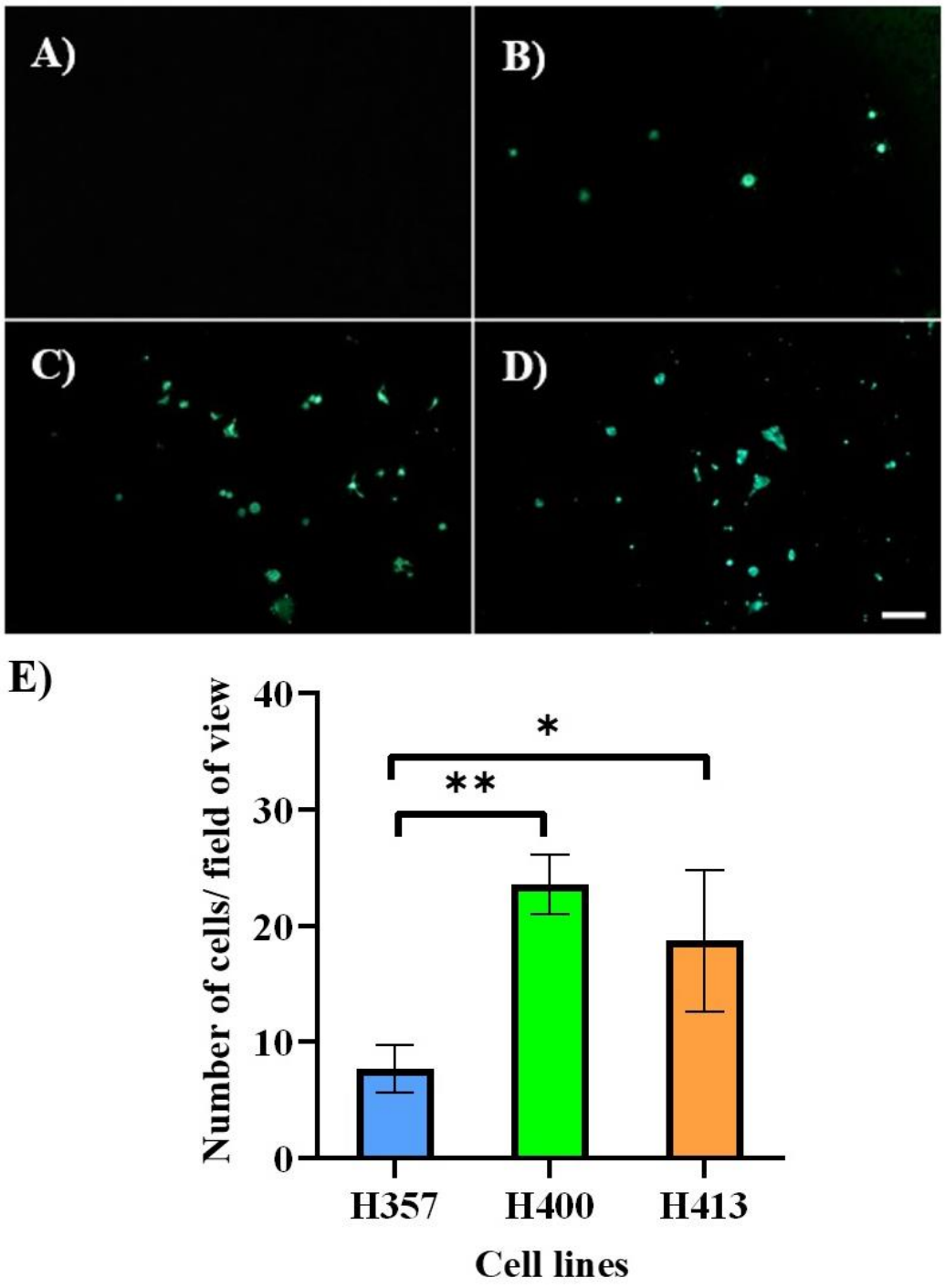

Figure 19. Transwell invasion assay of H357, H400 and H413 cultures. **A-D)** Representative images were captured using fluorescence microscopy. Cells were stained with calcein AM. **A)** Negative control well where the lower chamber contained FBS-free media showed no obvious cells stained with calcein AM. **B)** H357. **C)** H400. **D)** H413. **E)** H357 significantly invaded less than H400 and H413 cells. H400 invaded to the same level as H413 cells. (Scale bar shown represented 100 μm; X10 objective lens; Three biological replicates from independent experiments were performed with N=10 for each experiment; One-way ANOVA followed by *post-hoc* Tukey test, * = p-value < 0.05, ** = p-value < 0.01, data presented as mean ± 1 SD).

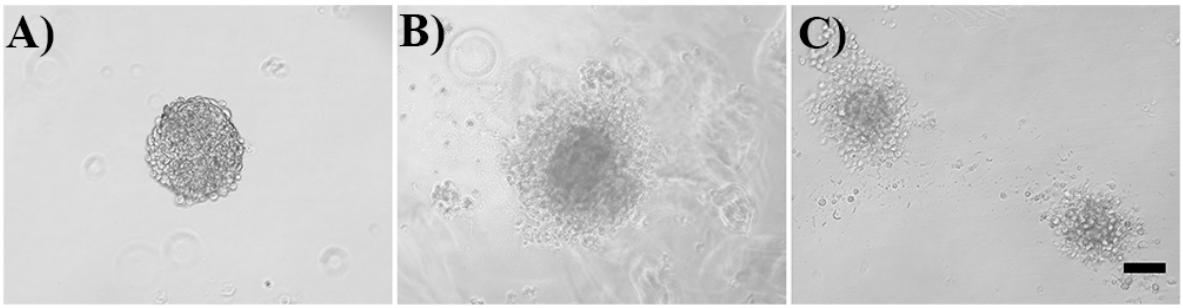

Figure 20. Selection of methods for generating MCTS. Representative images captured using phase contrast microscopy of H400 spheroids generated using three different culture methods. Each spheroid consisted of approximately 500 cells. **A)** The hanging-drop method provided a single compact spheroid (one day of incubation). **B)** Spheroids generated from the liquid-overlay method appeared loosely aggregated (one day of incubation). **C)** The ULA-microplate method provided multiple spheroids which varied in size (four days of incubation). (Scale bar shown represented 50 μm; X10 objective lens).

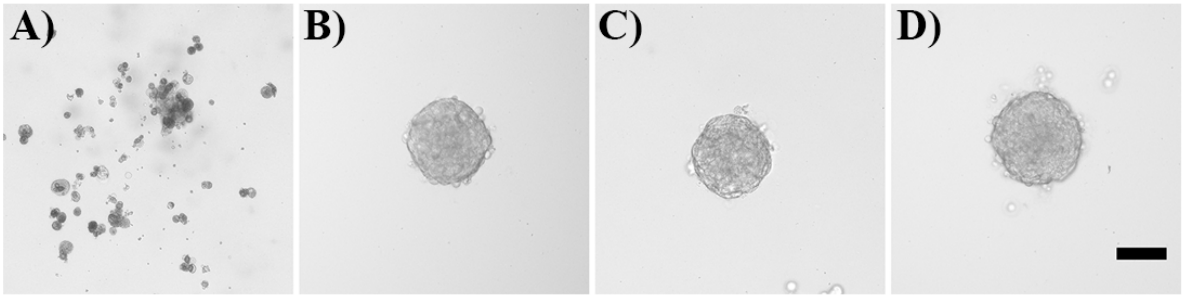

Figure 21. The requirement for FBS during spheroid generation step. Representative images captured using phase contrast microscopy. **A)** Example image of cells (in this figure was H400) in FBS-free media group did not aggregate, although the droplet was hung for five days. **B-D)** Spheroid of three cells generated using the hanging drop method, one day of incubation. **B)** H357. **C)** H400 spheroid. **D)** H413 spheroid. (Scale bar shown represented 50 μm; X10 objective lens).

The result shows that when droplets were hung for five days, none of the cell lines produced spheroids (remaining as single cells) in the FBS-free media group (**Figure 21A**), which suggested that the FBS supplement was a requirement for generating spheroids with this method. On the contrary, in the group supplemented with 10% FBS, cells aggregated into spheroids within one day (**Figure 21B-D**). An initial seeding of approximately 500 cells per droplet generated spheroids with an average diameter of 166.0 ± 13.4 μm (H357), 153.5 ± 30.0 μm (H400) and 182.3 ± 13.2 μm (H413) although these differences were not statistically significant. The initial shape of the H357 spheroids had an average circularity of 0.76 ± 0.03, which was statistically similar to H400 (0.74 ± 0.05) and H413 (0.75 ± 0.05) cells indicating that the cells were close to a circular morphology. Moreover, the lack of a statistical difference in circularity and the size of the spheroids was noted between the three biological replicates, which indicated reproducibility for spheroid generation.

3.8.1 The effect of matrix stiffness on invasion

After generating the spheroids for one day, these were embedded into three collagen gels with concentrations of 0.5, 1.5 and 3 mg/ml, treated with 8 μg/ml mitomycin C and were further observed microscopically for two days (**Figure 22A-C**). Upon embedding, the spheroids appeared as one cluster with a circular morphology however subsequently, cells at the edge of the spheroid extended spike-like invasive protrusions into the collagen matrix which caused the morphology to become more irregular. In addition, the spheroids fragmented into smaller clusters before continuing to spread. **Table III** shows that the number of clusters, maximum invading distance, fractal dimension and the maximum diameter of the main cluster (MDMC) of the three cell lines increased with the duration of incubation, whilst the circularity decreased. The effect of the collagen concentration using five morphological parameters is described in **sections 3.8.1.1-5**. Tables with the original data are presented in the **Appendix**.

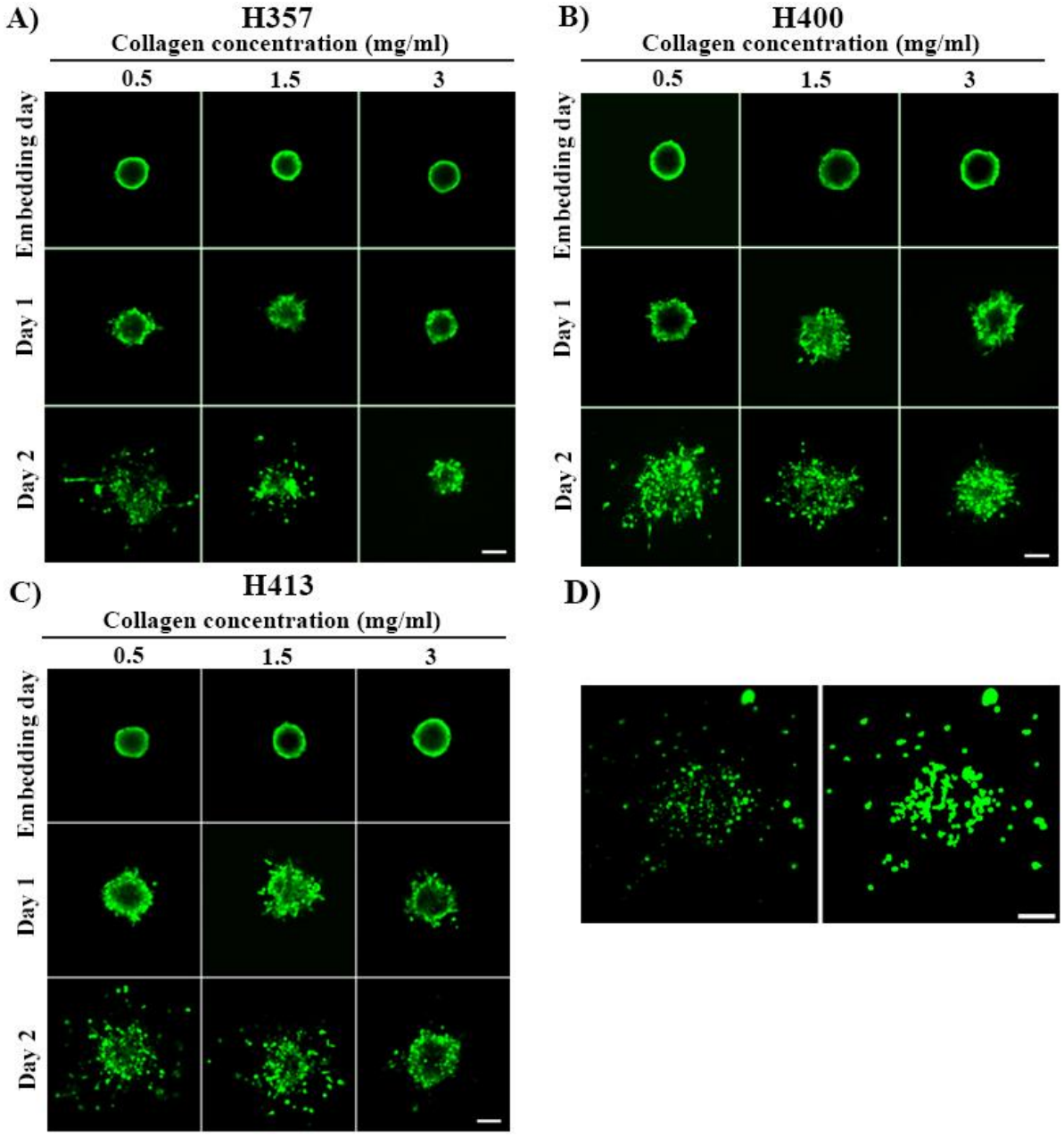

Figure 22. Representative images of MCTS of H357, H400 and H413 cells. Each spheroid was generated using the hanging drop method (one day of incubation). After being embedded into three collagen concentrations, cells were treated with 8 µg/ml mitomycin C for 2 h before staining with calcein AM and images were captured using a confocal microscopy. To identify an appropriate protocol for the subsequent studies, the MCTSs of the three OSCC lines were embedded in collagen gels at concentrations of 0.5, 1.5 and 3 mg/ml. The invasion of the cells generally increased according to the incubation period but decreased with increasing collagen concentrations. **A)** H357. **B)** H400. **C)** H413. **D)** Some samples, *e.g.* H413 spheroids embedded in 0.5 mg/ml collagen for two days, invaded the collagen and detached from each other until the main cluster could not be identified anymore. (Scale bar shown represented 100 µm; X10 objective lens; Three biological replicates from independent experiments were performed with N=10 for each experiment.)

Table III. Linear regression analysis showing the relationship between invading parameters and incubation duration (day) in the growth inhibited dataset

Cell lines	Collagen concentration											
	0.5 mg/ml				1.5 mg/ml				3 mg/ml			
	Slope	Offset	R^2	p-value	Slope	Offset	R^2	p-value	Slope	Offset	R^2	p-value
Number of clusters												
H357	2.93	0.74	0.91	<0.01	3.05	0.67	0.79	<0.01	1.65	0.88	0.78	<0.01
H400	3.73	0.52	0.63	<0.05	4.28	0.38	0.73	<0.01	2.50	0.56	0.66	<0.01
H413	10.88	0.46	0.66	<0.01	10.12	0.02	0.90	<0.01	4.87	0.41	0.67	<0.01
Maximum invading distance (µm)												
H357	58.97	159.10	0.84	<0.01	41.17	170.80	0.52	<0.05	32.44	153.90	0.76	<0.01
H400	84.08	186.90	0.84	<0.01	59.67	194.30	0.85	<0.01	46.28	184.30	0.62	<0.05
H413	110.30	184.90	0.70	<0.01	96.49	195.30	0.91	<0.01	74.58	182.90	0.91	<0.01
Circularity												
H357	-0.23	0.74	0.91	<0.01	-0.22	0.70	0.86	<0.01	-0.21	0.76	0.95	<0.01
H400	-0.26	0.72	0.84	<0.01	-0.24	0.69	0.87	<0.01	-0.22	0.74	0.93	<0.01
H413	-0.27	0.70	0.83	<0.01	-0.29	0.68	0.82	<0.01	-0.23	0.71	0.79	<0.01
Fractal dimension												
H357	0.04	1.11	0.72	<0.01	0.03	1.14	0.43	0.06	0.02	1.13	0.58	<0.05
H400	0.06	1.08	0.62	<0.05	0.05	1.09	0.58	<0.05	0.04	1.09	0.68	<0.01
H413	0.05	1.10	0.56	<0.05	0.05	1.12	0.32	0.11	0.05	1.11	0.75	<0.01
MDMC (µm)												
H357	26.09	131.50	0.73	<0.01	26.95	132.80	0.61	<0.05	20.56	125.20	0.68	<0.01
H400	59.88	151.20	0.82	<0.01	44.91	149.40	0.81	<0.01	32.65	146.50	0.45	<0.05
H413	39.36	160.40	0.56	<0.05	51.94	162.50	0.76	<0.01	37.74	153.60	0.74	<0.01

This study did not continue monitoring the morphology changes beyond two days as in some cases, invasion occurred resulting in the main cluster no longer being apparent (**Figure 22D**). Consequently, the parameters determined from the main cluster could not be determined (*e.g.* circularity, fractal dimension and MDMC).

3.8.1.1 Analysis of the number of clusters

Figure 23A shows that on embedding day, the spheroids of three OSCC lines (growth-inhibited dataset) were organised in a single cluster however cells then started invading the matrix and detaching from the main spheroid increasing the number of clusters (detailed in **Appendix table I**). The differences between the cultures in the three collagen concentrations were most prominent on day 2. The number of clusters of three OSCC lines on day 2 was higher than those observed on embedding day and day 1 ($p<0.05$ for H400 embedded in 3 mg/ml collagen; $p<0.01$ for the others, Two-way ANOVA) except for the H413 line which embedded in 3 mg/ml collagen.

Figure 23B shows the comparison of the number of clusters between three collagen concentration groups. On day 2, the number of clusters of H357 spheroids embedded in 0.5 mg/ml collagen was marginally lower than those embedded in 1.5 mg/ml collagen. The group embedded in 3 mg/ml collagen had the lowest number of clusters and the difference was lower than those embedded in 0.5 mg/ml (1.5 fold, $p<0.05$, Two-way ANOVA) and 1.5 mg/ml collagen (1.6 fold, $p<0.01$, Two-way ANOVA). For H400, no statistically significant differences in the number of clusters between the different collagen concentrations were identified at this time-point. For H413 cells, the number of clusters of spheroids embedded in 0.5 mg/ml collagen was marginally higher than the group embedded in 1.5 mg/ml collagen and 2.1 fold higher than those embedded in 3 mg/ml collagen ($p<0.05$, Two-way ANOVA).

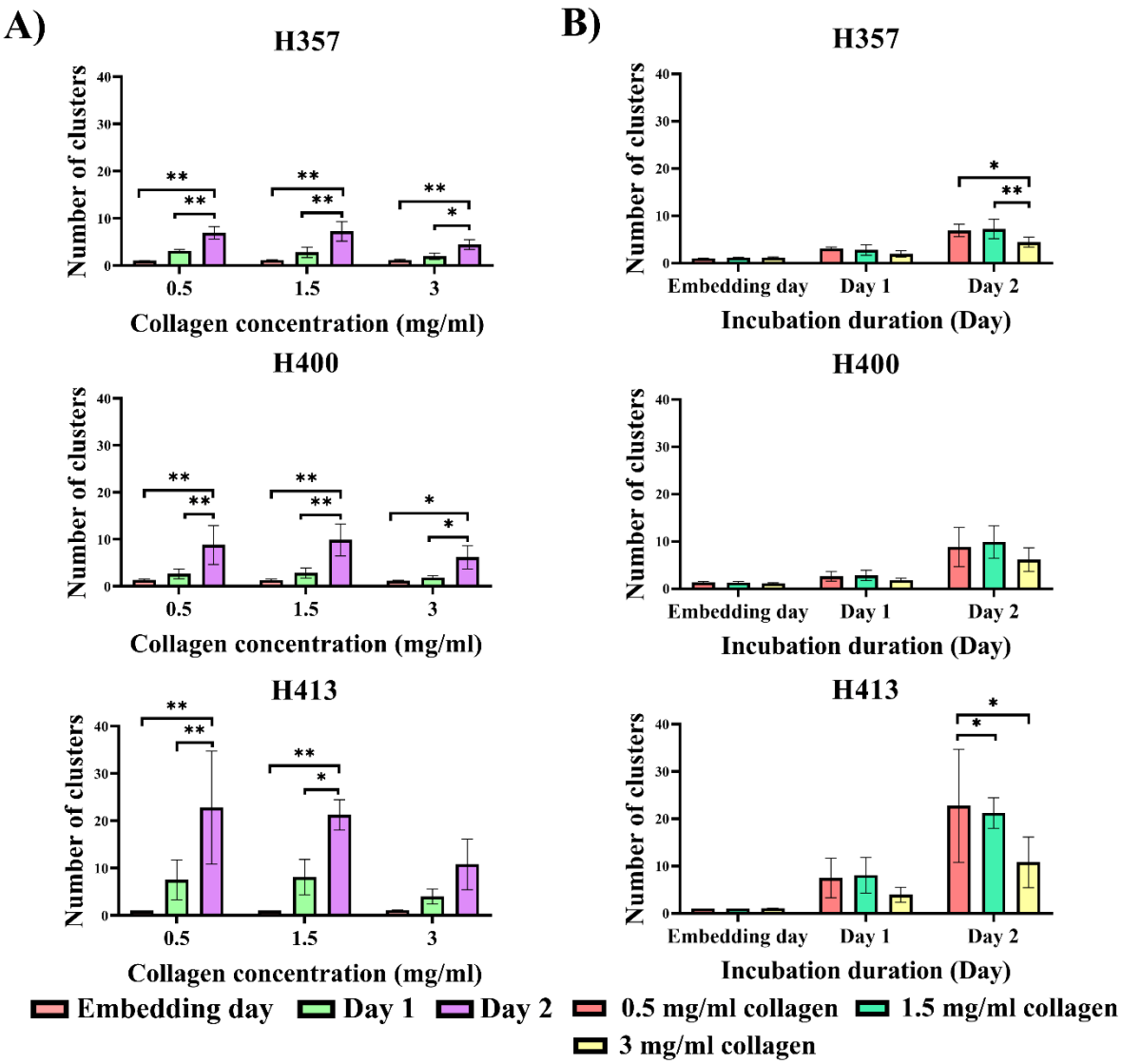

Figure 23. The number of clusters of invading spheroids embedded in 0.5, 1.5 and 3 mg/ml collagen matrices, two days of incubation (growth-inhibited dataset). Spheroids were generated using the hanging drop method (one day of incubation). After being embedded into three collagen concentrations, cells were treated with 8 µg/ml mitomycin C for 2 h. **A)** The number of clusters of three OSCC lines increased with incubation period. The number of clusters on day 2 of three cell lines was higher than those observed on embedding day and day 1, except for H413 embedded in 3 mg/ml collagen. **B)** The comparison of the number of clusters between three collagen concentrations. On day 2, for H357 and H413 cells, the number of clusters in the groups embedded in 0.5 mg/ml and 1.5 mg/ml collagen was higher than those embedded in 3 mg/ml collagen. However, no trend in cluster number was noted in H400 cultures. (Three biological replicates from independent experiments were performed with N=10 for each experiment; Two-way ANOVA followed by *post-hoc* Tukey tests, * = p-value < 0.05, ** = p-value < 0.01, data presented as mean ± 1 SD).

Figure 24 shows a comparison of the number of clusters between the three OSCC lines in which spheroids were embedded in 1.5 mg/ml collagen. On day 1, the number of clusters of H357 cells was similar to those of H400 cells, while for H413 cells this was 2.5 fold higher than H357 ($p<0.05$, Two-way ANOVA) and 2.7 fold higher than H400 cells ($p<0.05$, Two-way ANOVA). On day 2, H357 cells exhibited the lowest number of clusters, followed by H400 and H413 cultures, respectively. Again, H413 cells exhibited a significantly higher number of clusters than for H357 cells by 3.0 fold ($p<0.01$, Two-way ANOVA) and H400 by 2.2 fold ($p<0.01$, Two-way ANOVA).

3.8.1.2 Analysis of the maximum invading distance

The maximum invading distance on the embedding day refers to the diameter of the spheroids after the generation of one cluster per image. **Figure 25A** shows that cells increasingly invaded with the incubation period duration, elevating the maximum invading distance as detailed in **Appendix table II**. The maximum invading distances on day 2 in three collagen concentration groups of H357, H400 and H413 were statistically higher than those at the embedding day ($p<0.05$ for H357 embedded in 3 mg/ml; $p<0.01$ for the others, Two-way ANOVA).

No statistical differences were observed between the maximum invading distances between three collagen concentrations of three OSCC lines on embedding day and day 1. On day 2, the maximum invading distance of H357 spheroids embedded in 0.5 mg/ml was marginally higher than that for the group embedded in 1.5 mg/ml but significantly larger than that for the group embedded in 3 mg/ml collagen by 1.3 fold ($p<0.05$, Two-way ANOVA).

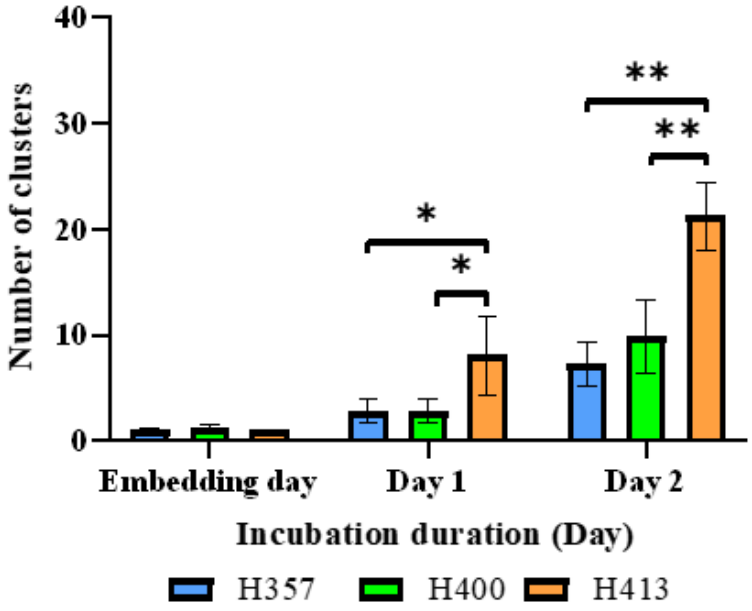

Figure 24. Comparison of the number of clusters in three OSCC lines, two days of observation (growth-inhibited dataset). Each spheroid was generated using the hanging drop method (one day of incubation). After being embedded into 1.5 mg/ml collagen concentrations, cells were treated with 8 μg/ml mitomycin C for 2 h. H413 generated more clusters than H357 and H400 on both days 1 and day 2. (Three biological replicates from independent experiments were performed with N=10 for each experiment; Two-way ANOVA followed by *post-hoc* Tukey tests, * = p-value < 0.05, ** = p-value < 0.01, data presented as mean ± 1 SD).

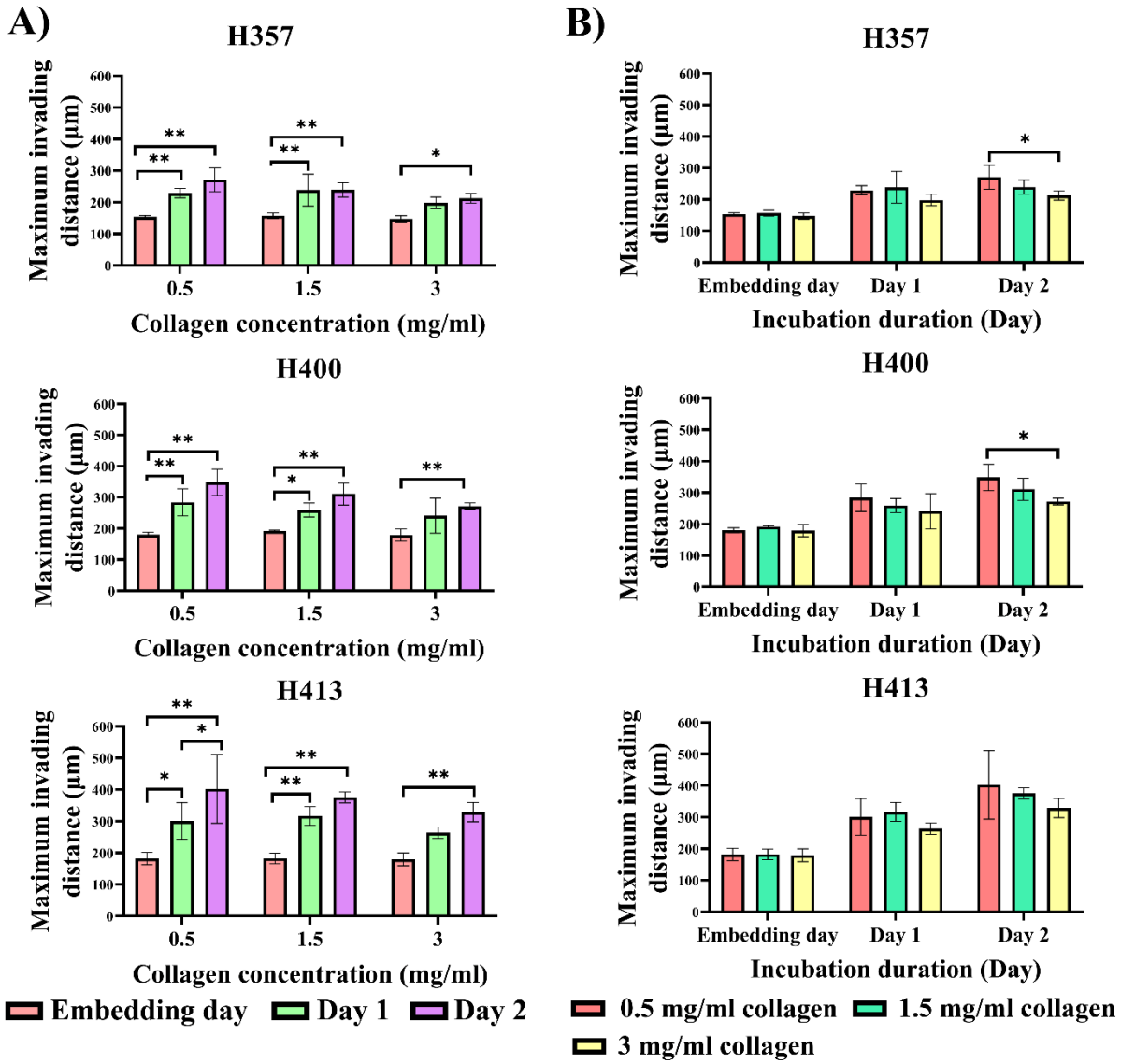

Figure 25. The maximum invading distance of spheroids embedded in 0.5, 1.5 and 3 mg/ml collagen matrices, after two days of incubation (growth-inhibited dataset). Spheroids were generated using the hanging drop method (one day of incubation). After being embedded into three collagen concentrations, cells were treated with 8 µg/ml mitomycin C for 2 h. **A)** The maximum invading distance increased with the incubation period. The result on day 2 was significantly higher than those observed on embedding day in all lines and all three collagen groups. **B)** On day 2, the maximum invading distance decreased with increasing collagen concentrations. (Three biological replicates from independent experiments were performed with N=10 for each experiment; Two-way ANOVA followed by *post-hoc* Tukey tests, * = p-value < 0.05, ** = p-value < 0.01, data presented as mean ± 1 SD).

Similarly, the maximum invading distance of the H400 spheroids embedded in 0.5 mg/ml collagen was marginally higher than the group embedded in 1.5 mg/ml and statistically higher than the group embedded in 3 mg/ml collagen by 1.3 fold ($p<0.05$, Two-way ANOVA). For H413 cells, the group embedded in 0.5 mg/ml collagen provided the largest maximum invading distance, followed by the group embedded in 1.5 mg/ml collagen and 3 mg/ml collagen, respectively (however the differences were not statistically significant) (**Figure 25B**). Linear regression analysis indicated that the maximum invading distance reduced following the increase of collagen concentration in only H357 ($R^2=0.53$, $p<0.05$) and H400 cultures ($R^2=0.58$, $p<0.05$).

Figure 26 provides comparison of the maximum invading distance of the three OSCC spheroid cultures embedded in 1.5 mg/ml collagen. Following embedding, the maximum invading distance of the three OSCC lines was statistically similar for all cell lines. On day 1, the maximum invading distance of H357 cells was marginally smaller than for H400 cells. H413 cultures exhibited the highest maximum invading distance which was 1.3 fold greater than for H357 ($p<0.01$, Two-way ANOVA) and 1.2 fold greater than H400 cells ($p<0.05$, Two-way ANOVA). On day 2, the maximum invading distance increased similarly to those observed on day 1, with H357 cultures exhibiting the smallest invading distance, lower than of H400 (1.3 fold, $p<0.05$, Two-way ANOVA) and those of H413 (1.6 fold, $p<0.01$, Two-way ANOVA). Moreover, the maximum invading distance for H400 cultures was statistically lower than observed for H413 (1.2 fold, $p<0.05$, Two-way ANOVA).

3.8.1.3 Analysis of the circularity of the main cluster

The circularity of all spheroids on embedding day appeared similar as the cells had not shown any invasive behaviour at this point. However, after continuous incubation, the circularity of the main clusters was reduced as a consequence of cell invasion (detailed in **Appendix table III**).

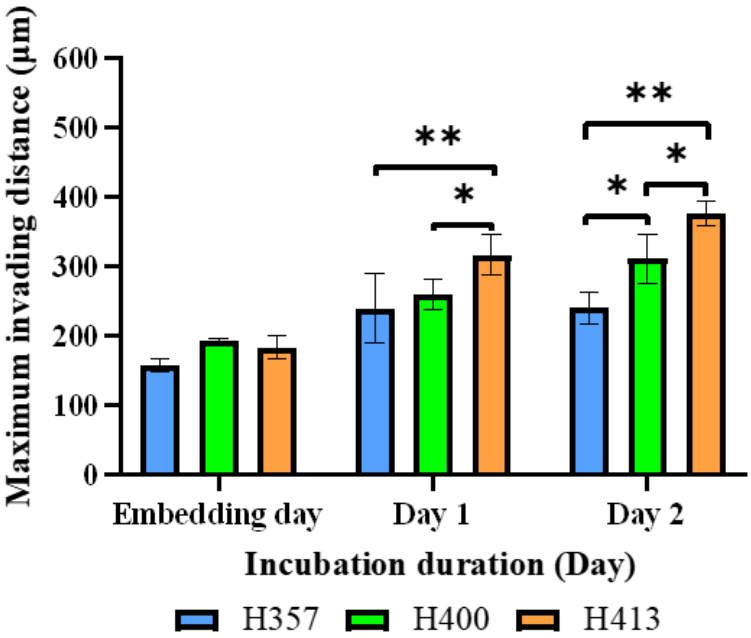

Figure 26. Comparison of the maximum invading distance in three OSCC lines, two days of observation (growth-inhibited dataset). Spheroids were generated using the hanging drop method (one day of incubation). After being embedded into 1.5 mg/ml collagen concentrations, cells were treated with 8 µg/ml mitomycin C for 2 h. The maximum invading distance of H357 cells was the lowest, followed by H400 and H413 cells on both days 1 and day 2. (Three biological replicates from independent experiments were performed with N=10 for each experiment; Two-way ANOVA followed by *post-hoc* Tukey tests, * = p-value < 0.05, ** = p-value < 0.01, data presented as mean ± 1 SD).

Regarding different time points, the circularity of H357, H400 and H413 spheroids on embedding day was significantly higher than those of day 1 and day 2 ($p<0.01$, Two-way ANOVA) (**Figure 27A**).

Figure 27B shows that the circularity of H357 cultures embedded in 0.5 mg/ml collagen was marginally higher than those embedded in a concentration of 1.5 mg/ml but lower than those embedded in 3 mg/ml collagen ($p<0.05$, Two-way ANOVA). No trend was identified on day 2 for this cell line. For H400 and H413 cultures, no statistical significance difference was noted between the three groups on both days 1 and 2.

When comparing cell lines (for those embedded in 1.5 mg/ml collagen), the circularity of the spheroids determined for the three OSCC lines on embedding day was statistically similar. On day 1, the circularity of H357 was slightly higher than for H400 cells and was statistically higher than for H413 cells, ($p<0.05$, Two-way ANOVA). No statistically significant difference was observed between circularity in H400 and H413 cultures. On day 2, the circularity of each cell line continued to decrease in the same order as detected for day 1. The cell line that had the highest circularity was H357, followed by H400 and H413 respectively, however the difference was not statistically significant (**Figure 28**).

3.8.1.4 Analysis of the fractal dimension of the main cell cluster

The second approach to assess the morphology of the main cluster was performed using fractal dimension analysis (**Appendix table IV**). **Figure 29A** shows that the fractal dimension increased with the incubation time. Regarding the incubation period, the fractal dimension on day 2 was significantly higher than embedding day ($p<0.01$ for H357 and H400 embedded in 0.5 mg/ml collagen; $p<0.05$ for the others, Two-way ANOVA) except for H400 embedded in 3 mg/ml collagen and H413 embedded in 1.5 mg/ml collagen. However, the concentration of the collagen matrix did not appear to exert an effect on either day 1 or day 2 (**Figure 29B**).

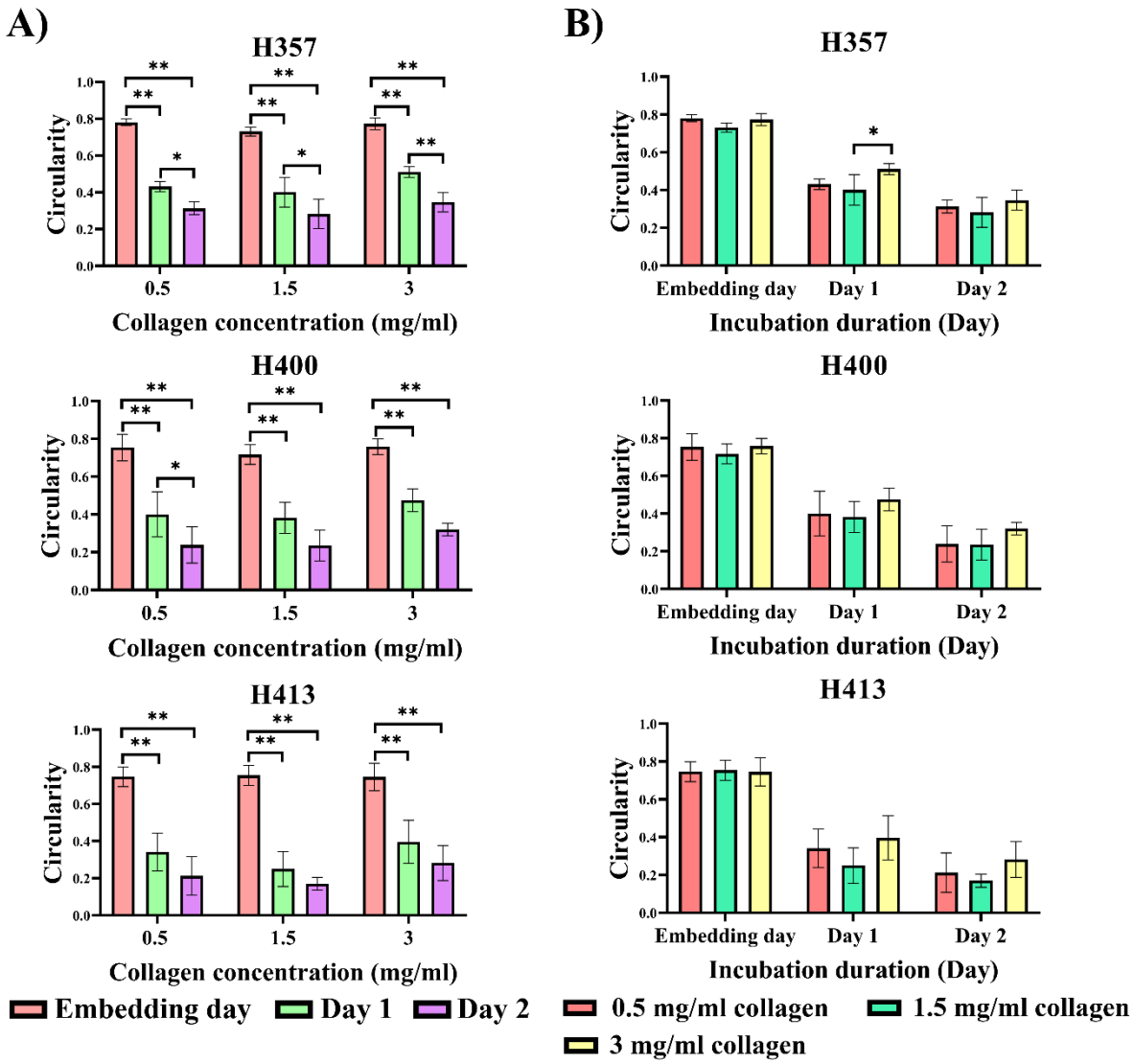

Figure 27. The circularity of invading spheroids embedded in 0.5, 1.5 and 3 mg/ml collagen matrices, two days of incubation (growth-inhibited dataset). Spheroids were generated using the hanging drop method (one day of incubation). After being embedded into three collagen concentrations, cells were treated with 8 µg/ml mitomycin C for 2 h. **A)** The circularity of all groups decreased according to the incubation period, with those observed on day 2 was significantly higher than of those observed on embedding day and day 1. **B)** Overall, the circularity deceased over the incubation period. For the three cell lines, no trend was identified when varying the collagen concentration. (Three biological replicates from independent experiments were performed with N=10 for each experiment; Two-way ANOVA followed by *post-hoc* Tukey tests, * = p-value < 0.05, data presented as mean ± 1 SD).

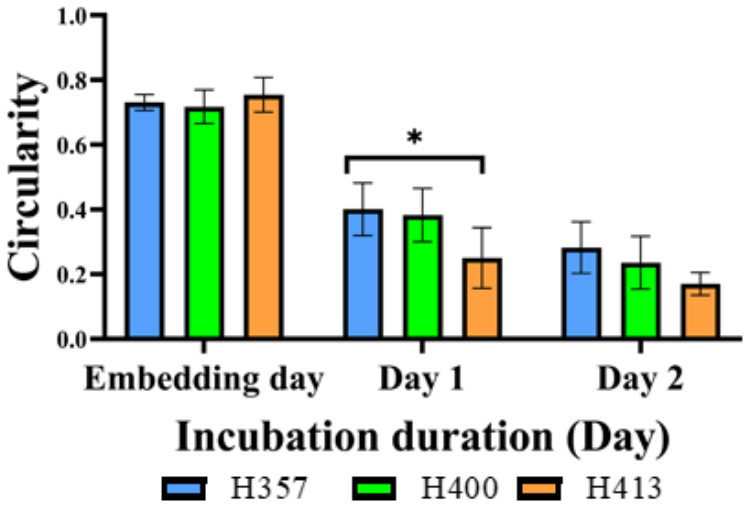

Figure 28. Comparison of the circularity of the main cluster in three OSCC lines, two days of observation (growth-inhibited dataset). Spheroid were generated using the hanging drop method (one day of incubation). After being embedded into 1.5 mg/ml collagen concentrations, cells were treated with 8 µg/ml mitomycin C for 2 h. Among the three cell lines, H357 had the highest circularity for the main cluster, followed by H400 and H413. (Three biological replicates from independent experiments were performed with N=10 for each experiment; Two-way ANOVA followed by *post-hoc* Tukey tests, * = p-value <0.05, data presented as mean ± 1 SD).

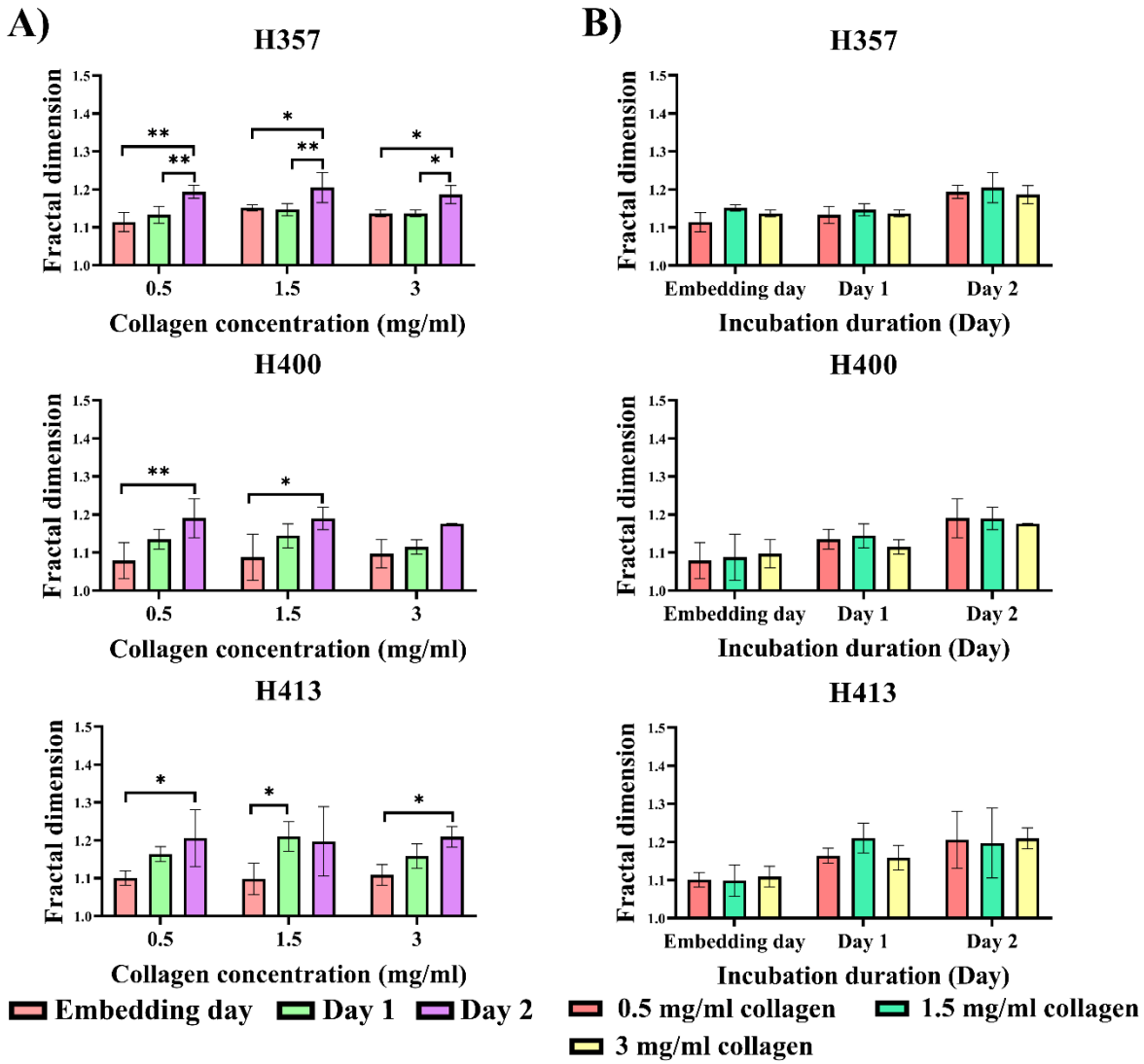

Figure 29. The fractal dimension of invading spheroids embedded in 0.5, 1.5 and 3 mg/ml collagen matrices, two days of incubation (growth-inhibited dataset). Spheroids were generated using the hanging drop method (one day of incubation). After being embedded into three collagen concentrations, cells were treated with 8 µg/ml mitomycin C for 2 h. **A)** The fractal dimension started with nearly 1, indicating the less complex of the spheroid's boundary outline. Fractal dimension of three OSCC lines increased with the incubation period. **B)** Over two days of incubation, no trend was identified when varying the collagen concentration. (Three biological replicates from independent experiments were performed with N=10 for each experiment; Two-way ANOVA followed by *post-hoc* Tukey tests, data presented as mean ± 1 SD).

In addition, no statistically significant differences in the fractal dimension between the three OSCC lines used were noted on both days 1 and 2 (**Figure 30**).

3.8.1.5 Analysis of the maximum diameter of the main cluster (MDMC)

Figure 31A illustrates the MDMC on embedding day refers to the diameter of the spheroids which increased with the incubation period (detailed in **Appendix table V**). The MDMC obtained on day 2 was statistically higher than those of embedding day ($p<0.01$ for H357 and H400 embedded in 0.5 mg/ml collagen; $p<0.05$ for the others, Two-way ANOVA) except H400 embedded in 3 mg/ml collagen and H413 embedded in 1.5 mg/ml collagen.

Regarding collagen concentrations, **Figure 31B** shows that no significant difference in MDMC between the three groups was observed on both days 1 and 2 for H357 and H413 cells. For H400 cultures, the significant difference in MDMC was noted only on day 2 where the group embedded in 0.5 mg/ml collagen had a 1.3 fold larger MDMC compared with those embedded in 3 mg/ml collagen ($p<0.05$, Two-way ANOVA). Linear regression analysis showed that the MDMC decreased with collagen concentration ($R^2 = 0.54$, $p<0.05$, linear regression). For the H357 and H413 lines no obvious trend was noted.

Figure 32 shows the comparison of MDMC between the three OSCC lines in 1.5 mg/ml collagen. On day 1, the MDMC of H357 was marginally lower than that for H400 cultures. The MDMC of H413 cells was 1.4 fold greater than for H357 ($p<0.01$, Two-way ANOVA) and 1.2 fold larger than H400 cells ($p<0.05$, Two-way ANOVA). On day 2, H357 cells exhibited the lowest MDMC which was 1.3 fold lower than H400 cells and 1.4 fold lower than H413 cells ($p<0.01$, Two-way ANOVA).

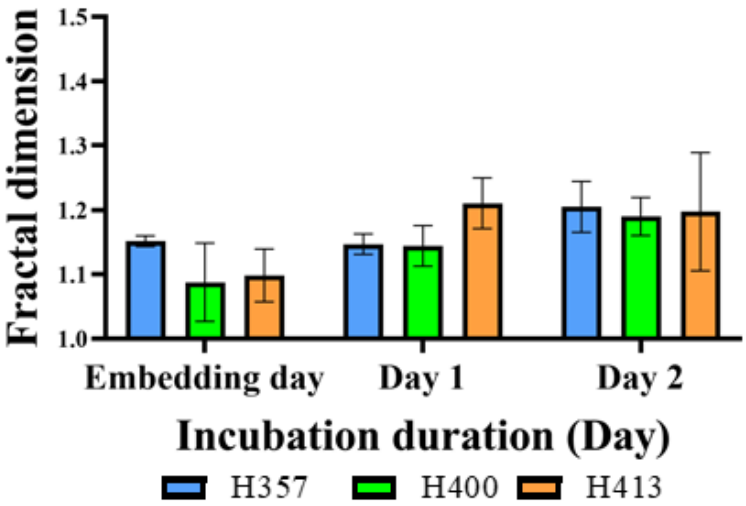

Figure 30. Comparison of the fractal dimension of the main cluster of spheroids in three OSCC lines (growth-inhibited dataset). Spheroids were generated using the hanging drop method (one day of incubation). After being embedded into 1.5 mg/ml collagen concentrations, cells were treated with 8 µg/ml mitomycin C for 2 h. The fractal dimension of the three OSCC lines appeared similar for both days 1 and 2. (Three biological replicates from independent experiments were performed with N=10 for each experiment; Two-way ANOVA followed by *post-hoc* Tukey tests, data presented as mean ± 1 SD).

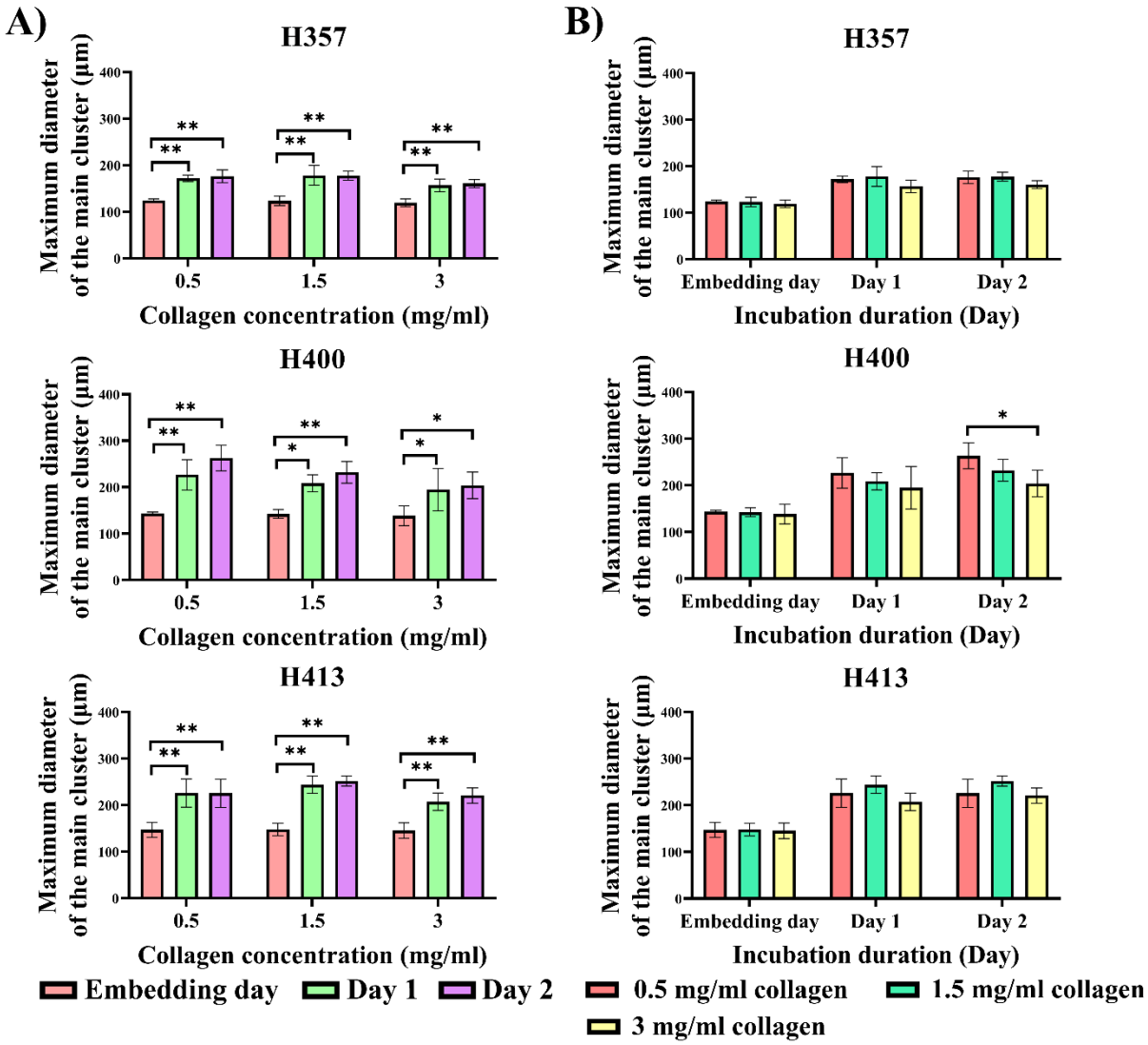

Figure 31. The MDMC of invading spheroids embedded in 0.5, 1.5 and 3 mg/ml collagen matrices, two days of incubation (growth-inhibited dataset). Spheroids were generated using the hanging drop method (one day of incubation). After being embedded into three collagen concentrations, cells were treated with 8 µg/ml mitomycin C for 2 h. **A)** The MDMC increased with the incubation period. The data obtained on the embedding day was significantly lower than those obtained on days 1 and 2. **B)** No statistical difference was identified between the three collagen concentrations for H357 and H413 cultures. For H400, the MDMC decreased, following the increased collagen concentration. (Three biological replicates from independent experiments were performed with N=10 for each experiment; Two-way ANOVA followed by *post-hoc* Tukey tests, * = p-value < 0.05, ** = p-value < 0.01, data presented as mean ± 1 SD).

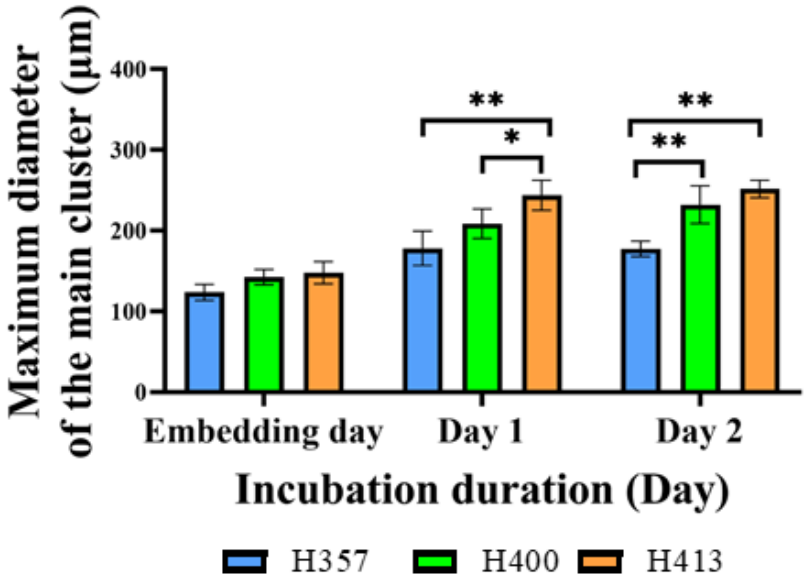

Figure 32. Comparison of MDMC of in three OSCC lines. Spheroids were generated using the hanging drop method (one day of incubation). After being embedded into 1.5 mg/ml collagen concentrations, cells were treated with 8 µg/ml mitomycin C for 2 h. H357 cells provided the smallest MDMC, followed by H400 and H413 on both days 1 and 2. (Three biological replicates from independent experiments were performed with N=10 for each experiment; Two-way ANOVA followed by *post-hoc* Tukey tests, * = p-value < 0.05, ** = p-value < 0.01, data presented as mean ± 1 SD).

3.8.2 The potential effect of proliferation on matrix invasion

The above data provided a baseline for determining invasiveness of the three cell lines in the three collagen concentrations in the condition where growth was inhibited. To study the relationship of proliferation with invasion, images of invading spheroids without mitomycin C treatment were obtained (**Figure 33**). The spread of the tumour cells was lower with the increasing collagen concentrations of the matrix. Details of the invasion characteristics of datasets without mitomycin C treatment are described in **sections 3.8.2.1-5**. Tables with the original data are presented in the **Appendix**.

3.8.2.1 Analysis of the number of clusters

Appendix table VI and **Figure 34** show the number of clusters of invading spheroids embedded in the three collagen concentrations without mitomycin C treatment. The number of clusters increased according to the incubation duration (**Figure 34A**). The number of clusters of H357 and H400 shown in this experiment appeared to be higher than those shown in **Figure 23A**, however statistical analysis could not be undertaken since experiments where spheroids were treated and not treated with mitomycin C were performed separately.

The comparison between three collagen concentrations in group without mitomycin C treatment is shown in **Figure 34B**. On day 1, no statistical difference was identified between the three collagen concentrations for H357 and H413. However, in H400 cells, the number of clusters of spheroids embedded in 0.5 mg/ml collagen was 1.9 fold higher than the group embedded in 3 mg/ml, ($p<0.05$, Two-way ANOVA).

On day 2, H357 spheroids embedded in 0.5 mg/ml collagen provided the highest number of clusters, marginally higher than the group embedded in 1.5 mg/ml collagen and significantly (4.0 fold) higher than the group embedded in 3 mg/ml collagen ($p<0.01$, Two-way ANOVA).

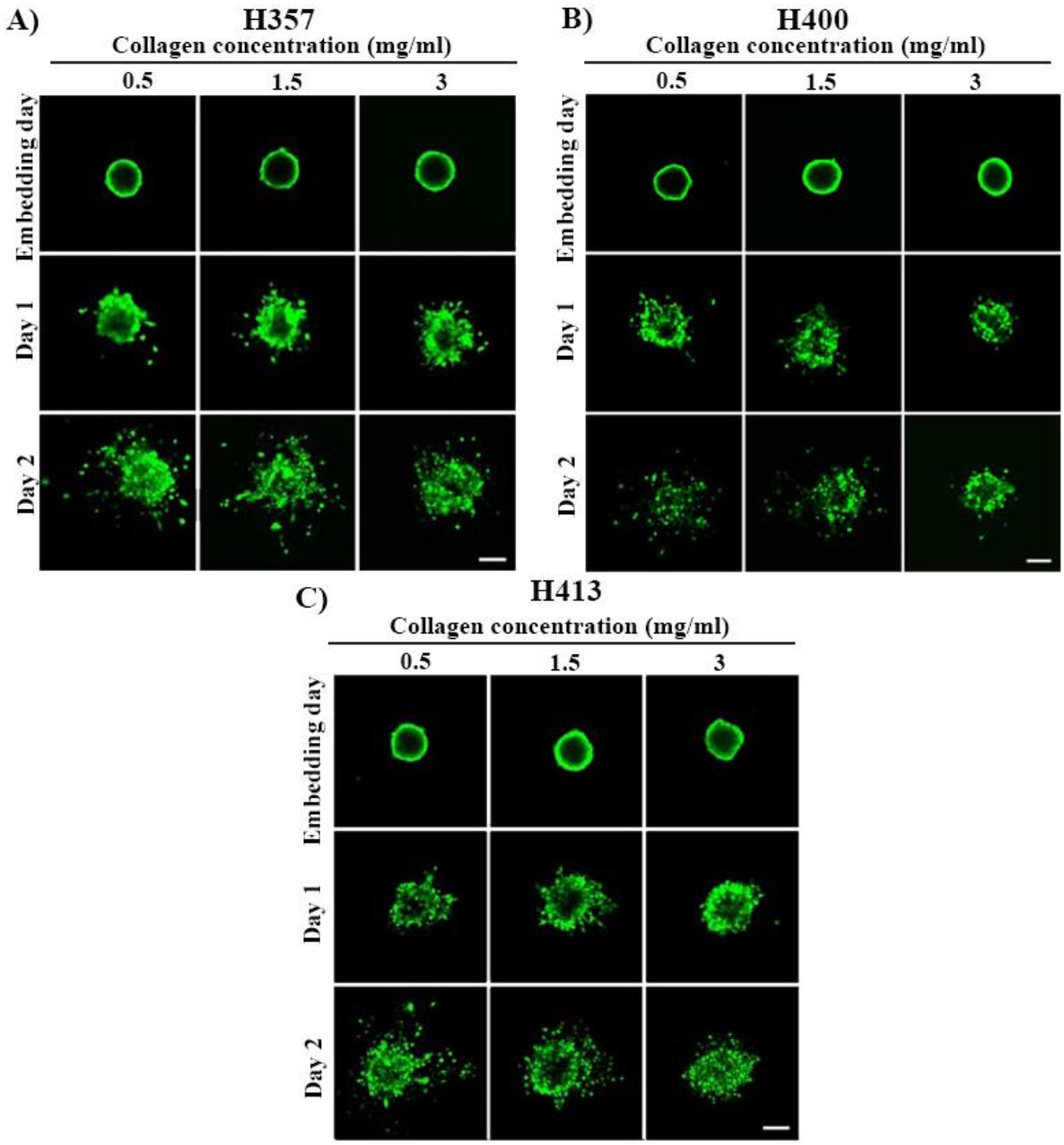

Figure 33. Representative images captured using confocal microscopy of spheroids embedded in the three collagen concentrations (0.5, 1.5 and 3 mg/ml) without mitomycin C treatment. Spheroids were generated using the hanging drop method (one day of incubation). After being embedded into three collagen concentrations, spheroids were stained with calcein AM. **A)** H357 cell line. **B)** H400 cell line and **C)** H413 cell line. Visibly, the spread of invading cells increased in response to the increasing incubation period. However, this spread decreased following an increase in collagen concentration. (Scale bar shown represented 100 μm; X10 objective lens; Three biological replicates from independent experiments were performed with N=10 for each experiment.)

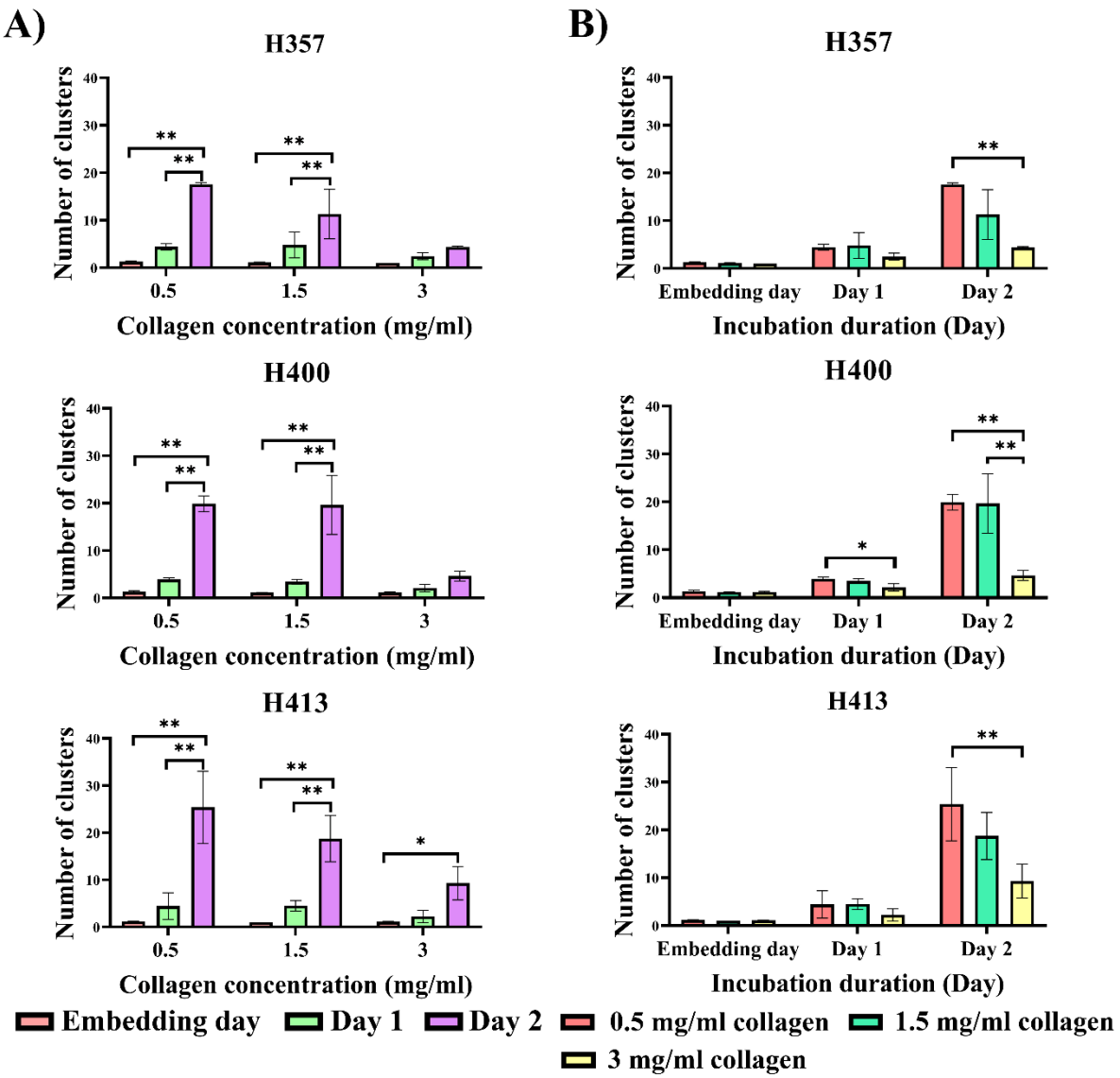

Figure 34. The number of clusters identified from invading spheroids of H357, H400 and H413 cells without proliferation inhibition (no mitomycin C treatment). Spheroids were generated using the hanging drop method, one day of incubation before embedded in three concentrations of collagen matrix. **A)** The number of clusters of three OSCC lines on day 2 was significantly higher than those observed on embedding day except in H357 and H400, embedded in 3 mg/ml collagen. **B)** On day 1, the number of clusters generated by the three collagen concentrations was similar except in H400 cells, in which the group embedded in 0.5 mg/ml collagen exhibited more clusters than those embedded in 3 mg/ml collagen. On day 2, the number of clusters decreased with the increase in collagen concentration. (Three biological replicates from independent experiments were performed with N=10 for each experiment; Two-way ANOVA followed by *post-hoc* Tukey tests, * = p-value < 0.05, ** = p-value < 0.01, data presented as mean ± 1 SD).

For H400 cells, the number of clusters identified in the group embedded in 0.5 mg/ml was similar to that observed in the group embedded in 1.5 mg/ml collagen. The number of clusters identified from the groups embedded in 0.5 and 1.5 mg/ml collagen were 4.3 fold higher than those embedded in 3 mg/ml collagen ($p<0.01$, Two-way ANOVA). The number of clusters in the H413 spheroids embedded in 0.5 mg/ml collagen was slightly higher than the group embedded in 1.5 mg/ml collagen and 2.7 fold higher than those embedded in 3 mg/ml collagen ($p<0.01$, Two-way ANOVA). According to the linear regression analysis, the number of clusters decreased following the increase in collagen concentration (R^2=0.82 for H357 cultures; R^2=0.82 for H400 cultures; R^2=0.67, $p<0.01$ for H413 cultures).

3.8.2.2 Analysis of the maximum invading distance

The maximum invading distance when the proliferation of OSCC cells was not inhibited is shown in **Appendix table VII** and **Figure 35**. Regarding the different time points, the maximum invading distance of three OSCC lines obtained on the embedding day was significantly lower than those obtained on day 2, except for H357 spheroids embedded in 3 mg/ml collagen (**Figure 35A**).

The comparison of the maximum invading distance between three collagen concentrations (without proliferation inhibition) is shown in **Figure 35B**. For H357 cells, the maximum invading distance decreased following the increase in collagen concentration, however no significant differences were noted between the three groups on both days 1 and 2. On day 1 for H400 cells, the group embedded in 0.5 mg/ml collagen exhibited the largest maximum invading distance, marginally greater than for those embedded in collagen at 1.5 mg/ml and 1.6 fold larger than those embedded in 3 mg/ml collagen ($p<0.01$, Two-way ANOVA). On day 2, the maximum invading distance for the group embedded in 0.5 mg/ml was statistically similar to the group embedded in 1.5 mg/ml collagen.

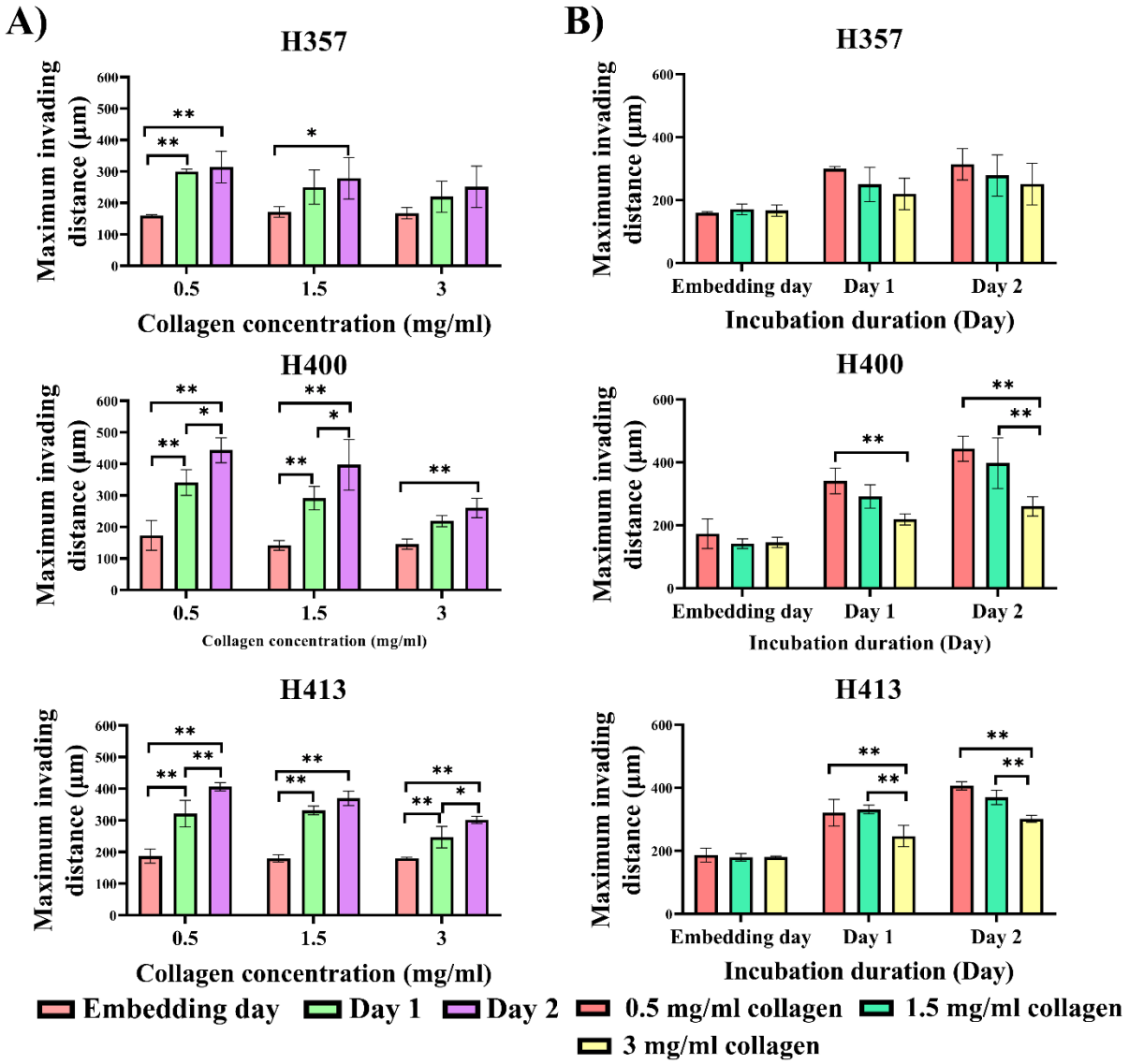

Figure 35. The maximum invading distance of the spheroids embedded in three collagen concentrations without mitomycin C treatment. Spheroids were generated using the hanging drop method (one day of incubation), before embedded in three collagen matrices. **A)** The maximum invading distance on embedding day was significantly lower than data obtained on day 2 except for H357 spheroids embedded in 3 mg/ml collagen. **B)** On day 1, the maximum invading distance for H357 and H400 cells decreased following an increase in collagen concentration. For H413 cells, the groups embedded in 0.5 mg/ml and 1.5 mg/ml collagen exhibited a higher maximum invading distance compared with those embedded in 3 mg/ml collagen. On day 2, the decrease in the maximum invading distance following the elevation of the collagen concentration was observed in all three OSCC lines. (Three biological replicates from independent experiments were performed with N=10 for each experiment; Two-way ANOVA followed by *post-hoc* Tukey tests, * = p-value < 0.05, ** = p-value < 0.01, data presented as mean ± 1 SD).

The group embedded in 3 mg/ml collagen exhibited the smallest maximum invading distance, 1.7 fold and 1.5 fold lower than those embedded in collagen at 0.5 and 1.5 mg/ml, respectively ($p<0.01$, Two-way ANOVA). On day 1 for H413 cells, the maximum invading distance for the group embedded in 0.5 mg/ml was similar to the group embedded in 1.5 mg/ml. The maximum invading distance of the group embedded in 3 mg/ml collagen was lower than the group embedded in collagen at 0.5 mg/ml and 1.5 mg/ml (1.3 fold, $p<0.01$, Two-way ANOVA). On day 2, no statistical difference was noted between groups embedded in 0.5 and 1.5 mg/ml collagen. However, spheroids embedded in 3 mg/ml collagen were statistically decreased compared with groups embedded in 0.5 and 1.5 mg/ml collagen by 1.4 fold and 1.2 fold, respectively ($p<0.01$ respectively, Two-way ANOVA). The linear regression indicated that the maximum invading distance decreased with the collagen concentration in only H400 ($R^2=0.73$, $p<0.01$, linear regression) and H413 ($R^2=0.91$, $p<0.01$, linear regression).

3.8.2.3 Analysis of the circularity of the main cluster

Appendix table VIII and **Figure 36** show data for circularity of the spheroids in the dataset without mitomycin C treatment. The circularity of three OSCC lines on the embedding day was significantly higher than those obtained on both days 1 and 2 ($p<0.01$, Two-way ANOVA). The circularity obtained on day 1 was significantly higher than those obtained on day 2 only in H400 (all collagen concentration) and H413 (embedded in 0.5 mg/ml) lines ($p<0.01$, Two-way ANOVA) (**Figure 36A**).

Figure 36B illustrates the comparison of the circularity of the main cluster in the three OSCC lines in embedded in three collagen concentrations. For all cell lines, on day 1, although the circularity increased with collagen concentration, this difference was not statistically significant. On day 2, the circularity of H357 spheroids embedded in 0.5 mg/ml collagen was statistically similar to the group embedded in 1.5 mg/ml.

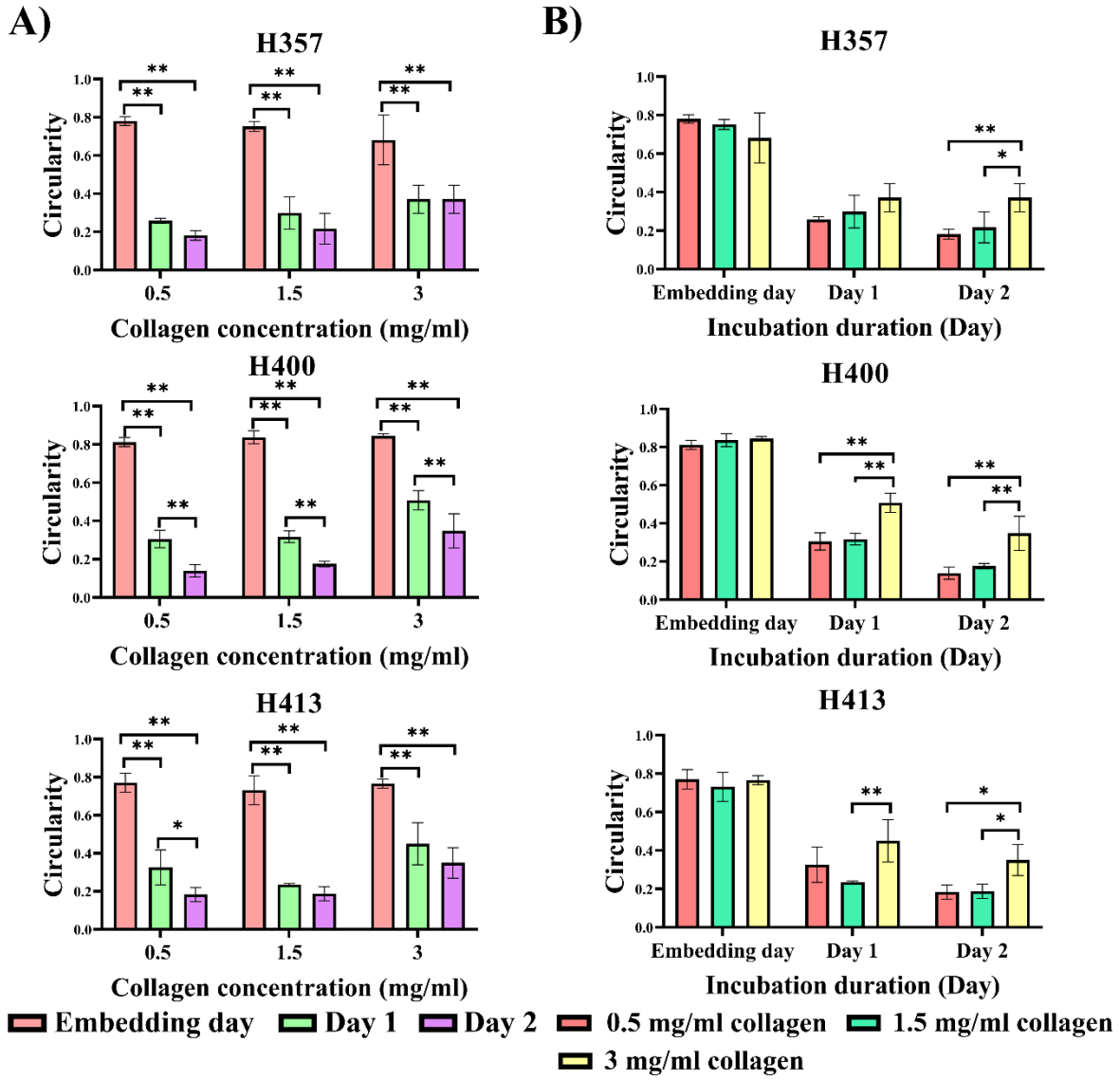

Figure 36. The circularity changes for the spheroids embedded in three collagen concentrations without mitomycin C treatment. Spheroids were generated using the hanging drop method (one day of incubation), before being embedded in three collagen matrices. **A)** In three cell lines, the circularity of invading spheroids on embedding day was significantly higher than those obtained on days 1 and 2. **B)** For H357 and H400 cells, the circularity was elevated with the increasing collagen concentration on both days 1 and 2. For H413 cells, the circularity of the group embedded in 1.5 mg/ml collagen was lower than the group embedded in 3 mg/ml collagen on day 1. On day 2, the group embedded in 3 mg/ml collagen provided a higher circularity than for those embedded in 0.5 and 1.5 mg/ml collagen. (Three biological replicates from independent experiments were performed with N=10 for each experiment; Two-way ANOVA followed by *post-hoc* Tukey tests, * = p-value < 0.05, ** = p-value < 0.01, data presented as mean ± 1 SD).

The circularity of the group embedded in 3 mg/ml was higher than those embedded in 0.5 mg/ml ($p<0.01$, Two-way ANOVA) and 1.5 mg/ml ($p<0.05$, Two-way ANOVA). For H400 cells, the circularity elevated with increased collagen concentration. The circularity of the group embedded in 3 mg/ml was significantly higher than the other two groups ($p<0.01$, Two-way ANOVA) on both days 1 and 2. For H413 cells, the group embedded in 1.5 mg/ml collagen, circularity was significantly lower than for those embedded in 3 mg/ml ($p<0.01$, Two-way ANOVA) on day 1. On day 2, the circularity of the group embedded in 0.5 mg/ml collagen decreased and was statistically similar to data for the group embedded in 1.5 mg/ml. The group embedded in 3 mg/ml collagen exhibited higher circularity compared with other groups ($p<0.05$, Two-way ANOVA). A trend in the reduction of circularity with decreasing collagen concentration was found to be significant ($R^2=0.67$ for H357 cultures; $R^2=0.75$ for H400 cultures; $R^2=0.64$ for H413 cultures, $p<0.01$, Linear regression).

3.8.2.4 Analysis of the fractal dimension analysis of the main cluster

The fractal dimension of the spheroids embedded in the three collagen concentrations without inhibiting proliferation is shown in **Appendix table IX** and **Figure 37**. The fractal dimension of three OSCC lines on the embedding day was significantly lower than those obtained on day 2 ($p<0.05$ for H357 spheroids embedded in 1.5 mg/ml collagen, $p<0.01$ for the others, Two-way ANOVA), except for H357 and H400 spheroids embedded in 3 mg/ml collagen. The fractal dimension on day 1 was lower than those obtained on day 2 only in H400 (all collagen concentration) and H413 (embedded in 0.5 and 1.5 mg/ml) lines (**Figure 37A**).

Figure 37B shows that no significant difference was noted between the three collagen concentrations on both days 1 and 2 for H357 cells. For H400 cells, the fractal dimension on day 1 for the group embedded in 0.5 mg/ml collagen was similar to those embedded in 1.5 mg/ml collagen.

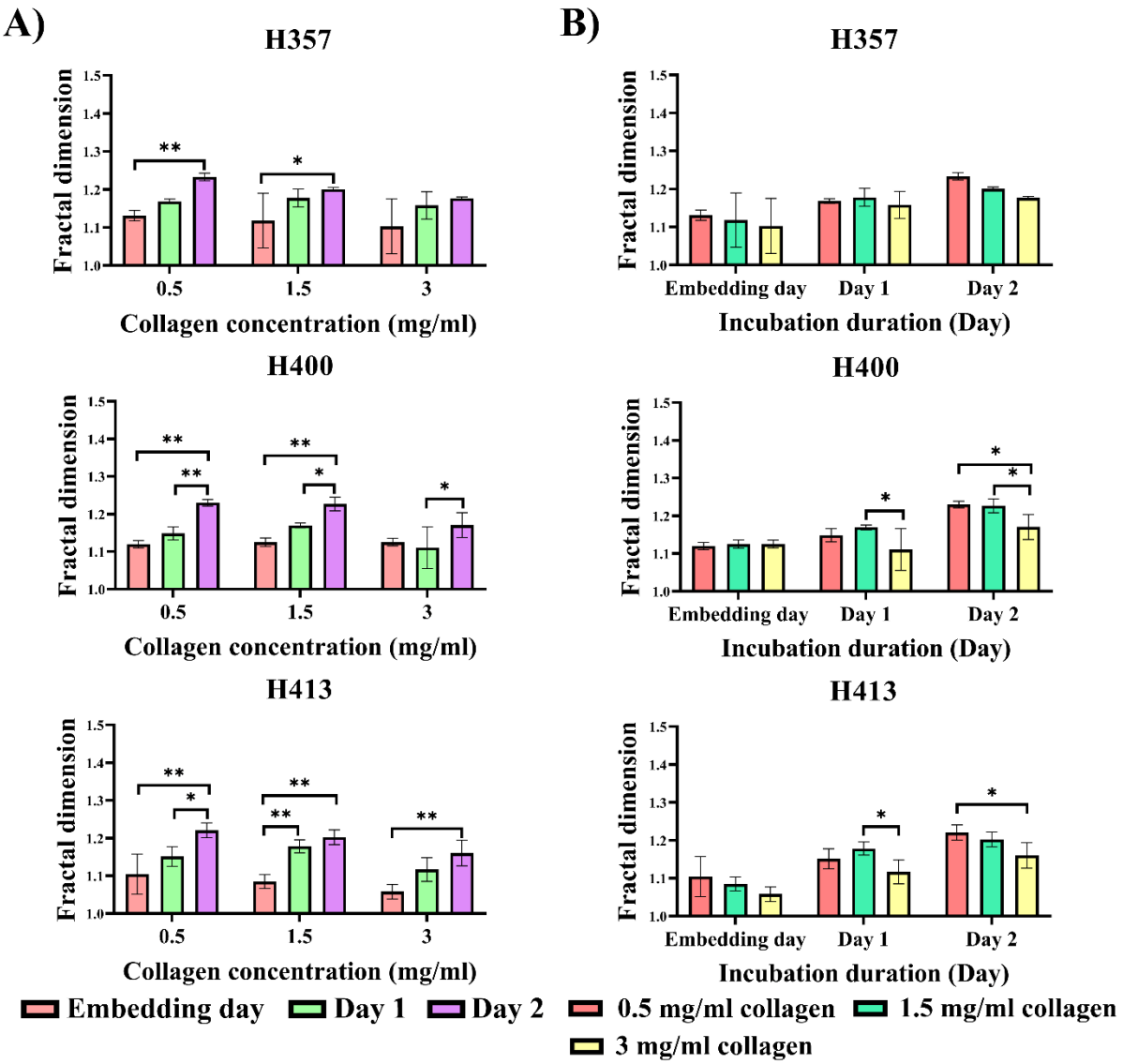

Figure 37. Fractal dimensions for the spheroids without mitomycin C treatment after two days of culture. Spheroids were generated using the hanging drop method (one day of incubation), before being embedded in three collagen matrices. **A)** The fractal dimension of the three OSCC lines on day 2 was significantly higher than those obtained on embedding day except for H357 and H400 spheroids that embedded in 3 mg/ml collagen matrix. **B)** On day 1, no significant difference was observed between the three collagen concentrations for H357 cells. In H400 and H413 cells, the group embedded in 1.5 mg/ml had a higher fractal dimension compared with those embedded in 3 mg/ml collagen. On day 2, all cell lines exhibited the same trend: the fractal dimension was reduced following the increase in collagen concentration. (Three biological replicates from independent experiments were performed with N=10 for each experiment; Two-way ANOVA followed by *post-hoc* Tukey tests, * = p-value < 0.05, data presented as mean ± 1 SD).

The group embedded in 3 mg/ml collagen had a statistically significant lower fractal dimension than the group embedded in 1.5 mg/ml collagen ($p<0.05$, Two-way ANOVA). On day 2, the fractal dimension for the group embedded in 0.5 mg/ml collagen was at the same level as the group embedded in 1.5 mg/ml. The fractal dimension of the group embedded in 3 mg/ml collagen was significantly lower than the other groups ($p<0.05$, Two-way ANOVA). For H413 cells, the fractal dimension of the group embedded in 3 mg/ml collagen was lower than the group embedded in 1.5 mg/ml collagen ($p<0.05$, Two-way ANOVA) on day 1 and lower than the groups embedded in 0.5 mg/ml on day 2 ($p<0.05$, Two-way ANOVA). Moreover, the linear regression analysis showed that the fractal dimension decreased with increasing collagen concentration ($R^2=0.91$, $p<0.01$ for H357 cultures; $R^2=0.60$, $p<0.05$ for H400 cultures; $R^2=0.59$, $p<0.05$ for H413 cultures).

3.8.2.5 Analysis of the maximum diameter of the main cluster (MDMC)

The MDMC of the spheroids embedded in three collagen concentrations without mitomycin C is shown in **Appendix table X** and **Figure 38**. **Figure 38A** shows that the MDMC increased with incubation time. The MDMC on embedding day was statistically lower than MDMC on days 1 and 2 ($p<0.01$, Two-way ANOVA) only in H400 and H413 lines.

Figure 38B shows the comparison of MDMC between three collagen groups of three OSCC lines. The MDMC for H357 cells on both days 1 and 2 of culture decreased following the increase in the collagen concentration, however this difference was not statistically significant. For H400 cells, the MDMC of the group embedded in 0.5 mg/ml collagen on day 1 was greater than for the group embedded in 1.5 mg/ml collagen but this was not statistically significant.

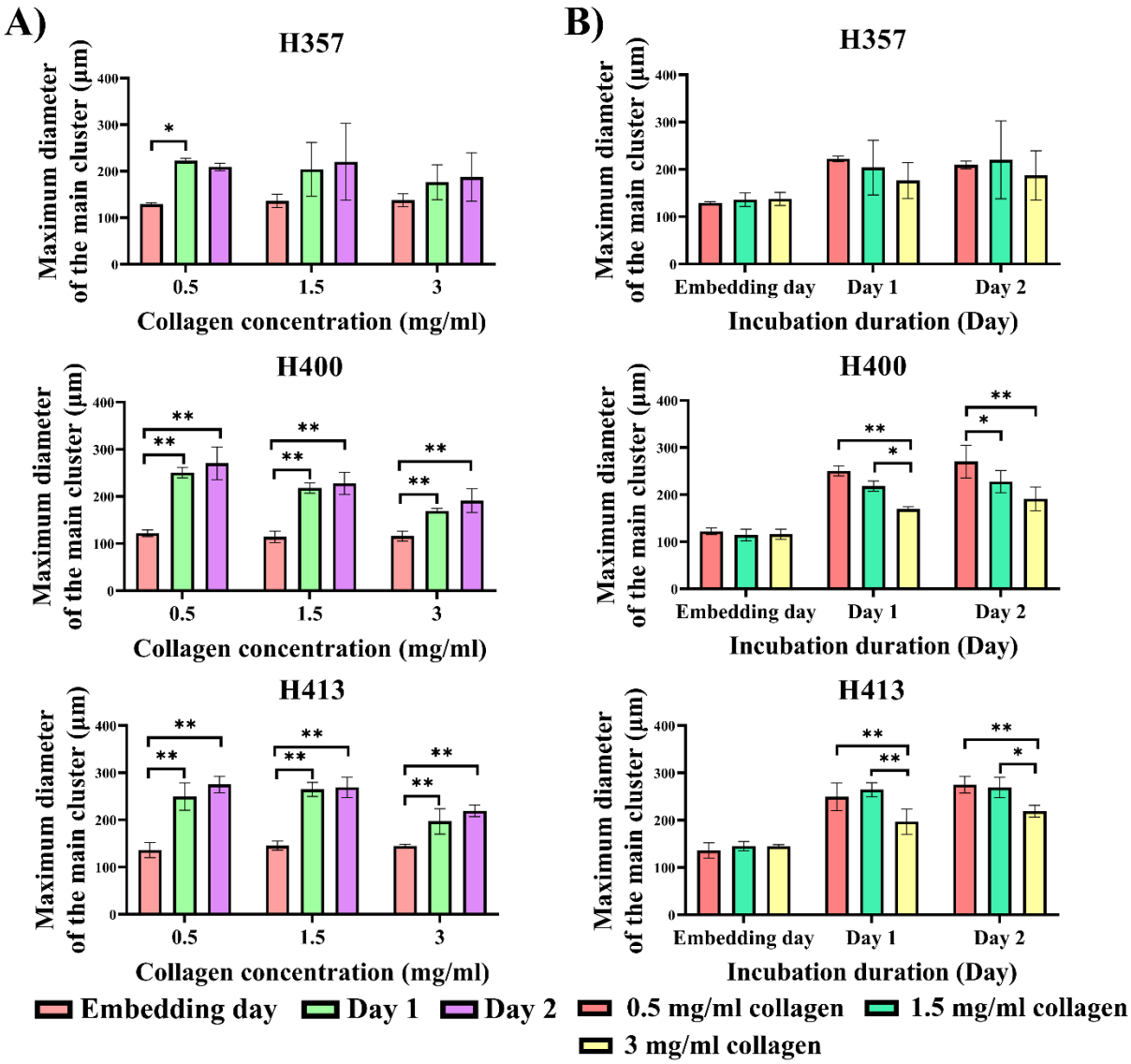

Figure 38. Comparison of the MDMC for spheroids embedded in three collagen concentrations without proliferation inhibition (no mitomycin C treatment). Spheroids were generated using the hanging drop method (one day of incubation), before being embedded in three collagen matrices. **A)** The MDMC increased with the incubation period. Only H400 and H413 showed that the MDMC on embedding day was significantly lower than those observed on days 1 and 2. **B)** The MDMC of H357 cells was decreased when the collagen concentration was increased on day 1, but no trend was observed on day 2. For H400, the MDMC was reduced following the elevation of the collagen concentration on both days 1 and 2. For H413 cells, the MDMC of the group embedded in 0.5 mg/ml and 1.5 mg/ml was higher than for those embedded in 3 mg/ml on both days 1 and 2. (Three biological replicates from independent experiments were performed with N=10 for each experiment; Two-way ANOVA followed by *post-hoc* Tukey tests, * = p-value < 0.05, ** = p-value < 0.01, data presented as mean ± 1 SD).

The group embedded in 3 mg/ml collagen had the lowest MDMC, which was significantly smaller than the group embedded in 0.5 mg/ml collagen by 1.5 fold ($p<0.01$, Two-way ANOVA) and 1.5 mg/ml collagen by 1.3 fold ($p<0.05$, Two-way ANOVA). On day 2, the MDMC of this cell line reduced according to the increase in collagen concentration. The MDMC of group embedded in 0.5 mg/ml collagen was significantly greater than for the group embedded at 1.5 mg/ml by 1.2 fold ($p<0.05$, Two-way ANOVA) and the group embedded at 3 mg/ml by 1.4 fold ($p<0.01$, Two-way ANOVA). Linear regression analysis indicated that the MDMC for this cell line decreased with the increase in collagen concentration ($R^2=0.82$, $p<0.01$, Linear regression). For H413 line, the MDMC on day 1 of group embedded in 0.5 mg/ml collagen was statistically similar to that of cultures embedded in 1.5 mg/ml collagen. For the group embedded in 3 mg/ml collagen this value was smaller than those of the other two groups (by 1.3 fold, $p<0.01$, Two-way ANOVA). On day 2, the MDMC of the group embedded in 0.5 mg/ml was statistically the same as for those embedded in 1.5 mg/ml collagen. The MDMC following embedding in 3 mg/ml collagen on this day was smaller that the group embedded in 0.5 mg/ml collagen (1.3 fold, $p<0.01$, Two-way ANOVA) and that for the group embedded in 1.5 mg/ml collagen (1.2 fold, $p<0.05$, Two-way ANOVA). Linear regression analysis showed that the MDMC for H413 cells was reduced in line with the increase in collagen concentration ($R^2=0.67$, $p<0.01$, Linear regression).

3.9 Conclusion

The three cell lines exhibited different proliferation, migration and invasion characteristics. For the MCTS model, the hanging drop method was the most suitable for further experimentation, but the generation step required a 10% FBS supplement. Increasing concentrations of collagen matrix hindered the invasion of these three OSCC lines, evidenced by a reduction of the number of clusters, maximum invading distance and MDMC and the clusters remaining circular.

Cultures on collagen at 1.5 mg/ml showed the greatest differences in invasion characteristics between three cell lines. Proliferation affected invasion which was evidenced by an elevation of the number of tumour clusters and since the baseline of the invasion of cell lines should be similar and the invasion of the control initially (untreated group) should not cover the entire field of view. The spheroids used in further experiments (**sections 4.9**, **5.9** and **6.6**) were generated using the hanging drop method (one day of incubation), embedded in 3 mg/ml collagen and were treated with 8 μg/ml mitomycin C. an increase in the maximum invading distance reached of some of the cell lines.

Chapter 4: Results

Effects of epidermal growth factor on proliferation, migration, invasion and gene expression in OSCC lines

4.1 Aims

Chapter 3 established baseline information on the proliferative, migratory and invasive behaviours of H357, H400 and H413 cells as well as identifying appropriate assay protocols. As this study planned to compare the effect of S1PR2 on migration and invasion of three OSCC lines with EGF, a molecule which is widely used as a positive control for these properties, this chapter aimed to determine the proliferative, migratory and invasive effects of EGF on these cell lines.

4.2 Objectives

The objectives of this chapter were to determine:

a) the expression of *EGFR* and *EGF* expression in H357, H400 and H413 cultures,
b) the effect of EGF on the proliferation, migration and invasion in H357, H400 and H413 cells
c) the effect of EGF on the expression of EMT-related genes, and
d) the effect of EGF on *Rac1* expression and Rac1 activity.

As mentioned in chapter 2, the present study determined the cellular and molecular effects of two concentrations of EGF, *e.g.* 1 ng/ml (representing a low dose) and 20 ng/ml (representing a high dose) (Kawamoto *et al.*, 1984, Cowley *et al.*, 1986, Kamata *et al.*, 1986, Prime *et al.*, 1994). Three experimental groups were set up for each cell line: 1) No EGF (control), 2) low dose EGF (1 ng/ml), and 3) high dose EGF (20 ng/ml).

4.3 *EGFR* expression and EGF production

From the sqRT-PCT analysis, H357 cells exhibited the lowest expression of *EGFR*, followed by H400 and H413 cells, respectively, however there were no statistical differences in *EGFR* expression between the three cell lines (**Figure 39A**).

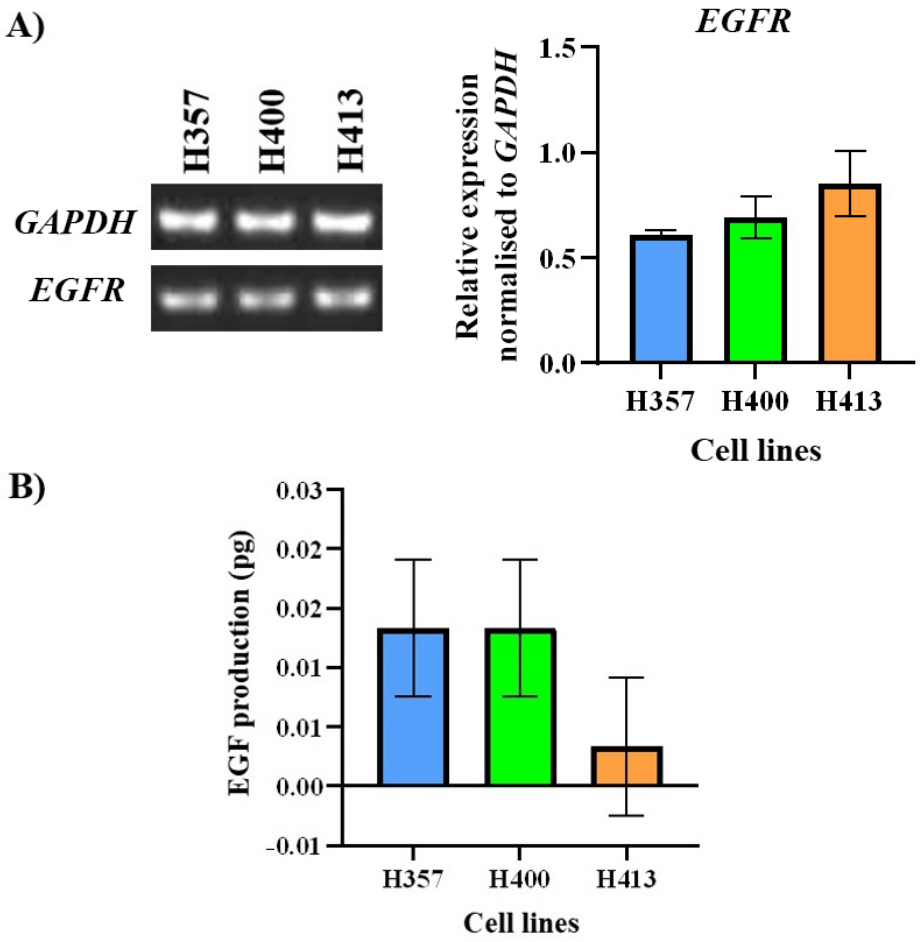

Figure 39. Baseline *EGFR* gene expression and EGF protein expression. **A)** Representative images of *EGFR* expression determination using sqRT-PCR analysis (left). The three OSCC lines expressed *EGFR* at similar levels (right). **B)** According to the ELISA, the three OSCC lines produced a relatively low amount of EGF at the picogram level. (Three biological replicates from independent experiments; One-way ANOVA followed by *post-hoc* Tukey tests, * = p-value < 0.05, ** = p-value < 0.01, data presented as mean ± 1 SD).

EGF expression in the three cell lines was undetectable using sqRT-PCT analysis. was undetectable using sqRT-PCT analysis. The ELISA, however showed that EGF production by the three OSCC lines was relatively low, at the picogram level, with no significant differences between the three cell lines investigated (**Figure 39B**).

4.4 Growth curve and doubling time analysis

For H357 cells, the control doubling time was 1.9 ± 0.1 days and when treated with 1 ng/ml EGF, the doubling time decreased to 1.5 ± 0.1 days which was 1.2 fold decrease from the control ($p<0.01$, One-way ANOVA). However, EGF treatment at 20 ng/ml elevated the doubling time to 2.5 ± 0.1 days, which was 1.3 fold higher than the control ($p<0.01$, One-way ANOVA) **(Figure 40A)**. For H400 cells, only the control group showed a log phase in the growth curve, providing a doubling time of 1.3 ± 0.1 days. In contrast, the number of cells in the EGF-treated groups decreased over the incubation period (**Figure 40B**). No statistical differences in cell numbers were identified between the groups treated with 1 ng/ml and 20 ng/ml EGF. Moreover, in both EGF-treated groups, the cultures were disaggregated into single cells rather than remaining in cell clusters and the typical polygonal morphology of H400 cells appeared to become rounder, indicating that cells were detaching from the substrate. Also, some cells appeared to develop protrusions (**Figure 41**), suggesting that cells were migrating. The H413 cultures exhibited a similar trend to the H357 cultures (**Figure 40C**). EGF at 1 ng/ml reduced the doubling time from 1.3 ± 0.1 days (control) to 1.2 ± 0.2 which was a 1.1 fold reduction from the control ($p<0.01$, One-way ANOVA). However, the group treated with 20 ng/ml EGF exhibited a doubling time of 1.8 ± 0.0 days which was a 1.4 fold increase compared with the control ($p<0.05$, One-way ANOVA).

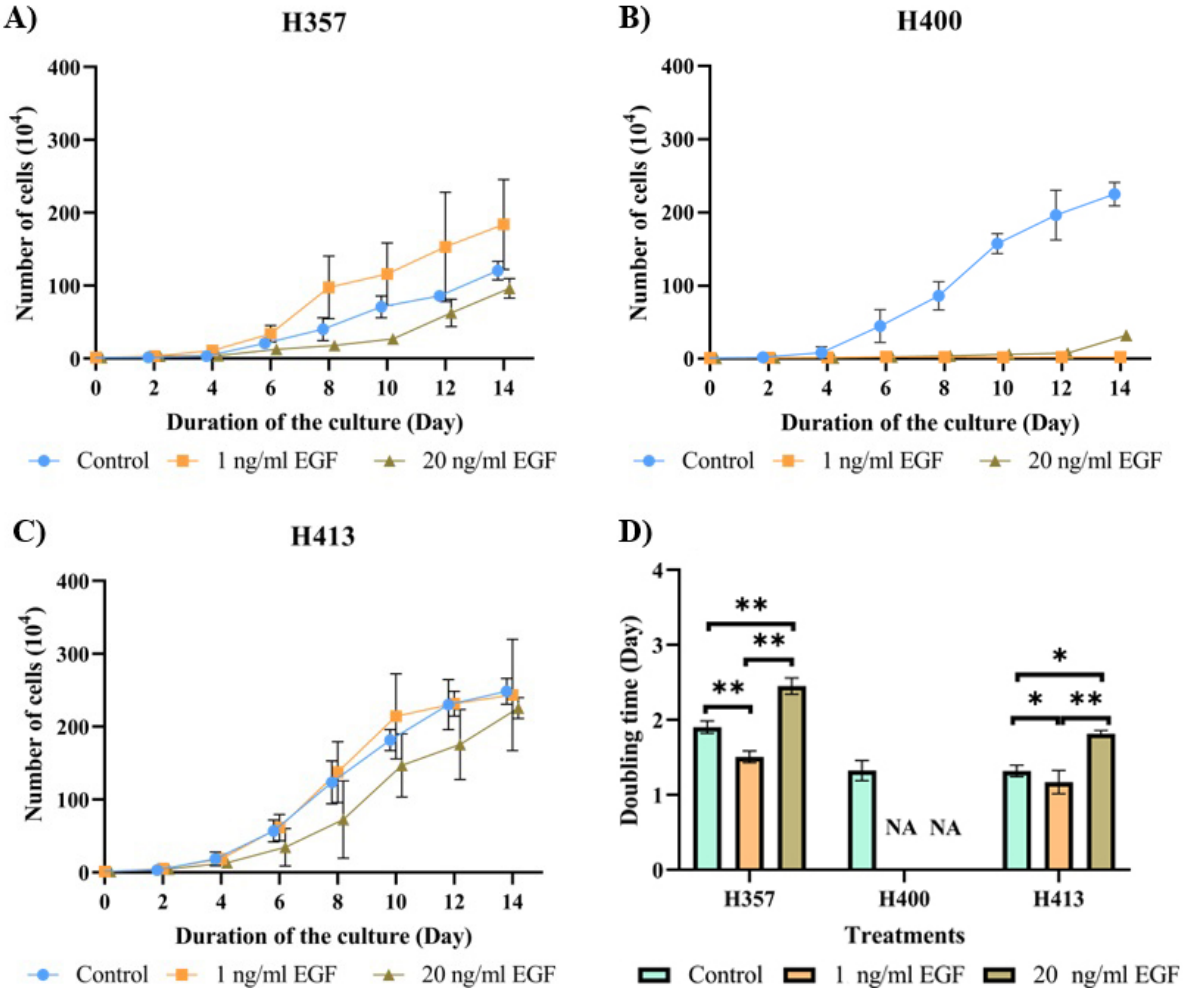

Figure 40. The effect of EGF on proliferation of H357, H400 and H413 cells determined using the growth curves and doubling times. Three cell lines were cultured with media supplemented with 10% FBS (control); 10% FBS with 1 ng/ml EGF; or 10% FBS with 20 ng/ml EGF. **A) & C)** The growth curve shows that the proliferation of H357 and H413 cells was elevated when treated with 1 ng/ml EGF but reduced when treated with 20 ng/ml EGF. **B)** The growth curve indicates that EGF treatments inhibited the proliferation of H400 cells at both concentrations used. **D)** The doubling time of H357, H400 and H413 cells was calculated from the growth curves. EGF at 1 ng/ml decreased the doubling time of H357 and H413 cells but EGF treatment at 20 ng/ml caused an increase. The doubling time of H400 cells could be calculated only in the control group. (N=3; Points on the line graphs have been jittered to prevent overlapping; One-way ANOVA followed by *post-hoc* Tukey tests, * = p-value <0.05, ** = p-value < 0.01, data presented as mean ± 1 SD).

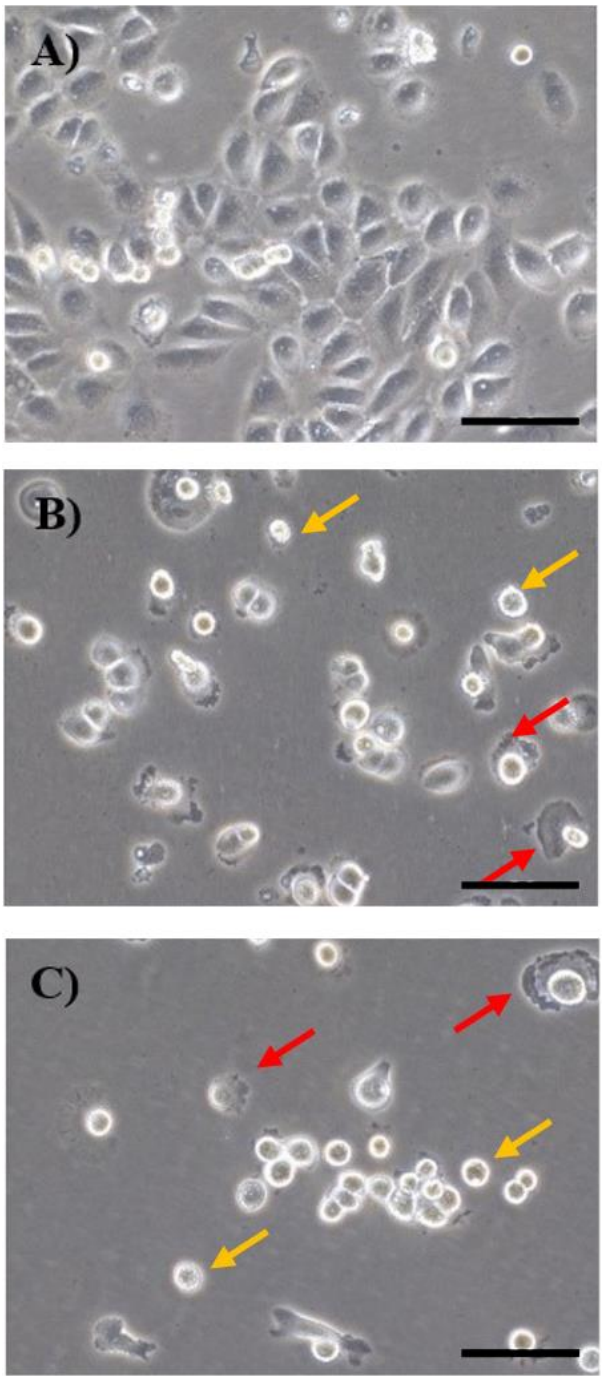

Figure 41. Representative images of H400 cells captured using a phase contrast microscopy on day 14 of culture. **A)** Cell morphology in the control group demonstrated a polygonal shape. **B)** Cells treated with 1 ng/ml EGF. **C)** Cells treated with 20 ng/ml EGF. Some cells in the groups supplemented with either 1 ng/ml or 20 ng/ml EGF appeared more rounded (yellow arrow), suggesting possible detachment from the culture plate. Some of the cells exhibited protrusions, indicating possible migration (red arrow), (X20 objective lens; the scale bar = 50 µm).

4.5 BrdU assay

A second approach to determine the relationship between EGF treatment and cell proliferation was investigated using the BrdU assay. The overall trend in the data was consistent with that obtained using the growth curve (**Figure 42**).

For H357 cells, EGF supplementation at 1 ng/ml increased the percentage of BrdU positive cells from 15.5 ± 1.6 (control) to 30.3 ± 1.6 (a 2.0 fold increase, $p<0.01$, One-way ANOVA). On the contrary, EGF treatment at 20 ng/ml reduced this percentage to 11.1 ± 1.4 which was a 1.4 fold decrease compared with the control ($p<0.05$, One-way ANOVA). For H400 cells, the percentage of positive BrdU cells in the control was 23.1 ± 3.3, a 1.8 fold and 2.0 fold higher than the groups treated with 1 ng/ml EGF (12. ± 2.0) and the group treated with 20 ng/ml EGF (11.9 ± 1.9) respectively (both $p<0.01$, One-way ANOVA). No significant differences were noted between the two EGF-treated groups. The group treated with 1 ng/ml EGF had 31.3% ± 1.8 of BrdU positive cells which was 1.4 fold higher than the control group (22.3% ± 1.1) ($p<0.01$, One-way ANOVA). Conversely, EGF at 20 ng/ml suppressed the proliferation of H413 cells, resulting in a percentage of BrdU positive cells of 16.1 ± 3.4, 1.4 fold reduction from the control ($p<0.05$, One-way ANOVA).

4.6 Scratch wound migration assay

The effect of EGF on the migration of H357 cells is shown in **Figure 43A**. At 12 h, the control group exhibited the lowest percentage wound closure (12.9% ± 2.4) which was, marginally lower than the group which received 1 ng/ml EGF (19.8 ± 6.5) but the difference did not reach significance. For the group treated with 20 ng/ml EGF, wound closure was 25.7% ± 2.1 which was 2.1 fold higher than the control ($p<0.01$, One-way ANOVA). At 18 h, the percentage wound closure of the control was 14.5 ± 0.4, while in the group treated with 1 ng/ml EGF this value rose to 27.0 ± 8.7 (1.9 fold higher than the control, $p<0.05$, One-way ANOVA).

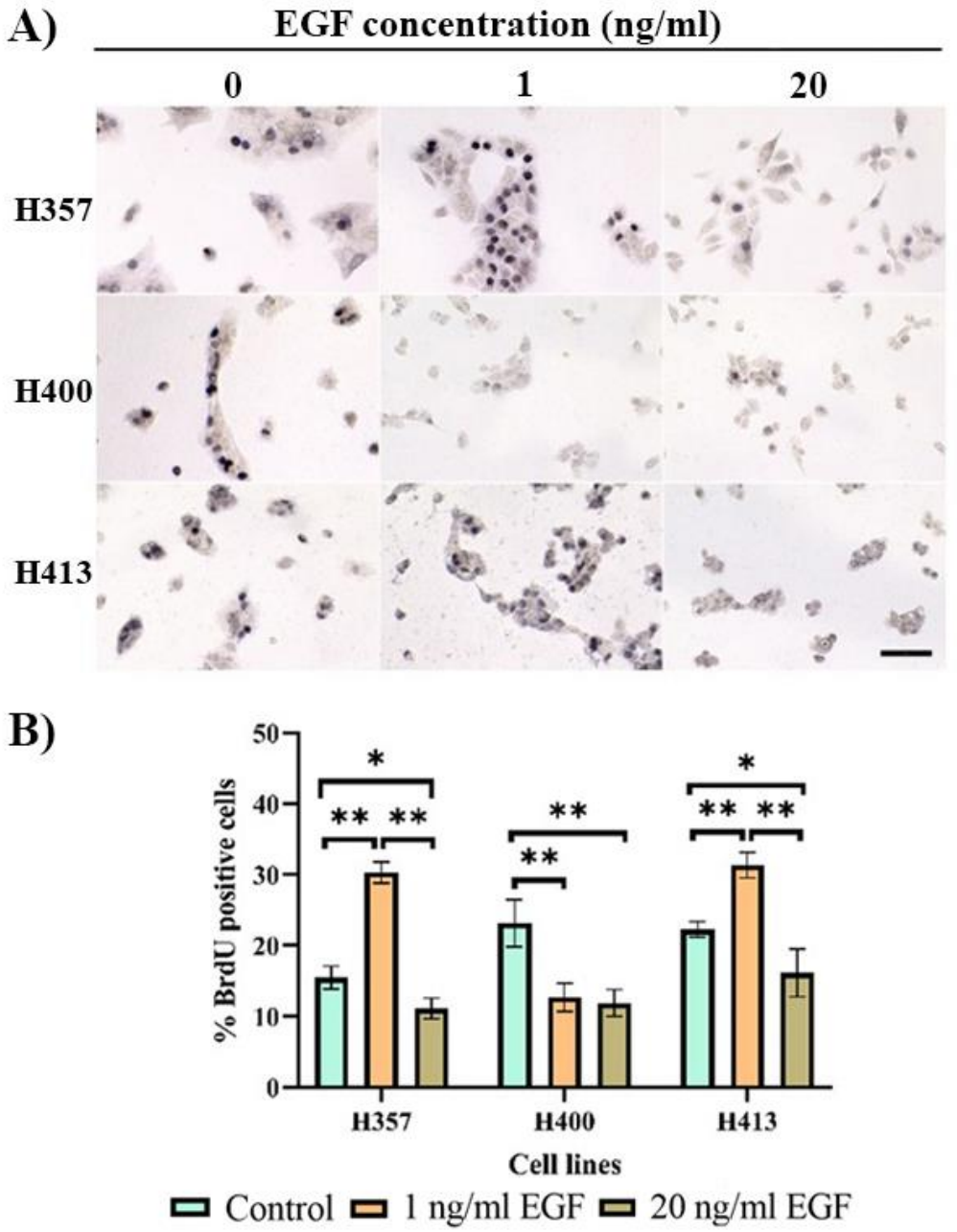

Figure 42. The effect of EGF on proliferation of three OSCC lines determined using BrdU assay. **A)** Representative phase contrast microscopy images show that BrdU positive cells of the 1 ng/ml-EGF treated group of H357 and H413 cultures was higher than the control, while the 20 ng/ml-EGF treated group was lower than the control. For H400, BrdU positive cells of both EGF treated groups were lower than the control. **B)** EGF treatment at 1 ng/ml increased the percentage of BrdU positive cells in H357 and H413 cultures but at 20 ng/ml, it decreased. Conversely, the percentage of BrdU positive cells in H400 cultures was reduced, following both EGF treatments. (Scale bar shown represents 50 µm; X20 objective lens; Three biological replicates from independent experiments, N = 1,000 cells; One-way ANOVA followed by *post-hoc* Tukey tests, * = p-value < 0.05, ** = p-value < 0.01, data presented as mean ± 1 SD).

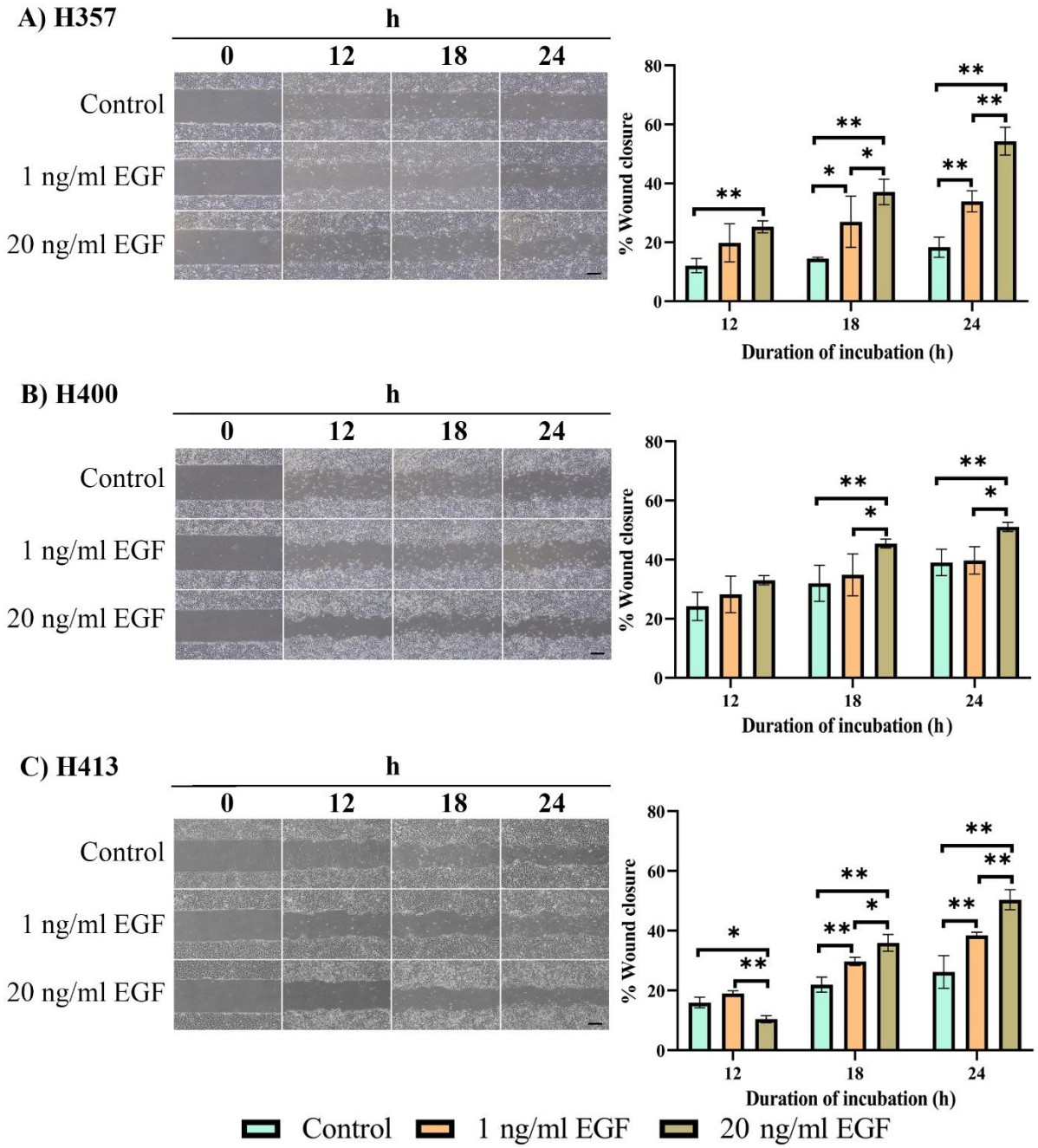

Figure 43. The effect of EGF on migration was determined using the scratch wound migration assay at three timepoints: 12, 18 and 24 h. Representative phase contrast microscopy images show that wound closure of three OSCC lines increased with EGF concentration (left side of each image). **A)** Migration of H357 cells increased according to the EGF concentration at the three timepoints. **B)** The migration of H400 cells also increased according to the EGF concentrations applied but statistical significance was observed only at 18 and 24 h. **C)** At 12 h, H413 cells treated with 20 ng/ml EGF migrated more slowly than the other cell lines. Nevertheless, the percentage wound closure for H413 cells increased following the concentration of EGF at 18 h and 24 h. (Scale bar shown represents 200 µm; X4 objective lens Three biological replicates from independent experiments were performed with N=4 for each experiment; One-way ANOVA followed by *post-hoc* Tukey test, * = p-value < 0.05 and ** = p-value < 0.01, data presented as mean ± 1 SD).

The percentage wound closure for the group treated with 20 ng/ml EGF at this time point was 37.1 ± 4.3 which represented a 2.6 fold higher than the control ($p<0.01$, One-way ANOVA) and 1.4 fold higher than the 1 ng/ml EGF-treated group ($p<0.05$, One-way ANOVA). At 24 h, 1 ng/ml EGF (33.9 ± 3.6) increased the percentage wound closure in H357 cultures from the control (18.4 ± 3.4) by 1.84 fold ($p<0.01$, One-way ANOVA). The group treated with 20 ng/ml had the highest percentage wound closure (54.3 ± 4.7), which was 3.0 fold higher than the control ($p<0.01$, One-way ANOVA) and 1.6 fold higher than the 1 ng/ml EGF-treated group ($p<0.01$, One-way ANOVA).

For H400, at 12 h, the group treated with 1 ng/ml and 20 ng/ml EGF had a marginally higher percentage wound closure than the control (28.2 ± 6.2, and (25.3 ± 2.1 respectively), however these differences were not statistically significant. At 18 h, the percentage wound closure in the control cultures continued to increase to 32.0 ± 6.1, similar to the group treated with 1 ng/ml EGF (34.9 ± 7.1). At this time-point, the 20 ng/ml EGF-treated group exhibited a percentage wound closure of 45.5 ± 1.5, which was 1.4 fold and 1.3 fold higher than the control and the 1 ng/ml EGF-treated group, respectively ($p<0.05$, One-way ANOVA). At 24 h, the percentage wound closure of the control (39.0 ± 4.5) was not statistically different from the group treated with 1 ng/ml EGF (39.7 ± 4.6). In the 20 ng/ml EGF-treated group the percentage wound closure was 51.1 ± 1.6 which was higher than the control by 1.9 fold ($p<0.01$, One-way ANOVA), and higher than the group treated with 1 ng/ml EGF by 1.3 fold ($p<0.05$, One-way ANOVA) (**Figure 43B**).

Figure 43C shows the effect of EGF on H413 cells. At 12 h, the group treated with 1 ng/ml EGF had a percentage wound closure of 19.0 ± 0.9, which was slightly higher than the control (16.0 ± 1.8). In contrast with the other cell lines, the group treated with 20 ng/ml EGF had the lowest percentage wound closure (10.4 ± 1.2) at this time point. That value was 1.5 fold decrease from the control ($p<0.05$, One-way ANOVA) and 1.8 fold decrease from the group

treated with 1 ng/ml EGF ($p<0.01$, One-way ANOVA). At 18 h, the percentage wound closure of the group treated with 1 ng/ml and 20 ng/ml EGF (29.7% ± 1.4 and 36.0% ± 2.8 respectively) were significantly higher than the control (22.0% ± 2.5), ($p<0.01$, One-way ANOVA). Also, the 20 ng/ml-EGF-treated group had a 1.2 fold higher percentage wound closure than that the group treated with 1 ng/ml EGF ($p<0.05$, One-way ANOVA). At 24 h, the percentage wound closure of the group treated with 1 ng/ml EGF increased to 38.5% ± 1.0, which was higher than the control (26.3 ± 5.5) by 1.5 fold ($p<0.01$, One-way ANOVA). The group treated with 20 ng/ml EGF had a percentage wound closure of 50.4 ± 3.4. This percentage was 1.9 fold and 1.3 fold higher than the control and the group treated with 1 ng/ml ($p<0.01$, One-way ANOVA).

Linear regression analysis indicated that at 24 h the percentage wound closure for the three OSCC lines increased with EGF concentration in a linear relationship ($R^2= 0.81$ for H357 cultures, $R^2= 0.76$ for H400 cultures, $R^2= 0.71$ for H413 cultures; $p<0.01$).

4.7 Transwell migration assay

Figure 44 shows that the number of migrated cells in the 1 ng/ml-EGF-treated group for the H357 cell line (51 ± 2) was 2.0 fold higher than the control (25 ± 7, $p<0.05$, One-way ANOVA). The group treated with 20 ng/ml EGF had 85 ± 14 migrated cells which was 3.4 fold and 1.7 fold higher than the control and the group treated with 1 ng/ml EGF ($p<0.01$, One-way ANOVA), respectively. For H400 cells, EGF at 1 ng/ml caused a 1.8 fold increase in cell migration from 111 ± 27 (control) to 198 ± 27 cells ($p<0.05$, One-way ANOVA). When the EGF concentration increased to 20 ng/ml, the number of migrated cells rose to 293 ± 18 which was 2.7 fold higher than the control and 1.5 fold higher than the group treated with 1 ng/ml EGF ($p<0.01$, One-way ANOVA). For H413 cells, the group treated with 1 ng/ml EGF had 72 ± 7 migrated cells.

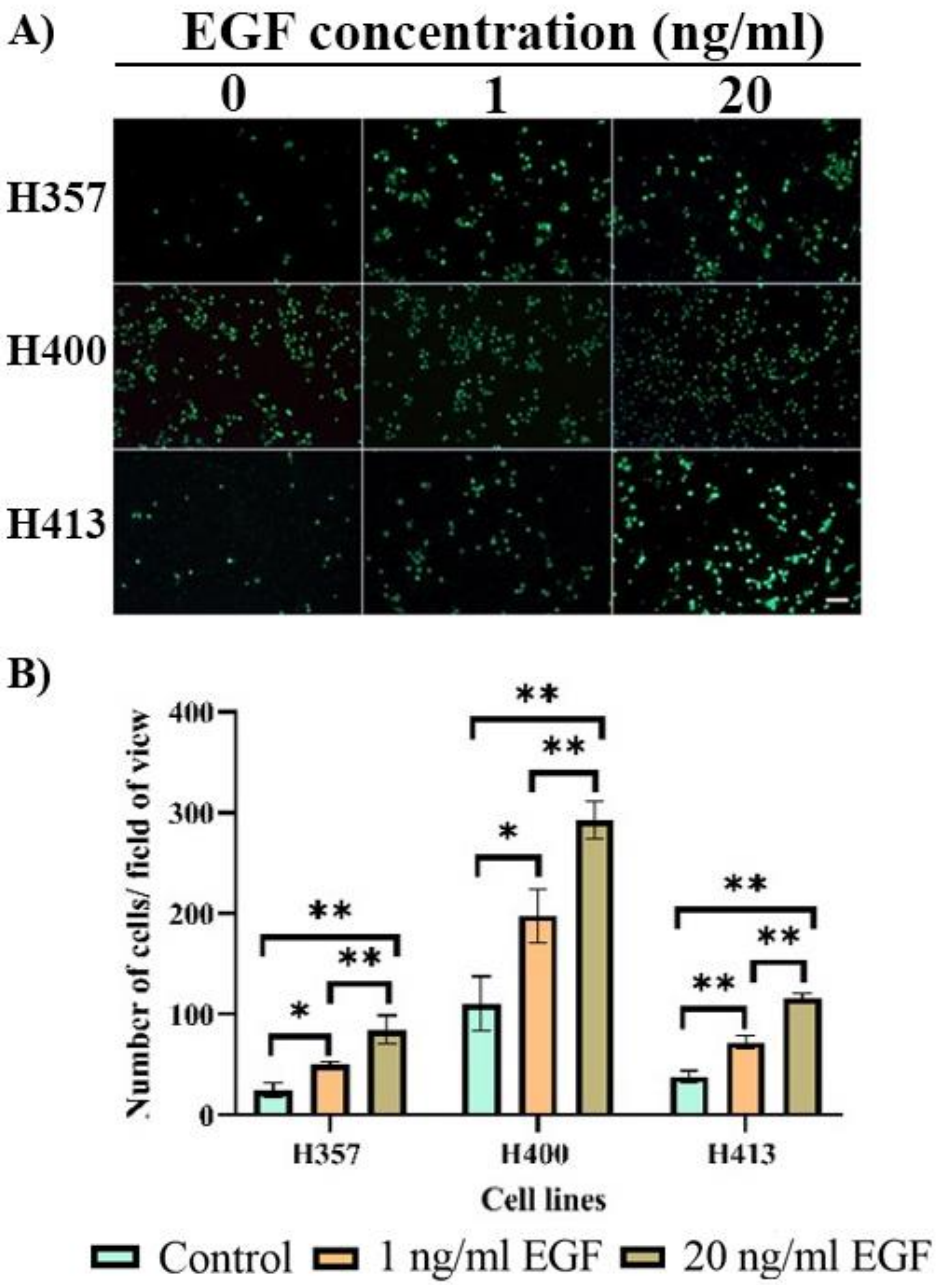

Figure 44. Transwell migration assay determining the effect of EGF on migration of H357, H400 and H413 cultures. **A)** Representative images captured using fluorescence microscopy of the three OSCC lines after incubation with 1 ng/ml and 20 ng/ml EGF for 24 h. Cells were stained with calcein AM. **B)** The effect of EGF on the migration of H357, H400 and H413 cultures determined using a transwell migration assay. EGF increased the number of migrated cells according to the concentration used. (Scale bar shown represents 100 µm; X10 objective lens; Three biological replicates from independent experiments were performed with N=10 for each experiment; One-way ANOVA followed by *post-hoc* Tukey test, ** = p-value < 0.05, ** = p-value < 0.01, data presented as mean ± 1 SD).

This number was 1.9 fold higher than the control group (38 ± 6 cells, $p<0.01$, One-way ANOVA). The 20 ng/ml EGF-treated group exhibited the highest number of migrated cells of 116 ± 5 which was 3.0 fold and 1.6 fold higher than the control and the group treated with 1 ng/ml EGF ($p<0.01$, One-way ANOVA), respectively. Linear regression analysis demonstrated that the number of migrated cells for H357, H400 and H413 cultures increased with increasing EGF concentration ($R^2= 0.78$ for H357 cultures, $R^2= 0.75$ for H400 cultures, $R^2= 0.82$ for H413 cultures; $p<0.01$).

4.8 Transwell invasion assay

It has been previously reported that EGF enhances cell migration in a dose-dependent manner (in the range of 1 - 20 ng/ml) (Vinci *et al.*, 2015), therefore this study investigated the effect of EGF on cell invasion. **Figure 45** shows the invasion of the three OSCC lines in response to EGF treatments. For H357 cells, 1 ng/ml EGF elevated the number of invaded cells from 7.7 ± 2 (control) to 28.6 ± 8, which was a 3.7 fold increase ($p<0.05$, One-way ANOVA). EGF at 20 ng/ml (64 ± 8 cells) increased the number of invading cells by 8.4 fold and 2.2 fold compared with the control and the group treated at 1 ng/ml ($p<0.01$, One-way ANOVA), respectively. For H400 cells, 1 ng/ml EGF treatment increased the number of invading cells from 23 ± 11 (control) to 49 ± 17 cells, however this difference was not statistically significant. The group treated with EGF at 20 ng/ml had 123 ± 33 invaded cells and this was 5.4 fold higher than the control ($p<0.01$, One-way ANOVA) and 2.5 fold higher than the group treated with 1 ng/ml ($p<0.05$, One-way ANOVA). For H413 cells, EGF exposure at 1 ng/ml increased the average number of invading cells from 13 ± 2 (control) to 24 ± 7 but the difference was not statistically significant. EGF at 20 ng/ml resulted in invading cells of 63 ± 7, which was 4.9 fold higher than the control and 2.6 fold higher than the group treated with 1 ng/ml EGF ($p<0.01$, One-way ANOVA).

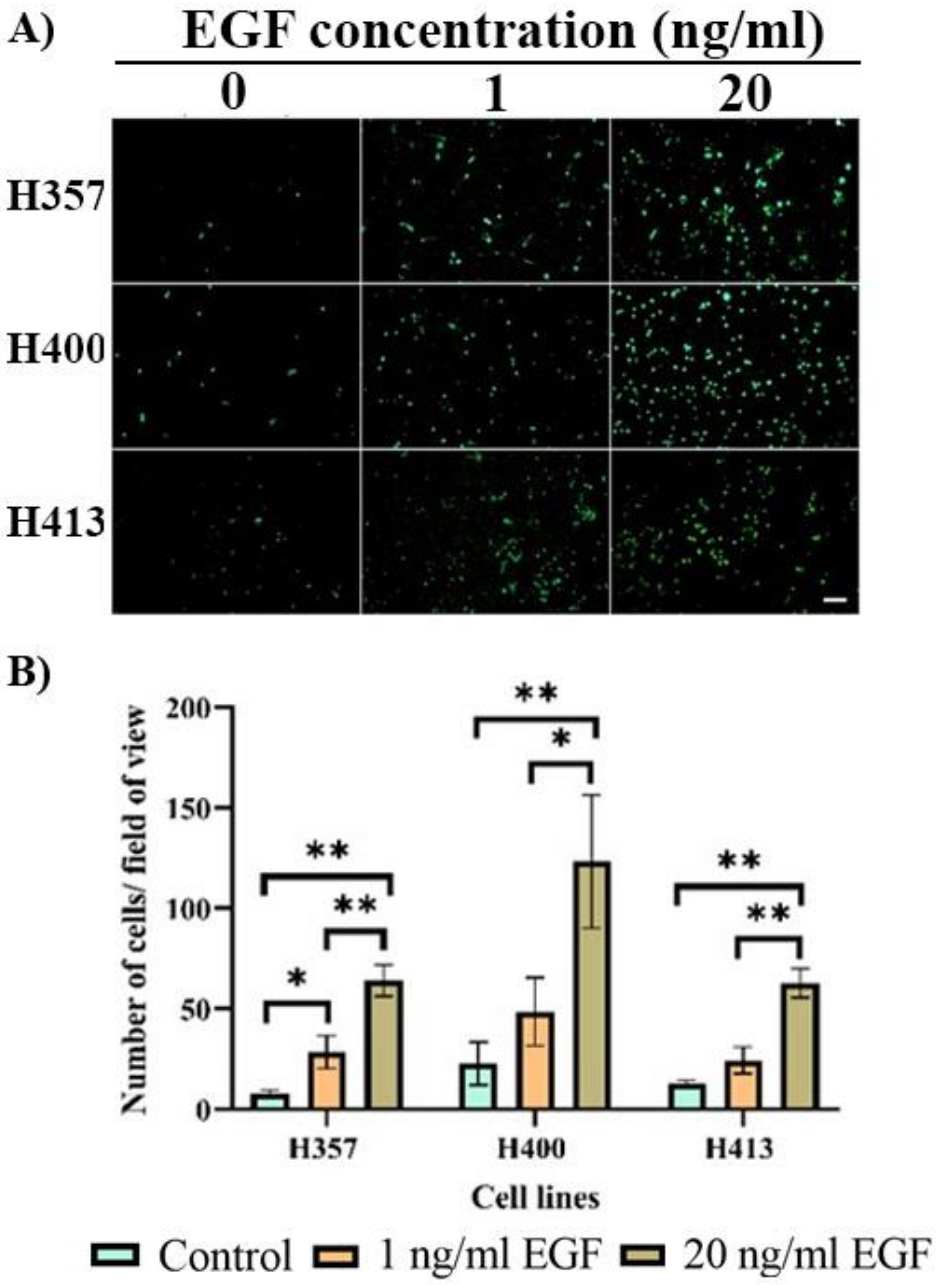

Figure 45. The effect of EGF on invasion was determined using the transwell invasion assay. **A)** Representative images captured using fluorescence microscopy after incubation with 1 ng/ml and 20 ng/ml EGF for 48 h. Cells were stained with calcein AM. **B)** EGF at 1 ng/ml and 20 ng/ml significantly improved the invasion of H357 cells. For H400 and H413 cells, both EGF concentrations increased invasion but only 20 ng/ml generated statistically significant differences. (Scale bar shown represented 100 μm; X10 objective lens; Three biological replicates from independent experiments were performed with N=10 for each experiment; One-way ANOVA followed by *post-hoc* Tukey test, * = p-value < 0.05, ** = p-value < 0.01, data presented as mean ± 1 SD).

Linear regression analysis indicated that the invasion of the three OSCC lines increased with EGF concentration in a linear manner (R^2= 0.84 for H357 cultures, R^2= 0.81 for H400 cultures, R^2= 0.92 for H413 cells cultures; $p<0.01$).

4.9 Multicellular tumour spheroid

The effect of EGF on the characteristics of the multicellular tumour spheroids was also investigated. The images of the invading spheroids for each experimental group on embedding day 1 and day 2 are shown in **Figure 46**. Tables with the original data are presented in the **Appendix**.

4.9.1 Analysis of the number of clusters

Appendix table XI and **Figure 47** illustrate the comparison of the number of clusters after the spheroids were incubated with EGF treatments for two days. Overall, both 1 ng/ml and 20 ng/ml EGF slightly increased the number of clusters on day 1 but this difference was not statistically significant. On day 2, the number of clusters for each of the three lines was increased substantially. Compared with the control, 1 ng/ml EGF treatment resulted in an increase of cell clusters in H357 cultures by 2.9 fold ($p<0.01$, Two-way ANOVA), while 20 ng/ml EGF treatment caused an increase by 3.8 fold ($p<0.01$, Two-way ANOVA). For H400 cultures, EGF at 1 ng/ml increased the number of clusters by 4.1 fold compared with the control ($p<0.01$, Two-way ANOVA), while EGF at 20 ng/ml had a 4.9 fold higher number of clusters compared with the control ($p<0.01$, Two-way ANOVA). For H413 cultures, the 1 ng/ml EGF-treated group had slightly higher clusters than the control, but this was not statistically significant. The group treated with 20 ng/ml EGF was 3.6 fold higher than the control ($p<0.01$, Two-way ANOVA) and 1.9 fold higher than the 1 ng/ml EGF-treated group ($p<0.05$, Two-way ANOVA).

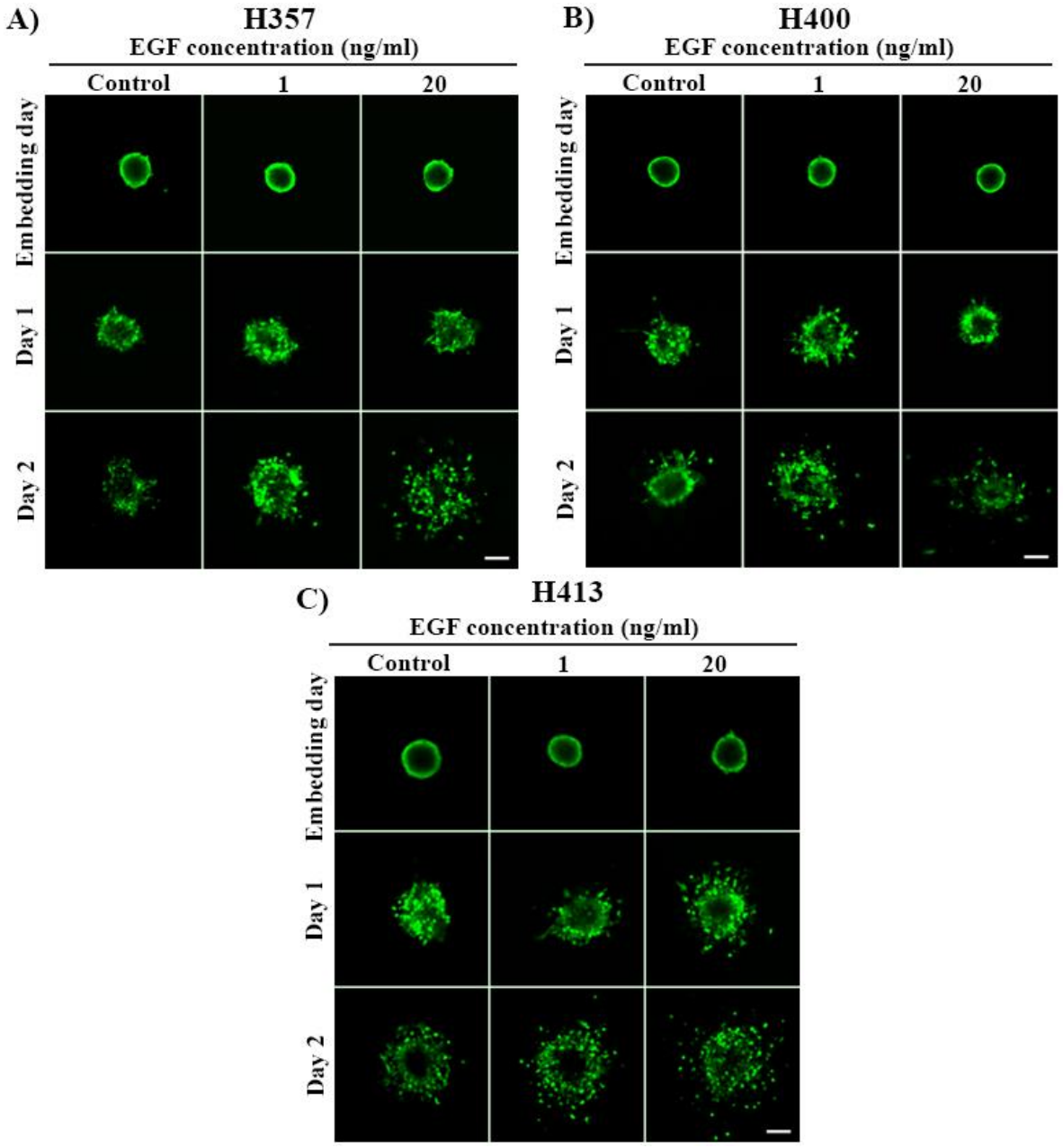

Figure 46. The effect of EGF on invasion was determined using the MCTS assay. Representative confocal microscopy images of spheroids, embedded in 3 mg/ml collagen, inhibited proliferation with 8 μg/ml mitomycin C for 2 h and incubated in three different conditions: DMEM only, DMEM with 1 ng/ml EGF and DMEM with 20 ng/ml for two days. Cells were stained with calcein AM. **A)** H357 **B)** H400 and **C)** H413 cells. Cell invasion increased according to the incubation period and the increase in EGF concentration. (Scale bar shown represented 100 μm; X10 objective lens; Three biological replicates from independent experiments were performed with N=10 for each experiment).

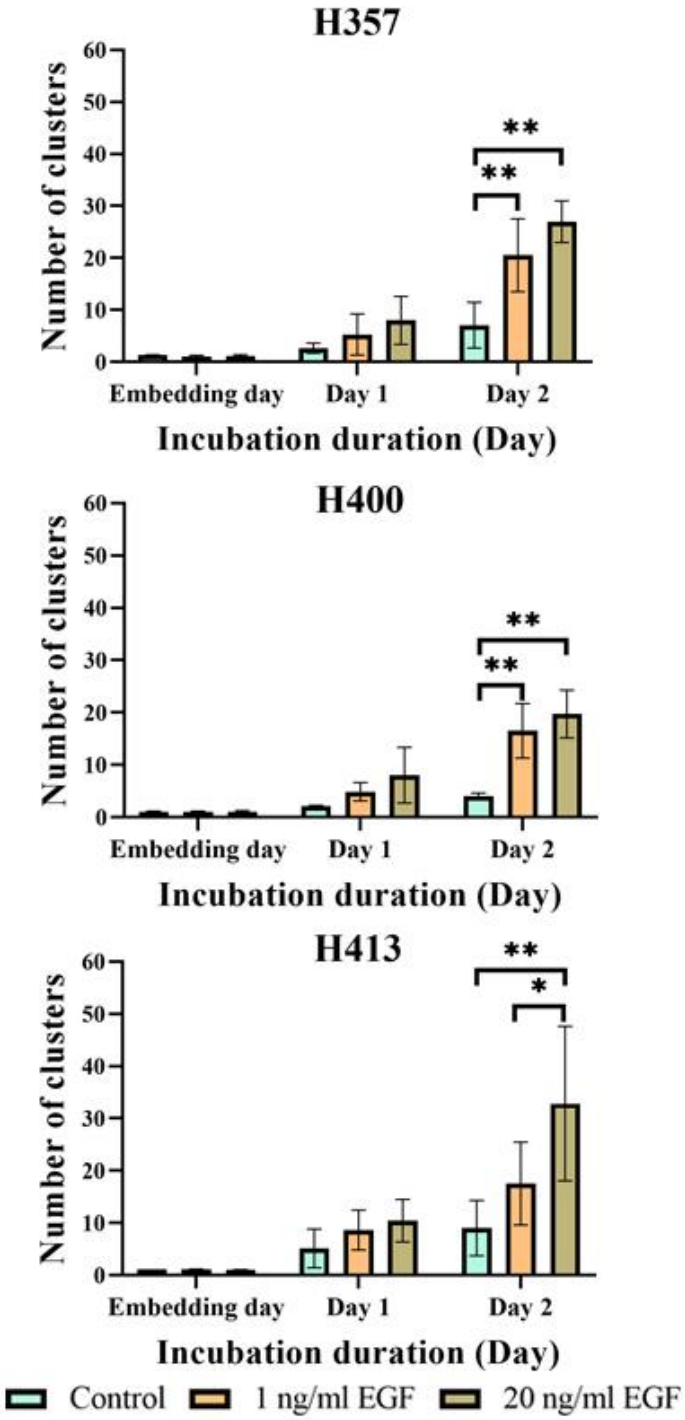

Figure 47. Comparison of the number of clusters following 1 and 20 ng/ml EGF treatments. Spheroid were generated using the hanging drop method (one day of incubation), embedded in 3 mg/ml collagen and treated with 8 μg/ml mitomycin C for 2 h before incubating with or without EGF treatments for two days. A significant difference in the number of clusters between the three groups was identified only on day 2. On day 2, both EGF concentrations increased the cluster numbers in H357 and H400 cultures but only EGF at 20 ng/ml increased the number of clusters in H413 cultures. (Three biological replicates from independent experiments were performed with N=10 for each experiment; Two-way ANOVA followed by *post-hoc* Tukey tests, * = p-value < 0.05, ** = p-value < 0.01, data presented as mean ± 1 SD).

Linear regression analysis on day 2 indicated that the number of clusters significantly increased with the EGF concentration used in only H357 and H413 cultures (R^2=0.47 for H357 cultures, R^2=0.53 for H413 cultures, $p<0.05$).

4.9.2 Analysis of the maximum invading distance

Appendix table XII and **Figure 48** illustrate the maximum invading distance of the three OSCC lines induced by EGF exposure. On day 1 of H357 cultures, EGF at 1 ng/ml marginally increased the maximum invading distance compared with the control. Treatment with EGF at 20 ng/ml induced the greatest maximum invading distance which was 1.4 fold higher than the control ($p<0.05$, Two-way ANOVA). On day 2, the maximum invading distance in the group treated with 1 ng/ml EGF was not statistically different to the control. Treatment with 20 ng/ml EGF induced the longest maximum invading distance, being 1.5 fold higher than the control ($p<0.01$, Two-way ANOVA) and 1.2 fold higher than the 1 ng/ml EGF-treatment group ($p<0.05$, Two-way ANOVA). In H400 cultures, the maximum invading distance of the control and the group treated with 1 ng/ml EGF were not statistically different on day 1. Treatment with 20 ng/ml-EGF induced the longest maximum invading distance, which was 1.3 fold greater than the control ($p<0.05$, Two-way ANOVA) but not different from the 1 ng/ml-EGF-treatment group. On day 2, the groups treated with EGF at 1 ng/ml induced a 1.4 fold longer invading distance than in the control ($p<0.05$, Two-way ANOVA), while EGF at 20 ng/ml caused an increase in the maximum invading distance by 1.5 fold ($p<0.01$, Two-way ANOVA). In H413 cultures, the maximum invading distance increased with the EGF concentration used on both days 1 and 2, but the significant differences only occurred on day 2. On day 2, the 1 ng/ml EGF-treated group had a slightly higher maximum invading distance than the control, while EGF at 20 ng/ml provided a 1.4 fold increase of the maximum invading distance compared with the control ($p<0.01$, Two-way ANOVA).

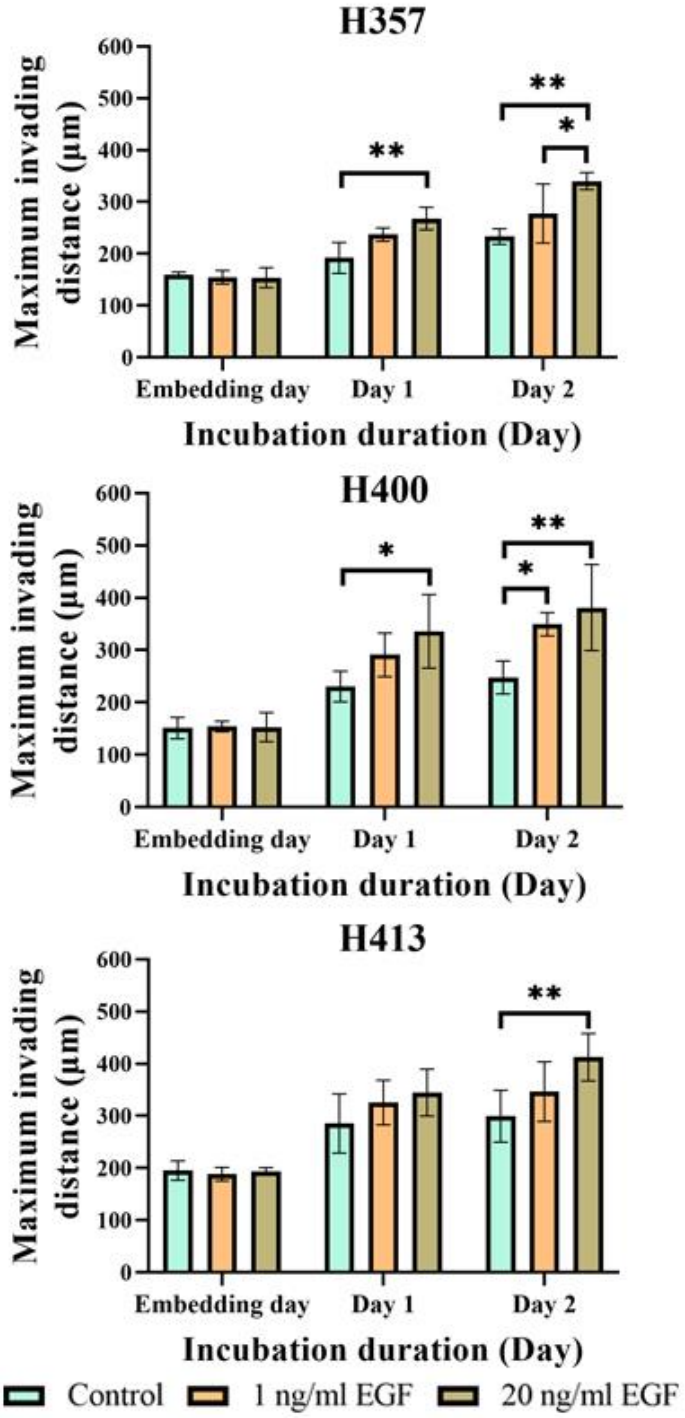

Figure 48. The effect of 1 and 20 ng/ml EGF on the maximum invading distance of the three OSCC lines. Spheroids were generated using the hanging drop method (one day of incubation), embedded in 3 mg/ml collagen and treated with 8 µg/ml mitomycin C for 2 h before incubating with or without EGF treatments for two days. EGF increased the maximum invading distance according to the concentration on both days 1 and 2. (Three biological replicates from independent experiments were performed with N=10 for each experiment; Two-way ANOVA followed by *post-hoc* Tukey tests, * = p-value < 0.05, ** = p-value < 0.01, data is presented as mean ± 1 SD).

However, linear regression analysis showed that the trend on day 2 was significant only for H357 cultures (R^2=0.60, $p<0.050$) and H413 cultures (R^2=0.48, $p<0.05$).

4.9.3 Analysis of the circularity of the main cluster

Subsequently, the effect of EGF on the circularity of the main cluster was investigated (**Appendix table XIII** and **Figure 49**). On both days 1 and 2 of H357 cultures, the control exhibited the highest circularity, followed by the groups treated with 1 ng/ml EGF and 20 ng/ml, respectively. However, a statistically significant difference was identified only between the control and cultures treated with 20 ng/ml EGF ($p<0.01$ for day 1, $p<0.05$ for day 2; Two-way ANOVA). For H400 cells, EGF at 1 and 20 ng/ml significantly reduced the circularity of the main cluster on days 1 and 2 ($p<0.01$, Two-way ANOVA). For H413 cells, no statistically significant was identified on day 1. However, it was detected on day 2, where the circularity was significantly reduced from 0.28 (control) to 0.14 (group treated with 20 ng/ml EGF) (**Table XVI**, $p<0.05$, Two-way ANOVA).

4.9.4 Analysis of the fractal dimension of the main cluster

The fractal dimension of the main cluster of the three OSCC lines in response to EGF treatment was analysed (**Appendix table XIV** and **Figures 50**). For H357 cultures, the fractal dimension of the groups treated with EGF at 1 ng/ml was significantly higher than the control ($p<0.05$, Two-way ANOVA) and EGF at 20 ng/ml ($p<0.01$, Two-way ANOVA) on both days 1 and 2 but no statistical difference was observed between the two EGF concentrations. For H400 cultures, the fractal dimension increased with the EGF concentration on days 1 and 2. The fractal dimension of the 20 ng/ml-EGF-treated group was significantly higher than the control ($p<0.05$, Two-way ANOVA) on day 1, while the fractal dimension of both EGF-treated groups was significantly higher than the control ($p<0.01$, Two-way ANOVA) on day 2.

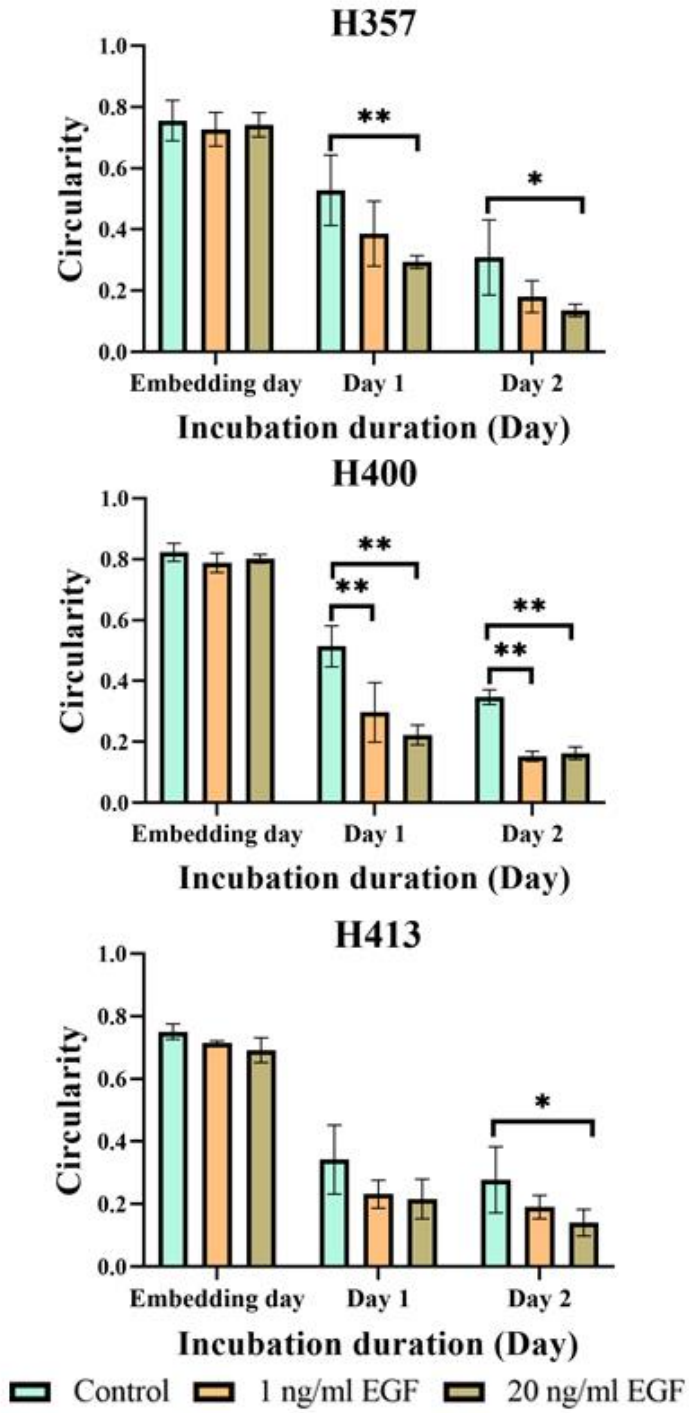

Figure 49. Comparison of the main cluster's circularity following 1 and 20 ng/ml EGF treatments. Spheroids were generated using the hanging drop method (one day of incubation), embedded in 3 mg/ml collagen and treated with 8 μg/ml mitomycin C for 2 h before incubating with or without EGF treatments for two days. On both days 1 and 2, EGF at 20 ng/ml reduced the circularity of H357 spheroids, while EGF at both concentrations decreased the circularity of H400 spheroids. For H413 cells, the circularity of the main cluster of the group treated with 20 ng/ml EGF was statistically significantly lower than the control only on day 2. (Three biological replicates from independent experiments were performed with N=10 for each experiment; Two-way ANOVA followed by *post-hoc* Tukey tests, * = p-value < 0.05, ** = p-value < 0.01, data presented as mean ± 1 SD).

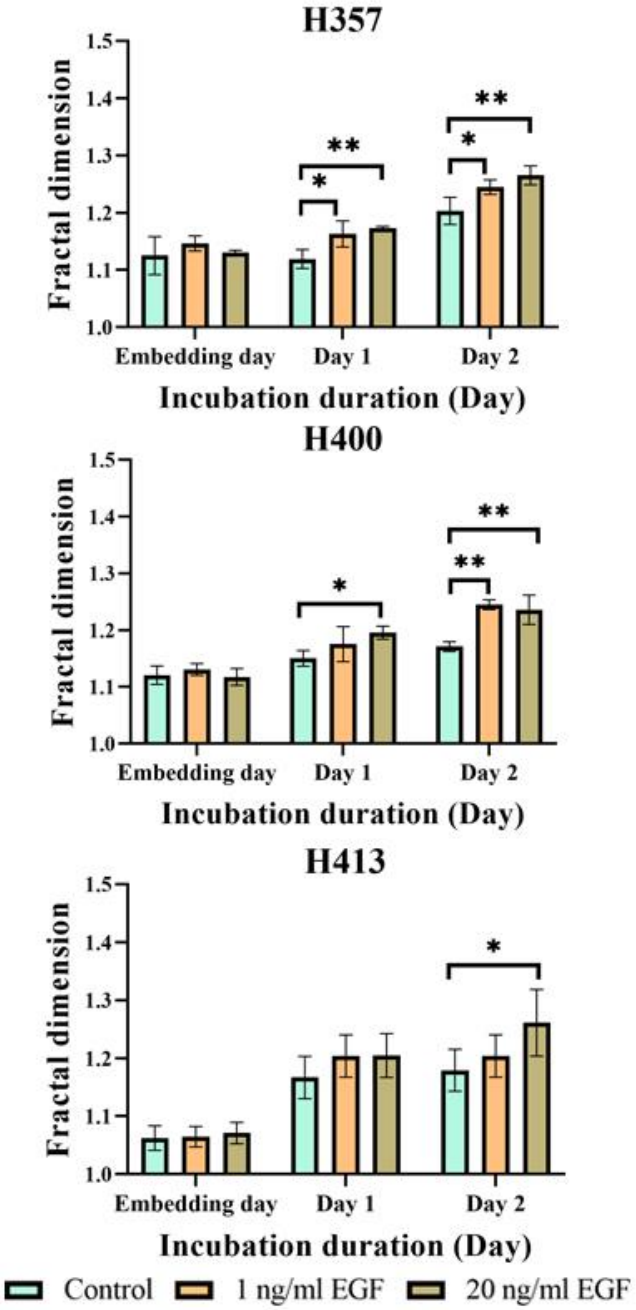

Figure 50. Fractal dimension of the three OSCC lines when treated with 1 and 20 ng/ml EGF. Spheroids were generated using the hanging drop method (one day of incubation), embedded in 3 mg/ml collagen and treated with 8 µg/ml mitomycin C for 2 h before incubating with or without EGF treatments for two days. The fractal dimension of H357 cultures increased according to the EGF concentration used on days 1 and 2. For H400 cells, only the EGF treatment at 20 ng/ml provided a higher fractal dimension than the control on day 1, while on day 2, both EGF concentrations caused an increase. For H413 cells, the fractal dimension of the three groups was similar on day 1. On day 2, the fractal dimension of the control was lower than the group treated with 20 ng/ml EGF. (Three biological replicates from independent experiments were performed with N=10 for each experiment; Two-way ANOVA followed by *post-hoc* Tukey tests, * = p-value < 0.05, ** = p-value < 0.01, data presented as mean ± 1 SD).

For H413 cultures, significant differences were noted only on day 2, when the fractal dimension increased with the increase in EGF concentration used, with a significant difference being identified between the control and the group treated with 20 ng/ml EGF ($p<0.05$, Two-way ANOVA). Although the fractal dimension of the three cell lines increased with the EGF concentration used, this trend was significant only for H357 cells ($R^2=0.46$, $p<0.05$; Linear regression).

4.9.5 Analysis of the maximum diameter of the main cluster (MDMC)

The effect of EGF on the MDMC is shown in **Appendix table XV** and **Figure 51**. For H357 cells, the MDMC of the control was the smallest, followed by the groups treated with 1 ng/ml and 20 ng/ml EGF, respectively. EGF at 20 ng/ml increased the MDMC compared to the control by 1.3 fold on both days 1 and 2 ($p<0.05$, Two-way ANOVA). For H400 cells, the MDMC increased with the elevation of EGF concentration, with 20 ng/ml EGF-treated group being 1.4 fold increase compared with the control on day 1 ($p<0.05$, Two-way ANOVA). For H413 cultures, no significant difference was observed at days 1 or 2 of culture.

4.10 The effect of EGF on epithelial mesenchymal transition (EMT) events

The data in **sections 4.8-9** illustrated that EGF increased the invasion of H357, H400 and H413 cells. To investigate the possible mechanisms by which EGF enhanced this invasion, the study evaluated the effect of EGF on the expression of known EMT markers. Data from sq-RT-PCR analysis showed that after 4 h of incubation, the EGF treatments did not affect *E-cadherin* and *vimentin* expression in any of the three cell lines investigated (**Figure 52A**).

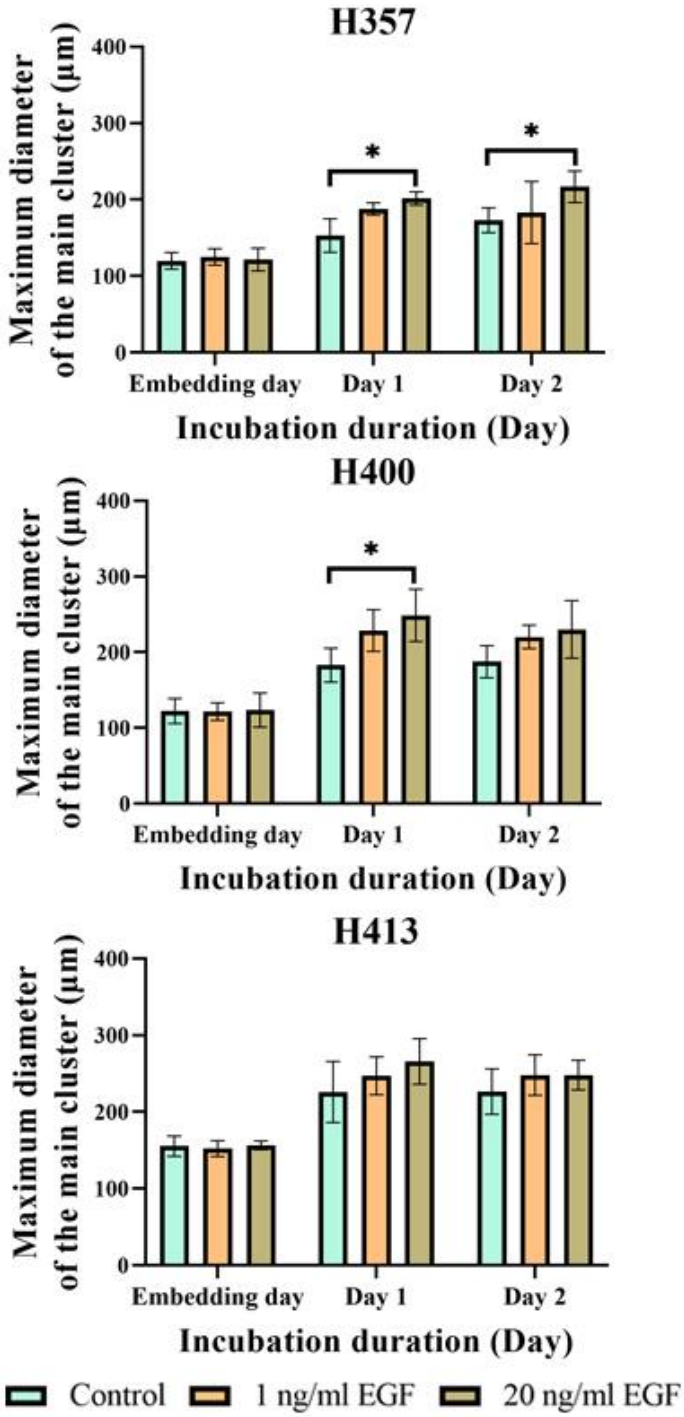

Figure 51. The MDMC of the three OSCC lines was increased by the 1 ng/ml and 20 ng/ml EGF treatments. Spheroids were generated using the hanging drop method (one day of incubation), embedded in 3 mg/ml collagen and treated with 8 µg/ml mitomycin C for 2 h before incubating with or without EGF treatments for two days. EGF at 20 ng/ml provided a greater MDMC than the control on days 1 and 2 in H357 cells, but only on day 1 in H400 cells. There were no statistical differences between the three groups of H413 cultures on both days 1 and 2. The MDMC of the three OSCC lines on day 1 was the same as that observed on day 2. (Three biological replicates from independent experiments were performed with N=10 for each experiment; Two-way ANOVA followed by *post-hoc* Tukey tests, * = $p < 0.05$, data presented as mean ± 1 SD).

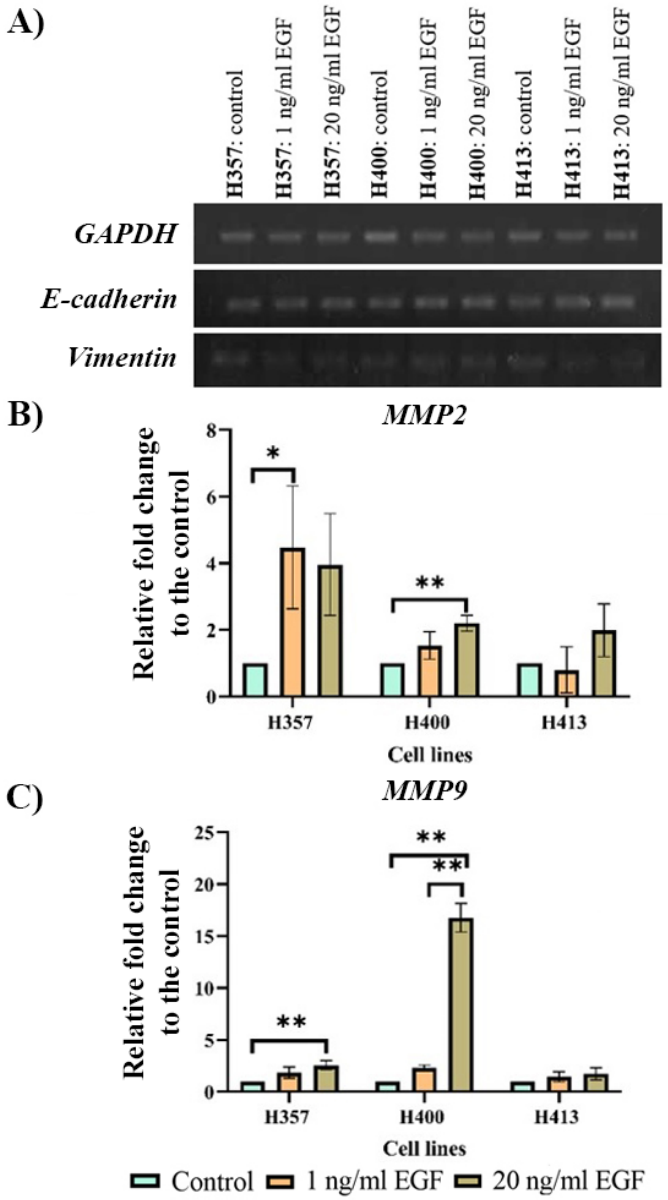

Figure 52. The effect of EGF on EMT marker expression was determined using two PCR analyses, 48 h of incubation. The results were normalized to the housekeeping gene and then were presented as a relative fold change to the control. **A)** In the preliminary work, the OSCC lines were treated with EGF at 1 and 20 ng/ml for 4 h before performing sqRT-PCR analysis. Neither *E-cadherin* nor *vimentin* gene expression was affected by both EGF treatments. **B) & C)** The cultures were incubated with both EGF treatments for 48 h before performing the real-time PCR analysis. Both EGF concentrations increased the *MMP2* expression in H357 cells but only EGF at 1 ng/ml generated a statistically significant difference. EGF enhanced *MMP2* expression in H400 cells but a significant difference was noted only between the control and the group treated with 20 ng/ml. EGF at 20 ng/ml also elevated the transcription of MMP9 in H357 and H400 cultures. Conversely, the expression of the *MMP2* and *MMP9* in H413 cells was not affected by the EGF treatments. (Three biological replicates from independent experiments with each experiment for both assays, but with the average of two technical replicates for only real-time PCR; One-way ANOVA followed by *post-hoc* Tukey tests, * = p-value < 0.05, ** = p-value < 0.01, data presented as mean ± 1 SD).

For H357 cultures, EGF at 1 ng/ml enhanced *MMP2* expression by 4.5 fold ($p<0.05$, One-way ANOVA), and at 20 ng/ml this was 4.0 fold (the difference between concentrations, however, was not statistically significant). For *MMP9*, EGF upregulated this gene in H357 cells dependent on the concentration, with a significant (2.5 fold) increase between the control and the group treated with EGF at 20 ng/ml ($p<0.01$, One-way ANOVA). For this cell line, only the upregulation of *MMP9* gene correlated with the increase in EGF concentration ($R^2= 0.60$, $p<0.05$; Linear regression), while *MMP2* did not.

For H400 cultures, EGF at 20 ng/ml induced a significant increase in *MMP2* expression (2.2 fold) compared with the control ($p<0.01$, One-way ANOVA). *MMP9* expression in H400 cultures was also affected by the EGF treatments. EGF at 1 ng/ml marginally increased *MMP9* expression however this difference was not statistically significant. Conversely, EGF at 20 ng/ml enhanced the expression of *MMP9* 16.8 fold compared with the control and by 7.2 fold when compared with the group treated with 1 ng/ml ($p<0.01$, One-way ANOVA). Linear regression analysis showed that both *MMP2* and *MMP9* were correlated with EGF concentration ($R^2= 0.69$, for *MMP2* gene; $R^2= 0.99$ for *MMP9* gene, $p<0.01$).

For H413 cultures, no trend in *MMP2* expression was identified following EGF treatments. For *MMP9*, the expression appeared to increase according to the EGF concentration used, however, this change was not statistically significant.

4.11 The effect of EGF on *Rac1* expression and Rac1 activity

Having established that EGF promoted migration and invasion, the present study then evaluated the effect of this growth factor on the *Rac1* transcription and activation of Rac1. Rac1 activity can be increased either via GDP-bound form/GPT-bound form switching by GEF or due to the upregulation of the *Rac1* gene; however, the evidence for growth factors that have this ability to modify transcription is limited (Croft & Olson, 2011). This study showed that after after incubation

for 4 h, *Rac1* expression in the three OSCC lines was not affected by either of the EGF treatments (**Figure 53A**). The effect of EGF on Rac1 activity was then investigated using a G-LISA which showed that both concentrations of EGF activated Rac1 (**Figure 53B**). Compared with the control, EGF at 1 ng/ml increased Rac1 activity in H357 cultures by 2.5 fold ($p<0.05$, One-way ANOVA), while EGF at 20 ng/ml increased it further to 3.2 fold ($p<0.01$). For H400 cultures, 1 ng/ml EGF increased Rac1 activity compared with the control by 1.5 fold ($p<0.05$, One-way ANOVA), while 20 ng/ml treatment increased this 1.4 fold greater than the control ($p<0.01$, One-way ANOVA). For H413 cultures, both EGF concentrations dramatically elevated Rac1 activity by 4.1 fold ($p<0.05$, One-way ANOVA). Although both EGF concentrations increased Rac1 activity compared with the control in all three cell lines, Rac1 activity induced by EGF at 1 ng/ml was statistically similar to that activated at 20 ng/ml. The elevation of the Rho GTPase's activity was reported to be caused by either increase in the gene expression or switching from the GDP-bound form to a GTP-bound form (Croft & Olson, 2011). The findings in this study suggested that in the three OSCC lines investigated, the increase of Rac1 activity following EGF treatments resulted from only GDP and GTP exchanging, but not from the upregulation of the Rac1 transcript since the expression of this gene did not alter with the treatments used. However, there was no difference in the level of Rac1 activity between group treated with 1 ng/ml and 20 ng/ml.

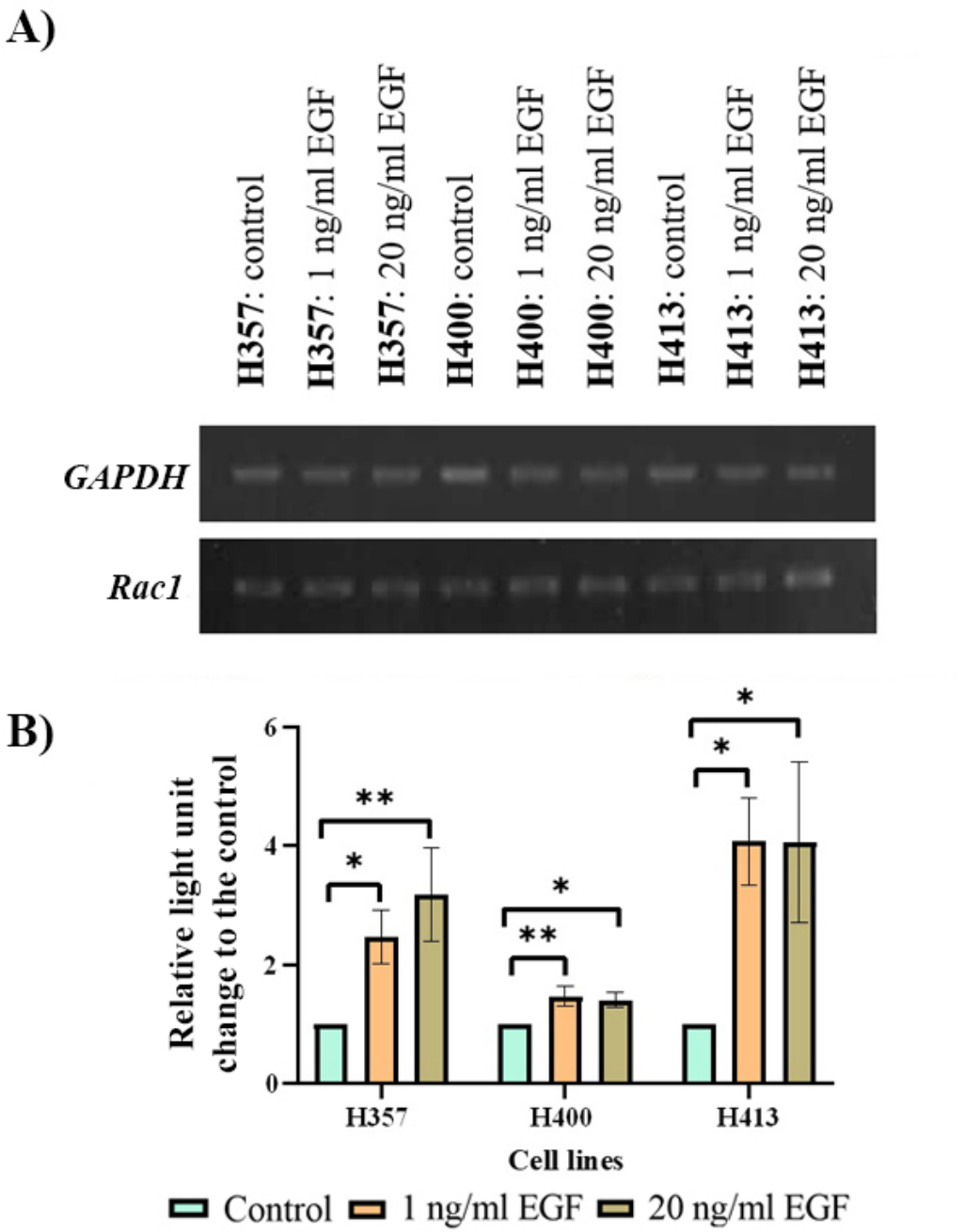

Figure 53. The effect of EGF on *Rac1* gene expression and Rac1 activity. **A)** The expression of *Rac1* was determined using sqRT-PCR analysis. *Rac1* expression did not change following both EGF concentrations exposures at 4 h of incubation. **B)** Rac1 activity was determined using G-LISA assay. Measured luminescence of each sample was normalised to the control. EGF at 1 ng/ml and 20 ng/ml stimulated Rac1 activity however the EGF concentration did not affect the level of Rac1 activity. (Three biological replicates from independent experiments with each experiment for both assays, but with the average of two technical replicates for only G-LISA assay; One-way ANOVA followed by *post-hoc* Tukey tests, * = p-value < 0.05, ** = p-value < 0.01, data presented as mean ± 1 SD).

4.12 Conclusion

In H357 and H413 cultures, 1 ng/ml EGF promoted proliferation, while 20 ng/ml, suppressed it. In H400 cultures, both EGF treatments caused growth inhibition. The increase in EGF concentration promoted migration and invasion in the three OSCC lines in the range of 0-20 ng/ml. EGF increased the expression of *MMP2* and *MMP9*. It also stimulated Rac1 activity, although the effect was similar for both EGF concentrations, while the Rac1 gene expression remained unchanged. Since 20 ng/ml EGF reduced proliferation of these cell lines, this concentration was used to stimulate migration and invasion in the further experiment in chapter 6.

Chapter 5: Results

Effects of S1PR2 on proliferation, migration, invasion and gene expression in OSCC lines

Having established the effect of EGF/EGF receptors on proliferation, migration and invasion, the study continued to investigate the effect of S1PR2. The present study focused on this receptor for two reasons. First, S1PR2 was reported to regulate various cellular activities similar to the EGF/EGF receptors axis, mainly controlling cellular motility. However, the effect of S1PR2 varies between types of cells (Arikawa *et al.*, 2003, Miller *et al.*, 2008, Du *et al.*, 2010, Price *et al.*, 2015, Patmanathan *et al.*, 2016, Pang *et al.*, 2020). In the case of OSCC, only one study has previously investigated this receptor (Patmanathan *et al.*, 2016),. Second, S1PR2 is expressed in most cell types, including oral epithelium. Although S1PR4 is also reported to control cellular motility, its expression was restricted to lymphoid tissues (Blaho & Hla, 2014). Therefore, the S1PR2 subtype may have more potential to impact epithelial cells than the S1PR4 subtype.

5.1 Aims

As described above, the data presented in this chapter aimed to elucidate the effects of S1PR2 on proliferation, migration and invasion in H357, H400 and H413 cell lines. Consequently, this study used two chemical reagents to alter the function of S1PR2, namely a) JTE013, a S1PR2 antagonist and b) CYM5478, a S1PR2 agonist, both using a concentration of 10 μM. Three experimental groups were tested for each cell line: 1) control, 2) group treated with the S1PR2 antagonist, and 3) group treated with the S1PR2 agonist.

5.2 Objectives

There were four objectives for this chapter to determine:

a) the expression of *S1PR 1-5* in H357, H400 and H413 cells,

b) the effect of S1PR2 on the proliferation, migration and invasion in H357, H400 and H413 cells,
c) the effect of S1PR2 on the expression of EMT-related genes, and
d) the effect of S1PR2 on Rac1 activity.

5.3 The expression of *S1PR*s

Three OSCC lines expressed *S1PR1-5*, but in different patterns (**Figure 54**). S1PR1 expression by H357 was significantly higher than H400 by 2.3 fold ($p<0.05$, One-way ANOVA). No difference in *S1PR2* and *S1PR5* expression was identified between H357, H400 and H413. H413 expressed higher levels of *S1PR3* than H400 by 2.9 fold ($p<0.05$, One-way ANOVA), but expressed lower levels of *S1PR4* than H357 by 1.5 fold ($p<0.0$, One-way ANOVA) and H400 by 1.3 fold ($p<0.05$, One-way ANOVA).

5.4 Growth curves and doubling times

The effect of S1PR2 on the proliferation of H357 cells is shown in **Figure 55A**. The H357 group treated with the S1PR2 antagonist exhibited a doubling time of 2.9 ± 0.3 days, which was 1.5 fold longer than observed in the control group (doubling time of 1.9 ± 0.1 days), ($p<0.01$, One-way ANOVA). However, the stimulation of S1PR2 with the agonist did not promote proliferation (the doubling time remained at 2.1 ± 0.2, which was not significantly different from the controls). H400 cells showed similar trends as H357 cells (**Figure 55B**). S1PR2 antagonist treatment increased the H400 doubling time from 1.5 ± 0.0 days (control) to 2.7 ± 0.3 days (1.8 fold, $p<0.01$, One-way ANOVA). The doubling time of H400 cultures treated with the S1PR2 agonist was 1.7 ± 0.2 days which was similar to the control.

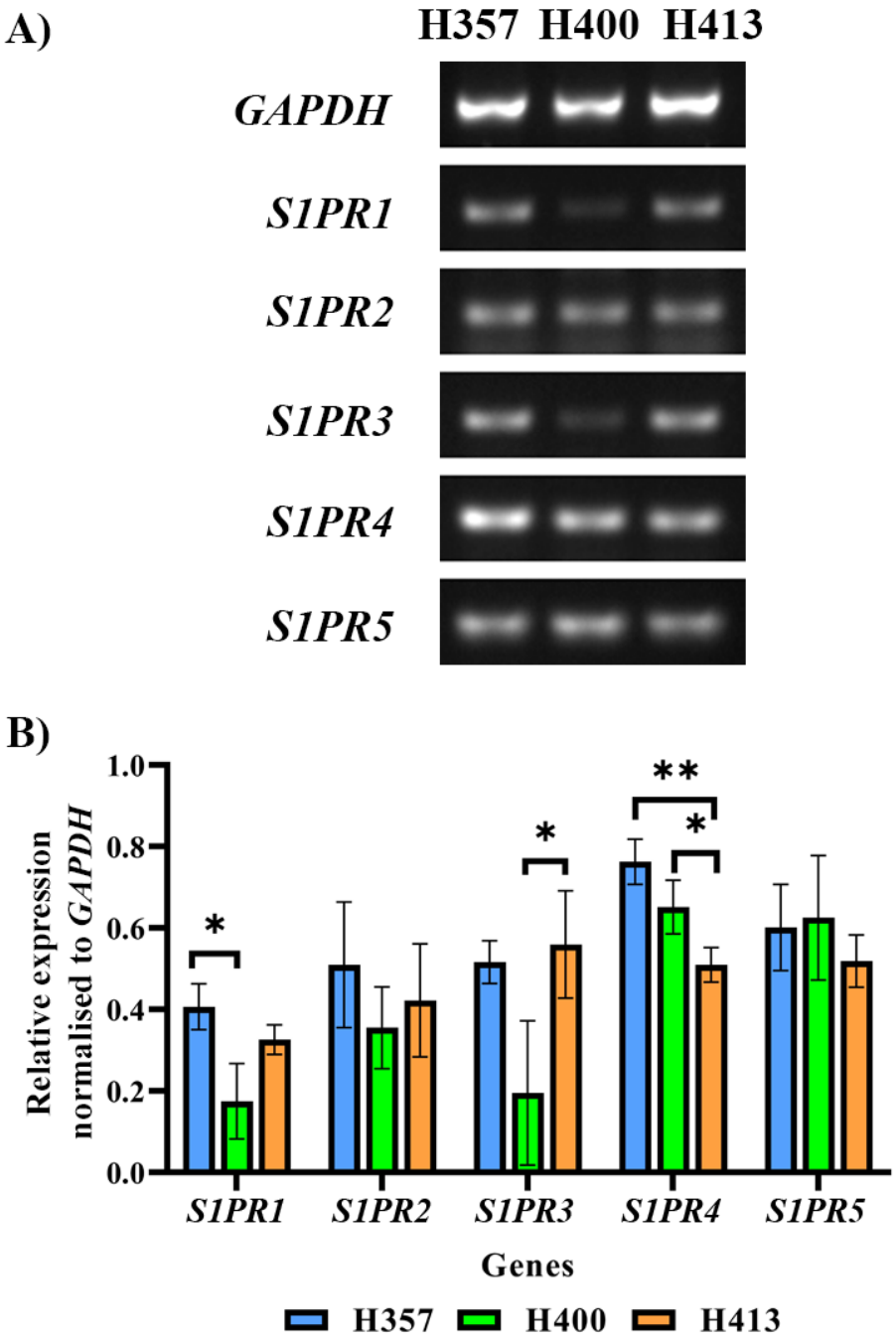

Figure 54. The expression of *S1PR1-5* was determined using sqRT-PCR analysis. **A)** Three OSCC lines expressed all five subtypes of S1PR, but at different levels**. B)** The expression of *S1PR1* by H400 was lower than in H357. No difference in *S1PR2* and *S1PR5* expression was observed between the three OSCC lines. The expression of *S1PR3* by H400 was lower than in H413. H357 and H400 expressed higher *S1PR4* than H413. (Three biological replicates from independent experiments; One-way ANOVA followed by *post-hoc* Tukey tests, * = p-value < 0.05, ** = p-value < 0.01, data presented as mean ± 1 SD).

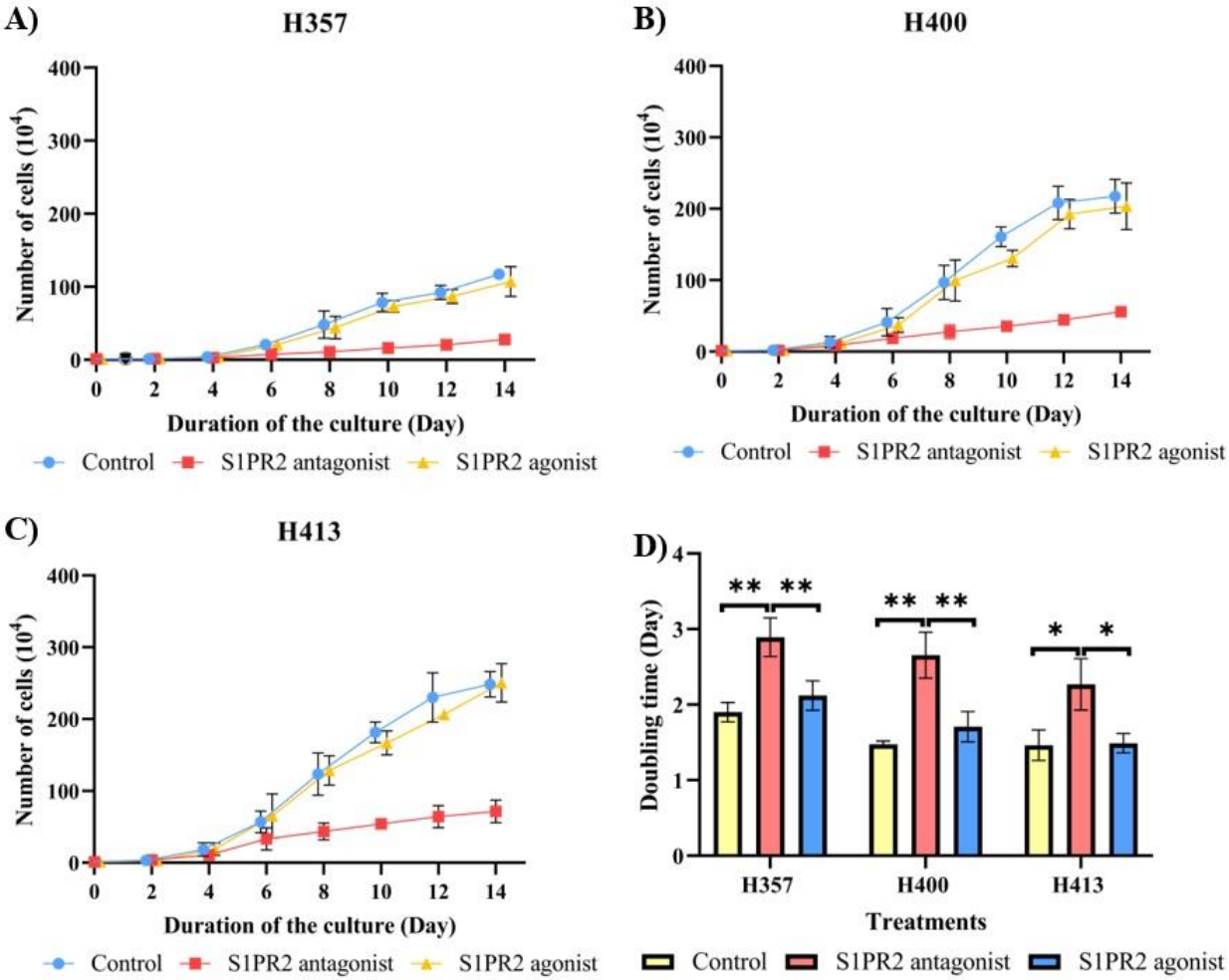

Figure 55. The effect of S1PR2 on proliferation of H357, H400 and H413 cell lines determined using growth curves and doubling times. The three OSCC cell lines were cultured with media supplemented with 10% FBS (control); 10% FBS with 10 μM S1PR2 antagonist; or 10% FBS with 10 μM S1PR2 agonist. **A-C)** The groups treated with the S1PR2 antagonist did not increase in cell number compared with controls, while groups exposed to the S1PR2 agonist generated similar growth curves as controls. **D)** Doubling times of the three lines increased following inhibition of S1PR2 however the stimulation of S1PR2 did not affect the doubling time. (Three biological replicates from independent experiments; Points on the line graphs have been jittered to prevent overlapping; One-way ANOVA followed by *post-hoc* Tukey tests, * = p-value < 0.05, ** = p-value < 0.01, data presented as mean ± 1 SD).

Figure 55C shows that H413 cells demonstrated similar trends to the H357 and H400 cell lines. The doubling time of the control was 1.5 ± 0.2 days. The doubling time increased to 2.3 ± 0.3 days when treated with the S1PR2 antagonist (1.5 fold, $p<0.05$, One-way ANOVA), however, it did not change and remained at 1.5 ± 0.1 days following S1PR2 stimulation with the agonist.

5.5 BrdU assay

The BrdU assay supported data presented in the growth curves and the calculated doubling times (**Figure 56**). Treating H357 cultures with the S1PR2 antagonist caused 1.5 fold reduction of the percentage of BrdU positive cells from 17.8% ± 2.3 (control) to 11.5% ± 1.6 ($p<0.05$, One-way ANOVA). The percentage of H357 BrdU positive cells in cultures treated with the S1PR2 agonist was 21.4 ± 2.6 which was higher than the controls but the difference was not statistically significant. For H400 cultures, the S1PR2 antagonist reduced the percentage of BrdU positive cells from 20.1% ± 2.8 (control) to 7.8% ± 2.49, which was a 2.7 fold reduction compared with controls ($p<0.01$, One-way ANOVA). The percentage of BrdU positive cells in the agonist-treated group remained at the same level as the controls at 18.7% ± 4.8, which indicated that the stimulation of S1PR2 did not affect the proliferation of this line either. The data for H413 cells showed similar trends as those identified for H357 and H400 cells. The percentage of BrdU positive cells decreased from 20.2% ± 1.1 (control) to 11.0% ± 1.2 following S1PR2 inhibition with the antagonist, which was a 1.8 fold decrease compared with controls ($p<0.05$, One-way ANOVA). The stimulation of this receptor minimally increased the percentage of BrdU positive cells to 26.3% ± 6.1, however, this difference was not statistically significant.

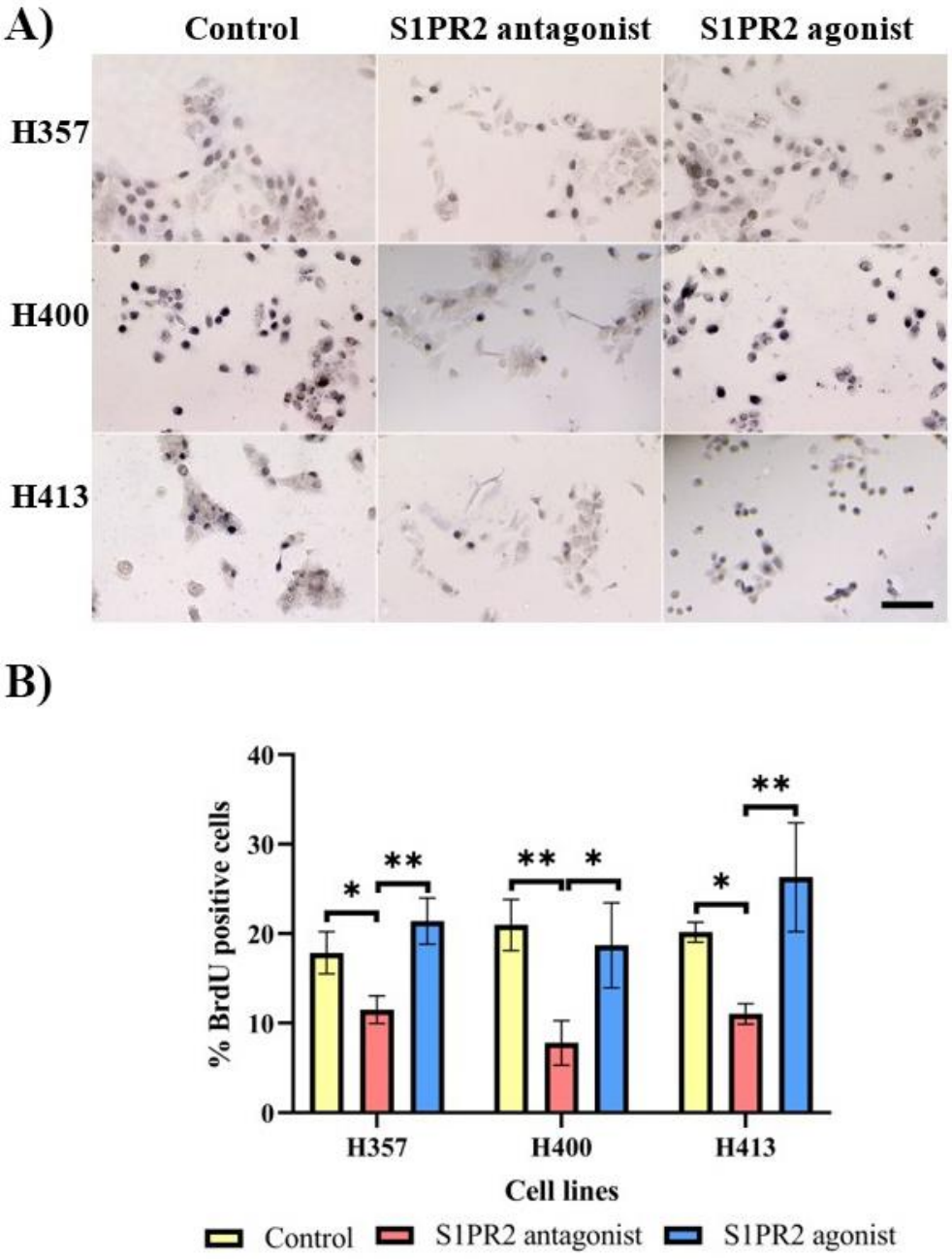

Figure 56. Effects of S1PR2 on proliferation using a BrdU assay on H357, H400 and H413 cells. **A)** Representative phase contrast microscopy images show that BrdU positive cells of three lines in the S1PR2 antagonist treated group was lower than the control, while S1PR2 agonist treated group did not differ from the control. **B)** The percentage of BrdU positive cells in all three cell lines decreased following inhibition of the S1PR2, however no change was observed following stimulation of S1PR2 with the agonist. (Scale bar shown represents 50 μm; X20 objective lens; Three biological replicates from independent experiments, N = 1,000 cells; One-way ANOVA followed by *post-hoc* Tukey tests, * = p-value < 0.05, ** = p-value < 0.01, data presented as mean ± 1 SD).

5.6 Scratch wound migration assay

The effect of S1PR2 on wound closure in H357 cultures is shown in **Figure 57A**. After 8 h, no significant difference in the percentage wound closure was noted between the three groups: the controls (2.8% ± 1.3), the S1PR2 antagonist-treated group (1.8% ± 1.4) and the S1PR2 agonist-treated group (2.3% ± 0.6). After incubation for 24 h, the percentage wound closure of the controls, the S1PR2 antagonist treated group and the S1PR2 agonist group rose to 6.1% ± 3.3, 4.4% ± 2.9 and 5.4% ± 1.3, respectively. However, no statistical significance was identified between these three groups at this time. For H400 cells, the percentage wound closure in the three groups was not statistically different at 8 h of incubation: 8.5% ± 1.9 (control), 4.2% ± 1.3 (S1PR2 antagonist) and 7.9% ± 2.3 (S1PR2 agonist). At 24 h, the group treated with the S1PR2 antagonist showed a percentage wound closure of 11.7% ± 2.0, which was a 1.8 fold decrease compared with controls (20.5% ± 0.4), ($p<0.01$, One-way ANOVA). Conversely, the S1PR2 agonist-treated group revealed a percentage wound closure of 32.2 ± 5.6, which was 1.6-fold higher than controls ($p<0.01$, One-way ANOVA) (**Figure 57B**). **Figure 57C** shows that at 8 h there was no difference in the percentage wound closure between the controls (5.1% ± 1.9) and the group treated with the S1PR2 antagonist (5.0% ± 1.2) for H413 cultures. The group treated with the S1PR2 agonist (11.7% ± 2.3) showed a 2.3-fold higher percentage wound closure than the other groups, ($p<0.01$, One-way ANOVA). After continuing the incubation for 24 h, the percentage wound closure of the S1PR2-suppressed group (14.4% ± 1.1) was 1.7 fold reduced compared with controls (24.3% ± 1.9) ($p<0.01$, One-way ANOVA). The S1PR2 agonist group had a percentage wound closure of 24.9% ± 0.6, which was not significantly different compared with controls.

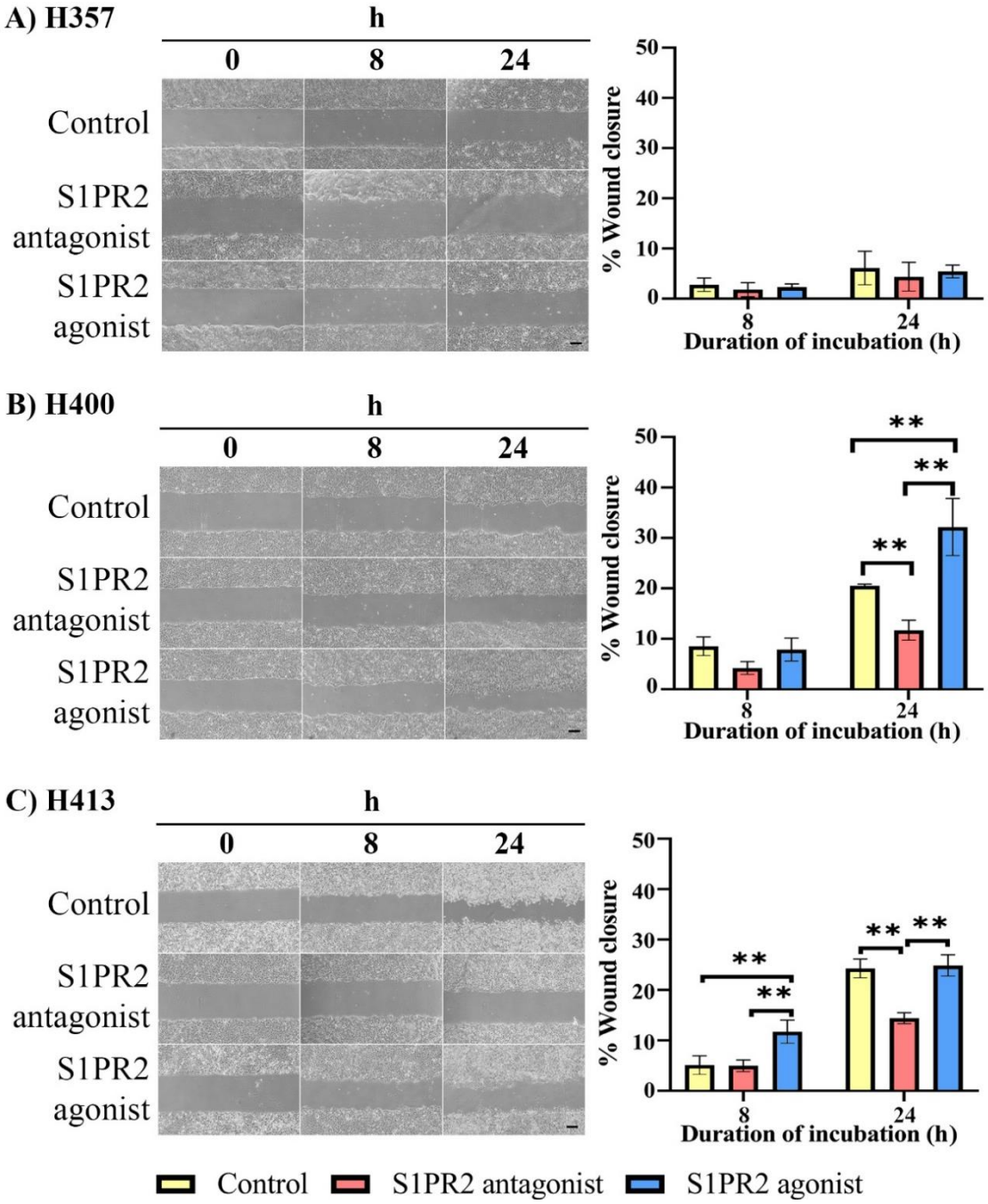

Figure 57. The scratch wound migration assay was used to determine the effect of S1PR2 on the migration of three OSCC lines. Representative phase contrast microscopy images (left side of each image) show that the response to S1PR2 inhibition and stimulation varied between the three OSCC lines. **A)** H357 cells: no significant differences were observed between the three groups at 8 or 24 h. **B)** H400 cells: at 24 h, inhibition of S1PR2 suppressed migration, whilst stimulation promoted cell migration. **C)** H413 cells: at 8 h, stimulation of S1PR2 increased migration compared with the other groups. At 24 h, suppression of S1PR2 reduced migration, but stimulation did not affect cell migration. (Scale bar shown represents 200 µm; X4 objective lens; Three biological replicates from independent experiments were performed with N=4 for each experiment; One-way ANOVA followed by *post-hoc* Tukey test, ** = p-value < 0.01, data presented as mean ± 1 SD).

5.7 Transwell migration assay

The effect of S1PR2 on migration using a transwell assay is shown in **Figure 58**. For H357, S1PR2 suppression reduced the number of migrated cells from 61 ± 2 (control) to 28 ± 7 cells (2.2 fold, $p<0.01$, One-way ANOVA). Conversely, S1PR2 stimulation (93 ± 5 cells) of this cell line increased migration by 1.5 fold ($p<0.01$, One-way ANOVA). For H400 cells, the S1PR2 antagonist suppressed migration, causing a 1.7 fold reduction in the number of migrated cells from 110 ± 27 cells (control) to 64 ± 20 cells ($p<0.05$, One-way ANOVA). Treatment with the S1PR2 agonist resulted in a slightly increased number of migrated cells (146 ± 25 cells) compared with controls, however this difference was not statistically significant. In H413 cells, the S1PR2 antagonist reduced the number of migrated cells, resulting in a decrease from 38 ± 6 cells (control) to 21 ± 3 cells (1.9 fold, $p<0.01$, One-way ANOVA), while the S1PR2 agonist increased the number of migrated cells to 71 ± 3 cells. This difference was a 1.9 fold increase compared with controls ($p<0.01$, One-way ANOVA).

5.8 Transwell invasion assay

Having established the involvement of S1PR2 in migration of three OSCC lines, the role of this receptor in invasion into the collagen matrix was investigated. **Figure 59** shows that when S1PR2 was inhibited, the number of H357 cells that invaded decreased from 10 ± 2 cells (control) to 1 ± 1 (10.0 fold decrease, $p<0.05$, One-way ANOVA). In contrast, H357 cells treated with the S1PR2 agonist demonstrated 19 ± 4 invading cells, 1.9 fold higher than controls, ($p<0.05$, One-way ANOVA). For H400 cells, the S1PR2-antagonist-treated group had 10 ± 2 invading cells, which was 2.4 fold reduction compared with controls (24 ± 3 cells), ($p<0.05$, One-way ANOVA). In contrast, the S1PR2-agonist-treated group (43 ± 6 cells) showed a 1.7 fold increase in invaded cells compared with controls ($p<0.01$, One-way ANOVA).

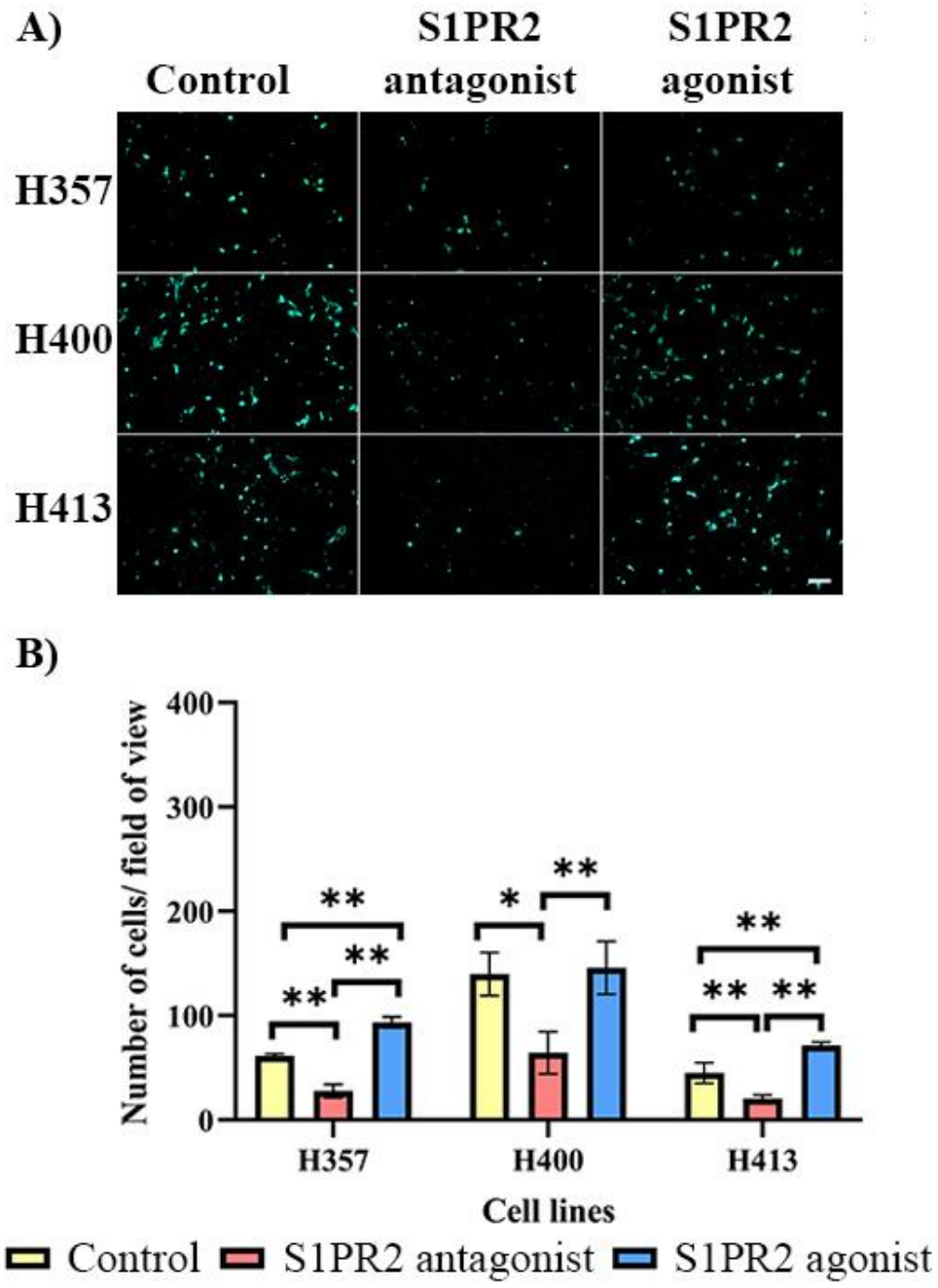

Figure 58. Effects of stimulation and inhibition of S1PR2 on the migration of H357, H400 and H413 cells using a transwell assay. **A)** Representative fluorescence microscopy images show that the S1PR2 antagonist-treated group of three OSCC lines had lower number of migrated cells than the control. The S1PR2 agonist-treated group had higher number of migrated cells than the control only in H357 and H413, but not H400. (Cells were stained with calcein AM.) **B)** The migration of the three cell lines was reduced following inhibition of S1PR2. Stimulation of S1PR2 promoted migration of H357 and H413 but not H400 cells. (Scale bar shown represents 100 μm; X10 objective lens; Three biological replicates from independent experiments were performed with N=10 for each experiment; One-way ANOVA followed by *post-hoc* Tukey test, * = p-value < 0.05, ** = p-value < 0.01, data presented as mean ± 1 SD).

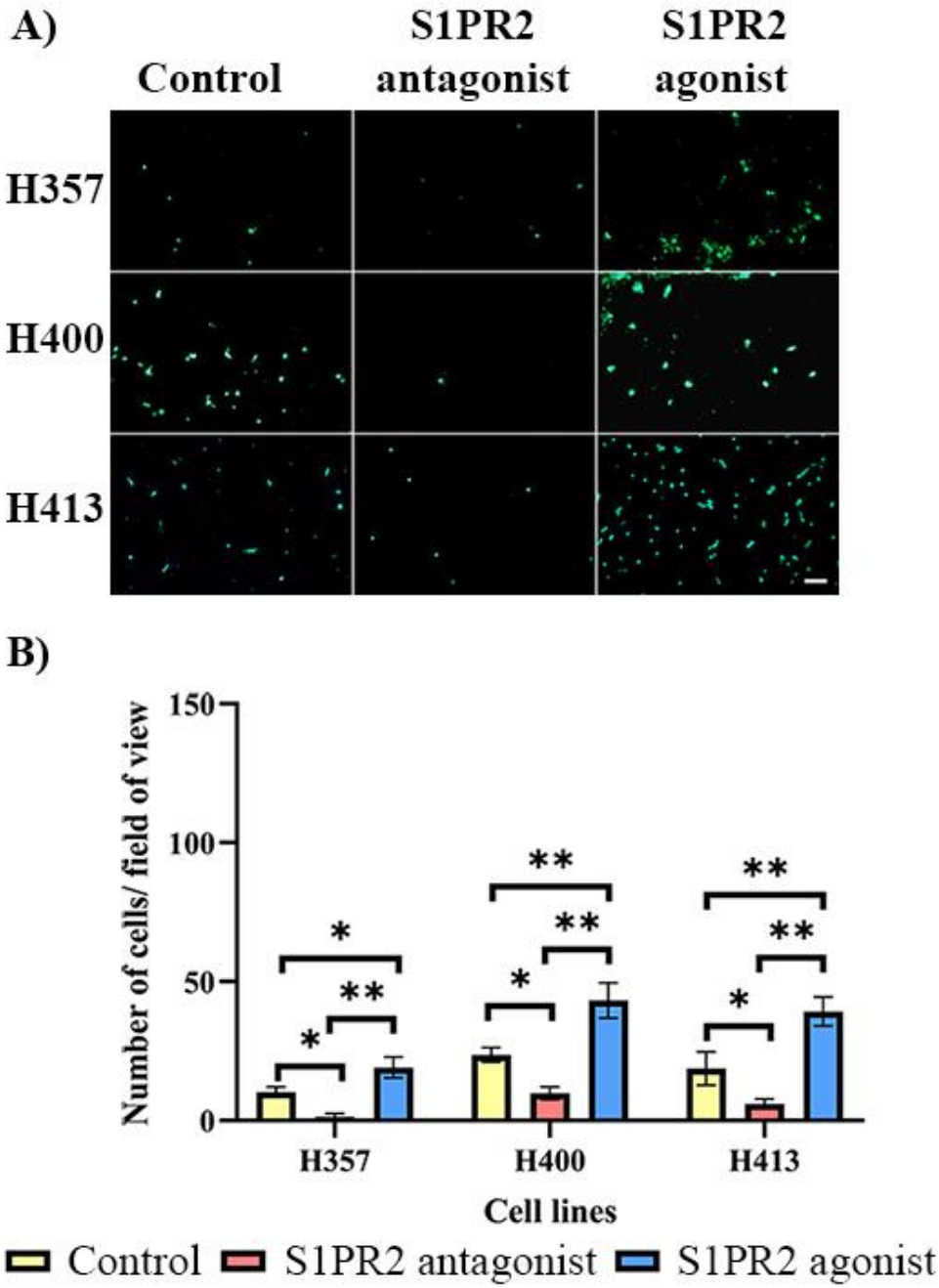

Figure 59. Transwell assay of H357, H400 and H413 cells, determining the role of S1PR2 on invasion. **A)** Representative fluorescence microscopy images show that, the number of invaded cells of three OSCC lines were reduced following S1PR2 inhibition but was increased following S1PR2 stimulation. (Cells were stained with calcein AM.) **B)** The number of invading cells in the three OSCC lines decreased when S1PR2 was inhibited and increased when S1PR2 was stimulated. (Scale bar shown represents 100 µm; X10 objective lens; Three biological replicates from independent experiments were performed with N=10 for each experiment; One-way ANOVA followed by *post-hoc* Tukey test, * = p-value < 0.05, ** = p-value < 0.01, data presented as mean ± 1 SD).

For H413 cells, the S1PR2 antagonist decreased the number of invading cells from 19 ± 6 (control) to 6 ± 2, which was a 3.1 fold reduction ($p<0.05$, One-way ANOVA). In contrast, the S1PR2-stimulated group (39 ± 5 cells) showed a 2.0 fold increase relative to controls ($p<0.01$, One-way ANOVA).

5.9 Multicellular tumour spheroids (MCTS)

The effect of S1PR2 on the invasive characteristics was further investigated using an MCTS assay (**Figure 60**). Overall, the penetration of cells into collagen matrix was reduced when S1PR2 was inhibited, while it was increased when S1PR2 was stimulated. Details are described in the following **sections 5.9.1-5**. Tables which included original data were attached in the **Appendix**.

5.9.1 Analysis of the number of clusters

The effect of S1PR2 on the fragmentation of spheroids is shown in **Appendix table XVI** and **Figure 61**. The S1PR2 antagonist did not affect the number of clusters of H357 spheroids on both days 1 and 2, whereas the S1PR2 agonist increased the number of clusters compared with controls by 4.3 fold on day 1 ($p<0.05$, Two-way ANOVA) and by 5.2 fold on day 2 ($p<0.01$, Two-way ANOVA). For H400 spheroids, no trend was noted on day 1. On day 2, inhibition of S1PR2 decreased the number of clusters, while stimulation resulted in an increase although this trend was not statistically significant. For H413 cultures, the group treated with the S1PR2 antagonist had fewer clusters than the control, while the group exposed to the S1PR2 agonist demonstrated more clusters than the controls on day 1, although this trend was not statistically significant at this time. On day 2, S1PR2 inhibition caused a 2.3 fold decrease in the number of clusters compared with controls, whilst S1PR2 stimulation increased cluster numbers by 1.92 fold ($p<0.01$, Two-way ANOVA).

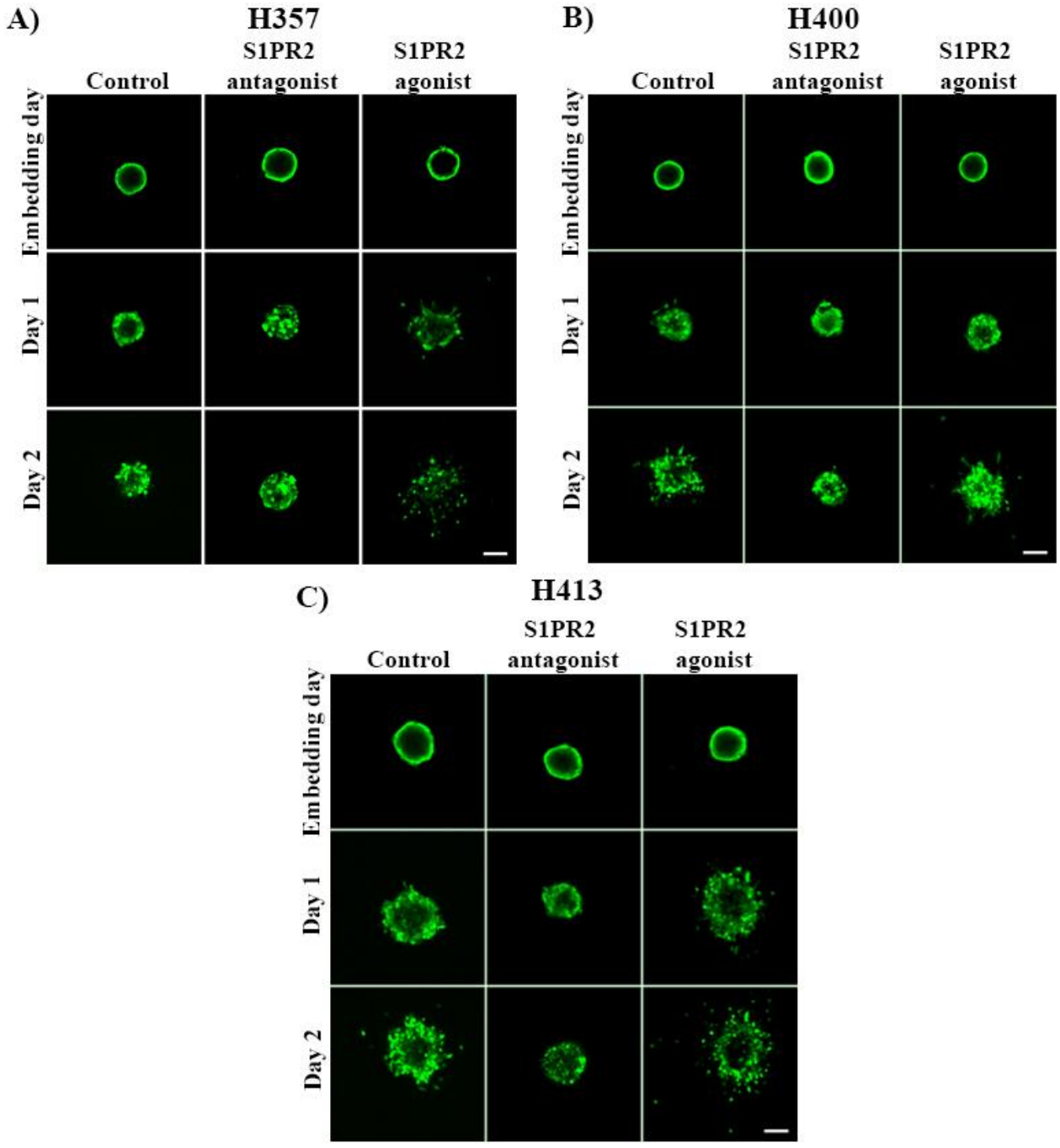

Figure 60. Effects of S1PR2 on invasion determined using MCTS assay. Spheroids of each line was embedded in 3 mg/ml collagen, inhibited proliferation with 8 µg/ml mitomycin C for 2 h and treated with 10 µM of either the S1PR2 antagonist or the agonist for two days. (Cells were stained with calcein AM.) **A)** H357 **B)** H400 and **C)** H413 cells. Representative confocal microscopy images of spheroids stained with calcein AM shows that overall, the invasive characteristics of the three cell lines were apparent from day 2. On this day, the groups in which S1PR2 was inhibited demonstrated fewer cells spreading into the collagen, whereas the groups incubated with the S1PR2 agonist exhibited more cells spreading into the collagen compared with the controls. (Scale bar = 100 µm; X10 objective lens; Three biological replicates from independent experiments were performed with N=10 for each experiment).

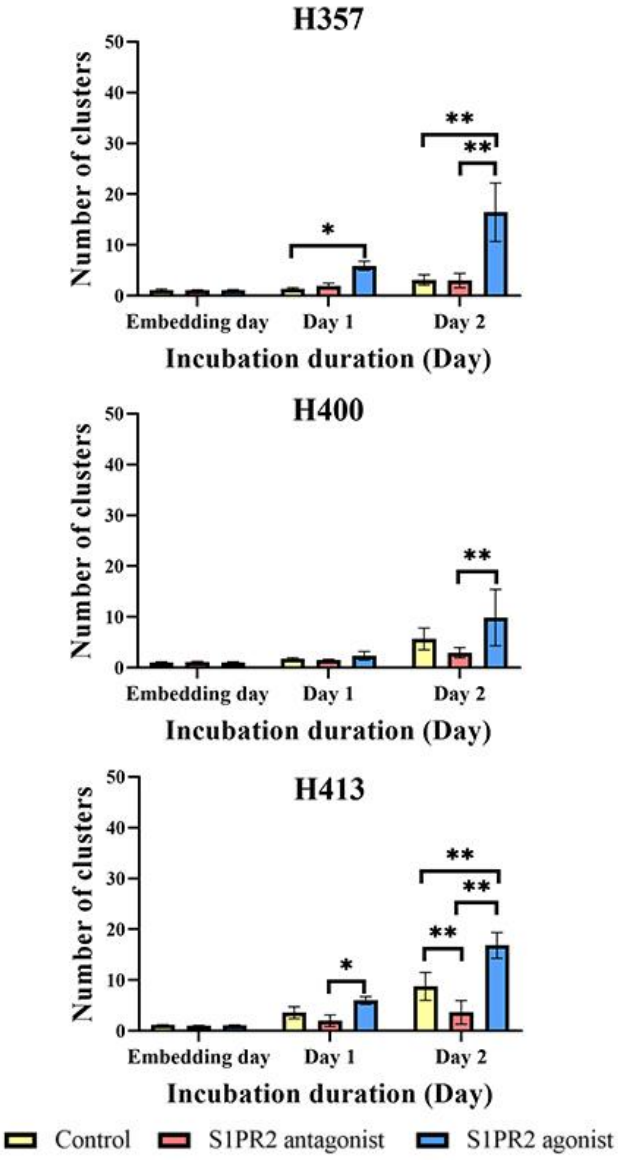

Figure 61. Number of clusters generated for each of the cell lines following either S1PR2 inhibition or stimulation. Spheroids were generated using the hanging drop method (one day of incubation), embedded in 3 mg/ml collagen and treated with 8 µg/ml mitomycin C for 2 h before incubating with DMEM only, DMEM with 10 µM S1PR2 antagonist and DMEM with 10 µM S1PR2 agonist for two days. There was no difference in the number of clusters in H357 spheroid cultures following inhibition of S1PR2 on days 1 and 2. However, the number of clusters increased when treated with the S1PR2 agonist. Neither the inhibition nor the stimulation of S1PR2 affected the number of clusters arising from 400 spheroids on day 1. On day 2, less H400 clusters were observed compared with controls when S1PR2 was inhibited whilst more clusters formed when S1PR2 was stimulated, however these differences were not statistically significant. For H413 cultures, neither the S1PR2 antagonist nor the agonist affected the number of clusters observed on day 1. On day 2, the S1PR2 antagonist reduced the number of clusters whilst the agonist caused an increase. (Three biological replicates from independent experiments were performed with N=10 for each experiment; Two-way ANOVA followed by *post-hoc* Tukey tests, * = p-value < 0.05, ** = p-value < 0.01, data presented as mean ± 1 SD).

5.9.2 Analysis of the maximum invading distance

Appendix table XVII and **Figure 62** show the maximum invading distance into collagen matrix for the three cell lines treated with either S1PR2 antagonist or S1PR2 agonist. On day 1, the H357 group treated with S1PR2 antagonist demonstrated a similar maximum invading distance to controls, whilst the S1PR2-agonist-treated group revealed a 1.4 fold increase ($p<0.01$, Two-way ANOVA). The trend on day 2 was similar to those observed on day 1 but no statistical significance was identified. For H400 cells, the maximum invading distance of the controls on both days 1 and 2 was similar to the group treated with the S1PR2 antagonist. The maximum invading distance in H400 cultures treated with the S1PR2 agonist was not statistically different from controls on day 1 but increased 1.21 fold compared with controls on day 2 ($p<0.05$, Two-way ANOVA). For H413 cells, the S1PR2-inhibited group decreased invading distance compared with controls on both days 1 and 2, whilst the S1PR2-stimulated group increased invading distance, although these difference were not statistically significant.

5.9.3 Analysis of the circularity and fractal dimension of the main cluster

No trend in the effect of S1PR2 on circularity was found for the three OSCC lines (**Appendix table XVIII** and **Figure 63**). On day 1, both the S1PR2 antagonist and agonist decreased the circularity of H357 cell clusters, however only the group treated with the S1PR2 agonist showed a significant decrease compared with the control ($p<0.01$, Two-way ANOVA). On day 2, the S1PR2-inhibited group had higher circularity than the controls but this was not a significant difference. The S1PR2-stimulated group demonstrated a significant lower circularity than the controls ($p<0.05$, Two-way ANOVA). No statistical differences were observed on days 1 and 2 for the H400 and H413 cultures.

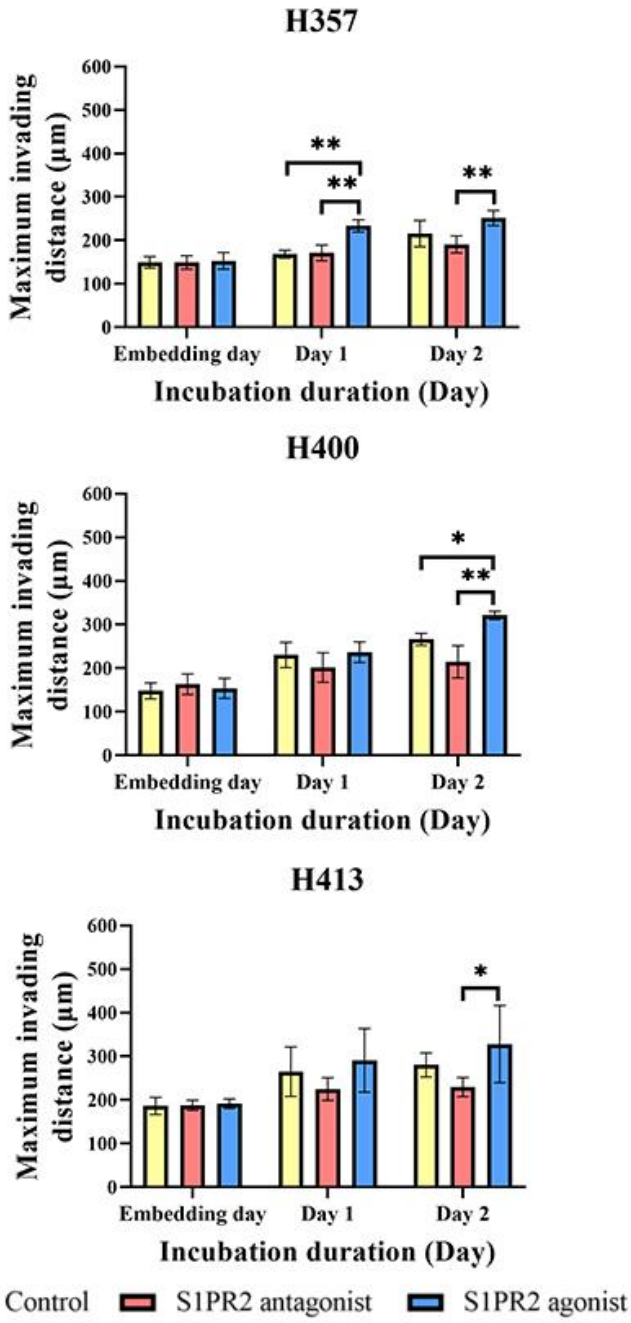

Figure 62. The maximum invading distance of three OSCC lines following S1PR2 inhibition and stimulation. Spheroids were generated using the hanging drop method (one day of incubation), embedded in 3 mg/ml collagen and treated with 8 µg/ml mitomycin C for 2 h before incubating with DMEM only, DMEM with 10 µM S1PR2 antagonist and DMEM with 10 µM S1PR2 agonist for two days. Generally, inhibition of S1PR2 reduced the maximum invading distance of the three OSCC lines, whilst S1PR2 stimulation increased invasion. However, there were no statistically significant difference in maximum invading distances except between the controls and the S1PR2 stimulated group of the H357 cultures on day 1 and between the controls and the S1PR2 stimulated group of H400 cultures on day 2. (Three biological replicates from independent experiments were performed with N=10 for each experiment; Two-way ANOVA followed by *post-hoc* Tukey tests, * = p-value < 0.05, ** = p-value < 0.01, data presented as mean ± 1 SD).

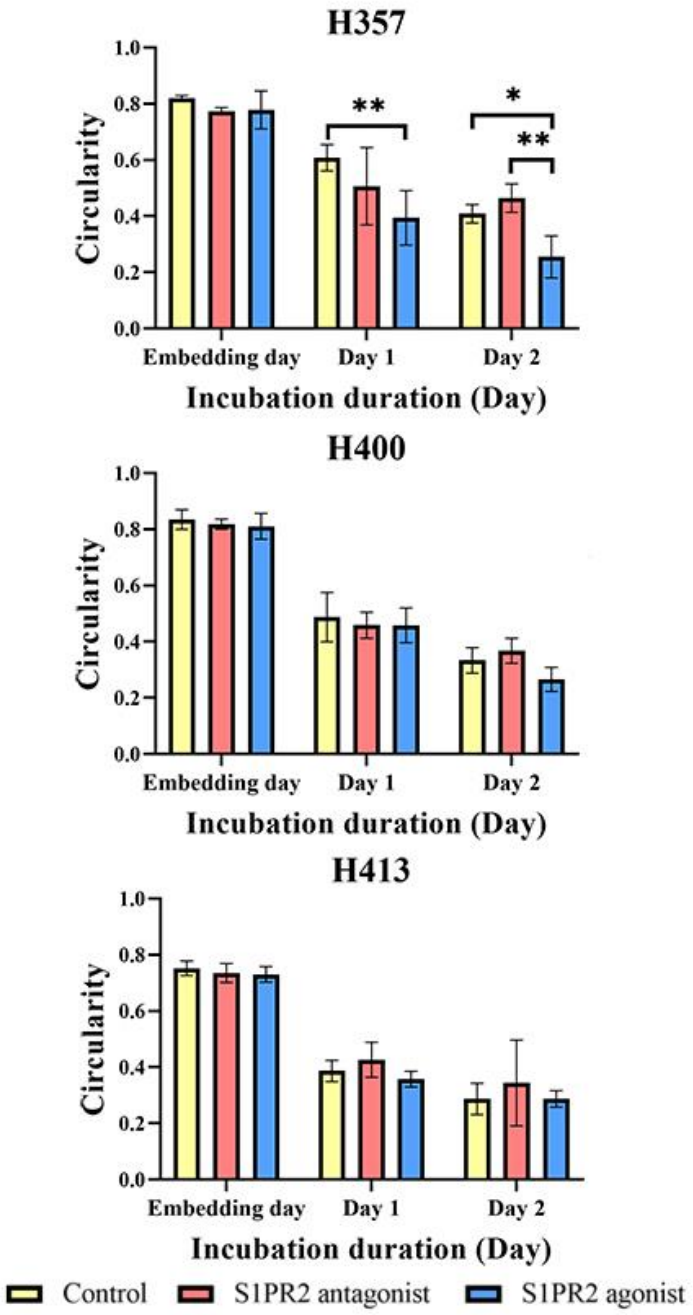

Figure 63. The effects of S1PR2 on the circularity of the main clusters of three OSCC lines. Spheroid were generated using the hanging drop method (one day of incubation), embedded in 3 mg/ml collagen and treated with 8 µg/ml mitomycin C for 2 h before incubating with DMEM only, DMEM with 10 µM S1PR2 antagonist and DMEM with 10 µM S1PR2 agonist for two days. The H357 cultures treated with the S1PR2 agonist had lower circularity than controls on both days 1 and 2. The controls for H400 and H413 cultures on day 2 appeared to have higher circularity than the group treated with S1PR2, but this difference was not statistically significant. (Three biological replicates from independent experiments were performed with N=10 for each experiment; Two-way ANOVA followed by *post-hoc* Tukey tests, * = p-value < 0.05, ** = p-value < 0.01, data presented as mean ± 1 SD).

Appendix table XIX shows the mean fractal dimension for the spheroids generated with the three cell lines. No statistical difference in fractal dimension was observed between groups of three OSCC lines (**Figure 64**).

5.9.4 Analysis of the maximum diameter of the main cluster (MDMC)

Appendix table XX and **Figure 65** show the effect of S1PR2 on MDMC for H357, H400 and H413 cultures. The MDMC of H357 spheroids was not affected by inhibition of S1PR2, but stimulation caused a 1.3 fold increase on both days 1 and 2 compared with controls ($p<0.01$, Two-way ANOVA). For H400 cultures, the S1PR2 antagonist minimally decreased the MDMC, whilst S1PR2 stimulation increased MDMC on both days 1 and 2, although differences were not statistically significant. For H413, the S1PR2 antagonist caused a 1.2 fold reduction in MDMC compared with controls on both days 1 and 2 ($p<0.01$, Two-way ANOVA), however stimulation of this receptor did not increase MDMC compared with controls on both days.

5.10 Matrix metalloproteinase production

With regards to MMP2 production, both S1PR2 suppression and stimulation for 48 h caused an increase in expression as detected by real-time PCR analysis of H357 cultures but this increase was not statistically significant. Inhibition of S1PR2 in H400 cultures reduced *MMP2* expression 2.0 fold ($p<0.01$, One-way ANOVA), but S1PR2 stimulation did not affect expression of this enzyme. In H413 cultures, *MMP2* expression was downregulated (1.6 fold) following exposure to the S1PR2 antagonist however this difference was not statistically significant in comparison with controls. Conversely, S1PR2 stimulation resulted in a 2.2 fold increase in expression compared with controls ($p<0.01$, One-way ANOVA) (**Figure 66A**).

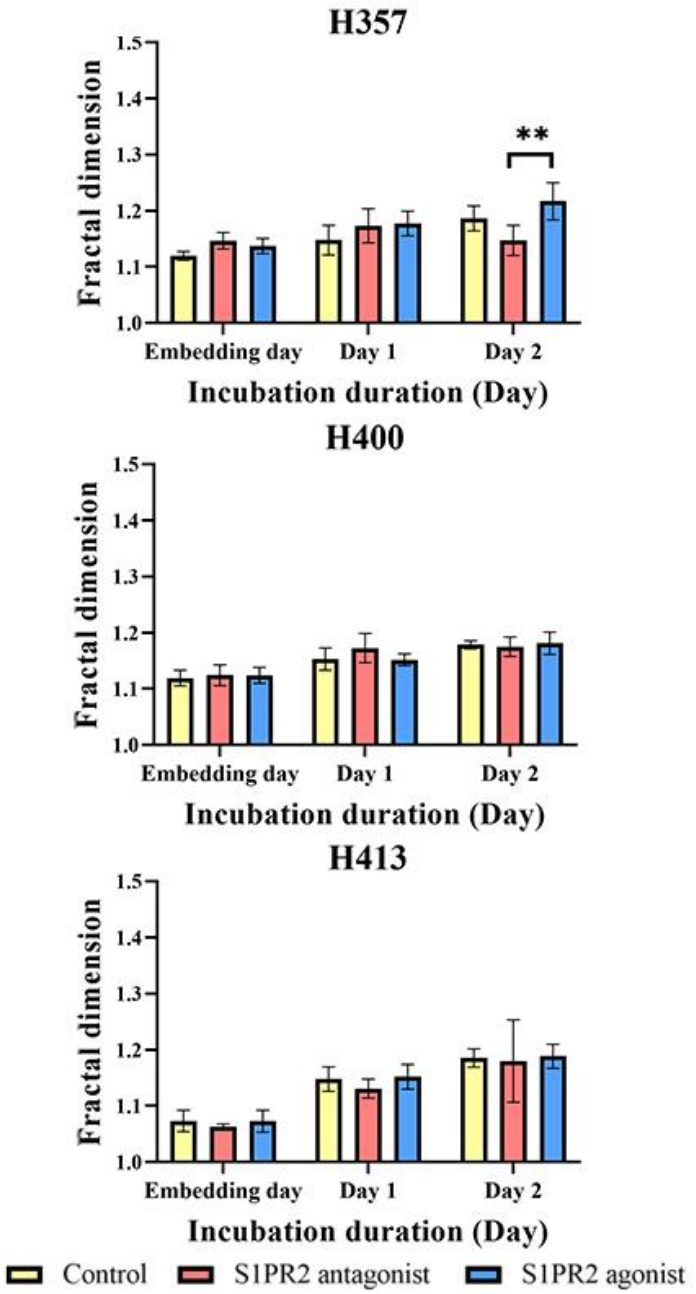

Figure 64. The effects of S1PR2 on the fractal dimension of the main clusters of H357, H400 and H413 spheroid cultures. Spheroids were generated using the hanging drop method (one day of incubation), embedded in 3 mg/ml collagen and treated with 8 μg/ml mitomycin C for 2 h before incubating with DMEM only, DMEM with 10 μM S1PR2 antagonist and DMEM with 10 μM S1PR2 agonist for two days. Neither S1PR2 inhibition nor stimulation affected the fractal dimension of three OSCC lines. (Three biological replicates from independent experiments were performed with N=10 for each experiment; Two-way ANOVA followed by *post-hoc* Tukey tests, * = p-value < 0.05, ** = p-value < 0.01, data presented as mean ± 1 SD).

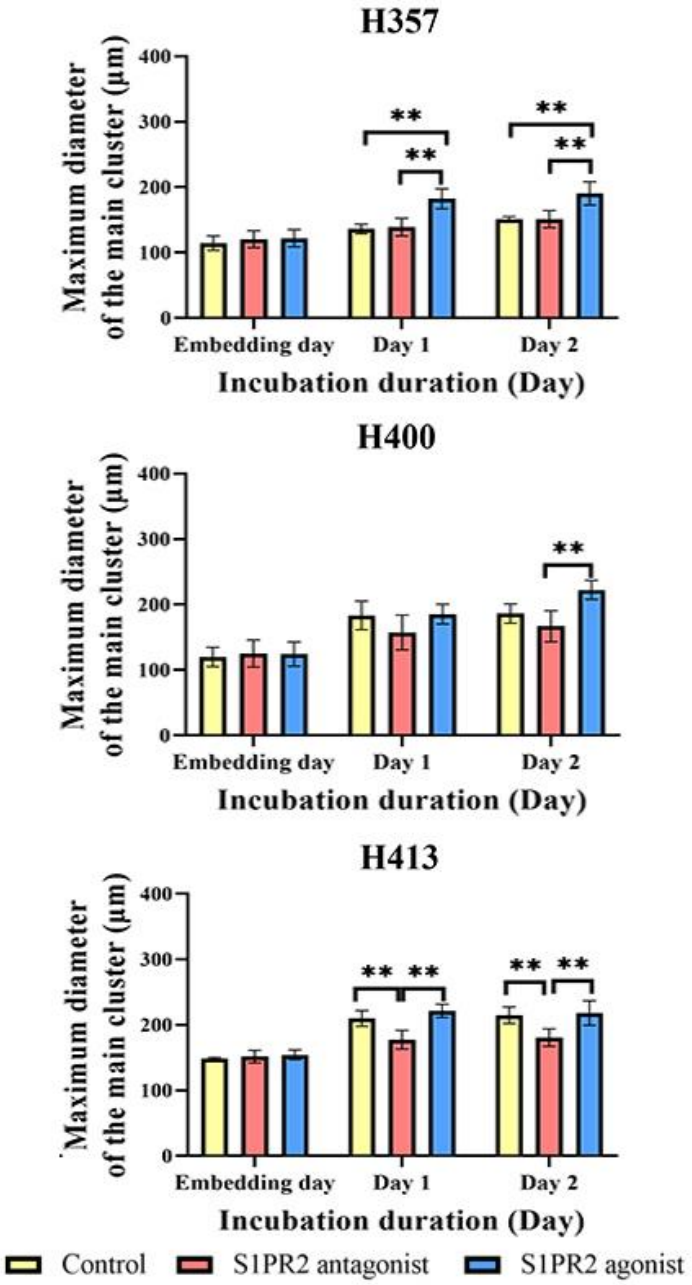

Figure 65. Effects of S1PR2 on the MDMC of invading spheroids of H357, H400 and H413 cell lines. Spheroids were generated using the hanging drop method (one day of incubation), embedded in 3 mg/ml collagen and treated with 8 µg/ml mitomycin C for 2 h before incubating with DMEM only, DMEM with 10 µM S1PR2 antagonist and DMEM with 10 µM S1PR2 agonist for two days. For H357 cells, inhibition of S1PR2 did not affect the MDMC, while stimulation increased the MDMC. H400 and H413 cells demonstrated similar trends following suppression of S1PR2 which decreased the MDMC, whilst stimulation did not significantly affect this parameter. (Three biological replicates from independent experiments were performed with N=10 for each experiment; Two-way ANOVA followed by *post-hoc* Tukey tests, ** = p-value < 0.01, data presented as mean ± 1 SD).

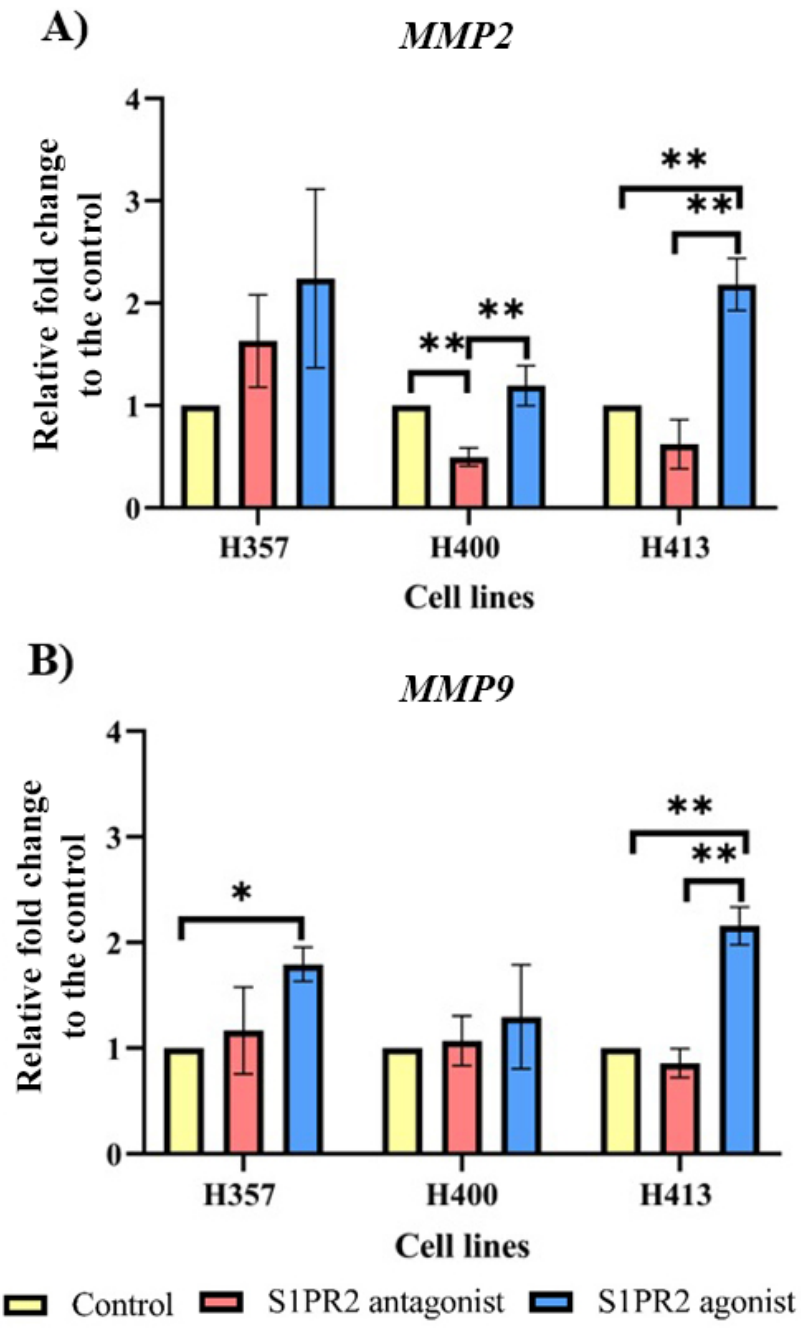

Figure 66. The effect of S1PR2 on *MMP2* and *MMP9* expression determined using real time-PCR analysis, 48 h of incubation. The results were normalized to the housekeeping gene and then were presented as a relative fold change to the control. **A)** The *MMP2* expression was elevated following S1PR2 inhibition as well as stimulation of H357 cultures. For H400 and H413 cultures, inhibition of S1PR2 downregulated *MMP2* gene expression, while stimulation of S1PR2 resulted in upregulation. **B)** Both inhibition and stimulation of S1PR2 increased *MMP9* expression in H357 and H400 cultures. For H413 cells, the gene expression of *MMP9* slightly decreased following S1PR2 inhibition (not statistically significant) but increased following S1PR2 stimulation. (Three biological replicates from independent experiments with each experiment was the average of two technical replicates; One-way ANOVA followed by *post-hoc* Tukey tests, * = p-value < 0.05, ** = p-value < 0.01, data presented as mean ± 1 SD).

In H357 and H400 cultures, both inhibition and stimulation of S1PR2 caused an increase in *MMP9* expression. However, a significant difference was observed only between the control and the S1PR2 stimulated group (H357 cultures) where expression was increased by 1.5 fold ($p<0.05$, One-way ANOVA). For H413 cultures, inhibition of S1PR2 slightly reduced the expression of *MMP9* (not statistically significant), while stimulation increased the expression by 1.8 fold ($p<0.01$, One-way ANOVA) (**Figure 66B**).

5.11 Sphingosine kinases expression

A previous study has shown that S1PR2 controlled migration and invasion through the regulation of *SPHK1* and *SPHK2* (Asghar *et al.*, 2018); therefore the effect of S1PR2 on the expression of *SPHK1* and *SPHK2* was examined in the present study. **Figure 67A** shows that inhibition of S1PR2 in H357 cultures minimally increased *SPHK1* expression whilst S1PR2 stimulation decreased expression although these differences were not statistically significant. In H400 cells, S1PR2 inhibition suppressed *SPHK1* expression (4.9 fold reduction compared with controls, $p<0.05$, One-way ANOVA), whereas S1PR2 stimulation increased *SPHK1* expression by 2.4 fold ($p<0.05$, One-way ANOVA). S1PR2 inhibition in H413 cultures reduced transcription of the *SPHK1* gene (not significant), whilst stimulation of S1PR2 increased expression of this gene 4.3 fold ($p<0.05$, One-way ANOVA). For *SPHK2*, no trend was identified in H357 and H400 cultures following both inhibition and stimulation of S1PR2 (**Figure 67B**). In contrast, the inhibition of S1PR2 in H413 cultures reduced *SPHK2* expression, whilst S1PR2 stimulation increased *SPHK2* expression by 1.6 fold compared with the controls ($p<0.05$, One-way ANOVA). These data suggested that in H400 and H413 cultures, inhibition of S1PR2 may lead to a reduction in S1P production (due to the downregulation of *SPHK1* in H400 and both *SPHK1* and *2* in H413 cells) whilst stimulation of S1PR2 had the opposite effect.

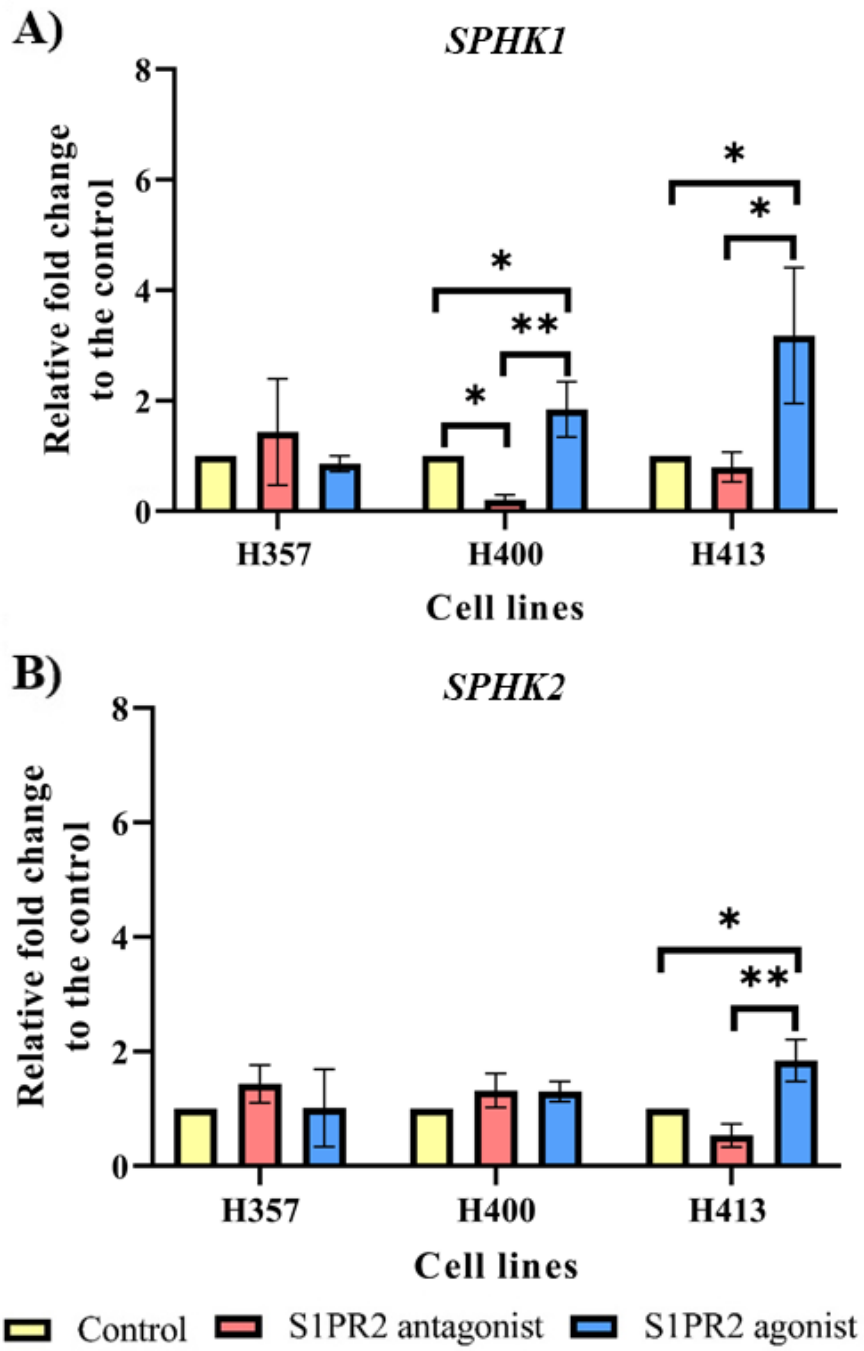

Figure 677. The regulation of *SPHK1* and *SPHK2* gene expression by S1PR2 using real-time PCR analysis, 48 h of incubation. The results were normalized to the housekeeping gene and then were presented as a relative fold change to the control. **A)** No significant change in *SPHK1* expression in H357 cells was observed following both S1PR2 inhibition and stimulation. In H400 and H413 cells, inhibition of S1PR2 downregulated expression of *SPHK1*, while stimulation of S1PR2 upregulated this gene. **B)** Neither inhibition and stimulation of S1PR2 did not alter the expression of *SPHK2* in H357 and H400 cultures. Inhibition of S1PR2 decreased *SPHK2* expression in H413 cultures and S1PR2 stimulation caused an increase. (Three biological replicates from independent experiments with each experiment was the average of two technical replicates; One-way ANOVA followed by post-hoc Tukey tests, * = p-value < 0.05, ** = p-value < 0.01, data presented as mean ± 1 SD.)

5.12 Conclusion

The inhibition of S1PR2 suppressed proliferation, but its stimulation did not promote proliferation. Migration and invasion of three OSCC lines were also suppressed by the inhibition of S1PR2. The stimulation of this receptor promoted migration of some lines, depending on the assay used, but it increased the invasion of the three OSCC lines in both assays. The inhibition of S1PR2 affected the expression of *MMP2* and *MMP9* differently, depending on the cell line. It also affected the transcription of *SPHK1* of H400 and H413 and *SPHK2* of H400, potentially affecting S1P production.

Chapter 6: Results

The crosstalk between EGF/EGFR and S1P/S1PR2 in controlling migration and invasion of OSCC lines

6.1 Aims

In Chapters 4 and 5, studies demonstrated that both EGF and S1PR2 play a role in controlling motility of the H357, H400 and H413 cell lines. This prompted the hypothesis that there may be overlapping functions between EGF and S1PR2. This chapter therefore aimed to investigate any involvement of S1PR2 in EGF-induced migration and the invasion of H357, H400 and H413 cell lines, as well as identify any potential crosstalk between S1P/S1PR2 and EGF/EGFR signalling. The experimental setup consisted of four treatment groups: 1) control, 2) 20 ng/ml EGF, 3) 10 μM S1PR2 antagonist and 20 ng/ml EGF, and 4) 10 μM S1PR2 agonist and 20 ng/ml EGF.

6.2 Objectives

The three objectives for this chapter were to determine:

a) the effect of S1PR2 on EGF-induced migration and invasion in H357, H400 and H413 cells,
b) the effect of EGF and S1PR2 on Rac1 activity in H357, H400 and H413 cells, and
c) the crosstalk between EGF/EGF receptors and S1P/S1PR2 pathways through the effect of one receptor on the production of the other receptor's ligand

6.3 Scratch wound migration assay

Figure 68A shows an absence of any clear trend between the four groups of H357 cultures at 8 h. At 24 h, EGF marginally increased migration (in terms of percentage wound closure) from 6.1% ± 3.3 (control) to 9.7% ± 1.0. The addition of S1PR2 antagonist reduced the EGF effects to 6.4% ± 0.4, while the addition of the S1PR2 agonist increased it to 13.8% ± 4.5. However, these differences were not statistically significant except between the control and the group treated with both EGF and the S1PR2 agonist which showed a 2.3 fold increase ($p<0.05$, One-way ANOVA).

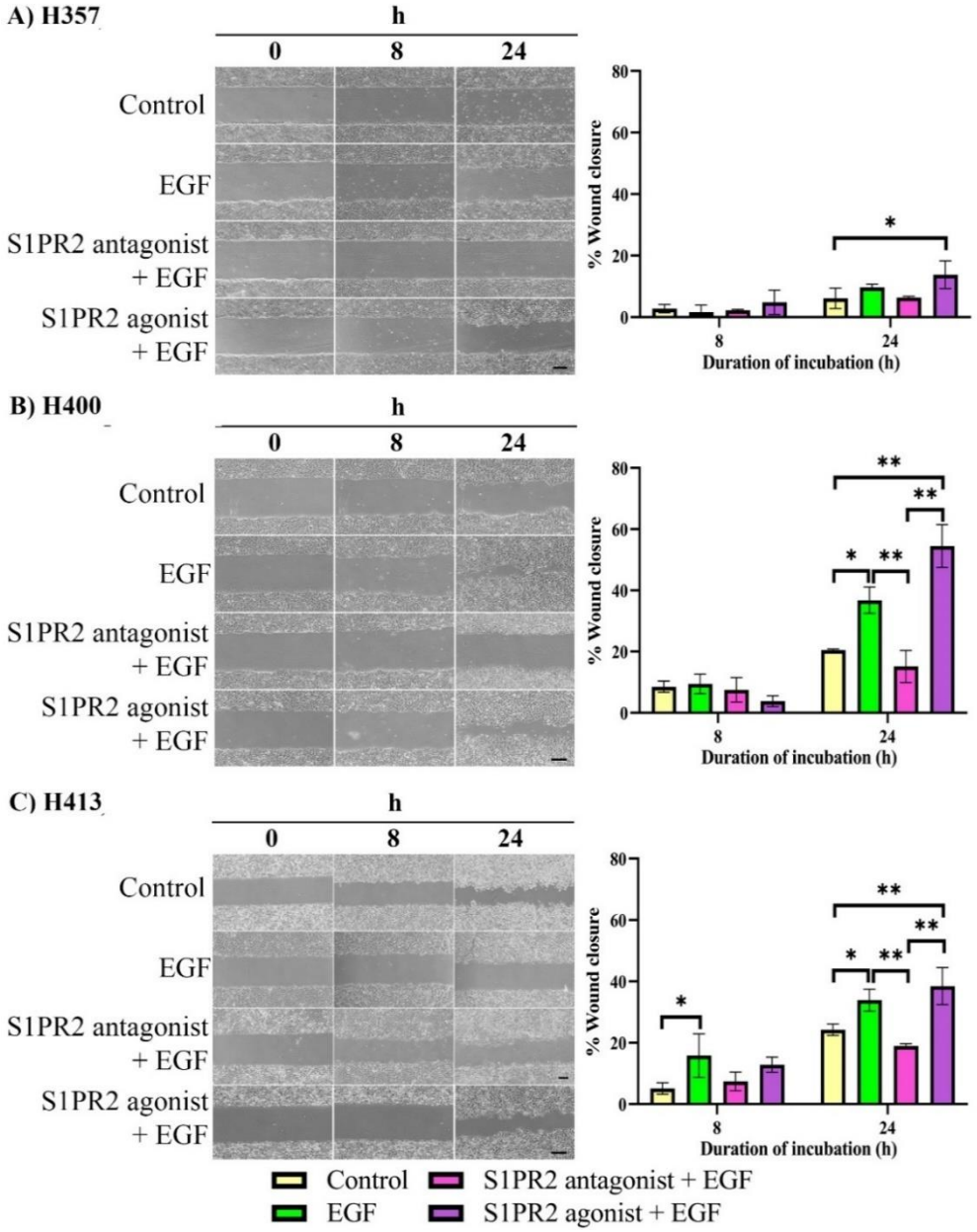

Figure 68. Scratch wound migration assay of the three OSCC lines to investigate the effect of S1PR2 on EGF-induced migration. Representative phase contrast microscopy images (left side of each panel) show that the wound gap in EGF-treated cultures were smaller than the controls. Wound gaps of EGF-treated groups were also smaller than in cultures treated with both EGF and the S1PR2 antagonist but did not differ from the cultures treated with EGF and the S1PR2 agonist. **A)** No significant differences were found between the four H357 cell groups at 8 h. At 24 h, EGF promoted migration but the effect was decreased and increased following inhibition and stimulation of S1PR2, respectively. **B) & C)** At 24 h, the groups of H400 and H413 cells treated with EGF showed a higher percentage wound closure than the control. This effect statistically decreased when S1PR2 was suppressed and slightly increased when S1PR2 was activated. (The result of the single control treatment of S1PR2 antagonist and agonist was presented in **Figure 57**, chapter 5; Scale bar shown represents 200 µm; X4 objective lens; Three biological replicates from independent experiments were performed with N=4 for each experiment; One-way ANOVA followed by *post-hoc* Tukey test, * = p-value < 0.05 and ** = p-value < 0.01, data presented as mean ± 1 SD).

For H400 cells, the wound closure rate between the four groups was not statistically different at 8 h. After 24 h incubation, EGF increased the percentage wound closure by 1.8 fold, from 20.5% ± 0.4 (control) to 36.8% ± 4.3 ($p<0.05$, One-way ANOVA). The addition of the S1PR2 antagonist caused a 2.4 fold decrease in the effect of EGF on migration and resulted in a percentage wound closure of 15.2% ± 5.2 ($p<0.01$, One-way ANOVA). EGF combined with the S1PR2 agonist increased the percentage wound closure to 54.5% ± 7.0, although it was not statistically significant when compared with the EGF-treated group (**Figure 68B**).

For H413 cultures, at 8 h, the group treated with EGF (15.8% ± 7.1) exhibited a 3.0 fold higher percentage wound closure than the control (5.1% ± 1.9) ($p<0.05$, One-way ANOVA). Inhibition of S1PR2 decreased the percentage wound closure to 7.4% ± 3.0, however this was not statistically significant compared with the EGF-treatment group. The group treated with both the S1PR2 agonist and EGF resulted in a percentage wound closure of 12.8% ± 2.5 (similar to the group treated with EGF only). At 24 h, EGF increased the percentage wound closure of this line from 24.3 ± 1.9 (control) to 33.9% ± 3.6, (1.4 fold increase, $p<0.05$, One-way ANOVA). The effect of EGF was decreased when the S1PR2 antagonist was added to the treatment, resulting in a 1.8 fold reduction in the percentage wound closure (19.0% ± 0.7) compared with the EGF-treated group ($p<0.01$, One-way ANOVA). For the group treated with both S1PR2 agonist and EGF, the wound closure percentage (38.4% ± 6.0) was higher than the EGF-treated group but was not statistically significantly different (**Figure 68C**).

6.4 Transwell migration assay

The study investigated the effect of S1PR2 on EGF-induced migration using a transwell migration assay (**Figure 69**). For H357 cultures, EGF at 20 ng/ml stimulated migration, resulting in a 1.7 fold increase in the number of migrated cells from 61 ± 22 (control) to 103 ± 18 ($p<0.05$, One-way ANOVA).

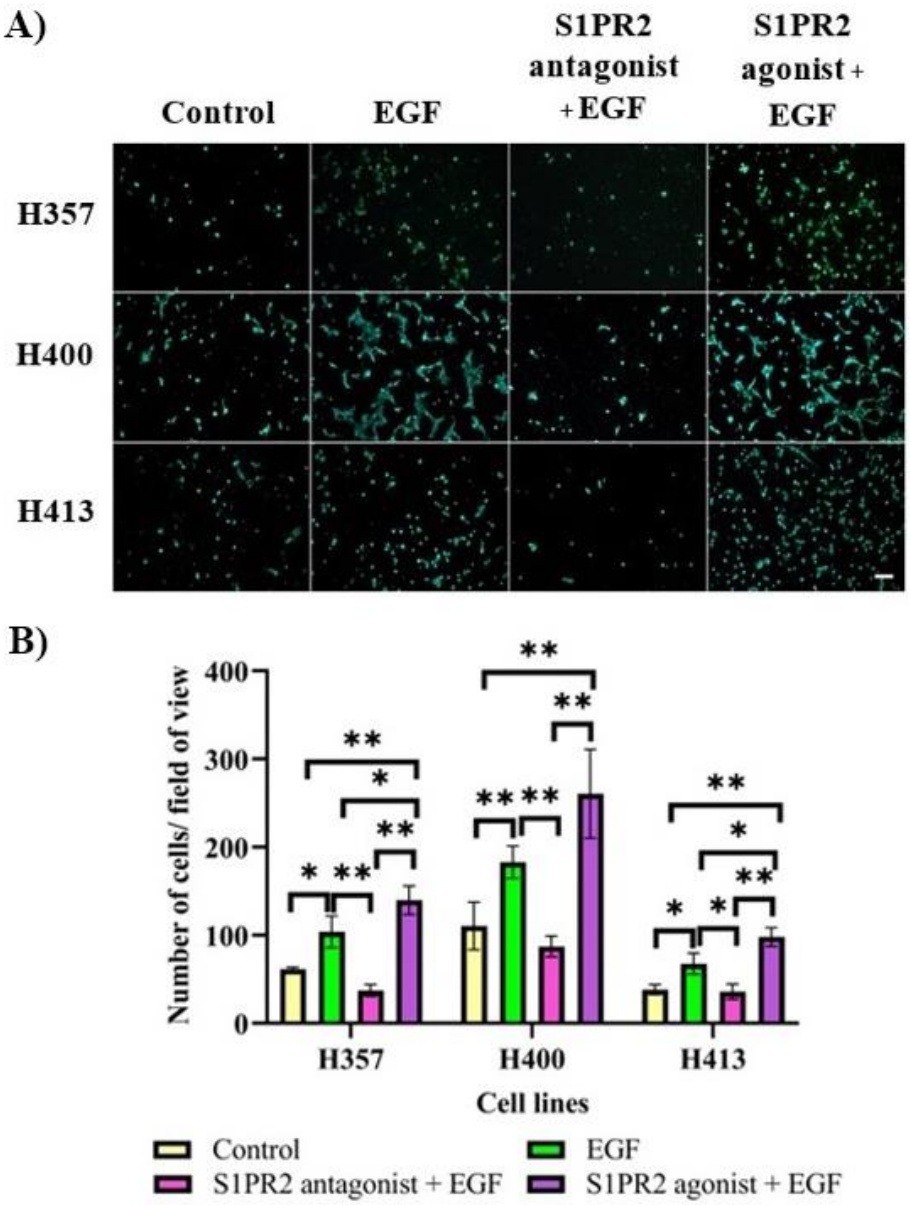

Figure 69. The effect of S1PR2 on EGF-induced migration for the three OSSC lines as determined using a transwell migration assay. **A)** Representative images captured using fluorescence microscopy of the three OSCC lines show that the number of migrated cells increased following EGF treatment. The groups treated with EGF and the S1PR2 antagonist had a smaller number of migrated cells compared with the EGF-treated group. Compared with the EGF-treated group, the addition of S1PR2 agonist increased migrated cells only in H357 and H413 cultures. (Cells were stained with calcein AM.) **B)** EGF treatment significantly increased the migration of the three cell lines. This effect was inhibited when S1PR2 was treated with an antagonist. The addition of the S1PR2 agonist to the EGF treatment increased the effect of EGF on the migration of the H357 and H413 cells but not the H400 cells. (The result of the single control treatment of S1PR2 antagonist and agonist was presented in **Figure 58**, chapter 5; Scale bar shown represents 100 μm; X10 objective lens; Three biological replicates from independent experiments were performed with N=10 for each experiment; One-way ANOVA followed by *post-hoc* Tukey test, * * = p-value < 0.05, ** = p-value < 0.01, data presented as mean ± 1 SD).

The EGF effect on migration was reduced when S1PR2 was inhibited, resulting in 37 ± 7 of migrated cells (2.8 fold reduction, $p<0.01$, One-way ANOVA). In contrast, stimulation of S1PR2 increased EGFs effect and increased the number of migrated cells to 140 ± 16, a 1.3 fold increase compared with the EGF-treated group ($p<0.05$, One-way ANOVA). EGF also promoted H400 migration, elevating the number of migrated cells from 110 ± 27 (control) to 183 ± 18, which was a 1.7 fold increase ($p<0.01$, One-way ANOVA). When S1PR2 was suppressed, the number of migrated cells was reduced to 87 ± 12 (2.1 fold lower than EGF treated group, $p<0.01$, One-way ANOVA). When S1PR2 was stimulated, the number of migrated cells was 261 ± 50, slightly higher than the group treated with EGF alone but this difference was not statistically significant. For H413 cells, the number of migrated cells was increased 1.8 fold following EGF treatment from 38 ± 6 (control) to 68 ± 12 (1.8 fold, $p<0.05$, One-way ANOVA). This increase was not observed when S1PR2 was inhibited as the number of migrated cells remained at 36 ± 9 (1.9 fold lower than the EGF treated group, $p<0.05$, One-way ANOVA). The addition of S1PR2 agonist to EGF increased the number of migrated cells to 98 ± 11, which was 1.5 fold higher than the EGF-treated group ($p<0.05$, One-way ANOVA).

6.5 Transwell invasion assay

Having established that S1PR2 affected EGF-induced migration, the study subsequently examined the role of S1PR2 on EGF-induced invasion into collagen matrices (**Figure 70**). For H357, the number of invaded cells increased from 10 ± 2 (control) to 75 ± 12 following EGF treatment (7.5 fold, $p<0.01$, One-way ANOVA). The increase following EGF treatment was not observed when S1PR2 was inactivated; the number of invading cells in this group was 7 ± 4 which was a 11.5 fold decrease from the EGF-treated group ($p<0.01$, One-way ANOVA).

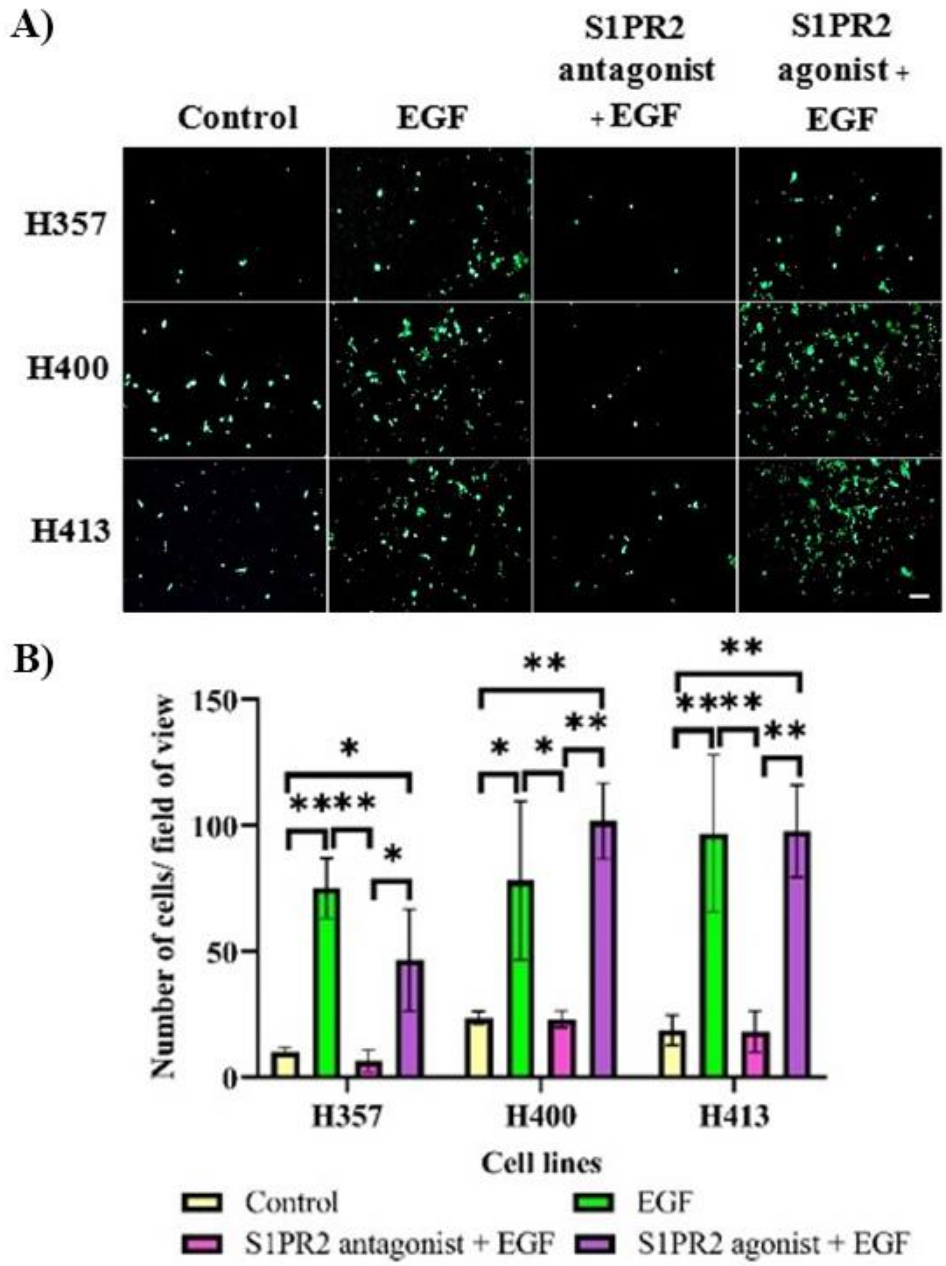

Figure 70. Transwell invasion assay used to determine the effect of S1PR2 on EGF-induced invasion. **A)** Representative images captured using fluorescence microscopy of the three OSCC lines show that the number of invading cells was elevated when the cultures were treated with EGF. The groups treated with EGF and the S1PR2 antagonist exhibited lower numbers of invading cells compared with the EGF-treated groups, while the groups treated with EGF and S1PR2 agonist were not significantly different from the EGF-treated group. (Cells were stained with calcein AM.) **B)** EGF treatment enhanced the invasion of the three cell lines, although this did not occur when S1PR2 was inactivated. When the S1PR2 agonist was added to the EGF treatment, no increase in invasion was identified. (The result of the single control treatment of S1PR2 antagonist and agonist was presented in **Figure 59**, chapter 5; Scale bar shown represented 100 μm; X10 objective lens; Three biological replicates from independent experiments were performed with N=10 for each experiment; One-way ANOVA followed by *post-hoc* Tukey test, * = p-value < 0.05, ** = p-value < 0.01, data presented as mean ± 1 SD).

Nevertheless, when combined S1PR2 agonist and EGF, the number of invaded cells (47 ± 20 cells) was reduced 1.6 fold compared with the EGF-treated group (not significant). For H400 cells, EGF also increased the number of invading cells by 3.3 fold, from 24 ± 3 (control) to 78 ± 32 ($p<0.05$, One-way ANOVA). When S1PR2 was suppressed, the number of invading cells was 23 ± 3, which was a 3.4 fold reduction compared with the EGF-treated group ($p<0.05$, One-way ANOVA). Conversely, stimulation of S1PR2 resulted in a slightly increased effect of EGF as the number of invading cells was 102 ± 15 (this was however not statistically significant compared to the EGF-treated group). For H413 cells, the number of invaded cells increased following EGF treatment from 19 ± 6 (control) to 97 ± 31 (5.1 fold, $p<0.05$, One-way ANOVA). EGF, however did not stimulate the invasion in a group where S1PR2 was suppressed, resulting in 18 ± 8 invaded cells (5.4 fold decrease from the group treated with EGF only, $p<0.01$, One-way ANOVA). The number of invaded cells in the group treated with both S1PR2 agonist and EGF for this cell line was 98 ± 19 (a similar level as found in the EGF treated group).

6.6 Multicellular tumour spheroids

The effect of S1PR2 on EGF-induced invasion was investigated using an MCTS assay. The spheroid's morphology for the three lines changed following the treatments (**Figure 71**). The details are described in **sections 6.6.1-5**. Tables with the original data are presented in the **Appendix**.

6.6.1 Analysis of the number of clusters

Appendix table XXI and **Figure 72** show that on day 1, EGF treatment appeared to increase the number of clusters in spheroids of the three cell lines, however EGF treatment did not increase the number of clusters when S1PR2 was inhibited.

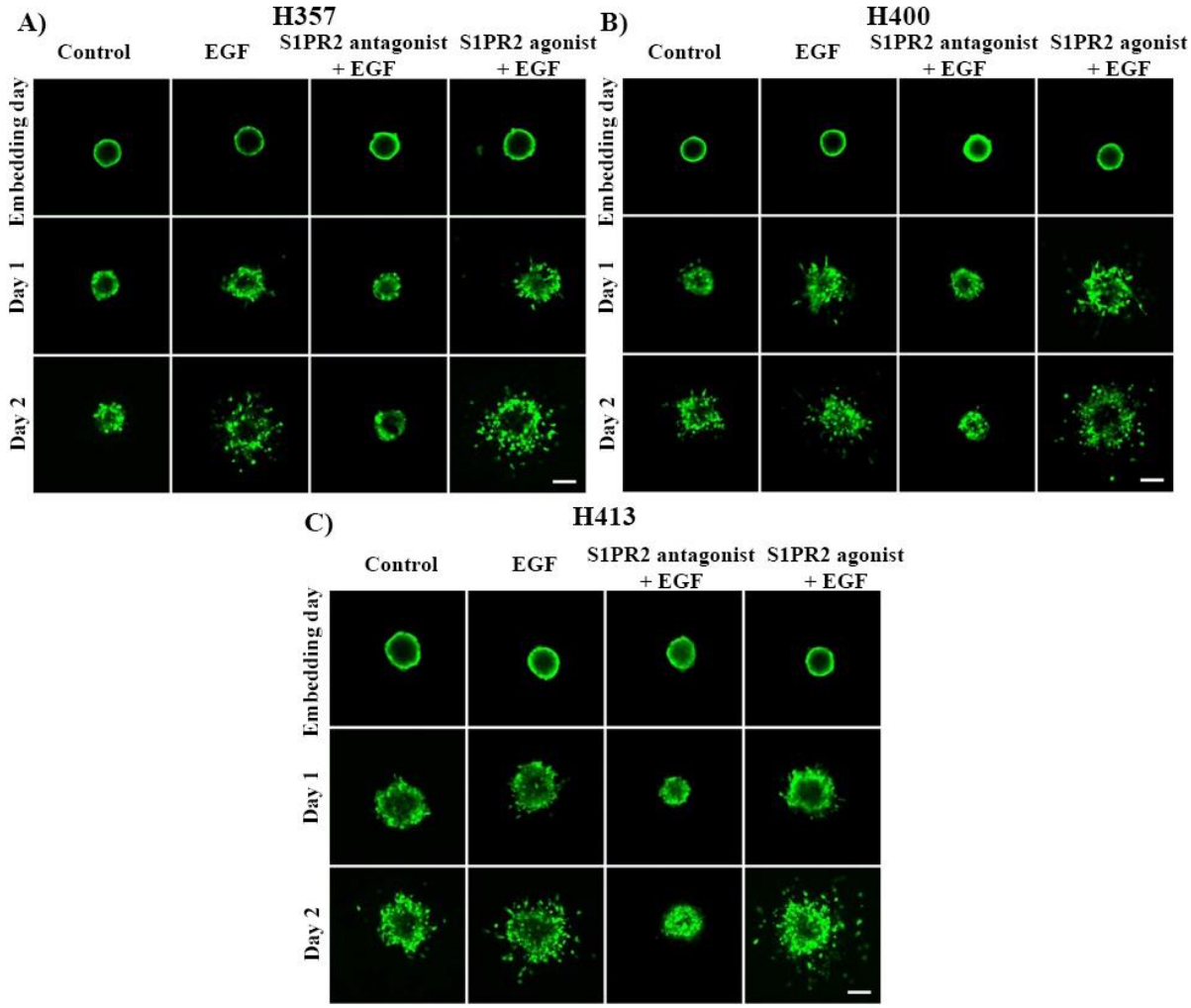

Figure 71. The effects of S1PR2 on EGF-induced invasion determined using a MCTS assay. Spheroids were embedded in 3 mg/ml collagen, inhibited proliferation with 8 µg/ml mitomycin C for 2 h and incubated in four conditions: DMEM only; DMEM containing 20 ng/ml EGF; DMEM containing 20 ng/ml EGF with either 10 µM S1PR2 antagonist or the agonist for two days. Representative confocal microscopy images of spheroids stained with calcein AM show that cells could invade into the collagen matrix more easily in the group treated with EGF compared with controls. Inhibition of S1PR2 reduced this EGF effect, while the stimulation of S1PR2 did not seem to affect it. **A)** H357 **B)** H400 and **C)** H413. The difference in the appearance of tumours spreading between the four groups was evident on day 2. The tumour cells in the EGF-treated group and the group treated with EGF and the S1PR2 agonist spread into the collagen matrix more than in the control, while the spheroids treated with the combination of EGF and the S1PR2 antagonist demonstrated limited spreading. (Images of the single control treatment of S1PR2 antagonist and agonist was presented in **Figure 60**, chapter 5; Scale bar shown represented 100 µm; X10 objective lens; Three biological replicates from independent experiments were performed with N=10 for each experiment.)

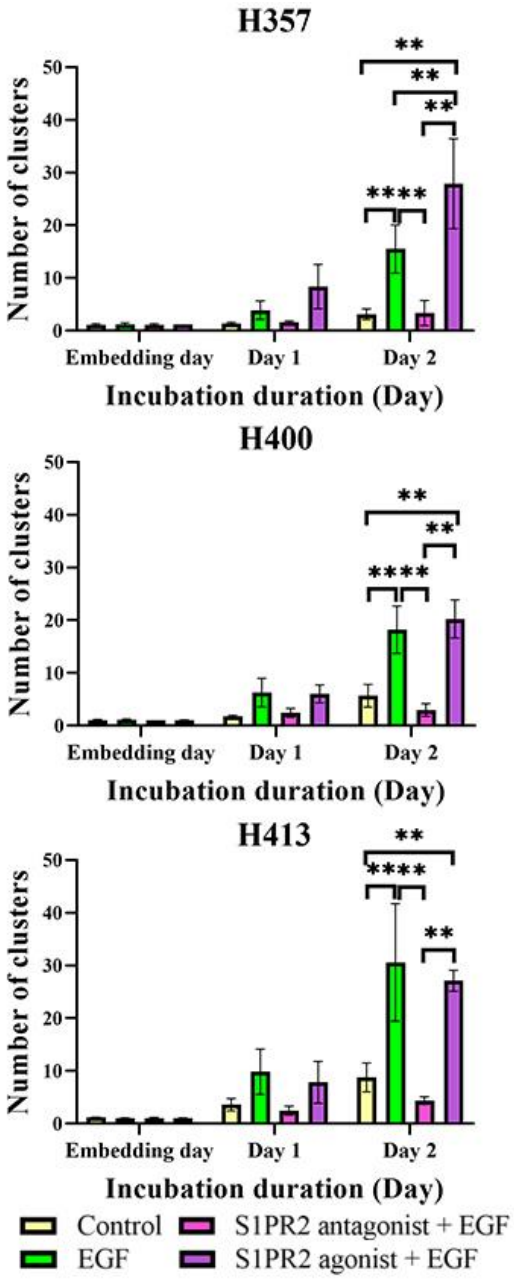

Figure 72. Effects of S1PR2 on EGF-induced increase in the number of clusters of three OSCC lines. Spheroids were generated using the hanging drop method (one day of incubation), embedded in 3 mg/ml collagen and treated with 8 µg/ml mitomycin C for 2 h before incubating with DMEM only, DMEM with 20 ng/ml EGF; and DMEM with 20 ng/ml EGF plus either 10 µM S1PR2 antagonist or DMEM with 10 µM S1PR2 agonist for two days The number of clusters for H357, H400 and H413 cells was increased following EGF treatment on day 2. This effect decreased to a similar level as the control when S1PR2 was inhibited. The combination of EGF and the S1PR2 agonist increased the number of clusters compared with the EGF treated group in H357 but not in H400 or H413 cultures. (The result of the single control treatment of S1PR2 antagonist and agonist was presented in **Figure 61**, chapter 5; Three biological replicates from independent experiments were performed with N=10 for each experiment Two-way ANOVA followed by *post-hoc* Tukey tests, ** = p-value < 0.01, data presented as mean ± 1 SD).

The group treated with the S1PR2 agonist and EGF exhibited slightly more clusters than the EGF-treated group alone in the H357 cell line. In contrast, the group treated with the S1PR2 agonist and EGF in H400 and H413 appeared to have a similar number of clusters compared with the EGF-treated group. Nevertheless, the trends observed on day 1 were not statistically significantly different.

On day 2, EGF treatment also elevated the number of clusters compared with controls by 5.3 fold in H357 cells ($p<0.01$, Two-way ANOVA). This EGF effect was decreased when S1PR2 was inhibited (5.3 fold, $p<0.01$, Two-way ANOVA). Addition of the S1PR2 agonist increased the influence of EGF by 1.8 fold ($p<0.01$, Two-way ANOVA). For H400 cells, the number of clusters elevated by 3.0 fold following EGF treatment ($p<0.01$, Two-way ANOVA). EGF did not stimulate the breakdown into clusters of this line when S1PR2 was suppressed and showed a 6.0 fold reduction compared with the EGF-treated group ($p<0.01$, Two-way ANOVA). The group treated with both the S1PR2 agonist and EGF exhibited a slightly increased number of clusters compared with the EGF-treated group but this difference was not statistically significant. In H413 cultures, the clusters increased following EGF treatment by 3.4 fold ($p<0.01$, Two-way ANOVA). Compared with the EGF-treated group, the group treated with EGF and S1PR2 antagonist resulted in a 7.8 fold reduction compared with the EGF-treated group ($p<0.01$, Two-way ANOVA), while the EGF combined with the S1PR2 agonist caused a slight reduction but this difference was not statistically significant.

6.6.2 Analysis of the maximum invading distance

The effect of S1PR2 on EGF-increased maximum invading distance are shown in **Appendix table XXII** and **Figure 73**.

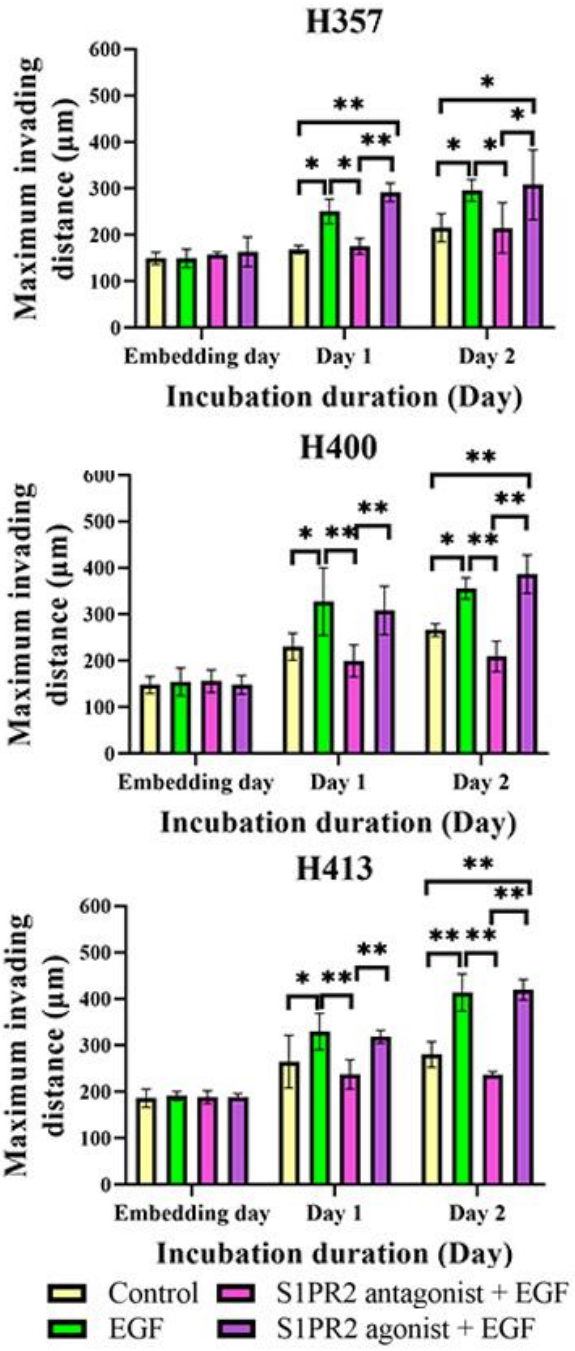

Figure 73. Effects of S1PR2 on EGF-induced maximum invading distance for H357, H400 and H413 spheroids. Spheroids were generated using the hanging drop method (one day of incubation), embedded in 3 mg/ml collagen and treated with 8 µg/ml mitomycin C for 2 h before incubating with DMEM only, DMEM with 20 ng/ml EGF; and DMEM with 20 ng/ml EGF plus either 10 µM S1PR2 antagonist or DMEM with 10 µM S1PR2 agonist for two days. The effect of EGF was reduced when S1PR2 was inhibited. However, the S1PR2 agonist did not increase the EGF-induced the maximum invading distance of three OSCC lines. (The result of the single control treatment of S1PR2 antagonist and agonist was presented in **Figure 62**, chapter 5; Three biological replicates from independent experiments were performed with N=10 for each experiment; Two-way ANOVA followed by *post-hoc* Tukey tests, * = p-value < 0.05, ** = p-value < 0.01, data presented as mean ± 1 SD).

EGF at 20 ng/ml increased the maximum invading distance of H357 cells by 1.5 fold on day 1 ($p<0.05$, Two-way ANOVA) and 1.4 fold on day 2 ($p<0.05$, Two-way ANOVA). For the treatment with the S1PR2 antagonist and EGF, the maximum invading distance was reduced 1.4 fold compared with the EGF treated group ($p<0.05$, Two-way ANOVA) on days 1 and 2. The maximum invading distance of the group treated with both the S1PR2 agonist and EGF was slightly higher than the EGF treated group but this difference was not statistically significant.

For the H400 cultures, EGF treatment resulted in a significant increase in the maximum invading distance by 1.4 fold on day 1 ($p<0.05$, Two-way ANOVA) and by 1.3 fold on day 2 ($p<0.05$, Two-way ANOVA). This effect of EGF was not noted when S1PR2 was suppressed, where a 1.6 fold and 1.7 fold reduction was observed compared with the EGF-only-treated group ($p<0.01$, Two-way ANOVA) on days 1 and 2. However, the group treated with the S1PR2 agonist and EGF did not increase the effect between EGF and S1PR2 in H400 cells as the maximum invading distance of this group was similar to the EGF-treated group.

For H413 cells, EGF treatment elevated the maximum invading distance by 1.2 fold on day 1 ($p<0.05$, Two-way ANOVA) and by 1.5 fold on day 2 ($p<0.01$, Two-way ANOVA). When treated with EGF and the S1PR2 antagonist, the maximum invading distance of this group was 1.4 fold and 1.7 fold less than the group treated with EGF ($p<0.01$, Two-way ANOVA) on days 1 and 2. The group treated with both EGF and the S1PR2 agonist provided a slightly higher maximum invading distance compared with the EGF-treated group on both days 1 and 2, however this increase was not statistically significant.

6.6.3 Analysis of the circularity of the main cluster

Appendix table XXIII and **Figure 74** show that EGF treatment significantly reduced the circularity of the main cluster of spheroids for H357 cultures on both days 1 and 2 ($p<0.01$, Two-way ANOVA). The addition of the S1PR2 antagonist slightly reduced this effect on day 1 (statistically lower than the control but not significantly different from the EGF treated group). On day 2, the addition of the S1PR2 antagonist caused a significantly higher circularity than the EGF-treated group ($p<0.01$, Two-way ANOVA). The combination of EGF and S1PR2 agonist induced a slight reduction in circularity on both days 1 and 2, but these differences were not statistically significant when compared with the EGF-treated group.

For H400, the stimulation of EGF resulted in the reduction of circularity of the main cluster on both days 1 and 2 ($p<0.01$, Two-way ANOVA). However, the circularity of the group treated with EGF and the S1PR2 antagonist did not decrease as much as the EGF-treated group ($p<0.05$ on day 1; $p<0.01$ on day 2, Two-way ANOVA), which indicated the EGF effect was suppressed. The circularity of the group treated with EGF and the S1PR2 agonist was not statistically different from those observed in the group treated with EGF only on either day, implying that the stimulation of S1PR2 did not elevate the effect of EGF.

EGF treatment resulted in a reduction of circularity for H413 spheroids on day 1 and day 2 ($p<0.01$, Two-way ANOVA). This EGF effect on circularity was not observed when EGF treatment was combined with an S1PR2 antagonist. The circularity of this group (EGF with S1PR2 antagonist) was higher than the EGF-treated group ($p<0.01$, Two-way ANOVA). The S1PR2 agonist did not alter the effect of EGF on the circularity of the spheroids.

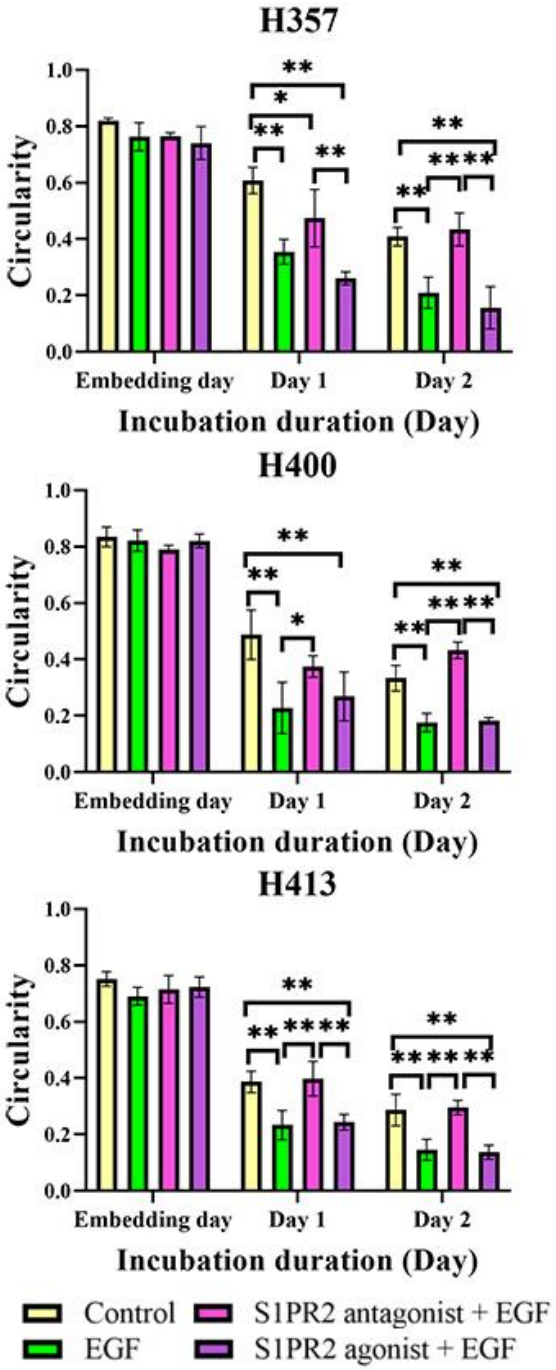

Figure 74. Effects of S1PR2 on EGF-reduced circularity for H357, H400 and H413. Spheroids were generated using the hanging drop method (one day of incubation), embedded in 3 mg/ml collagen and treated with 8 µg/ml mitomycin C for 2 h before incubating with DMEM only, DMEM with 20 ng/ml EGF; and DMEM with 20 ng/ml EGF plus either 10 µM S1PR2 antagonist or DMEM with 10 µM S1PR2 agonist for two days. EGF reduced the circularity of spheroids on both days 1 and 2 in the three OSCC lines. This morphological change of the main cluster was suppressed by inhibiting S1PR2 function with the antagonist compound. Adding the S1PR2 agonist did not significantly reduce the circularity of the spheroid. (The result of the single control treatment of S1PR2 antagonist and agonist was presented in **Figure 63**, chapter 5; Three biological replicates from independent experiments were performed with N=10 for each experiment; Two-way ANOVA followed by *post-hoc* Tukey tests, * = p-value < 0.05, ** = p-value < 0.01, data presented as mean ± 1 SD).

6.6.4 Analysis of the fractal dimension of the main cluster

Appendix table XXIV and **Figure 75** illustrate the effect of S1PR2 on the fractal dimension of the main cluster. On day 1, no statistical difference was observed between the four groups of three lines. On day 2, EGF slightly increased the fractal dimension for H357 cells but this was not a statistically significant increase. Compared with the EGF-treated group, addition of the S1PR2 antagonist reduced the fractal dimension, while the addition of the S1PR2 agonist caused an increase, however these values were not significantly different. For H400 cells, EGF significantly elevated the fractal dimension ($p<0.01$, Two-way ANOVA) but this effect of EGF was statistically reduced following the addition of the S1PR2 antagonist ($p<0.05$, Two-way ANOVA). The group treated with EGF and the S1PR2 agonist had a similar fractal dimension as the EGF treated group, which indicated that there was no increase in effect when combining EGF with S1PR2 agonist. For H413 cultures, EGF significantly increased the fractal dimension ($p<0.01$, Two-way ANOVA). This value was slightly decreased when S1PR2 was suppressed (not statistically significant when compared with the group treated with EGF only). As observed in the H400 cultures, stimulation of S1PR2 did not increase the fractal dimension of H413 cells compared with the EGF-treated group.

6.6.5 Analysis of the maximum diameter of the main cluster (MDMC)

Appendix table XXV and **Figure 76** illustrate that EGF at 20 ng/ml increased the MDMC of H357 by 1.4 fold on day 1 and by 1.3 fold on day 2 ($p<0.01$, Two-way ANOVA). This effect of EGF was not observed when the treatment contained the antagonist, as the MDMC of this group was reduced 1.4 fold and 1.3 fold compared with the EGF-treated cultures on both days 1 and 2, respectively ($p<0.01$, Two-way ANOVA).

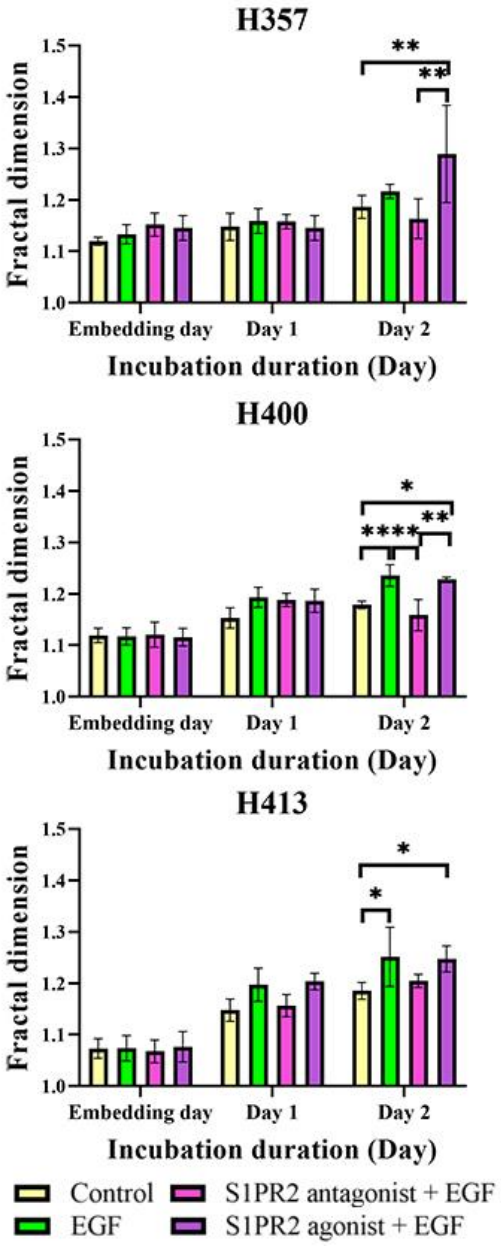

Figure 75. Effects of S1PR2 on EGF-induced complexity of the invading spheroid as determined by the fractal dimension of the boundaries. Spheroids were generated using the hanging drop method (one day of incubation), embedded in 3 mg/ml collagen and treated with 8 µg/ml mitomycin C for 2 h before incubating with DMEM only, DMEM with 20 ng/ml EGF; and DMEM with 20 ng/ml EGF plus either 10 µM S1PR2 antagonist or DMEM with 10 µM S1PR2 agonist for two days. For H357 cultures, the group treated with the combination of S1PR2 agonist and EGF had a higher fractal dimension than the control. For H400 and H413 cells, EGF treatment elevated the fractal dimension, but it did not exert this effect when S1PR2 was treated with the antagonist. The addition of the S1PR2 agonist did not appear to alter the effect of EGF. (The result of the single control treatment of S1PR2 antagonist and agonist was presented in **Figure 64**, chapter 5; Three biological replicates from independent experiments were performed with N=10 for each experiment; Two-way ANOVA followed by *post-hoc* Tukey tests, * = p-value < 0.05, ** = p-value < 0.01, data presented as mean ± 1 SD).

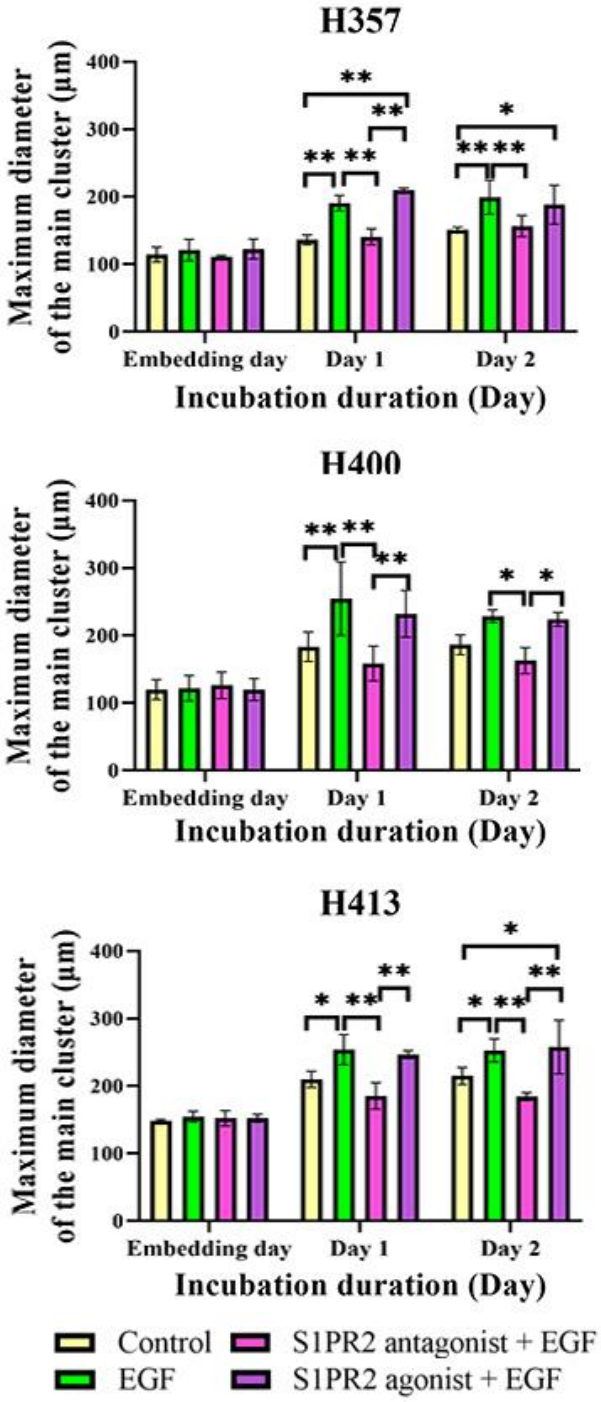

Figure 76. Effects of S1PR2 on EGF-induced MDMC in the three OSCC lines. Spheroids were generated using the hanging drop method (one day of incubation), embedded in 3 mg/ml collagen and treated with 8 µg/ml mitomycin C for 2 h before incubating with DMEM only, DMEM with 20 ng/ml EGF; and DMEM with 20 ng/ml EGF plus either 10 µM S1PR2 antagonist or DMEM with 10 µM S1PR2 agonist for two days. EGF increased the MDMC of H357, H400 and H413 cells on both days 1 and 2. The antagonist reduced the effect of EGF, however when the S1PR2 agonist with EGF were combined, no increase in effect was observed. (The result of the single control treatment of S1PR2 antagonist and agonist was presented in **Figure 65**, chapter 5; Three biological replicates from independent experiments were performed with N=10 for each experiment; Two-way ANOVA followed by *post-hoc* Tukey tests, * = p-value < 0.05, ** = p-value < 0.01, data presented as mean ± 1 SD).

The MDMC of H357 cells treated with both EGF and the S1PR2 agonist was not statistically different from the group treated with EGF alone on both days.

On day 1, treating H400 spheroids with EGF resulted in the elevation of MDMC by 1.4 fold compared with controls ($p<0.01$, Two-way ANOVA). Inhibition of S1PR2 decreased the effect of EGF on the MDMC (1.6 fold decrease from the EGF treated group, $p<0.01$, Two-way ANOVA), while the addition of the S1PR2 agonist to the EGF treatment did not enhance the EGF-induced MDMC effect. On day 2, EGF slightly elevated the MDMC compared with the control, but this difference was not significant. The addition of the S1PR2 antagonist decreased the MDMC to lower than that detected in EGF treated group (1.4 fold reduction, $p<0.05$, Two-way ANOVA). No statistical difference was observed between the EGF treated group and the group treated with the S1PR2 agonist and EGF.

For H413 cultures, the MDMC of the EGF-treated group was higher than the control by 1.2 fold on days 1 and 2 ($p<0.05$, Two-way ANOVA). Suppression of S1PR2 with the antagonist significantly reduced the MDMC (1.4 fold) compared with the EGF-treated group on days 1 and 2 ($p<0.01$, Two-way ANOVA). Again, the addition of the S1PR2 agonist to the EGF treatment did not appear to elevate the effect as the MDMC of this group was statistically similar to the EGF-only treated group on both days.

6.7 Matrix metalloproteinases expression

Having established the requirement for S1PR2 in EGF-induced migration and invasion, subsequently, the study investigated the involvement of S1PR2 in EGF-induced *MMP2* and *MMP9* expression. **Figure 77A** shows that EGF increased *MMP2* expression 4.0 fold in H357 ($p<0.05$, One-way ANOVA). The increase in *MMP2* expression was also observed in the group treated with the combination of EGF and the S1PR2 antagonist (4.3 fold, $p<0.05$, One-way ANOVA) and the group treated with EGF and the S1PR2 agonist (4.7 fold, $p<0.01$, One-way ANOVA) when compared with controls.

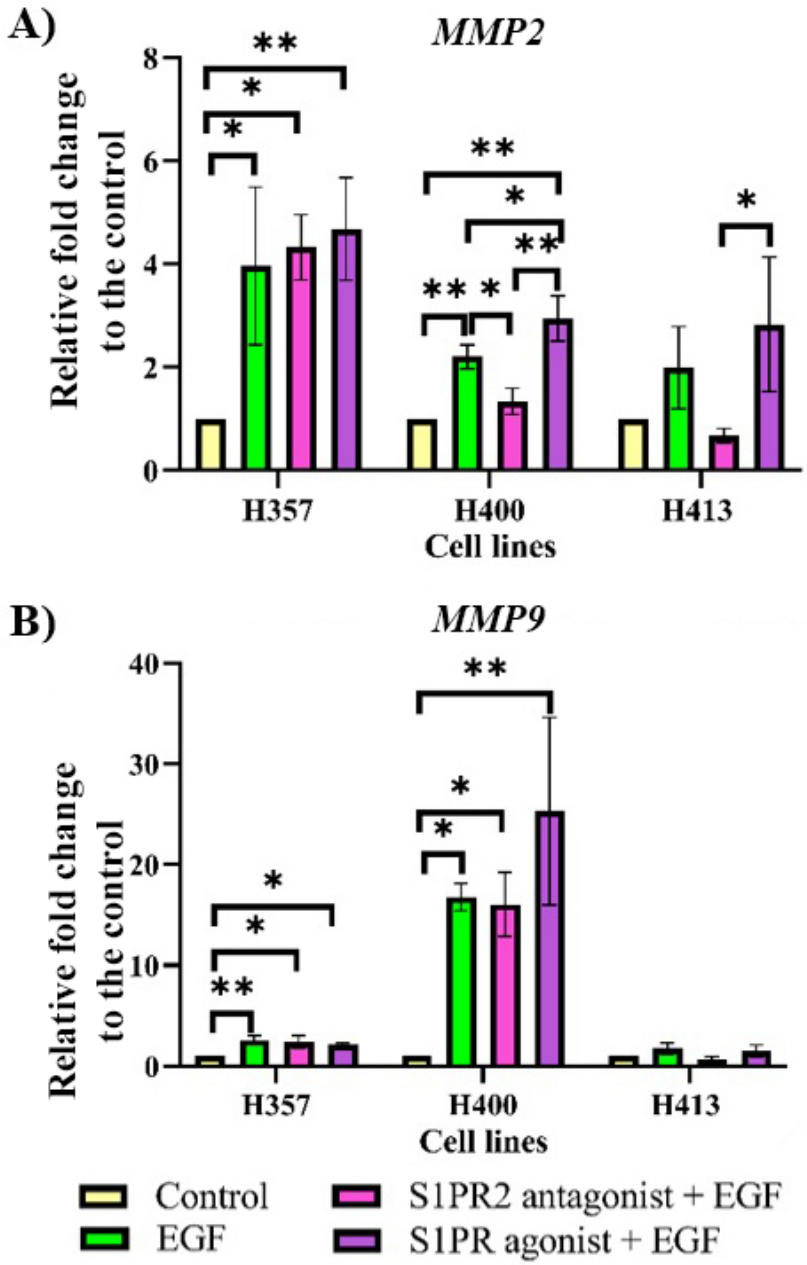

Figure 77. Real time-PCR analysis determining the effect of S1PR2 on EGF-induced *MMP2* and *MMP9* expression, 48 h of incubation. The results were normalized to the housekeeping gene and then were presented as a relative fold change to the control. **A)** EGF promoted *MMP2* expression on H357. Both S1PR2 antagonist and agonist increased the effect of EGF, but not significantly. EGF also induced *MMP2* expression in H400 cells. EGF-induced *MMP2* gene upregulation was decreased when S1PR2 was inhibited but was increased when S1PR2 was stimulated. H413 exhibited the same trend as H400 cells, but the differences were not statistically significant. **B)** EGF upregulated *MMP9* in H357 and H400 cultures. These data indicated that the effect did not involve the regulation of S1PR2. (The result of the single control treatment of S1PR2 antagonist and agonist was presented in **Figure 66**, chapter 5; Three biological replicates from independent experiments with each experiment was the average of two technical replicates; One-way ANOVA followed by *post-hoc* Tukey tests, * = p-value < 0.05, ** = p-value < 0.01, data presented as mean ± 1 SD).

However, differences in the level of *MMP2* expression were not noted between the EGF treated group, the EGF with S1PR2 antagonist group, and the EGF with S1PR2 agonist group. For H400 cultures, the *MMP2* gene was upregulated 2.2 fold following EGF treatment. When S1PR2 was inhibited, *MMP2* expression was reduced 1.6 fold compared with the EGF-treated group ($p<0.05$, One-way ANOVA) and when S1PR2 was stimulated, *MMP2* expression was elevated 1.3 fold ($p<0.05$, One-way ANOVA). For H413 cells, EGF increased *MMP2* expression by 2.0 fold compared with controls and when S1PR2 was inhibited the expression decreased 2.5 fold compared with the EGF-treated group. Addition of the S1PR2 agonist increased EGF-induced *MMP2* expression by 1.4 fold compared with the EGF-treated group although these differences were not statistically significant.

Figure 77B shows that EGF increased the expression of *MMP9* in H357 cultures by 2.6 fold. Again, both the S1PR2 antagonist and agonist increased the EGF-induced *MMP9* expression, but this was not statistically significant. For H400 cultures, EGF caused a 16.8 fold upregulation of the *MMP9* gene compared with the control. The relative increase compared with the control was also observed following inhibition and stimulation of S1PR2. No statistical difference was observed between the groups treated with EGF, EGF with the S1PR2 antagonist and EGF with the S1PR2 agonist in both H357 and H400. For H413 cultures, EGF treatment elevated the *MMP9* expression 1.8 fold compared with the control. When S1PR2 was inhibited, the expression of *MMP9* was reduced 2.5 fold compared with the EGF treated group. However, the effect of EGF on *MMP9* expression did not change following the addition of the S1PR2 agonist. The trends in *MMP9* expression in H413 cultures appeared similar to those observed for *MMP2* expression and the differences were not statistically significant.

6.8 Effects of EGF/EGF receptors and S1P/S1PR2 on Rac1 activity

The above results suggested that S1PR2 was required for EGF-induced migration and invasion and therefore, the involvement of Rac1 was further investigated using the G-LISA assay. In this experiment, cultures of the three OSCC lines were pretreated with S1PR2 antagonist and agonist for 15 min before the introduction of EGF treatment to ensure that S1PR2 was entirely inhibited (Szczepaniak *et al.*, 2010). **Figure 78** shows that stimulation of three cell lines with the S1PR2 antagonist or the S1PR2 agonist for 15 min did not affect the activity of Rac1. A significant increase of Rac1 activity was observed following EGF treatment for 2 min: a 3.2 fold increase in Rac1 activity relative to controls in H357 ($p<0.01$, One-way ANOVA); a 1.8 fold increase in H400 ($p<0.05$, One-way ANOVA) and a 4.2 fold in H413 ($p<0.01$, One-way ANOVA) cultures. This effect, however, was not observed when the three OSCC cultures were pre-treated with the S1PR2 antagonist before receiving EGF treatment. The group treated with EGF following the S1PR2 agonist had higher Rac1 activity compared with the group treated with the S1PR2 agonist alone by 2.7 fold in H357, by 1.9 fold in H400 and by 4.6 fold in H413 cultures ($p<0.01$, One-way ANOVA). Nevertheless, no statistical difference was noted between groups treated with EGF alone and EGF with the S1PR2 agonist. This implied a requirement of S1PR2 for Rac1 activation, and that EGF was the main molecule responsible for stimulating Rac1 activity.

6.9 Determination of crosstalk between S1P/S1PR2 and EGF/EGF receptors

The above data showed that S1PR2 was involved in EGF-induced motility of H357, H400 and H413 cells. Therefore, a potential crosstalk between S1P/S1PR2 and EGF/EGF receptors signalling pathway was further investigated. The three cell lines were treated with either the S1PR2 antagonist or agonist for 48 h and the production of EGF and TGF-β1 (two growth factors that preferentially bind to EGF receptors) was assayed in supernatants.

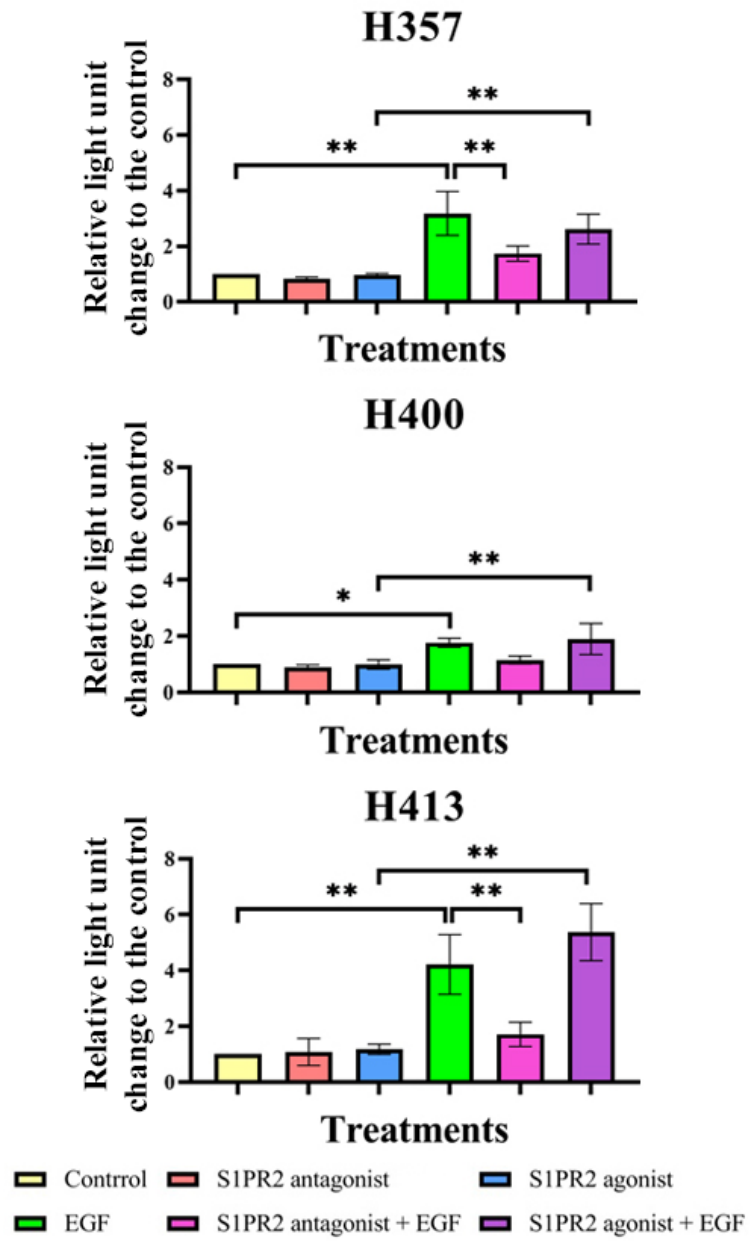

Figure 78. G-LISA analysis determining Rac1 activity of three OSCC lines following either EGF or S1PR2 treatments. Measured luminescence of each sample were normalised to the control. A similar pattern was found between three cell lines. A significant change in Rac1 activity was not identified when cells were treated with either the S1PR2 antagonist or the S1PR2 agonist alone. EGF treatment statistically increased Rac1 activity. This effect was suppressed when EGF was combined with the S1PR2 antagonist but did not increase when combined EGF with S1PR2 agonist. (Three biological replicates from independent experiments with each experiment was the average of two technical replicates; One-way ANOVA followed by *post-hoc* Tukey tests, * = p-value < 0.05, ** = p-value < 0.01, data presented as mean ± 1 SD).

Figure 79 shows that the baseline of EGF and TGF-β1 production by the three cell lines was at the picogram level. No significant change in the production of these two growth factors was identified following either S1PR2 antagonist or agonist treatments. Subsequently, the study indirectly determined the effect of EGF on S1P production through the expression of *SPHK1* and *SPHK2*, two enzymes that convert sphingosine into S1P. The *SPHK1* gene in the three cell lines was marginally upregulated following 1 ng/ml EGF treatment (3.8 fold in H357, 1.6 fold in H400 and 2.7 fold in H413 cells). However, this upregulation was not statistically significant. *SPHK1* expression in the three cell lines significantly increased when treated with 20 ng/ml of EGF compared with controls (9.6 fold in H357, 4.6 fold in H400 and 13.8 fold in H413 cells, $p<0.01$, One-way ANOVA) (**Figure 80A**). *SPHK2* expression was not affected by EGF treatment (**Figure 80B**).

6.10 Conclusion

The inhibition of S1PR2 suppressed EGF-induced migration and invasion in the three OSCC lines, indicating the S1P/S1PR2 pathway could control the EGF/EGF receptors pathway. Rac1 activity was stimulated by EGF/EGF receptors rather than S1P/S1PR2, but Rac1 could not be activated without the control of S1PR2. EGF/EGF receptors and S1P/S1PR2 pathway showed crosstalk at the metabolic level. EGF upregulated only the *SPHK1* gene of the three OSCC lines according to concentration, but the S1PR2 inhibition and stimulation did not affect EGF production.

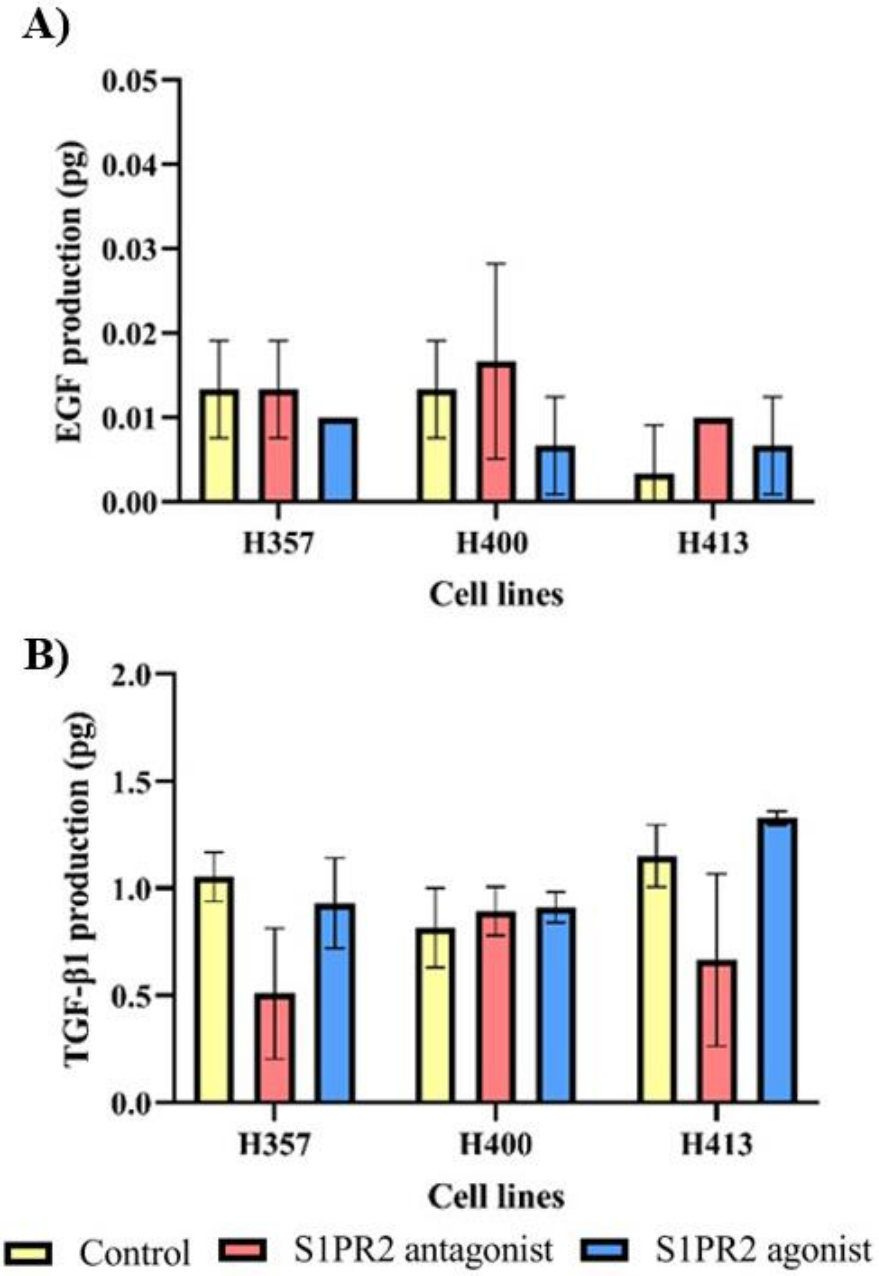

Figure 79. ELISA, determining the effect of S1PR2 on **A)** EGF and **B)** TGF-β1 production. Neither S1PR2 inhibition nor stimulation affected the production of EGF and TGF-β1 of H357, H400 and H413. (Three biological replicates from independent experiments with each experiment was the average of two technical replicates; One-way ANOVA followed by *post-hoc* Tukey tests, data presented as mean ± 1 SD).

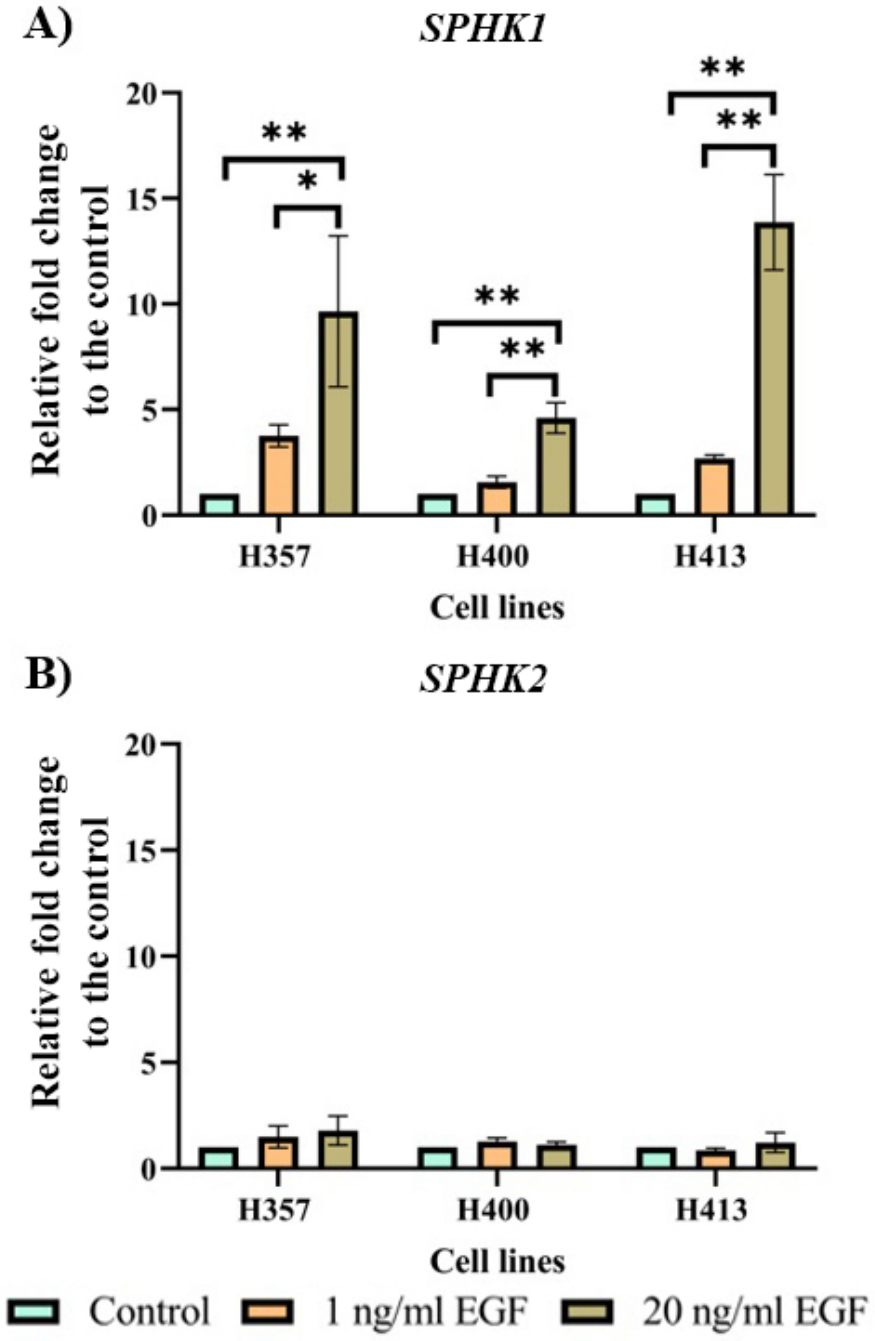

Figure 80. Real time-PCR analysis determining the effect of 1 ng/ml and 20 ng/ml EGF on *SPHK1* and *SPHK2* expression, 48 h of incubation. The results were normalized to the housekeeping gene and then were presented as a relative fold change to the control. **A)** Expression of *SPHK1* significantly increased following EGF treatment at 20 ng/ml. **B)** The expression of *SPHK2* was not affected by any of the two concentrations of EGF. (Three biological replicates from independent experiments with each experiment was the average of two technical replicates; One way ANOVA followed by *post-hoc* Tukey tests, * = p-value < 0.05, ** = p-value < 0.01, data presented as mean ± 1 SD).

Chapter 7: Discussion

Metastasis is the major cause of death in cancer patients (Ganjre *et al.*, 2017). For this reason, preventing cancer invasion, a preliminary step of metastasis, might help reduce death rates in cancer patients and become a promising treatment (Veiseh *et al.*, 2011). Until now, numerous molecules and receptors have been shown to be involved in cellular motility. Two relevant axes that have been the subject of investigation include EGF/EGF receptors (Patel *et al.*, 2007, Gandy *et al.*, 2013, Islam *et al.*, 2017, Ohnishi *et al.*, 2017) and S1P/S1PR2 (Lepley *et al.*, 2005, Takuwa *et al.*, 2011, Patmanathan *et al.*, 2016, Pang *et al.*, 2020). For this reason, this study aimed to investigate the effect of EGF/EGF receptors and S1P/S1PR2 on migration and invasion of three OSCC lines, as well as the coordination and interactions between these two pathways in controlling cell motility.

7.1 *EGF*, *EGFR* and *S1PR*s expression

This study characterised the baseline proliferation, migration and expression of *EGF* and *S1PR2* in H357, H400 and H413 OSCC cell lines. sq-RT PCR showed that the three OSCC lines expressed the EGFR gene, although EGF could not be detected with either sq-RT PCR or ELISA (EGF production at the picogram level was below the detection limit of the assay). This agreed with a previous study (Prime *et al.*, 1994) using eight OSCC lines (including the three cell lines investigated here) that these cell lines expressed EGFR but did not express EGF. The same study also reported that among the eight OSCC lines, H413 had the highest total cell-surface *EGFR* expression (the only line which overexpressed EGFR relative to normal keratinocytes), followed by H357 and H400. However, the present study detected similar levels of *EGFR* expression in all three cell lines, so the signal from exogenous EGF binding to EGFR in the three lines would be the same.

Next, this study investigated the expression of five *S1PR* genes in three OSCC lines. While *S1PR2* had been reported to be expressed in most types of tissue, some cells such as

Hodgkin/Reed-Sternberg cells (Vrzalikova *et al.*, 2018), T lymphocytes (Jin *et al.*, 2003) and HUVEC (an endothelial cell line) (Ruiz *et al.*, 2017) lack expression of this receptor. Other studies showed overlapping functions between S1PR subtypes (Tanimoto *et al.*, 2004, Young & Van Brocklyn, 2007). Considered together, this raised the possibility that the behaviour of OSCC could be controlled by other S1PR types rather than just S1PR2. The present study confirmed that all three cell lines expressed *S1PR1* to *5*. The results from the three OSCC lines were consistent with a study using OSCC lines, where three or more S1PRs were highly expressed (Patmanathan *et al.*, 2016), but differed from those of a human oesophageal cancer study, where *S1PR2* had relatively lower expression levels compared with the other subtypes, except for *S1PR4*, which was absent (Hu *et al.*, 2010). The present results also supported the possibility that different cell lines have different patterns of *S1PR* expression. Since each S1PR subtype might regulate different aspects of cellular activity, those relative differences in receptor subtype expression may be one of the reasons for the differences in behaviour between cell lines.

7.2 Cell proliferation

Proliferation is an essential characteristic of cancer development and progression (Feitelson *et al.*, 2015), but it also makes it difficult to interpret data in some tumour invasion models. For example, the increase in cell number in the collagen matrix due to growth may appear similar to cell invasion in the MCTS assay (discussed later). Therefore, this study also considered differences in growth rates between the OSCC lines as well as the growth response following EGF and S1PR2 treatments.

7.2.1 Comparison of proliferative profiles

H357, H400 and H413 cells have been used in a variety of studies (Prime *et al.*, 1994, Dorrego, 2004, Prime *et al.*, 2004, Patmanathan *et al.*, 2016, Halah, 2018, Celentano *et al.*, 2021), however data comparing the proliferation of these lines have been limited. The present study showed that the growth rate of H357 cells was lower than the other two cell lines, whereas there were no statistical differences between H400 and H413 cells. This appeared to disagree with a previous study (Dorrego, 2004) that determined growth using the MTS assay (an assay for determining the metabolic activity of cells using a tetrazolium salt, 3-(4,5-dimethylthiazol-2-yl)-5-(3-carboxymethoxyphenyl)-2-(4-sulfophenyl)-2H-tetrazolium). Of the eight OSCC lines investigated in Dorrego's study, at 72 hours, H400 had the slowest proliferation, followed by H413 and H357. The present study's proliferation data were more similar to a study by Halah (2018) which determined the percentage of positive nuclei (PPN) after Ki67 staining. In Halah's study, the PPN (~47%) of H357 cells was significantly lower than in the other eight OSCC cell lines (including H400 and H413), while the PPN of H400 (~92%) was higher than that of H413 (~66%) (percentage figures estimated from the published thesis graphs). This led to the conclusion that some differences between studies may be due to the different techniques used. Although doubling time, the BrdU assay, the MTS assay and Ki67 staining have been widely used to determine growth, these all assess different aspects of proliferation. The present study used doubling time and the BrdU assay (a measure of the amount of newly synthesised DNA) (Mead & Lefebvre, 2014). These assays may be more closely related to nuclear expression of Ki67 during the cell cycle. In contrast, the MTS assay which is similar to the MTT assay, measures metabolic activity instead of cell division and thus are not a direct measure of growth rate (Wang *et al.*, 2010). For example, a cell line with low proliferation but high metabolic activity (*e.g.* cells that have received cytotoxic treatments or doses of radiation) may generate similar results to those obtained from cell lines with high

proliferation but low metabolic activity (Ghasemi *et al.*, 2021). To emphasise this, a review (Coller, 2019) showed that embryonic stem cells (high proliferation rate cells) seemed to have similar level of metabolic activity to adult stem cells (usually seen in haematopoietic tissue) which were quiescent. These adult stem cells had high glycolytic activity to prevent epigenetic marks to induce proliferation or lineage commitment and provided an example where metabolic activity and proliferation were not directly linked. However, whether this hypothesis applies to these OSCC lines remains to be substantiated as the metabolic activity and proliferation rate has not been compared between each of the cell lines.

7.2.2 The effect of EGF on cell proliferation

This study showed how the growth of the three OSCC lines was affected by EGF. The proliferation of H357 and H413 cells was enhanced following 1 ng/ml EGF treatment but was inhibited at 20 ng/ml. In contrast, growth of H400 cells was inhibited by both EGF concentrations when compared with the controls. Previous studies showed that EGF could either stimulate or inhibit cell growth, depending on the type of epithelial cell line and concentrations used (Kawamoto *et al.*, 1984, Cowley *et al.*, 1986, Kamata *et al.*, 1986, Prime *et al.*, 1994). OSCC lines therefore are understood to exhibit biphasic behaviour: at low concentrations (<10 ng/ml) EGF stimulated proliferation, whereas, at higher concentrations (>10 ng/ml) it had an inhibitory effect (Kawamoto *et al.*, 1984, Cowley *et al.*, 1986, Prime *et al.*, 1994) which was suggested to be related to the existence of different subtypes of EGF receptors. According to the affinity of EGF binding, the receptors were classified into high- and low-affinity subtypes. The high-affinity subtype was responsible for growth stimulation, while the low-affinity was responsible for growth inhibition (Kawamoto *et al.*, 1984). While some OSCC lines were reported to express different ratios of these two subtypes (Prime *et al.*, 1994), not all squamous cell carcinomas (SCC) lines exhibited this biphasic response. A study

using 15 human SCC lines (5 of these were OSCC lines) reported that EGF concentrations from 0.1 ng/ml to 100 ng/ml inhibited growth in a dose-dependent manner (Kamata *et al.*, 1986). Taken together, this implies that the response to EGF did not only depend on the type of cancer cells (cells from different tissue) but also depend on the type of cell lines (same cell types, but derived from different patients *e.g.* H357, H400 and H413).The alteration of growth rate in response to EGF of OSCC lines were noted to vary between studies (Kawamoto *et al.*, 1984, Cowley *et al.*, 1986, Kamata *et al.*, 1986, Prime *et al.*, 1994). The variation between the three lines in the present study may therefore be explained by the tumour heterogeneity theory (cells within a tumour exhibiting different phenotypic and genotypic features) (Dagogo-Jack & Shaw, 2018) for two reasons. First, the cell lines were derived from different patients (inter-tumoural heterogeneity), therefore patient-specific factors including germline genetic variation, differences in somatic mutation profiles and environmental factors, could influence cancer characteristics. Second, the cell lines were derived from different anatomical areas: H357 was from the tongue, H400 was from the alveolar process and H413 was from buccal mucosa. Since the epithelium at each location has typically different characteristics, it would be reasonable to speculate that tumours derived from those tissues might exhibit different molecular expression profiles which influence cell behaviour.

The present study used the same cell lines described by Prime *et al*. (1994) and while H357 and H413 showed the same response to EGF as identified by Prime's study, H400 cells did not. The rounded morphology of H400 cells after the two EGF treatments suggested loss of attachment from the substrate, which was similar to the results from a previous study (Lu *et al.*, 2001). In that study after treating breast carcinoma cells and OSCC cells with 100 ng/ml EGF, the activity of tyrosine-phosphorylated protein (focal adhesion kinase or FAK) was suppressed, causing a refractile morphology of cells, detachment from the ECM, as well as promotion of cellular motility. Also, in the present study, some cells developed protrusions,

implying migration (De Donatis *et al.*, 2010). This difference may be due to the cell line authentication. H400 cells used at the School of Dentistry were a kind gift, from Professor Stephen Prime, University of Bristol**.** The present study did not perform authentication testing, so it is not possible to confirm whether the frozen cell lines stored in the lab were identical to the H400 cells in Prime's original study. Another possible explanation for the differences in results from those of Prime *et al*. (1994) is related to the higher passage number used compared with the original study. A high passage number may result in genotypic and phenotypic divergence and altered the number of each EGFR subtype (Prime *et al.*, 1994). This study neither investigated whether the effect of EGF specifically resulted from which type of EGF receptor (EGFR and ErbB2-4) and which subtype of EGFR (high affinity- or low-affinity EGFR) nor monitored changes in the ratio of these receptors or receptor subtype when the passage number increased and therefore this possibility cannot be substantiated.

7.2.3 The effect of S1PR2 on cell proliferation

In addition to EGF, S1PR2 is reported to be involved in the control of proliferation (Young & Van Brocklyn, 2007, Du *et al.*, 2010, Petti *et al.*, 2020). This study investigated its effects on growth in the three OSCC lines and represented the first investigation of S1PR2 effects on the mitogenic activity of OSCC. Data from growth curves and BrdU assay showed that 10 μM S1PR2 antagonist reduced proliferation by 1.5 - 2.7 fold compared with the control, but the S1PR2 agonist at the same concentration did not affect proliferation in three OSCC lines.

Unlike EGF, the effect of S1PR2 on proliferation appeared to vary and it has been reported to either suppress growth (as reported in the majority of cell types) (Du *et al.*, 2010, Price *et al.*, 2015, Petti *et al.*, 2020) or promote growth (Cheng *et al.*, 2018). The different roles of S1PR2 could be explained by the interaction of SIPR2 with the protein kinase B (Akt) pathway (the serine/threonine kinase family) since the activation of S1PR2 could lead to phosphorylation

(Beckham *et al.*, 2013) or dephosphorylation of Akt (Schüppel *et al.*, 2008, Takuwa *et al.*, 2011, Petti *et al.*, 2020). As Akt was shown to be responsible for growth stimulation (Xu *et al.*, 2012), the activation of S1PR2 could either promote or suppress proliferation. Another explanation of the S1PR2 involvement in growth was through the Hippo pathway (Miller *et al.*, 2012, Yu *et al.*, 2012) where S1PR2 activated Ras homolog family member A (RhoA) through Gα12/13, resulting in the stimulation of downstream effectors of the Hippo pathway termed Yes-associated protein (YAP) and the transcriptional coactivator with PDZ-binding motif (TAZ) (Miller *et al.*, 2012, Yu *et al.*, 2012). As the Hippo pathway played a role in controlling cell growth (Han, 2019), S1PR2 may also be able to modulate cell proliferation. However, as described earlier, some cell types did not express S1PR2, implying that it was unlikely to be involved in the proliferation of them all. Taken together, these data support the notion that the function of S1PR2 varied between cell types.

The present study suggested that the three OSCC lines required the function of S1PR2 for growth, although it may not be the main pathway for cellular mitogenic activity. The observed pattern of *S1PR* expression may be an indication of this since the baseline S1P can bind to other S1PR subtypes when S1PR2 is inhibited and some of these may also regulate proliferation. This possibility was supported by studies of glioma and oesophageal carcinoma (Young & Van Brocklyn, 2007, Hu *et al.*, 2010, Bäcker, 2012, Liu *et al.*, 2019). In glioma, the ligation of S1P to S1PR1-3 stimulates proliferation, with S1PR1 being the most potent receptor subtype. However, it was observed that S1PR1 did not provide a maximal mitogenic response to S1P without the presence of S1PR2 and S1PR3 (Young & Van Brocklyn, 2007). In oesophageal carcinoma, the activation of S1PR1 promoted proliferation via the signal transducer and activator of transcription 3 (STAT3) pathway (Liu *et al.*, 2019), whereas S1PR5 activation caused the coupling to Gα12/13 and decreased proliferation by inhibiting a type of serine/threonine-protein kinase termed extracellular signal-regulated kinase (ERK) activity

(Hu *et al.*, 2010). Nevertheless, no study has elucidated the function of the five S1PRs on OSCC proliferation, and therefore this remains to be substantiated.

7.3 Determination of migration and invasion

Having established the proliferation profile of three OSCC lines as well as the effect of EGF and S1PR2 on these lines' growth rate, the study continued investigating the migration and invasion profiles of these cells.

7.3.1 Comparison of migratory and invasive profiles between the three OSCC lines

From both scratch wound and transwell assays, the present study showed that H400 cells migrated more rapidly than the other cell lines which did not agree with data from Celentano *et al*. (2021) who reported that in a transwell assay, at 24 hours more H357 cells migrated in comparison with H400 cells. For invasion, the present study's data from both transwell invasion and MCTS assays was consistent with previous studies, showing that H400 invaded more rapidly than H357 cells (Patmanathan *et al.*, 2016, Celentano *et al.*, 2021). However, no other study has compared both migration and invasion of H413 with either H357 or H400 cells**.**

7.3.2 Generation of a protocol for the MCTS model

Next, this study investigated the invasion characteristics of the three OSCC lines using an MCTS model**.** For standardisation purposes and to eliminate the involvement of the proliferation due to the effect of FBS on invasion, the study investigated whether spheroids could form in serum-free conditions None of the three cell lines could form spheroids without 10% FBS supplementation**.** This was similar to a study on mouse mucosal cell cultures (Liu *et al.*, 2019) but different from those using human mesenchymal stem cells (Alimperti *et al.*, 2014) and glioblastoma (Hong *et al.*, 2012) which were able to form spheroids in serum-free

conditions**.** Moreover, it appeared that the type of serum supplement was specific to each cell type. While the OSCC lines studied here required FBS for aggregation, KAIMRC1 cells (human breast cancer) required newborn calf serum, otherwise cultures grew in monolayers when supplemented with media containing FBS (Ali *et al.*, 2021). Additionally, spheroid size and shape appeared to be important parameters since different starting morphologies of spheroids appeared to influence invasion**.** Indeed, spheroids of human lung and colorectal cancer cell lines generated a wide range of spheroid sizes even when experiments were performed using a standard protocol (Godugu *et al.*, 2013, Kang *et al.*, 2016). The present study showed that with approximately 500 cells per droplet, the hanging drop method reproducibly provided spheroids of similar size and circularity.

The ECM is another factor that has been shown to influence tumour invasion (Puls *et al.*, 2018). In particular, the stiffness of ECM appeared to affect rate of invasion (Staneva *et al.*, 2018, Wullkopf *et al.*, 2018, Matte *et al.*, 2019) and expression of certain genes, such as *N-cadherin* (Matte *et al.*, 2019), *EGFR* (Grasset *et al.*, 2018) and *vimentin* (Rice *et al.*, 2017). The mechanisms of invasion also appeared to be affected by the rigidity of the ECM. It was reported that breast cancer cells embedded in low stiffness gels (2 kPa) methacrylate/collagen hydrogel could invade without proteolytic activity; however, in high stiffness gels (12 kPa), the invasion shifted to become proteolytic-dependent (Berger *et al.*, 2020).

Previous studies devised parameters to quantify the invasion characteristics, including size and geometry of the tissue (total invasive area, maximum invading distance, perimeter and volume) (Basu *et al.*, 2013, Goertzen *et al.*, 2018, Hou *et al.*, 2018, Puls *et al.*, 2018, Liu *et al.*, 2020), number of invading cells or clusters (De Wever *et al.*, 2010, Puls *et al.*, 2018), cell density (Blacher *et al.*, 2014), invading boundary irregularity (De Wever *et al.*, 2010, Jiang *et al.*, 2014, Hou *et al.*, 2018, He *et al.*, 2020) and proposed indices (Staneva *et al.*, 2018, Kim *et al.*, 2019, Lim *et al.*, 2020, Liu *et al.*, 2020, Suh *et al.*, 2022). The present study used five parameters,

including the number of clusters, maximum invading distance, circularity, fractal dimension and MDMC, to interpret the invasion, but it did not use previously published indices for three reasons**.** Firstly, some of those indices in previous studies (Attieh *et al.*, 2017) required data that the present study could not obtain, such as the number of invading cells or longer time points**.** Secondly, some comparisons could not be made because a given 'invasion index' often referred to different definitions between studies. For example, one definition was the ratio of the number of nuclei of invading cancer cells to the area of the spheroid contour (Attieh *et al.*, 2017), whilst another study referred to the index as the percentage of the edge area of the spheroid to the total area of the spheroid (Lim *et al.*, 2020) which, are clearly not directly comparable. Thirdly, using only a single index to describe invasion may lead to under- or over-estimation because each index captured different aspects of the invasion process (Puls *et al.*, 2018, Lim *et al.*, 2020).

The present study showed that OSCC lines could invade the collagen matrix spontaneously and these data are in agreement with a previous study (Jiang *et al.*, 2014), where it was reported that the matrix provided haptotaxis, which directed cells to move toward the matrix. The possible reason for spontaneous invasion of three OSCC lines into collagen may be due to the matrix providing ECM-mimicry components which attracted cells to move towards it. This possibility was supported by the study using Lewis lung carcinoma cells (Liu *et al.*, 2020), which highlighted the importance of the ECM components of the matrix for invasion. In that study, cells could spontaneously invade into 5 mg/ml growth factor reduced Matrigel, 1.6 mg/ml collagen I, but could not invade into 0.3% agar (lack of ECM components). That study suggested that the addition of ECM components to the embedding matrix may create a condition in which cells could reside and, therefore, increased invasive performance.

Regarding the invasion pattern, this study showed that the three OSCC lines collectively invaded the collagen matrix and when a critical point was reached, clusters of cells detached

from the main cluster and continued invading. This pattern of invasion was also observed in glioblastoma (Young & Van Brocklyn, 2007), human breast cancer (Berger *et al.*, 2020, Suh *et al.*, 2022), pancreatic cancer (Puls *et al.*, 2018) and lymphatic endothelial cells (Blacher *et al.*, 2014). In contrast, spheroids of human fibrosarcoma tended to extend protrusions but were less likely to detach from the main cluster (Lim *et al.*, 2020). Another study (Basu *et al.*, 2013) revealed that two main invasion patterns were observed in SCC spheroids: a *collective invasion* with a pushing invasive front where cells conserved the epithelial morphology and a *mesenchymal invasion* with the infiltrative invasive front in which cells had a spindle-shaped morphology. The invasion pattern of spheroids in the present study was similar to that reported by Basu *et al*'s mesenchymal invasion pattern. Conversely, the pushing invasive front pattern was not observed unless the spheroid reached the base of the well or the upper air interface, where cells quickly reverted to a monolayer and spread along those surfaces. This highlighted the importance of positioning the spheroid while embedding (Goertzen *et al.*, 2018, Liu *et al.*, 2020) as in 2D images, inappropriate spheroid embedding could lead to misinterpretation of how cells invaded the matrix. This type of artefact could also occur in spheroid cultures embedded using the 'sandwich technique' where one part of the collagen was crosslinked before the other, creating an interface between the two (Liu *et al.*, 2020).

7.3.3 The effect of matrix stiffness on invasion characteristics

The present study did not use nuclear staining to prevent interfering with cell physiology as observations were completed longitudinally over two days, so only the number of clusters but not an actual number of invading cells could be consistently determined**.** Fragmentation, or the ability of the spheroid cells to detach into smaller groups, has been shown to be a crucial feature of invasion as it facilitated tumour spread (Guan, 2015). Increased collagen concentration in the matrix limited the number of clusters formed, which suggested that the fragmentation

decreased in stiffer matrices. The present study also investigated the effect of matrix rigidity by measuring the total area and maximum invading distance of detached clusters. The area of the spheroid in 2D images was closely correlated with the maximum invading diameter, so the study presented only the maximum invading distance. However, although the area and the maximum invading distance were correlated, the two parameters measured different morphological aspects. While the maximum invading distance referred to the distance travelled by some cells/clusters, the area was a measure of the whole cell population. The trend observed for the maximum invading distance according to collagen concentration also seemed to be correlated with by the number of clusters (increasing collagen concentration decreased this length or area) and this was in agreement with previous studies on pancreatic cancer (Puls *et al.*, 2018) and melanoma (Liu *et al.*, 2020). A likely explanation for this effect was that increased collagen concentrations resulted in lower porosity of the hydrogel, making it more difficult for cells to invade. Previous studies also identified similar trends in human breast (Berger *et al.*, 2020) and pancreatic cancers (Puls *et al.*, 2018). In breast cancer, the invasion of the spheroids embedded in low stiffness matrices (2kP) appeared to proportionally increase with time, suggesting it was the result of a gradual and fixed invasion rate. In contrast, for spheroids embedded in high stiffness matrices (12 kPa) there was a delayed invasion phase with cells starting to invade only at 48 hours after embedding (Berger *et al.*, 2020). Interestingly, several studies also showed that cancer cells could migrate and invade at an increased rate in stiffer matrices (Tilghman *et al.*, 2010, Grasset *et al.*, 2018, Matte *et al.*, 2019). Cal27 (tongue) and FaDu (hypopharyngeal) SSC cells slowly invaded 20 kPa polyacrylamide hydrogel (PAAG) but migrated faster than those seeded on 0.48 kPa PAAG which was in contrast to the previous statement. Variability in the outcome of studies may also arise from differences between 2D and 3D assays (Lam *et al.*, 2014, Puls *et al.*, 2018, Berger *et al.*, 2020, Chang *et al.*, 2020, Liu *et al.*, 2020). In 2D models, cancer cells formed focal adhesion contacts

with the substrate to enable invasion**.** Hence, a stiffer matrix provided a higher number of binding molecules and was likely to facilitate increased motility compared with a softer matrix. In contrast, focal-contacts for migration did not seem to occur in 3D assays (Fraley *et al.*, 2010). It was reported that focal adhesions in human fibrosarcoma cells could not be detected when fully embedded in a collagen matrix. It was further hypothesised that if cells expressed focal adhesions, these might be smaller than 0.3 μm and exist for less than one second (Fraley *et al.*, 2010). A reduction of invasion with the stiffening of the matrix was observed in human breast adenocarcinoma, where cells extended shorter and more transient invadopodia in 4.4 and 9.3 kPa alginate than in 0.4 kPa alginate gels (Chang *et al.*, 2020). Nevertheless, although the matrix rigidity reduced the invasion in 3D in many studies (Lam *et al.*, 2014, Puls *et al.*, 2018, Berger *et al.*, 2020, Chang *et al.*, 2020, Liu *et al.*, 2020), this effect was understood to depend on the onset of invasion. A study on mouse intestinal cancer showed that stiffening of the matrix before the tumour started invading, constrained the invasion as well as prevented collagen fibre realignment by the tumour cells. On the contrary, if the stiffening occurred after the tumour had already invaded, it appeared to promote further invasion (Staneva *et al.*, 2018). Focusing on the main spheroid cluster, previous studies showed that the epithelial-connective tissue interface could be used to distinguish between normal and pathological epithelia such as pseudoepitheliomatous hyperplasia, oral dysplasia and SCC (Landini & Rippin, 1996, Abu Eid & Landini, 2003, Abu Eid & Landini, 2005, Jiang *et al.*, 2014). The present study revealed that invasion caused a change in the cluster morphology measurable as a reduction in the circularity and an increase of MDMC and fractal dimension. This was consistent with the study of human breast adenocarcinoma (Jiang *et al.*, 2014) which showed that the invading diameter, higher fractal dimension and rougher surface of the spheroid were increased over four days of incubation.

The present study showed that collagen concentration did not affect the MDMC except in H400 cultures, where the MDMC decreased when collagen concentration was increased. The reason for the variations between cell lines may be due to intrinsic differences in the cell lines themselves. In the case of H357 and H413 spheroids, the concentration of collagen did not affect MDMC. In contrast, the concentration of collagen may hinder the invasion as well as detachment in H400 cells, so the group embedded in 3 mg/ml exhibited smaller MDMC compared with the group embedded in 0.5 mg/ml. Nevertheless, these represented the MDMC only within two days of incubation, so it was not possible to extrapolate how MDMC could change after longer periods of incubation. For the circularity and fractal dimension, no study has previously determined the implications of the rigidity of the matrix on these parameters. However, it was also possible that collagen concentration was not a pivotal factor related to the increase of protrusions, as the alteration of the matrix concentration alone did not result in changes of circularity or fractal dimension between those groups.

Comparing the invasion characteristics of the three lines, H357 generated the lowest number of clusters, invading distance, fractal dimension and MDMC and had higher circularity than H400 and H413 cells. This suggested H357 cells to be the least invasive line of the three and this was consistent with two previous studies (Patmanathan *et al.*, 2016, Celentano *et al.*, 2021). This was also supported by previous studies (Landini & Rippin, 1993, Landini & Rippin, 1996, Abu Eid & Landini, 2005) which suggested that higher grade dysplasia was likely to have more epithelial-connective tissue interface complexity than the lower grade. This was due to more severe dysplasia generating more pathological changes including uncontrollable proliferation as well as architectural disturbances.

Proliferation, migration and invasion assays indicated that H357 showed less invasive potential than H400 and H413 cells. This might be related to the original tumour stage from which these lines derived: H357 originated from a stage I tumour, potentially less aggressive than H400

and H413, which were derived from stage II tumours (Prime *et al.*, 1994, Prime *et al.*, 2004). Although H400 migrated and invaded to a greater extent than H413 cells (transwell assay), in 3D, H413 appeared to be more aggressive than H400 cells as determined by the five invasion parameters investigated.

7.3.4 The relationship between the proliferation and invasion

The differences between proliferation and invasion, in 2D images, area, invasion distance and the number of invading clusters could be influenced by proliferation, resulting in an increased number of cells causing outer cells of the tumour to be 'pushed' towards the surrounding matrix (expansive growth). The present study attempted to determine the interference of proliferation on the extent of invasion in the MCTS assay by comparing experiments with and without mitomycin C treatment. Since the experiments were performed separately, it was not possible to make a statistical comparison. Nevertheless, the number of clusters of the datasets without proliferation inhibition were higher than those with mitomycin C treatment, especially in H357 and H400 lines. The maximum invading distance (only the H400 line) of the non-inhibited growth group also was relatively higher than those cultures with growth inhibition. For the remaining invasion parameters, including the circularity, fractal dimension and MDMC, the data with and without mitomycin C treatment were similar. This might have been due to an increase in fragmentation with increasing number of cells**.** The increase in cell number could have provided an additional 'pushing' force at the spheroid edge towards the matrix (Vinci *et al.*, 2015).

While spheroids treated with mitomycin C showed no trends in circularity, fractal dimension or MDMC; in those without mitomycin C treatment, the group embedded in 0.5 mg/ml collagen had significantly lower circularity and higher fractal dimension and MDMC than the group embedded in 3 mg/ml collagen. Comparing the invading parameters of the groups with and

without mitomycin C treatment revealed that the number of clusters and maximum invading distance were significantly different when the collagen concentrations were altered, which further suggested that proliferation affected invasion data differently, depending on the matrix concentration.

It was difficult to distinguish between proliferation and invasion in the MCTS model (Vinci *et al.*, 2015) since the appearance of cells moving into the matrix could have arisen from proliferation, true invasion or a combination of both processes. However, a recent study (He *et al.*, 2020) proposed that proliferation might eventually evolve into invasion and that the two stages could be distinguished by studying the spheroid boundary shape. During the proliferation stage (or so-called expansive invasion), spheroids grew larger but were less likely to generate projections, resulting in a preservation of a smooth boundary. When increased in size, spheroids underwent a proliferation-to-invasion transition and entered the invasive stage (or so-called infiltrative invasion). At this stage, spheroids extended projections and the boundary appeared more irregular. Nevertheless, the reason why the spheroids exhibited the switching feature when enlarging was not addressed in the study by He (2020). Instead, a smooth round morphology was observed mainly on the embedding day. It is possible that in H357, H400 and H413 spheroids, proliferation and invasion occurred simultaneously and therefore no precise transition stage could be identified.

7.3.5 The effect of EGF on migration and invasion

Having established the MCTS model protocol, the study determined the effect of EGF and S1PR2 on the migration and invasion of H357, H400 and H413 cells**.** Migration and invasion in the three OSCC lines increased with raising EGF concentrations. This was in agreement with previous studies (Hu *et al.*, 2012, Vinci *et al.*, 2015, Chen *et al.*, 2019, Xie *et al.*, 2020) where EGF was considered a strong inducer for cellular motility and invasion in a dose-dependent

manner (Ohnishi *et al.*, 2017). However, it has been also noted that each cell type had a threshold related to the EGF concentration where maximum motility could be achieved, after which the motility decreased with further EGF concentration increase (Hu *et al.*, 2012, Vinci *et al.*, 2015, Xie *et al.*, 2020). Indeed, it has been reported that 10 ng/ml EGF provided the maximum migration of hepatoma cells (Hu *et al.*, 2012) while for OSCC cells, at least two studies reported that 20 ng/ml EGF treatment generated maximum migration and invasion (Vinci *et al.*, 2015, Xie *et al.*, 2020). The present study determined the effect of EGF using two concentrations (1 ng/ml and 20 ng/ml), so while 20 ng/ml EGF increased migration and invasion more than 1 ng/ml EGF, it was not possible to clarify whether 20 ng/ml was the optimal concentration for inducing the maximum migration and invasion or whether the effects followed a dose-dependent manner over a particular range of concentrations.

EGF also increased the number of clusters, maximum invading distance, irregularity of the main cluster and MDMC which were similar to observations in the MCTS models for other cell types (Vinci *et al.*, 2015, Chen *et al.*, 2019, Suh *et al.*, 2022). A study of head and neck squamous cell carcinoma (HNSCC) reported that EGF treatment elevated the extent of invasion, providing a greater invading area and invasion index (Chen *et al.*, 2019). Although EGF was reported to induce scattering of cells (Patmanathan *et al.*, 2016) and promoted the invasion in spheroids (Vinci *et al.*, 2015, Chen *et al.*, 2019, Suh *et al.*, 2022), it also appeared to facilitate the aggregation during spheroid generation (Liu *et al.*, 2019).

Various pathways have been proposed to explain the mode of action of EGF on migration and invasion and it has been proposed that EGF induced EMT (Xu *et al.*, 2016, Ohnishi *et al.*, 2017, Xie *et al.*, 2020). Previous studies revealed that EGF binding to EGFR caused downregulation of epithelial markers, such as E-cadherin and ZO-1 (Chavez *et al.*, 2012, Tumur *et al.*, 2015, Xu *et al.*, 2016) with an upregulation of mesenchymal markers including vimentin, Snail, slug and zinc finger E-box binding homeobox 1 (Zeb1) (Xu *et al.*, 2016). EGF can induce *MMP2*

and *MMP9* expression, facilitating the invasion by their enzymatic disruption of the extracellular matrix (Kim *et al.*, 2019, Xie *et al.*, 2020). In agreement with the previous two studies, incubation of the three OSCC lines with EGF for 48 hours elevated levels of MMP2 and MMP9 according to the concentration used. However, no significant change was identified in *E-cadherin* and *vimentin* expression following both EGF treatments at four hours. This contrasted with a study of HNSCC (Kim *et al.*, 2019), which reported that EGF downregulated the E-cadherin gene within three hours. However this discrepancy may have been due to the differences in concentrations used (20 ng/ml versus Kim *et al.* study using 50 ng/ml). Another possible reason for this was that four hours may not be a sufficient time to alter *E-cadherin* and *vimentin* expression, as previous studies showed that both genes required at least 24 hours to cause a transcriptional change (Chavez *et al.*, 2012). Nevertheless, it was reported that EGF at 50 ng/ml induced migration of oral adenoid squamous cells while upregulating *E-cadherin* expression and downregulating *vimentin* expression. This indicated that it was likely that mechanisms other than EMT might cause migration stimulated by EGF, for example, actin reorganization (Islam *et al.*, 2017).

7.3.6 The effect of S1PR2 on OSCC migration and invasion

S1PR2 regulated the motility of cells depending on cell type (summarised in **Table IV**). The majority of studies have indicated that S1PR2 can act as a tumour suppressor receptor that negatively regulates motility (Arikawa *et al.*, 2003, Du *et al.*, 2010, Price *et al.*, 2015, Pang *et al.*, 2020). However, the underlying mechanisms also appeared to vary depending on cell types. For example, the suppression of S1PR2 stimulated migration and invasion of melanoma by reducing ERK phosphorylation (Arikawa *et al.*, 2003), but in mesenchymal stem cells, S1PR2 inhibition increased the motility via activating ERK phosphorylation (Price *et al.*, 2015).

In addition, previous study (Young & Van Brocklyn, 2007) showed that although migration was decreased following the S1PR2 stimulation, invasion did not necessarily decrease. In that study, *S1PR2* overexpression in glioma cells activated Rho and decreased migration, but enhanced invasion by increasing the adhesion to the matrix (Matrigel), although the underlying mechanism for this was not fully explained. Regarding the inhibition of motility, S1PR2 stimulation was reported to reduce proteolytic enzyme production, particularly of MMP2 and MMP9 (Asghar *et al.*, 2018, Pang *et al.*, 2020). In thyroid cancer, binding of S1P to S1PR2 suppressed the expression, secretion and activity of MMP2 as well as inhibiting calpain (an endopeptidase that cleaved pro-MMPs and generates the active forms) (Asghar *et al.*, 2018). Similarly, in multiple myeloma, knocking down *S1PR2* expression increased MMP9 production (Pang *et al.*, 2020).

Studies have also indicated the positive regulation of S1PR2 in both migration and invasion (Miller *et al.*, 2008, Patmanathan *et al.*, 2016). In human adenocarcinoma, inhibition of S1PR2 did not alter baseline migration and invasion, but this did reduce TGF-β- and S1P-induced migration and invasion. This suggested that the function of S1PR2 was to facilitate rather than inhibit mobility (Miller *et al.*, 2008). In OSCC, S1PR2 inhibition decreased migration, invasion and cell scattering, whereas stimulation increased these parameters (Patmanathan *et al.*, 2016). Regarding the invasion stimulation function, S1PR2 was identified as regulating *MMP*s positively. In pancreatic stellate cells, inhibition of S1PR2 suppressed the effect of S1P that induced *MMP9* expression (Bi *et al.*, 2014), whereas it suppressed both *MMP2* and *MMP9* expression in cholangiocarcinoma (Liu *et al.*, 2015).

Table IV. The effect of S1PR2 on cellular motility and MMP production

Effect	Cells	References
S1PR2 negatively regulates cellular mobility.	Melanoma cells	(Arikawa *et al.*, 2003)
	Mice bone marrow-derived macrophages	(Du *et al.*, 2010)
	Mesenchymal stem cells	(Price *et al.*, 2015)
	Multiple myeloma cells	(Pang *et al.*, 2020)
S1PR2 activation downregulates MMP production.	Thyroid cancer cells	(Asghar *et al.*, 2018)
	Multiple myeloma cells	(Pang *et al.*, 2020)
S1PR2 positively regulates cellular mobility.	Human adenocarcinoma	(Miller *et al.*, 2008)
	OSCC	(Patmanathan *et al.*, 2016)
S1PR2 activation stimulates MMP production.	Pancreatic stellate cells	(Bi *et al.*, 2014)
	Cholangiocarcinoma cells	(Liu *et al.*, 2015)
S1PR2 not involved in cellular mobility or MMP production.	Human breast epithelial cells	(Kim *et al.*, 2011)
	Human colon cancer cells	(Petti *et al.*, 2020)

Furthermore, some studies have suggested that S1PR2 did not contribute to migration and invasion (Kim *et al.*, 2011, Petti *et al.*, 2020). In human colon carcinoma, the overexpression of S1PR2 neither altered migration nor the expression of *MMP1* and *MMP2* (Petti *et al.*, 2020), whereas, in human breast epithelial cells, MMP9 facilitated invasion induced by S1PR3 rather than S1PR2 (Kim *et al.*, 2011).

The present study agreed with studies that showed the role of S1PR2 in promoting cellular motility (Miller *et al.*, 2008, Patmanathan *et al.*, 2016). While the findings in this study indicated that S1PR2 inhibition decreased migration, the effect of this receptor stimulation was varied. In the scratch wound assay, only H400 cells showed increased migration after enhanced S1PR2 stimulation. In contrast, H400 was the only cell line in the transwell migration assay that showed no increase in migration following S1PR2 stimulation which agreed with a previous study (Brocklyn, 2010) reporting that this cell type and experimental set-up can influence the effect of S1PRs. Moreover, the reason for the lack of effect of the agonist in stimulating the migration observed in the experiment may be due to basal over-saturation. Until now, documentation regarding the level of S1P and other molecules capable of binding to S1PR2 in media is limited. Therefore, it is possible that these molecules are over-saturated, so the S1PR2 agonist could not induce stimulation.

The present study identified that S1PR2 inhibition suppressed invasion, while its stimulation reversed this effect in the transwell invasion assay. For the MCTS assay, blocking S1PR2 activity reduced the number of clusters, maximum invading distance, irregularity and MDMC. Comparison of the OSCC cells, indicated differences with some previous studies, for example in the Patmanathan *et al.* (2016) study: 5 μM of the S1PR2 antagonist or agonist in the present study did not significantly affect the migration of any of the three OSCC lines in the preliminary work (data not shown). For the proteolytic enzyme production, this study's findings were not consistent with those of Asghar *et al.* (2018) or Pang *et al.* (2020) which reported the negative

regulation of S1PR2 on *MMP9* expression but agreed with studies showing a positive regulation (Kim *et al.*, 2011, Bi *et al.*, 2014, Liu *et al.*, 2015, Petti *et al.*, 2020). However, the three OSCC lines responded to S1PR2 stimulation differently: increasing *MMP2* expression in both H400 and H413 and increasing *MMP9* expression in H413 cells. On the contrary, both S1PR2 stimulation and inhibition increased *MMP2* expression in H357 and *MMP9* expression in both H357 and H400 cells. Since this study did not determine the secretion or activity of MMP2 and MMP9, it could be hypothesised that the difference in the MMPs responses to S1PR2 may be an intrinsic characteristic of the cell lines which further reflect their invasion characteristics.

Previous studies also demonstrated the requirement of SPHK1 and SPHK2 to induce migration and invasion (Goparaju *et al.*, 2005, Hait *et al.*, 2005, Miller *et al.*, 2008, Kato *et al.*, 2018). In human adenocarcinoma, knockdown of *SPHK1* and *SPHK2* resulted in the decrease of TGF-β-induced migration and invasion, with *SPHK1* being the more potent isoform (Miller *et al.*, 2008), while in OSCC, the high expression of *SPHK1* correlated with EMT events, high invasion grade (III and IV), cervical node metastasis and poor survival rate (Kato *et al.*, 2018). Moreover, there is evidence that showed S1PR2 was implicated in the expression of *SPHK1* and *SPHK2*. Some evidence for this relied on the observation that *S1PR2* knockout increased *SPHK1* expression in mouse embryonic fibroblasts but did not affect *SPHK2* expression (Goparaju *et al.*, 2005). The present study partially agreed with Goparaju *et al*. (2005) as S1PR2 inhibition reduced *SPHK1* expression (in H400 and H413 cells) and *SPHK2* (only H413 cells), while the stimulation of this receptor led to a reverse effect. This implied that S1PR2 inhibition not only directly suppressed motility in some OSCC lines but also caused feedback which reduced S1P production via the downregulation of *SPHK1* in H400 and both *SPHK1* and *-2* in H413 cells. Subsequently, the binding between produced S1P (from SPHK1) and S1PR2 decreased which suppressed cell motility. A previous study indicated that *SPHK1*

overexpression marginally increased cellular S1P but the S1P elevation did not correlate clearly with SPHK1 activity (Olivera *et al.*, 1999). More importantly, the present study showed changes of *SPHK1* and *SPHK2* only at the mRNA level, so it was possible that the transcription changes might have caused insignificant alteration at the cellular level.

7.3.7 The effect of S1PR2 on EGF-induced migration and invasion

The above data indicated that both EGF and S1PR2 regulated the mobility of H357, H400 and H413 cells. Since 20 ng/ml EGF promoted migration and invasion of three OSCC lines without stimulating growth all following experiments used this concentration to induce motility while S1PR2 was neither inhibited nor stimulated. Although EGF was a potent inducer of cellular motility for the three OSCC lines, it failed to promote both migration and invasion without the function of S1PR2. This means that the motility control from S1PR2 possibly inhibited the pathway generated from EGF/ EGF receptors. This agreed with a previous study (Gandy *et al.*, 2013) that reported the requirement of S1PR2 for invasion of human cervical adenocarcinoma and suggested that EGF promoted lamellipodia formation, causing motility by providing the phosphorylation of ezrin, radixin and moesin (ERM), a family of proteins that connect cortical actin with the plasma membrane. This mechanism was suppressed following the knocking down of S1PR2. In the present study, although the inhibition of S1PR2 significantly decreased the effect of EGF on migration and invasion of the three OSCC lines, the increase of the EGF effect was not observed following S1PR2 stimulation together with EGF treatment. The reason for this may be explained by the competitive inhibition theory (Palleria *et al.*, 2013): when two compounds with the same mechanism of action are co-applied, both compete for the same binding site, reducing the maximum efficacy of action. In the case of OSCC, S1P/S1PR2 and EGF/EGF receptors have the same action, so it was possible that these two axes shared some part of the same pathway in driving the motility of cells. Therefore, the stimulation with S1PR2

or EGF alone promoted migration and invasion, but the co-stimulation did not increase the effect.

7.4 The effect of EGF and S1PR2 on Rac1 activity

Cytoskeleton orientation plays an important role in driving non-muscular cell movement. To determine the relationship between EGF and S1PR2, the activity of Rac1 (a downstream molecule which linked EGF and S1PR2 to the biological events) was investigated. It was previously reported that the factors determining whether Rac1 would be activated or inactivated, depended on the cell type and the external stimuli used (Marei & Malliri, 2017). The present study indicated that in OSCC, Rac1 activity was stimulated by EGF/EGF receptors rather than the S1P/S1PR2 axis. EGF stimulation for two minutes rapidly increased the Rac1 activity, but the concentration of EGF did not affect the level of Rac1 activity. In contrast, neither S1PR2 inhibition nor stimulation altered Rac1 activity, despite S1PR2 function being required for EGF to induce Rac1 activity. Several previous studies supported this showing that EGF was an inducer for Rac1 (Kurokawa *et al.*, 2004, Patel *et al.*, 2007, Dise *et al.*, 2008, Li *et al.*, 2009). In fibroblasts, it has been proposed that EGF induced filamentous actin formation and migration via stimulating phospholipase C-γ1, a protein involved in cell growth, migration and apoptosis, to act as a specific guanine exchange factor (GEF) for Rac1 (Li *et al.*, 2009). Although it appeared that EGF-induced Rac1 activation was a parallel pathway to EGF-induced phosphoinositide 3-kinase (PI3K)/Akt and mitogen-activated protein kinase (MEK)/ERK pathways, some studies found that Rac1 was a molecule that created a link between EGF and these two pathways (Dise *et al.*, 2008, Hu *et al.*, 2012). In colonic cancer, EGF binding to EGFR stimulated Rac1 to activate both PI3K and Src family kinase, subsequently promoting migration (Dise *et al.*, 2008). Meanwhile, in human hepatoma cells, EGF stimulated ADP-ribosylation factor (arf6), a GTP-binding protein in the Ras family, causing ERK phosphorylation and activating Rac1 (Hu *et al.*, 2012). In HNSCC, EGF was

reported to induce migration by increasing Rac1 activity (Li *et al.*, 2009, Hu *et al.*, 2012). According to these studies, EGF could stimulate Rac1 activity via two pathways depending on the cell line. The first pathway was through the activation of VAV guanine nucleotide exchange factor 2 (VAV2), a type of GEF. The second pathway was through H-Ras, which was proposed to mediate Rac1 activity by downstream molecules such as PI3K or other GEFs (Patel *et al.*, 2007). Nevertheless, the present study, using G-LISA assay, investigated the effect of EGF and S1PR2 only on Rac1's first wave activity. A later study on human epidermoid carcinoma and oesophageal cancer cells reported two waves of Rac1 activation following EGF treatment: the first wave occurred after treatment with EGF for two to five minutes and the second wave occurred after treatment for 6 to 12 hours (Kobayashi *et al.*, 2011). This study indicated that two waves of Rac1 activation were due to EGF activating different GEFs. While the first wave of Rac1 was stimulated through VAV2 and Rho guanine nucleotide exchange factor 4 (Asef), the second wave was stimulated via TIAM Rac1 associated GEF 1 (TIAM1) (Kobayashi *et al.*, 2011). Therefore, to link the invasion features from the MCTS model, Rac1 activity monitoring may be required.

While EGF appeared to activate Rac1 in most studies (Kurokawa *et al.*, 2004, Patel *et al.*, 2007, Dise *et al.*, 2008, Li *et al.*, 2009, Hu *et al.*, 2012), S1PR2 could either activate or inactivate Rac1. S1PR2 was reported to activate Rac1 in glioma and vascular smooth muscle cells (Malchinkhuu *et al.*, 2008, Takashima *et al.*, 2008), while it inhibited Rac1 activity in glioblastoma and primary murine lung endothelial cells (Lepley *et al.*, 2005, Du *et al.*, 2010). Differences in the effect of S1PR2 on Rac1 activity were explained by the different cell types and also by the type of G-protein bound to S1PR2. It has been shown that S1PR2 could couple to GαI, GαQ or Gα12/13 (Adada *et al.*, 2013, Nema *et al.*, 2016), which stimulated different upstream GEF of Rac1, resulting in activation or inactivation of Rac1 (Miller *et al.*, 2008). Additionally, evidence has demonstrated that S1P treatment did not alter Rac1 activity of

mouse mesenchymal cells, suggesting that S1PR2 affects Rac1 activity but not in all cell types (Quint *et al.*, 2013). The present study found that S1PR2 inhibition appeared to suppress only EGF-induced Rac1 activity but not with the baseline of Rac1 activity in the three OSCC cell lines as the level of Rac1 activity of groups treated with either S1PR2 antagonist or agonist (without EGF) appeared to be the same as that of the control.

Rho GTPase activity was previously shown to be activated by switching between the GDP- and GTP-bound forms (Parri & Chiarugi, 2010, Zegers & Friedl, 2014), but more recently it was found to be also regulated through transcription modification (Croft & Olson, 2011). In laryngeal papilloma and normal laryngeal epithelial cells, 20 ng/ml EGF stimulation for 48 hours increased total Rac1 protein and Rac1 activity (Wu *et al.*, 2007). This is in contrast to the present study, in which EGF at either 1 or 20 ng/ml did not affect *Rac1* expression in any of the three OSCC lines, suggesting that the regulation of Rac1 in the three OSCCs was due to GDP and GTP switching.

7.5 Crosstalk between EGF/EGF receptors and S1P/S1PR2 pathways

Interestingly, the present study showed that Rac1 activity did not increase in the three OSCC lines incubated with both EGF and the S1PR2 agonist. This implied the possibility that EGF/EGF receptors and S1P/S1PR2 may not be separate cascades in regulating Rac1. Several studies have postulated mechanisms to explain the crosstalk between EGF and S1P (Gandy *et al.*, 2013, Tamashiro *et al.*, 2014, Cattaneo *et al.*, 2018). The first model (Lebman & Spiegel, 2008) proposed that growth factors, including platelet-derived growth factor (PDGF) (Goparaju *et al.*, 2005), vascular endothelial growth factor (VEGF) (Shu *et al.*, 2002), EGF (Cattaneo *et al.*, 2018) and tumour necrosis factor-alpha (TNF-α) (Pitson *et al.*, 2003) as well as certain enzymes, such as acid ceramidase (Beckham *et al.*, 2013), could rapidly stimulate *SPHK* expression. Upon phosphorylation, SPHK translocated from cytosol to the plasma

membrane, where it turned into an active form and converts sphingosine into S1P (Pitson *et al.*, 2005). After being produced, S1P was exported from the cell and bound to S1PRs, resulting in the triggering of various cellular activities (Lebman & Spiegel, 2008). Furthermore, a study using breast cancer cells (Sukocheva *et al.*, 2006) proposed another model with a three-way relationship between oestrogen, S1P and EGF. This alternative model proposed that oestrogen caused SPHK activation, resulting in S1P production. After S1P was exported to the intercellular space and binds to S1PRs (mainly via S1PR3) it activated a downstream signaling cascade. Subsequently, HB-EGF was converted into EGF and also exported to the intercellular space, where it could bind to EGF receptors (Sukocheva *et al.*, 2006). This was observed in a study of vascular smooth muscle cells, where the activation of S1PR1 (and possibly by S1PR3 and S1PR5) induced EGF production (Tanimoto *et al.*, 2004). The present study aligned with the first model (Lebman & Spiegel, 2008) as activation of S1PR2 in three OSCC lines did not promote EGF or TGF-β1 production. Conversely, EGF induced S1P production by increasing only *SPHK1* expression (summarised in **Figure 81**). This concept was supported by a previous study which demonstrated that sphingosine was mainly converted into S1P by SPHK1 (Gandy *et al.*, 2013). The current study contrasted with a previous study of human cervical adenocarcinoma cells (Adada *et al.*, 2015), which demonstrated that EGF binding to EGFR stimulated SPHK2 within the endoplasmic reticulum or Golgi apparatus, increasing intracellular S1P production. Adada *et al.* (2015) proposed that S1P generated from SPHK2 was not exported to the intercellular space as is the S1P generated from SPHK1 in response to sphingosine treatment. Instead, after production, the intracellular S1P was imported into the inner surface of intracellular vesicles through sphingolipid transporter 2 (SPNS2), a lipid transporter. When these vesicles fused with vesicles containing S1PR2, then S1PR2 activated ERM phosphorylation and subsequently this promoted invasion.

7.6 Limitations of this study

One limitation of the present study was that the function of S1PR2 was modified using reagents only. JTE013 is a selective antagonist reagent used to determine the effect of S1PR2 on specific biological events. However, at a concentration of 10 μM, it is reported to inhibit S1PR3 by 4.2%. Moreover, it has been found in a study on human breast cancer cells to function also as an S1PR4 antagonist (Long *et al.*, 2010). JTE013 was used at concentrations of up to 10 μM in a number of studies (Schüppel *et al.*, 2008, Herr *et al.*, 2016, Asghar *et al.*, 2018, Cheng *et al.*, 2018), but it was reported that this reagent selectively inhibited the function of S1PR2 at concentrations lower or equal to 1 μM (Salomone & Waeber, 2011). In addition, a study in mice demonstrated that JTE013 appeared to be non-specific to S1PR2 when applied at a concentration of 10 μM (Salomone *et al.*, 2008). However, no study has investigated the effects of concentration on the selectivity of JTE013 in OSCC.

Although the present study showed that EGF and S1PR2 were involved with cell motility and Rac1 activation, the effect of Rac1 on migration and invasion has not been determined. Consequently, it could only be suggested that EGF and S1PR2 may control the migration and invasion by regulating Rac1 activity.

Finally, although EGF shows preferential binding to EGFR (or so-called ErbB1) rather than other ErbB receptors (*e.g.* including ErbB2-4), from the present study it could not be assumed that the effect of EGF observed arose from binding to EGFR exclusively as the presence of *ErbB2-4* expression and subsequent effects were not determined.

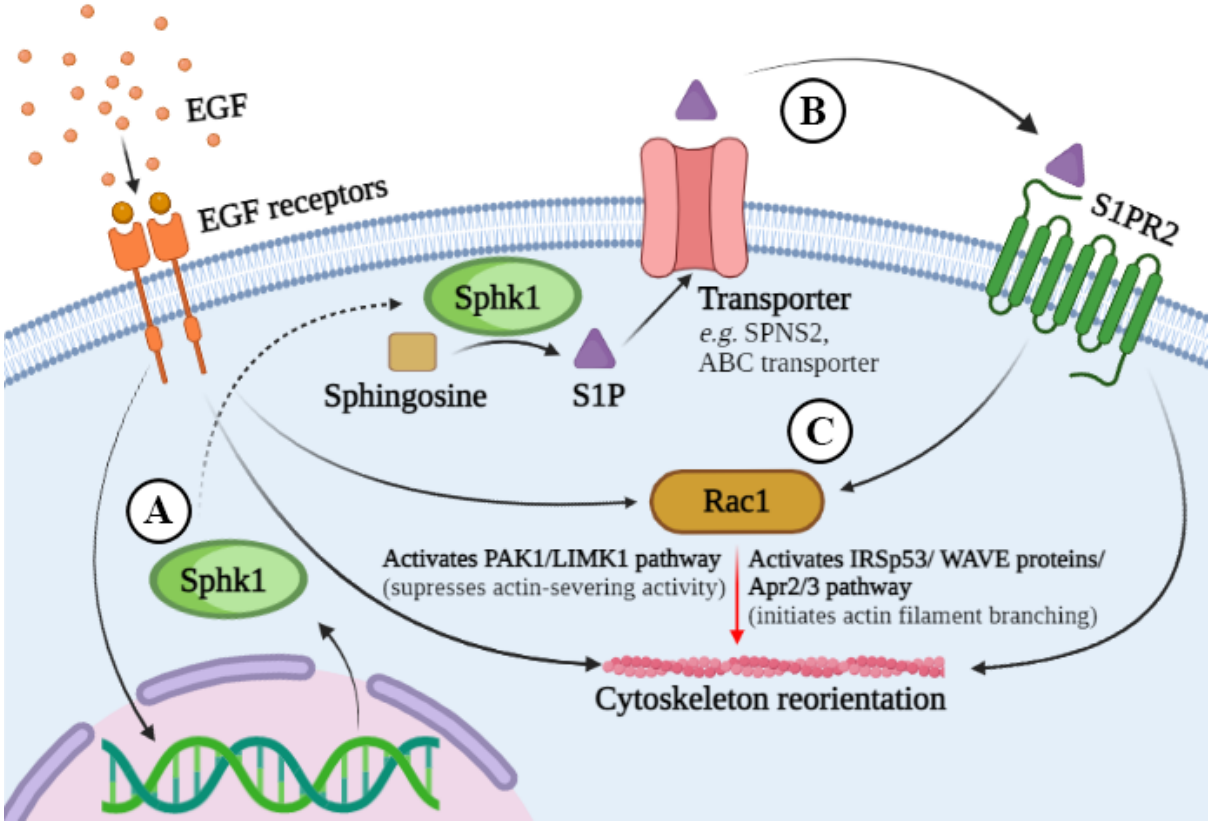

Figure 81. Proposed crosstalk model between EGF and S1PR2 in H357, H400 and H413 cells. **A)** EGF stimulates SPHK1 transcription resulting in the increase in S1P production. **B)** S1P is exported to the intercellular space and binds to S1PR2, providing a signal required for migration and invasion. **C)** Both EGF and S1PR2 in coordination work to regulate the motility of H357, H400 and H413 cells as well as Rac1 activity. Rac1 regulates cytoskeleton reorientation via two pathways: IRSp53/WAVE proteins/Apr2/3 pathway and PAK1/LIMK1 pathway. Notably, this activity (red arrow) was not substantiated in the present study. (SPNS2 = Sphingolipid transporter 2, ABC transporter = AATP-binding cassette transporter; Image created with BioRender.com).

7.7 Potential future studies and applications

Additional work is required to fully elucidate the cellular mechanisms underpinning the processes involved. Future studies can focus on the following five themes.

First, the current study has not determined the amount of each EGFR subtype present, so it could not be definitely concluded that the biphasic growth response of H357 and H413 cells was due to the differences in EGFR subtypes. Also, this study did not monitor changes in the EGFR subtype ratios following culture passage. Therefore, it could not be concluded whether the high-affinity subtype of EGFR in H400 cells was altered with the increase in passage number, resulting in the absence of growth stimulatory effects with low-dose EGF. To substantiate the earlier hypothesis, it should be worth evaluating these issues.

Second, the effect of Rac1 on proliferation, migration and invasion should be further investigated. Although S1PR2 could either activate or inactivate Rac1 (depending on cell types) it appeared that the role of Rac1 was to promote migration and invasion in H357, H400 and H413 cells (Malchinkhuu *et al.*, 2008, Takashima *et al.*, 2008, Du *et al.*, 2010). However, Rac1 itself exhibited dual roles in controlling migration and invasion (Marei & Malliri, 2017); either promoting (Malchinkhuu *et al.*, 2008, Takashima *et al.*, 2008, Yang *et al.*, 2015) or suppressing (Engers *et al.*, 2001, Uhlenbrock *et al.*, 2004). Moreover, there has been evidence presented that in human glioblastoma, Rac1 was inhibited following S1PR2 stimulation, and the mechanism involved did not utilise S1P-mediated inhibition of migration (Lepley *et al.*, 2005), which suggested that the activation of Rac1 following any treatment may be only a coincidence. Therefore, to substantiate the hypothesised model, the proliferation, migration and invasion could be further investigated by setting up five experimental groups:1) a control, 2) Rac1 inhibited (without other treatments), 3) Rac1 stimulated (without other treatments), 4) Rac1 inhibited together with other treatments, and 5) Rac1 is stimulated together with other treatments. Rac1 is stimulated together with other treatments. Also, since Rac1 activation was

biphasic and the present study incubated MCTS with EGF and S1PR2 treatments for two days, the second (long term) wave of Rac1 activity should be monitored to clarify the proposed model.

Third, S1PR subtypes were potentially responsible for specific functions in controlling cellular activities (Nema *et al.*, 2016) and sometimes more than one receptor subtype worked together (Tanimoto *et al.*, 2004, Young & Van Brocklyn, 2007). Therefore, it is possible that the ratio of *S1PR*s expression and the affinity of reaction may be an underlying reason for the different characteristics of the cell lines. Nevertheless, the expression of S1PR subtypes in this study was determined using sq-PCR, but was unable to compare the level of expression between these five genes in each line. To clarify the role of these receptors, the properties of each S1PR subtype and any interactions should be investigated. Moreover, the present study did not directly evaluate baseline of S1P production in the three OSCC lines. In case that the S1PR ratios affect the behaviour of the cell lines, the amount of baseline S1P should be examined because the high amount of S1P may result in a high chance of binding to S1PRs which in turn will amplify the effect of those receptors.

Fourth, while this study investigated Rac1 activity, it was reported that S1PR2 can regulate other Rho GTPases, including RhoA and Cell division control protein 42 homolog (Cdc42) (Lepley *et al.*, 2005, Medlin *et al.*, 2010). RhoA, was reported to promote cancer propagation by inducing membrane blebbing (a type of cellular protrusion which appear as bulky, rounded the membrane) in amoeboid movement and inducing retraction of the cell tail edge in mesenchymal movement. Cdc42 was reported to play a role in maintaining cell polarity and filopodia formation (Parri & Chiarugi, 2010) by helping RhoA to maintain amoeboid movement (Gadea *et al.*, 2008) and also to work in tandem with Rac1 in directing the actin polymerisation in the lamellipodia protrusion step of mesenchymal movement (Kurokawa *et al.*, 2004, Murali & Rajalingam, 2014) and CCM (Zegers & Friedl, 2014). It would be worth

studying the coordinated influence of RhoA and Cdc42 on proliferation, migration and invasion to further elucidate the underlying mechanisms of action of S1PR2. Moreover, it has been suggested that Cdc42 and Rac1 activity in controlling actin polymerisation is spatio-temporal and separated from Rho's activity in relation to actinomyosin engagement and concretion (Kurokawa *et al.*, 2004, Dise *et al.*, 2008, Zegers & Friedl, 2014), so the location and order of action may be key factors in the coordination between these three molecules. Future experiments could include identifying how variation in stimulation time influences the order of Rho GTPases response and location.

Fifth, previous studies have shown that S1P/S1PR2 played roles in both physiological (Sanchez *et al.*, 2007, Price *et al.*, 2015, Yamamoto *et al.*, 2015) and pathological conditions (Young & Van Brocklyn, 2007, Patmanathan *et al.*, 2016, Asghar *et al.*, 2018), therefore, to better understand the impact on non cancerous cells, future studies should investigate the role of S1P/S1PRs on primary keratinocytes.

Finally, the present study demonstrated that S1PR2 was essential for the proliferation, migration and invasion of H357, H400 and H413 cells. Any agent that inhibits this receptor is a potential therapeutic target for controlling cancer growth. Nevertheless, since S1PR2 appeared to regulate a variety of cellular activities in both physiological and pathological conditions and its function is cell type dependent, such therapeutic targeting could also have side-effects. Possible routes of administration, concentration and timing should be closely considered to reduce any potential undesirable effects on healthy tissues.

Chapter 8: Conclusions

The H357, H400 and H413 had different proliferation, migration and invasion characteristics which could be regulated by EGF and S1PR2. The effect of EGF on proliferation depended on cell type and concentrations used, but both 1 and 20 ng/ml EGF stimulated migration and invasion in all three OSCC lines investigated.

S1PR2 inhibition suppressed growth, migration and invasion. The stimulation of S1PR2 promoted migration and invasion, but not growth. The study also showed that although these three OSCC lines were treated with EGF, which is a potent chemotaxis reagent widely used to stimulate cellular motility, migration and invasion rarely occurred when S1PR2 was inhibited, indicating a critical function of this receptor on the chemotaxis induced by EGF.

These migration and invasion responses were consistent with those influenced by Rac1 activity (which was EGF activated). S1PR2 did not affect baseline Rac1, but it reduced EGF-induced Rac1 activity. EGF was implicated with S1PR2 at the metabolic level as it potentially upregulated S1P production by increasing *SPHK1* expression.

Taking the results of this study together, the role of S1PR2 in promoting tumour propagation was clearly indicated. Since cancer can cause death due to uncontrollable growth and motility, suppression of S1PR2 may be a promising therapeutic route to treat OSCC patients, leading to a medical advance that could decrease the two causes of death by cancer.

Appendix

Appendix table I. The number of clusters of the three OSCC lines embedded in the three collagen concentrations, with proliferation inhibition

Cell lines	Number of clusters in each collagen concentration		
	0.5 mg/ml	1.5 mg/ml	3 mg/ml
Day 1			
H357	3 ± 0	3 ± 1	2 ± 1
H400	3 ± 1	3 ± 1	2 ± 0
H413	8 ± 4	8 ± 4	4 ± 2
Day 2			
H357	7 ± 1	7 ± 2	4 ± 1
H400	9 ± 4	10 ± 3	6 ± 2
H413	23 ± 12	21 ± 3	11 ± 5

Appendix table II. The maximum invading distance of the three OSCC lines embedded in the three collagen concentrations, with proliferation inhibition

Cell lines	Maximum invading distance (μm) in each collagen concentration		
	0.5 mg/ml	1.5 mg/ml	3 mg/ml
Embedding day			
H357	159.8 ± 3.5	171.1 ± 17.0	167.2 ± 18.0
H400	173.3 ± 46.9	141.7 ± 15.4	145.6 ± 16.5
H413	186.9 ± 22.3	179.9 ± 11.9	180.1 ± 3.8
Day 1			
H357	229.3 ± 14.8	238.8 ± 50.4	198.4 ± 18.2
H400	284.2 ± 43.7	259.3 ± 22.6	241.0 ± 56.1
H413	300.9 ± 57.9	316.8 ± 30.1	263.6 ± 18.3
Day 2			
H357	271.5 ± 38.0	239.7 ± 22.8	212.7 ± 15.0
H400	348.5 ± 42.1	311.0 ± 35.3	271.6 ± 10.5
H413	402.6 ± 108.7	375.7 ± 17.3	329.0 ± 30.2

Appendix table III. The circularity of three OSCC lines embedded in three collagen concentrations, with proliferation inhibition

Cell lines	Circularity in each collagen concentration		
	0.5 mg/ml	1.5 mg/ml	3 mg/ml
Embedding day			
H357	0.78 ± 0.02	0.73 ± 0.02	0.77 ± 0.03
H400	0.75 ± 0.07	0.72 ± 0.05	0.76 ± 0.04
H413	0.75 ± 0.05	0.75 ± 0.05	0.75 ± 0.07
Day 1			
H357	0.43 ± 0.03	0.40 ± 0.08	0.51 ± 0.03
H400	0.40 ± 0.12	0.38 ± 0.08	0.48 ± 0.06
H413	0.34 ± 0.10	0.25 ± 0.09	0.40 ± 0.12
Day 2			
H357	0.31 ± 0.03	0.28 ± 0.08	0.35 ± 0.05
H400	0.24 ± 0.10	0.24 ± 0.08	0.32 ± 0.03
H413	0.21 ± 0.10	0.17 ± 0.04	0.28 ± 0.09

Appendix table IV. The fractal dimensions of the three OSCC line spheroids embedded in the three collagen concentrations, with proliferation inhibition

Cell lines	Fractal dimension in each collagen concentration		
	0.5 mg/ml	1.5 mg/ml	3 mg/ml
Embedding day			
H357	1.11 ± 0.03	1.15 ± 0.01	1.14 ± 0.01
H400	1.08 ± 0.05	1.09 ± 0.06	1.10 ± 0.04
H413	1.10 ± 0.02	1.10 ± 0.04	1.11 ± 0.03
Day 1			
H357	1.13 ± 0.02	1.15 ± 0.02	1.14 ± 0.01
H400	1.13 ± 0.03	1.14 ± 0.03	1.11 ± 0.02
H413	1.16 ± 0.02	1.21 ± 0.04	1.16 ± 0.03
Day 2			
H357	1.19 ± 0.02	1.20 ± 0.04	1.19 ± 0.02
H400	1.19 ± 0.05	1.19 ± 0.03	1.18 ± 0.00
H413	1.21 ± 0.07	1.20 ± 0.09	1.21 ± 0.03

Appendix table V. The MDMC of the three OSCC lines embedded in the three collagen concentrations, with proliferation inhibition

Cell lines	MDMC (µm) in each collagen concentration		
	0.5 mg/ml	**1.5 mg/ml**	**3 mg/ml**
Day 1			
H357	172.3 ± 7.0	178.3 ± 21.3	157.1 ± 13.5
H400	226.7 ± 32.5	208.6 ± 18.1	195.0 ± 45.4
H413	226.2 ± 30.4	243.8 ± 18.6	207.6 ± 18.7
Day 2			
H357	176.4 ± 13.9	177.5 ± 9.5	160.7 ± 8.5
H400	263.2 ± 27.7	232.1 ± 23.3	203.9 ± 28.5
H413	226.0 ± 30.3	251.7 ± 10.9	220.9 ± 16.3

Appendix table VI. The number of clusters identified for the three OSCC lines embedded in three collagen concentrations, without proliferation inhibition

Cell lines	Number of clusters in each collagen concentration		
	0.5 mg/ml	**1.5 mg/ml**	**3 mg/ml**
Day 1			
H357	4 ± 1	5 ± 3	2 ± 1
H400	4 ± 0	3 ± 0	2 ± 1
H413	4 ± 3	5 ± 1	2 ± 1
Day 2			
H357	18 ± 0	11 ± 5	4 ± 0
H400	20 ± 2	20 ± 6	5 ± 1
H413	25 ± 8	19 ± 5	9 ± 4

Appendix table VII. The maximum invading distance for the three OSCC lines embedded in three collagen concentrations, without proliferation inhibition

Cell lines	Maximum invading distance (μm) in each collagen concentration		
	0.5 mg/ml	**1.5 mg/ml**	**3 mg/ml**
Embedding day			
H357	159.8 ± 3.5	171.1 ± 17.0	167.2 ± 18.0
H400	173.3 ± 46.9	141.7 ± 15.4	145.6 ± 16.5
H413	186.9 ± 22.3	179.9 ± 11.9	180.1 ± 3.8
Day 1			
H357	299.8 ± 7.3	250.2 ± 54.5	220.2 ± 49.8
H400	341.2 ± 41.1	291.7 ± 37.2	219.2 ± 17.7
H413	321.3 ± 41.8	331.3 ± 14.1	246.8 ± 33.7
Day 2			
H357	314.2 ± 50.0	278.5 ± 66.0	251.2 ± 66.0
H400	443.5 ± 39.7	397.5 ± 80.2	260.7 ± 30.7
H413	406.6 ± 12.9	369.9 ± 22.5	302.0 ± 11.2

Appendix table VIII. The circularity for spheroid cultures for the three OSCC lines embedded in three collagen concentrations, without proliferation inhibition

Cell lines	Circularity in each collagen concentration		
	0.5 mg/ml	**1.5 mg/ml**	**3 mg/ml**
Embedding day			
H357	0.78 ± 0.02	0.75 ± 0.03	0.68 ± 0.13
H400	0.81 ± 0.02	0.84 ± 0.03	0.84 ± 0.01
H413	0.77 ± 0.05	0.73 ± 0.08	0.77 ± 0.02
Day 1			
H357	0.26 ±0.01	0.30 ± 0.08	0.37 ± 0.07
H400	0.31 ± 0.05	0.32 ± 0.03	0.51 ± 0.05
H413	0.33 ± 0.09	0.24 ± 0.01	0.45 ± 0.11
Day 2			
H357	0.18 ± 0.03	0.22 ± 0.08	0.37 ± 0.07
H400	0.14 ± 0.03	0.18 ± 0.01	0.35 ± 0.09
H413	0.18 ± 0.04	0.19 ± 0.04	0.35 ± 0.08

Appendix table IX. The fractal dimension for spheroids for the three OSCC lines embedded in three collagen concentrations, without proliferation inhibition

Cell lines	Fractal dimension in each collagen concentration		
	0.5 mg/ml	1.5 mg/ml	3 mg/ml
Embedding day			
H357	1.13 ± 0.01	1.12 ± 0.07	1.10 ± 0.07
H400	1.12 ± 0.01	1.13 ± 0.01	1.13 ± 0.01
H413	1.10 ± 0.05	1.08 ± 0.02	1.06 ± 0.02
Day 1			
H357	1.17 ± 0.01	1.18 ± 0.02	1.16 ± 0.04
H400	1.15 ± 0.02	1.17 ± 0.01	1.11 ± 0.06
H413	1.15 ± 0.03	1.18 ± 0.02	1.12 ± 0.03
Day 2			
H357	1.23 ± 0.01	1.20 ± 0.00	1.18 ± 0.00
H400	1.23 ± 0.01	1.23 ± 0.02	1.17 ± 0.03
H413	1.22 ± 0.02	1.20 ± 0.02	1.16 ± 0.03

Appendix table X. The MDMC of the three OSCC lines embedded in three collagen concentrations without proliferation inhibition, without proliferation inhibition

Cell lines	MDMC (µm) in each collagen concentration		
	0.5 mg/ml	1.5 mg/ml	3 mg/ml
Day 1			
H357	222.4 ± 5.6	204.1 ± 57.8	176.5 ± 37.6
H400	250.6 ± 10.9	218.2 ± 10.9	169.4 ± 5.0
H413	249.6 ± 29.1	264.7 ± 14.9	197.1 ± 26.8
Day 2			
H357	209.4 ± 8.1	220.3 ± 82.6	187.5 ± 52.2
H400	270.4 ± 34.6	228.0 ± 23.6	191.1 ± 25.3
H413	275.0 ± 17.5	269.0 ± 21.5	219.3 ± 12.3

Appendix table XI. The effect of EGF treatment on the number of clusters in the three OSCC lines

Cell lines	Number of clusters in each EGF concentration		
	Control	1 ng/ml	20 ng/ml
Day 1			
H357	3 ± 1	5 ± 4	8 ± 5
H400	2 ± 0	5 ± 2	8 ± 5
H413	5 ± 4	9 ± 4	10 ± 4
Day 2			
H357	7 ± 4	21 ± 7	27 ± 4
H400	4 ± 1	17 ± 5	20 ± 5
H413	9 ± 5	18 ± 8	33 ± 15

Appendix table XII. The effect of EGF on the maximum invading distance in the three OSCC lines

Cell lines	Maximum invading distance (µm) in each EGF concentration		
	Control	1 ng/ml	20 ng/ml
Embedding day			
H357	159.0 ± 5.6	151.3 ± 20.5	195.1 ± 18.5
H400	154.7 ± 13.2	154.4 ± 10.0	188.3 ± 12.8
H413	153.8 ± 19.2	152.9 ± 27.7	193.6 ± 7.1
Day 1			
H357	192.0 ± 29.6	237.0 ± 12.6	267.8 ± 21.8
H400	230.5 ± 29.1	291.2 ± 41.8	336.0 ± 70.3
H413	285.6 ± 56.9	325.5 ± 42.8	344.8 ± 45.1
Day 2			
H357	233.3 ± 14.9	277.6 ± 56.9	340.4 ± 16.5
H400	247.7 ± 31.6	349.7 ± 22.2	381.3 ± 82.2
H413	299.4 ± 49.8	346.6 ± 57.2	412.6 ± 45.1

Appendix table XIII. The effect of EGF on the circularity of the three OSCC lines

Cell lines	XII		
	Control	1 ng/ml	20 ng/ml
Embedding day			
H357	0.76 ± 0.07	0.73 ± 0.05	0.74 ± 0.04
H400	0.82 ± 0.03	0.79 ± 0.03	0.80 ± 0.01
H413	0.75 ± 0.02	0.71 ± 0.01	0.69 ± 0.04
Day 1			
H357	0.53 ± 0.11	0.39 ± 0.11	0.29 ± 0.02
H400	0.51 ± 0.07	0.30 ± 0.10	0.22 ± 0.03
H413	0.34 ± 0.11	0.23 ± 0.04	0.22 ± 0.06
Day 2			
H357	0.31 ± 0.12	0.18 ± 0.05	0.14 ± 0.02
H400	0.35 ± 0.02	0.15 ± 0.02	0.16 ± 0.02
H413	0.28 ± 0.11	0.19 ± 0.04	0.14 ± 0.04

Appendix table XIV. The effect of EGF on the fractal dimension of the three OSCC lines

Cell lines	Fractal dimension in each EGF concentration		
	Control	1 ng/ml	20 ng/ml
Embedding day			
H357	1.13 ± 0.03	1.15 ± 0.01	1.13 ± 0.00
H400	1.12 ± 0.02	1.13 ± 0.01	1.12 ± 0.01
H413	1.06 ± 0.02	1.06 ± 0.02	1.07 ± 0.02
Day 1			
H357	1.12 ± 0.02	1.16 ± 0.02	1.17 ± 0.00
H400	1.15 ± 0.01	1.18 ± 0.03	1.20 ± 0.01
H413	1.17 ± 0.04	1.20 ± 0.04	1.20 ± 0.04
Day 2			
H357	1.20 ± 0.02	1.24 ± 0.01	1.27 ± 0.02
H400	1.17 ± 0.01	1.24 ± 0.01	1.24 ± 0.03
H413	1.18 ± 0.04	1.20 ± 0.04	1.26 ± 0.06

Appendix table XV. The effect of EGF on the MDMC in the three OSCC lines

Cell lines	MDMC (µm) in each EGF concentration		
	Control	1 ng/ml	20 ng/ml
Day 1			
H357	153.0 ± 22.0	188.0 ± 8.0	201.6 ± 8.7
H400	182.9 ± 22.3	228.7 ± 27.5	248.7 ± 34.5
H413	226.0 ± 39.8	247.2 ± 24.7	265.9 ± 29.6
Day 2			
H357	173.0 ± 16.1	183.1 ± 40.7	216.9 ± 20.6
H400	187.4 ± 21.1	220.3 ± 15.5	230.1 ± 38.0
H413	226.7 ± 29.7	248.1 ± 26.2	248.2 ± 19.4

Appendix table XVI. The effect of S1PR2 on the number of clusters of the three OSCC lines

Cell lines	Control	S1PR2 antagonist	S1PR2 agonist
Day 1			
H357	1 ± 0	2 ± 1	6 ± 1
H400	2 ± 0	2 ± 0	2 ± 1
H413	4 ± 1	2 ± 1	6 ± 1
Day 2			
H357	3 ± 1	3 ± 1	16 ± 6
H400	6 ± 2	3 ± 1	10 ± 6
H413	9 ± 3	4 ± 2	17 ± 3

Appendix table XVII. The effect of S1PR2 on the maximum invading distance (μm) of three OSCC lines

Cell lines	Control	S1PR2 antagonist	S1PR2 agonist
Embedding day			
H357	149.5 ± 13.1	149.2 ± 15.6	152.9 ± 19.2
H400	148.2 ± 18.3	163.1 ± 23.5	153.9 ± 23.0
H413	186.4 ± 19.5	187.5 ± 11.8	191.5 ± 11.0
Day 1			
H357	168.2 ± 9.1	171.1 ± 17.9	233.3 ± 14.0
H400	230.2 ± 29.1	201.6 ± 33.8	236.3 ± 23.8
H413	264.6 ± 56.5	224.7 ± 26.1	290.7 ± 73.1
Day 2			
H357	215.5 ± 30.2	190.8 ± 19.4	251.2 ± 17.4
H400	266.1 ± 13.6	214.7 ± 36.9	321.2 ± 9.8
H413	280.2 ± 27.4	229.5 ± 21.9	327.9 ± 88.8

Appendix table XVIII. The effect of S1PR2 on the circularity of three OSCC lines

Cell lines	Control	S1PR2 antagonist	S1PR2 agonist
Embedding day			
H357	0.82 ± 0.01	0.77 ± 0.01	0.78 ± 0.07
H400	0.83 ± 0.04	0.82 ± 0.02	0.81 ± 0.05
H413	0.75 ± 0.03	0.73 ± 0.03	0.73 ± 0.03
Day 1			
H357	0.61 ± 0.05	0.51 ± 0.14	0.39 ± 0.10
H400	0.49 ± 0.09	0.46 ± 0.05	0.46 ± 0.06
H413	0.39 ± 0.04	0.43 ± 0.06	0.36 ± 0.03
Day 2			
H357	0.41 ± 0.03	0.46 ± 0.05	0.26 ± 0.07
H400	0.33 ± 0.05	0.37 ± 0.04	0.27 ± 0.04
H413	0.29 ± 0.06	0.34 ± 0.15	0.29 ± 0.03

Appendix table XIX. The effect of S1PR2 on the mean fractal dimension of spheroids for the three OSCC lines

Cell lines	Control	S1PR2 antagonist	S1PR2 agonist
Embedding day			
H357	1.12 ± 0.01	1.15 ± 0.01	1.14 ± 0.01
H400	1.12 ± 0.01	1.12 ± 0.02	1.12 ± 0.01
H413	1.07 ± 0.02	1.06 ± 0.00	1.07 ± 0.02
Day 1			
H357	1.15 ± 0.03	1.17 ± 0.03	1.18 ± 0.02
H400	1.15 ± 0.02	1.17 ± 0.03	1.15 ± 0.01
H413	1.15 ± 0.02	1.13 ± 0.02	1.15 ± 0.02
Day 2			
H357	1.19 ± 0.02	1.15 ± 0.03	1.22 ± 0.03
H400	1.18 ± 0.01	1.17 ± 0.02	1.18 ± 0.02
H413	1.19 ± 0.02	1.18 ± 0.07	1.19 ± 0.02

Appendix table XX. The effect of S1PR2 on the MDMC (μm) for the three OSCC lines

Cell lines	Control	S1PR2 antagonist	S1PR2 agonist
Day 1			
H357	136.1 ± 7.4	139.0 ± 13.6	182.1 ± 15.4
H400	183.3 ± 21.9	157.3 ± 26.5	185.2 ± 15.2
H413	209.9 ± 11.9	177.2 ± 14.2	221.4 ± 10.1
Day 2			
H357	150.9 ± 3.9	151.2 ± 13.0	190.3 ± 17.8
H400	186.3 ± 14.7	166.9 ± 23.8	222.3 ± 14.5
H413	214.8 ± 12.6	180.5 ± 13.3	217.9 ± 18.8

Appendix table XXI. The effect of S1PR2 on EGF-increased the number of clusters of three OSCC lines

Cell lines	Control	EGF	S1PR2 antagonist +EGF	S1PR2 agonist +EGF
Day 1				
H357	1 ± 0	4 ± 2	2 ± 0	8 ± 4
H400	2 ± 0	6 ± 3	2 ± 1	6 ± 2
H413	4 ± 1	10 ± 4	2 ± 1	8 ± 4
Day 2				
H357	3 ± 1	16 ± 5	3 ± 2	28 ± 9
H400	6 ± 2	18 ± 4	3 ± 1	20 ± 4
H413	9 ± 3	31 ± 11	4 ± 1	27 ± 2

Appendix table XXII. The effect of S1PR2 on EGF-increased the maximum invading distance (μm) of three OSCC lines

Cell lines	Control	EGF	S1PR2 antagonist +EGF	S1PR2 agonist +EGF
Embedding day				
H357	149.5 ± 13.1	149.5 ± 19.6	157.7 ± 5.7	163.6 ± 31.7
H400	148.2 ± 18.3	154.7 ± 29.9	156.2 ± 24.3	220.9 ± 145.6
H413	186.4 ± 19.5	191.0 ± 9.8	188.3 ± 14.0	188.4 ± 7.3
Day 1				
H357	168.2 ± 9.1	250.3 ± 26.3	175.8 ± 16.8	291.5 ± 19.7
H400	230.2 ± 29.1	327.2 ± 72.9	199.6 ± 34.4	308.7 ± 52.3
H413	264.6 ± 56.5	329.6 ± 39.6	237.2 ± 31.7	318.3 ± 13.9
Day 2				
H357	215.5 ± 30.2	295.8 ± 23.5	215.0 ± 54.4	308.2 ± 75.3
H400	266.1 ± 13.7	355.9 ± 22.8	209.2 ± 33.2	386.5 ± 41.2
H413	280.2 ± 27.4	413.7 ± 40.0	237.0 ± 6.3	419.7 ± 21.9

Appendix table XXIII. The effect of S1PR2 on EGF-decreased the circularity of the main cluster of three OSCC lines

Cell lines	Control	EGF	S1PR2 antagonist +EGF	S1PR2 agonist +EGF
Embedding day				
H357	0.82 ± 0.01	0.76 ± 0.05	0.76 ± 0.01	0.74 ± 0.06
H400	0.83 ± 0.04	0.82 ± 0.04	0.79 ± 0.01	0.82 ± 0.02
H413	0.75 ± 0.03	0.69 ± 0.03	0.71 ± 0.05	0.72 ± 0.04
Day 1				
H357	0.61 ± 0.05	0.35 ± 0.04	0.47 ± 0.10	0.26 ± 0.02
H400	0.49 ± 0.09	0.23 ± 0.09	0.37 ± 0.04	0.27 ± 0.09
H413	0.39 ± 0.04	0.23 ± 0.05	0.40 ± 0.06	0.24 ± 0.03
Day 2				
H357	0.41 ± 0.03	0.21 ± 0.06	0.43 ± 0.06	0.16 ± 0.07
H400	0.33 ± 0.05	0.18 ± 0.03	0.43 ± 0.03	0.18 ± 0.01
H413	0.29 ± 0.06	0.15 ± 0.04	0.30 ± 0.03	0.14 ± 0.03

Appendix table XXIV. The effect of S1PR2 on EGF-increased the fractal dimension of the main cluster of three OSCC lines

Cell lines	Control	EGF	S1PR2 antagonist +EGF	S1PR2 agonist +EGF
Embedding day				
H357	1.12 ± 0.01	1.13 ± 0.02	1.15 ± 0.02	1.15 ± 0.02
H400	1.12 ± 0.01	1.12 ± 0.02	1.12 ± 0.02	1.12 ± 0.02
H413	1.07 ± 0.02	1.07 ± 0.02	1.07 ± 0.02	1.08 ± 0.03
Day 1				
H357	1.15 ± 0.03	1.16 ± 0.02	1.16 ± 0.01	1.15 ± 0.02
H400	1.15 ± 0.02	1.19 ± 0.02	1.19 ± 0.01	1.19 ± 0.02
H413	1.15 ± 0.02	1.20 ± 0.03	1.16 ± 0.02	1.20 ± 0.02
Day 2				
H357	1.19 ± 0.02	1.22 ± 0.01	1.16 ± 0.04	1.29 ± 0.09
H400	1.18 ± 0.01	1.24 ± 0.02	1.16 ± 0.03	1.23 ± 0.00
H413	1.19 ± 0.02	1.25 ± 0.06	1.20 ± 0.01	1.25 ± 0.03

Appendix table XXV. The effect of S1PR2 on EGF-increased the MDMC (μm) of three OSCC lines

Cell lines	Control	EGF	S1PR2 antagonist +EGF	S1PR2 agonist +EGF
Day 1				
H357	136.1 ± 7.4	190.5 ± 11.2	140.7 ± 11.8	209.8 ± 2.9
H400	183.3 ± 21.9	254.4 ± 54.4	158.4 ± 25.7	232.1 ± 34.6
H413	209.9 ± 11.9	254.1 ± 22.3	185.2 ± 19.5	246.6 ± 5.8
Day 2				
H357	150.9 ± 3.9	199.3 ± 25.2	156.5 ± 15.8	188.2 ± 28.8
H400	186.3 ± 14.7	228.6 ± 9.5	162.8 ± 19.2	224.1 ± 10.7
H413	214.8 ± 12.6	252.9 ± 17.1	184.3 ± 5.9	258.0 ± 39.7

References

Abdulkareem, A. A., Shelton, R. M., Landini, G., Cooper, P. R. & Milward, M. R. 2018. Periodontal pathogens promote epithelial-mesenchymal transition in oral squamous carcinoma cells in vitro. *Cell Adhesion and Migration*, 12, 127-37.

Abu Eid, R. & Landini, G. 2003. Quantification of the global and local complexity of the epithelial-connective tissue interface of normal, dysplastic, and neoplastic oral mucosae using digital imaging. *Pathology Research and Practice*, 199, 475-82.

Abu Eid, R. & Landini, G. 2005. Morphometry of pseudoepitheliomatous hyperplasia: objective comparison to normal and dysplastic oral mucosae. *Analytical and Quantitative Cytology and Histology*, 27, 232-40.

Adada, M., Canals, D., Hannun, Y. A. & Obeid, L. M. 2013. Sphingosine-1-phosphate receptor 2. *FEBS journal*, 280, 6354-66.

Adada, M. M., Canals, D., Jeong, N., Kelkar, A. D., Hernandez-Corbacho, M., Pulkoski-Gross, M. J., Donaldson, J. C., Hannun, Y. A. & Obeid, L. M. 2015. Intracellular sphingosine kinase 2-derived sphingosine-1-phosphate mediates epidermal growth factor-induced ezrin-radixin-moesin phosphorylation and cancer cell invasion. *FASEB Journal*, 29, 4654-69.

Alemany-Ribes, M. & Semino, C. E. 2014. Bioengineering 3D environments for cancer models. *Advanced Drug Delivery Reviews*, 79-80, 40-9.

Ali, R., Huwaizi, S., Alhallaj, A., Al Subait, A., Barhoumi, T., Al Zahrani, H., Al Anazi, A., Latif Khan, A. & Boudjelal, M. 2021. New born calf serum can induce spheroid formation in breast cancer KAIMRC1 cell line. *Frontiers in Molecular Biosciences*, 8, 769030-44.

Alimperti, S., Lei, P., Wen, Y., Tian, J., Campbell, A. M. & Andreadis, S. T. 2014. Serum-free spheroid suspension culture maintains mesenchymal stem cell proliferation and differentiation potential. *Biotechnology Progress* 30, 974-83.

Arber, S., Barbayannis, F. A., Hanser, H., Schneider, C., Stanyon, C. A., Bernard, O. & Caroni, P. 1998. Regulation of actin dynamics through phosphorylation of cofilin by LIM-kinase. *Nature*, 393, 805-9.

Arikawa, K., Takuwa, N., Yamaguchi, H., Sugimoto, N., Kitayama, J., Nagawa, H., Takehara, K. & Takuwa, Y. 2003. Ligand-dependent inhibition of B16 melanoma cell migration and invasion via endogenous S1P2 G protein-coupled Receptor: requirement of inhibition of cellular rac activity. *Journal of Biological Chemistry*, 278, 32841-51.

Asghar, M. Y., Kemppainen, K., Lassila, T. & Törnquist, K. 2018. Sphingosine 1-phosphate attenuates MMP2 and MMP9 in human anaplastic thyroid cancer C643 cells: Importance of S1P2. *PLOS One*,13, e0196992-7011.

Attieh, Y., Clark, A. G., Grass, C., Richon, S., Pocard, M., Mariani, P., Elkhatib, N., Betz, T., Gurchenkov, B. & Vignjevic, D. M. 2017. Cancer-associated fibroblasts lead tumor invasion through integrin-β3-dependent fibronectin assembly. *Journal of Cell Biology*, 216, 3509-20.

Bäcker, V. 2012. ImageJ macro tool sets for biological image analysis. ImageJ User and Developer Conference 2012. Luxembourg. Plugin available from [https://biii.eu/wound-healing-tool] [Last accessed 1 March 2022].

Basu, D., Bewley, A. F., Sperry, S. M., Montone, K. T., Gimotty, P. A., Rasanen, K., Facompre, N. D., Weinstein, G. S., Nakagawa, H., Diehl, J. A., Rustgi, A. K. & Herlyn, M. 2013. EGFR inhibition promotes an aggressive invasion pattern mediated by mesenchymal-like tumor cells within squamous cell carcinomas. *Molecular Cancer Therapeutics*, 12, 2176-86.

Beckham, T. H., Cheng, J. C., Lu, P., Shao, Y., Troyer, D., Lance, R., Marrison, S. T., Norris, J. S. & Liu, X. 2013. Acid ceramidase induces sphingosine kinase 1/S1P receptor 2-mediated activation of oncogenic Akt signaling. *Oncogenesis*, 2, e49-59.

Berens, E. B., Holy, J. M., Riegel, A. T. & Wellstein, A. 2015. A cancer cell spheroid assay to assess invasion in a 3D setting. *Journal of Visualized Experiments*, 2015, e53409-14.

Berger, A. J., Renner, C. M., Hale, I., Yang, X., Ponik, S. M., Weisman, P. S., Masters, K. S. & Kreeger, P. K. 2020. Scaffold stiffness influences breast cancer cell invasion via EGFR-linked Mena upregulation and matrix remodeling. *Matrix Biology*, 85-6, 80-93.

Bi, Y., Li, J., Ji, B., Kang, N., Yang, L., Simonetto, D. A., Kwon, J. H., Kamath, M., Cao, S. & Shah, V. 2014. Sphingosine-1-phosphate mediates a reciprocal signaling pathway between stellate cells and cancer cells that promotes pancreatic cancer growth. *American Journal of Pathology*, 184, 2791-802.

Blacher, S., Erpicum, C., Lenoir, B., Paupert, J., Moraes, G., Ormenese, S., Bullinger, E. & Noel, A. 2014. Cell Invasion in the spheroid sprouting assay: a spatial organisation analysis adaptable to cell behaviour. *PLOS One*, 9, e97019-28.

Blaho, V. A. & Hla, T. 2014. An update on the biology of sphingosine 1-phosphate receptors. *Journal of Lipid Research*, 55, 1596-608.

Blankenbach, K. V., Schwalm, S., Pfeilschifter, J. & Meyer Zu Heringdorf, D. 2016. Sphingosine-1-phosphate receptor-2 antagonists: therapeutic potential and potential risks. *Frontiers in Pharmacology*, 7**,** 167-80.

Brad, W. N., Douglas, D. D., Carl, M. A. & Angela, C. C., *Oral and maxillofacial pathology*, 3rd Ed., Elsevier Health Sciences, 2009a. Ch8, Noninfectious oral complications of antineoplastic therapy. p294.

Brad, W. N., Douglas, D. D., Carl, M. A. & Angela, C. C., *Oral and maxillofacial pathology*, 3rd Ed., Elsevier Health Sciences, 2009b. Ch10, Epithelial pathology. p418-20.

Bravo-Cordero, J. J., Hodgson, L. & Condeelis, J. 2012. Directed cell invasion and migration during metastasis. *Current Opinion in Cell Biology*, 24, 277-83.

Brito, C. & Sousa, S. 2020. Non-muscle myosin 2A (NM2A): structure, regulation and function. *Cells*, 9, 1590-613.

Brocklyn, J. R. V. 2010. Regulation of cancer cell migration and invasion by sphingosine-1-phosphate. *World Journal of Biological Chemistry*, 1, 307-12.

Burridge, K. & Wittchen, E. S. 2013. The tension mounts: stress fibers as force-generating mechanotransducers. *Journal of Cell Biology*, 200, 9-19.

Canel, M., Serrels, A., Frame, M. C. & Brunton, V. G. 2013. E-cadherin-integrin crosstalk in cancer invasion and metastasis. *Journal of Cell Science*, 126**,** 393-401.

Cattaneo, M. G., Vanetti, C., Samarani, M., Aureli, M., Bassi, R., Sonnino, S. & Giussani, P. 2018. Cross-talk between sphingosine-1-phosphate and EGFR signaling pathways enhances human glioblastoma cell invasiveness. *FEBS Letters*, 592, 949-61.

Cedervall, J., Zhang, Y. & Olsson, A. K. 2016. Tumor-induced NETosis as a risk factor for metastasis and organ failure. *Cancer Research*, 76, 4311-5.

Celentano, A., Yap, T., Paolini, R., Yiannis, C., Mirams, M., Koo, K., McCullough, M. & Cirillo, N. 2021. Inhibition of matrix metalloproteinase-2 modulates malignant behaviour of oral squamous cell carcinoma cells. *Journal of Oral Pathology and Medicine*, 50, 323-32.

Chang, J., Pang, E. M., Adebowale, K., Wisdom, K. M. & Chaudhuri, O. 2020. Increased stiffness inhibits invadopodia formation and cell migration in 3D. *Biophysical Journal*, 119, 726-36.

Chavez, M. G., Buhr, C. A., Petrie, W. K., Wandinger-Ness, A., Kusewitt, D. F. & Hudson, L. G. 2012. Differential downregulation of E-cadherin and desmoglein by epidermal growth factor. *Dermatology Research and Practice*, 2012, 309587-600.

Chen, Y. Q., Kuo, J. C., Wei, M. T., Chen, Y. C., Yang, M. H. & Chiou, A. 2019. Early stage mechanical remodeling of collagen surrounding head and neck squamous cell carcinoma spheroids correlates strongly with their invasion capability. *Acta Biomaterialia*, 84, 280-92.

Cheng, J. C., Wang, E. Y., Yi, Y., Thakur, A., Tsai, S.-H. & Hoodless, P. A. 2018. S1P stimulates proliferation by upregulating CTGF expression through S1PR2-mediated YAP activation. *Molecular Cancer Research*, 16, 1543-55.

Cherng, S., Young, J. & Ma, H. 2008. Alpha-smooth muscle actin (α-SMA). *American Journal of Science*, 4, 7-9.

Clark, A. G. & Vignjevic, D. M. 2015. Modes of cancer cell invasion and the role of the microenvironment. *Current Opinion in Cell Biology*, 36, 13-22.

Coffin, D. 2008. *DCRAW: decoding raw digital photos in linux* [Online]. Available: https://www.dechifro.org/dcraw/. [Accessed 26 February 2022].

Coller, H. A. 2019. The paradox of metabolism in quiescent stem cells. *FEBS Letters*, 593, 2817-39.

Cooper, G. M. 2013. Contractile assemblies of actin and myosin in nonmuscle cells. *The Cell: A Molecular Approach.* 6th ed.: Sinauer Associates

Costa, E. C., Moreira, A. F., de Melo-Diogo, D., Gaspar, V. M., Carvalho, M. P. & Correia, I. J. 2016. 3D tumor spheroids: an overview on the tools and techniques used for their analysis. *Biotechnology Advances*, 34, 1427-41.

Cowley, G. P., Smith, J. A. & Gusterson, B. A. 1986. Increased EGF receptors on human squamous carcinoma cell lines. *British Journal of Cancer*, 53, 223-29.

Croft, D. R. & Olson, M. F. 2011. Transcriptional regulation of Rho GTPase signaling. *Transcription*, 2, 211-15.

Dagogo-Jack, I. & Shaw, A. T. 2018. Tumour heterogeneity and resistance to cancer therapies. *Nature Clinical Practice Oncology*, 15, 81-94.

Dangi-Garimella, S., Redig, A. J., Shields, M. A., Siddiqui, M. A. & Munshi, H. G. 2010. Rho-ROCK-myosin signaling mediates membrane type 1 matrix metalloproteinase-induced cellular aggregation of keratinocytes. *Journal of Biological Chemistry*, 285, 28363-72.

Däster, S., Amatruda, N., Calabrese, D., Ivanek, R., Turrini, E., Droeser, R. A., Zajac, P., Fimognari, C., Spagnoli, G. C., Iezzi, G., Mele, V. & Muraro, M. G. 2017. Induction of hypoxia and necrosis in multicellular tumor spheroids is associated with resistance to chemotherapy treatment. *Oncotarget*, 8, 1725-36.

De Donatis, A., Ranaldi, F. & Cirri, P. 2010. Reciprocal control of cell proliferation and migration. *Journal of Cell Communication and Signaling*, 8, 20-3.

De Wever, O., Hendrix, A., De Boeck, A., Westbroek, W., Braems, G., Emami, S., Sabbah, M., Gespach, C. & Bracke, M. 2010. Modeling and quantification of cancer cell invasion through collagen type I matrices. *International Journal of Developmental Biology*, 54, 887-96.

Delorme, V., Machacek, M., DerMardirossian, C., Anderson, K. L., Wittmann, T., Hanein, D., Waterman-Storer, C., Danuser, G. & Bokoch, G. M. 2007. Cofilin activity downstream of Pak1 regulates cell protrusion efficiency by organizing lamellipodium and lamella actin networks. *Developmental Cell*, 13, 646-62.

Dise, R. S., Frey, M. R., Whitehead, R. H. & Polk, D. B. 2008. Epidermal growth factor stimulates Rac activation through Src and phosphatidylinositol 3-kinase to promote colonic epithelial cell migration. *American journal of physiology. Gastrointestinal and liver physiology*, 294, G276-85.

Dorrego, M. V. 2004. *Studies of immunological molecules in human oral keratinocytes.* PhD, University of London.

Du, W., Takuwa, N., Yoshioka, K., Okamoto, Y., Gonda, K., Sugihara, K., Fukamizu, A., Asano, M. & Takuwa, Y. 2010. S1P(2), the G protein-coupled receptor for sphingosine-1-phosphate, negatively regulates tumor angiogenesis and tumor growth in vivo in mice. *Cancer Research*, 70, 772-81.

Engers, R., Springer, E., Michiels, F., Collard, J. G. & Gabbert, H. E. 2001. Rac affects invasion of human renal cell carcinomas by up-regulating tissue inhibitor of metalloproteinases (TIMP)-1 and TIMP-2 expression. *Journal of Biological Chemistry*, 276, 41889-97.

Epstein, J. & Elad, S. 2015. Staging of oral cancer--TNM system. *In:* MEHTA, L. H. (ed.) *Burket's oral medicine.* 12th ed. 2 Enterprise Drive, Suite 509, Shelton, CT 06484: People's Medical Publishing House-USA.

Feitelson, M. A., Arzumanyan, A., Kulathinal, R. J., Blain, S. W., Holcombe, R. F., Mahajna, J., Marino, M., Martinez-Chantar, M. L., Nawroth, R., Sanchez-Garcia, I., Sharma, D., Saxena, N. K., Singh, N., Vlachostergios, P. J., Guo, S., Honoki, K., Fujii, H., Georgakilas, A. G., Bilsland, A., Amedei, A., Niccolai, E., Amin, A., Ashraf, S. S., Boosani, C. S., Guha, G., Ciriolo, M. R., Aquilano, K., Chen, S., Mohammed, S. I., Azmi, A. S., Bhakta, D., Halicka, D., Keith, W. N. & Nowsheen, S. 2015. Sustained proliferation in cancer: mechanisms and novel therapeutic targets. *Seminars in Cancer Biology*, 35 Suppl, S25-54.

Fenu, M., Bettermann, T., Vogl, C., Darwish-Miranda, N., Schramel, J., Jenner, F. & Ribitsch, I. 2019. A novel magnet-based scratch method for standardisation of wound-healing assays. *Scientific reports*, 9, 12625-9.

Fraley, S. I., Feng, Y., Krishnamurthy, R., Kim, D.-H., Celedon, A., Longmore, G. D. & Wirtz, D. 2010. A distinctive role for focal adhesion proteins in three-dimensional cell motility. *Nature Cell Biology*, 12, 598-604.

Gadea, G., Sanz-Moreno, V., Self, A., Godi, A. & Marshall, C. J. 2008. DOCK10-mediated Cdc42 activation is necessary for amoeboid invasion of melanoma cells. *Current Biology*, 18, 1456-65.

Gandy, K. A. O., Adada, M., Canals, D., Carroll, B., Roddy, P., Hannun, Y. A. & Obeid, L. M. 2013. Epidermal growth factor-induced cellular invasion requires sphingosine-1-phosphate/sphingosine-1-phosphate 2 receptor-mediated ezrin activation. *FASEB Journal*, 27, 3155-66.

Ganjre, A., Kunjir, G., Inamdar, H. & Pande, S. 2017. Molecular characterization of collective cell migration at invasive front in oral squamous cell carcinoma. *Journal of International Oral Health*, 9, 97-104.

Garrod, D. & Chidgey, M. 2008. Desmosome structure, composition and function. *Biochimica et Biophysica Acta - Biomembranes*, 1778, 572-87.

Ghasemi, M., Turnbull, T., Sebastian, S. & Kempson, I. 2021. The MTT Assay: utility, limitations, pitfalls, and interpretation in bulk and single-cell analysis. *International Journal of Molecular Sciences*, 22, 12827-56.

Godugu, C., Patel, A. R., Desai, U., Andey, T., Sams, A. & Singh, M. 2013. AlgiMatrix™ based 3D cell culture system as an in-vitro tumor model for anticancer studies. *PLOS One*, 8, e53708-20.

Goertzen, C., Eymael, D. & Magalhaes, M. 2018. Three-dimensional quantification of spheroid degradation-dependent invasion and invadopodia formation. *Biological Procedures Online*, 20, 20-30.

Goodenough, D. A. & Paul, D. L. 2009. Gap junctions. *Cold Spring Harbor Perspectives in Biology*, 1, a002576-95.

Goparaju, S. K., Jolly, P. S., Watterson, K. R., Bektas, M., Alvarez, S., Sarkar, S., Mel, L., Ishii, I., Chun, J., Milstien, S. & Spiegel, S. 2005. The S1P2 receptor negatively

regulates platelet-derived growth factor-induced motility and proliferation. *Molecular and Cellular Biology*, 25, 4237-49.

Gorovoy, M., Niu, J., Bernard, O., Profirovic, J., Minshall, R., Neamu, R. & Voyno-Yasenetskaya, T. 2005. LIM kinase 1 coordinates microtubule stability and actin polymerization in human endothelial cells. *Journal of Biological Chemistry*, 280, 26533-42.

Grada, A., Otero-Vinas, M., Prieto-Castrillo, F., Obagi, Z. & Falanga, V. 2017. Research techniques made simple: analysis of collective cell migration using the wound healing assay. *Journal of Investigative Dermatology*, 137, e11-6.

Grasset, E. M., Bertero, T., Bozec, A., Friard, J., Bourget, I., Pisano, S., Lecacheur, M., Maiel, M., Bailleux, C., Emelyanov, A., Ilie, M., Hofman, P., Meneguzzi, G., Duranton, C., Bulavin, D. V. & Gaggioli, C. 2018. Matrix stiffening and EGFR cooperate to promote the collective invasion of cancer cells. *Cancer Research*, 78, 5229-42.

Greenspon, J., Li, R., Xiao, L., Rao, J. N., Marasa, B. S., Strauch, E. D., Wang, J.-Y. & Turner, D. J. 2009. Sphingosine-1-phosphate protects intestinal epithelial cells from apoptosis through the Akt signaling pathway. *Digestive Diseases and Sciences*, 54, 499-510.

Groeger, S. & Meyle, J. 2019. Oral mucosal epithelial cells. *Frontiers in Immunology*, 10, 208-29.

Guan, X. 2015. Cancer metastases: challenges and opportunities. *Acta Pharmaceutica Sinica B*, 5, 402-18.

Gudipaty, S. A. & Rosenblatt, J. 2017. Epithelial cell extrusion: pathways and pathologies. *Seminars in Cell and Developmental Biology*, 67, 132-40.

Gupta, P. & Sivasankari, P. 2017. Specific role of targeted molecular therapy in treatment of oral squamous cell carcinoma. *Targeted Oncology*, 4, 1-8.

Hait, N. C., Sarkar, S., Le Stunff, H., Mikami, A., Maceyka, M., Milstien, S. & Spiegel, S. 2005. Role of sphingosine kinase 2 in cell migration toward epidermal growth factor. *Journal of Biological Chemistry*, 280, 29462-9.

Halah, F. A. 2018. *Evaluation of the role of Epsins and Notch1 in oral carcinogenesis.* PhD, Newcastle University.

Han, Y. 2019. Analysis of the role of the Hippo pathway in cancer. *Journal of Translational Medicine*, 17, 116-32.

Hand, A. R. & Frank, M. E. 2015. Oral mucosa. *Fundamentals of oral histology and physiology.* Somerset, USA: John Wiley & Sons, Incorporated.

Hartsock, A. & Nelson, W. J. 2008. Adherens and tight junctions: structure, function and connections to the actin cytoskeleton. *Biochimica et Biophysica Acta,* 1778**,** 660-9.

He, Y., Xiong, L., Gao, X., Hai, M., Liu, Y., Wang, G., Chen, G., Shuai, J., Jiao, Y., Zhang, X., Liu, R. & Liu, L. 2020. Morphological quantification of proliferation-to-invasion transition in tumor spheroids. *Biochimica et Biophysica Acta*, 1864, 129460-5.

Heissler, S. M. & Sellers, J. R. 2015. Four things to know about myosin light chains as reporters for non-muscle myosin-2 dynamics in live cells. *Cytoskeleton*,72, 65-70.

Herr, D. R., Reolo, M. J. Y., Peh, Y. X., Wang, W., Lee, C.-W., Rivera, R., Paterson, I. C. & Chun, J. 2016. Sphingosine 1-phosphate receptor 2 (S1P2) attenuates reactive oxygen species formation and inhibits cell death: implications for otoprotective therapy. *Scientific Reports*, 6, 24541-51.

Holly, J. M., Zeng, L. & Perks, C. M. 2013. Epithelial cancers in the post-genomic era: should we reconsider our lifestyle? *Cancer and Metastasis Reviews*, 32, 673-705.

Hong, X., Chedid, K. & Kalkanis, S. N. 2012. Glioblastoma cell line-derived spheres in serum-containing medium versus serum-free medium: a comparison of cancer stem cell properties. *International Journal of Oncology*, 41, 1693-700.

Hotulainen, P. & Lappalainen, P. 2006. Stress fibers are generated by two distinct actin assembly mechanisms in motile cells. *Journal of Cell Biology,* 173**,** 383-94.

Hou, Y., Konen, J., Brat, D. J., Marcus, A. I. & Cooper, L. A. D. 2018. TASI: A software tool for spatial-temporal quantification of tumor spheroid dynamics. *Scientific Reports*, 8, 7248-56.

Hu, W. M., Li, L., Jing, B. Q., Zhao, Y. S., Wang, C. L., Feng, L. & Xie, Y.-E. 2010. Effect of S1P5 on proliferation and migration of human esophageal cancer cells. *World Journal of Gastroenterology*, 16, 1859-66.

Hu, Z., Du, J., Yang, L., Zhu, Y., Yang, Y., Zheng, D., Someya, A., Gu, L. & Lu, X. 2012. GEP100/Arf6 is required for epidermal growth factor-induced ERK/Rac1 signaling and cell migration in human hepatoma HepG2 Cells. *PLOS One*, 7, e38777-86.

Hulkower, K. I. & Herber, R. L. 2011. Cell migration and invasion assays as tools for drug discovery. *Pharmaceutics*, 3, 107-24.

Islam, M., Mane, S., Hyder, E., Jones, S. & Ellis, I. 2017. The motogenic effect of EGF and TGF-α on the migration of tumor cells from the oral region: A role of epithelial-to-mesenchymal transition in cancer and a route for translation into the clinic. *Translational Research in Oral Oncology*, 2, 2057178-86.

Jenei, V., Nystrom, M. L. & Thomas, G. J. 2011. Measuring invasion in an organotypic model. *Methods in Molecular Biology*, 769, 223-32.

Jiang, C., Cui, C., Li, L. & Shao, Y. 2014. The anomalous diffusion of a tumor invading with different surrounding tissues. *PLOS One*, 9, e109784-99.

Jin, Y., Knudsen, E., Wang, L., Bryceson, Y., Damaj, B., Gessani, S. & Maghazachi, A. A. 2003. Sphingosine 1-phosphate is a novel inhibitor of T-cell proliferation. *Blood*, 101, 4909-15.

Joo, C. K., Kim, H. S., Park, J. Y., Seomun, Y., Son, M. J. & Kim, J. T. 2008. Ligand release-independent transactivation of epidermal growth factor receptor by transforming growth factor-β involves multiple signaling pathways. *Oncogene*, 27, 614-28.

Justus, C. R., Leffler, N., Ruiz-Echevarria, M. & Yang, L. V. 2014. In vitro cell migration and invasion assays. *Journal of Visualized Experiments*, e51046-53.

Kalluri, R. & Weinberg, R. A. 2009. The basics of epithelial-mesenchymal transition. *Journal of Clinical Investigation*, 119, 1420-28.

Kamata, N., Chida, K., Rikimaru, K., Horikoshi, M., Enomoto, S. & Kuroki, T. 1986. Growth-inhibitory effects of epidermal growth factor and overexpression of its receptors on human squamous cell carcinomas in culture. *Cancer Research*, 46, 1648-53.

Kang, J., Lee, D. W., Hwang, H. J., Yeon, S. E., Lee, M. Y. & Kuh, H. J. 2016. Mini-pillar array for hydrogel-supported 3D culture and high-content histologic analysis of human tumor spheroids. *Lab on a Chip*, 16, 2265-76.

Kassianidou, E. & Kumar, S. 2015. A biomechanical perspective on stress fiber structure and function. *Biochimica et Biophysica Acta*, 1853, 3065-74.

Kato, K., Shimasaki, M., Kato, T., Segami, N. & Ueda, Y. 2018. Expression of sphingosine kinase-1 is associated with invasiveness and poor prognosis of oral squamous cell carcinoma. *Anticancer Research*, 38, 1361-8.

Kawamoto, T., Mendelsohn, J., Le, A., Sato, G. H., Lazar, C. S. & Gill, G. N. 1984. Relation of epidermal growth factor receptor concentration to growth of human epidermoid carcinoma A431 cells. *Journal of Biological Chemistry*, 259, 7761-6.

Kierszenbaum, A. L. & Tres, L. 2019. Epithelium *In:* 5TH (ed.) *Histology and cell biology: an introduction to pathology* Elsevier Health Sciences.

Kim, E. S., Kim, J. S., Kim, S. G., Hwang, S., Lee, C. H. & Moon, A. 2011. Sphingosine 1-phosphate regulates matrix metalloproteinase-9 expression and breast cell invasion through S1P3–Gαq coupling. *Journal of Cell Science*, 124, 2220-30.

Kim, J., Kang, S. M., Oh, S. Y., Lee, H. J., Lee, I., Hwang, J. C. & Hong, S. H. 2019. NGFI-A binding protein 2 promotes EGF-dependent HNSCC cell invasion. *Cancers*, 11, 315-28.

Kimura, I., Kitahara, H., Ooi, K., Kato, K., Noguchi, N., Yoshizawa, K., Nakamura, H. & Kawashiri, S. 2016. Loss of epidermal growth factor receptor expression in oral squamous cell carcinoma is associated with invasiveness and epithelial-mesenchymal transition. *Oncology Letters*, 11, 201-7.

Knösel, T., Emde, V., Schlüns, K., Schlag, P. M., Dietel, M. & Petersen, I. 2006. Cytokeratin profiles identify diagnostic signatures in colorectal cancer using multiplex analysis of tissue microarrays. *Cellular Oncology*, 28, 167-75.

Kobayashi, H., Ogura, Y., Sawada, M., Nakayama, R., Takano, K., Minato, Y., Takemoto, Y., Tashiro, E., Watanabe, H. & Imoto, M. 2011. Involvement of 14-3-3 proteins in the second epidermal growth factor-induced wave of Rac1 activation in the process of cell migration. *Journal of Biological Chemistry*, 286, 39259-68.

Komatsu, S. & Ikebe, M. 2007. The phosphorylation of myosin II at the Ser1 and Ser2 is critical for normal platelet-derived growth factor induced reorganization of myosin filaments. *Molecular Biology of the Cell*, 18, 5081-90.

Kottke, M. D., Delva, E. & Kowalczyk, A. P. 2006. The desmosome: cell science lessons from human diseases. *Journal of Cell Science*, 119, 797-806.

Kozera, B. & Rapacz, M. 2013. Reference genes in real-time PCR. *Journal of Applied Genetics*, 54, 391-406.

Kramer, N., Walzl, A., Unger, C., Rosner, M., Krupitza, G., Hengstschläger, M. & Dolznig, H. 2013. In vitro cell migration and invasion assays. *Mutation Research*, 752, 10-24.

Krisanaprakornkit, S. & Iamaroon, A. 2012. Epithelial-mesenchymal transition in oral squamous cell carcinoma. *ISRN Oncology*, 2012, 681469-78.

Kumar, G. S., *Orban's oral histology & embryology*, 13th Ed., Elsevier Health Sciences, 2014. Ch10, Oral mucous membrane. p238-70.

Kurokawa, K., Itoh, R. E., Yoshizaki, H., Nakamura, Y. O. T. & Matsuda, M. 2004. Coactivation of Rac1 and Cdc42 at lamellipodia and membrane ruffles induced by epidermal growth factor. *Molecular Biology of the Cell*, 15, 1003-10.

Lam, C. R., Wong, H. K., Nai, S., Chua, C. K., Tan, N. S. & Tan, L. P. 2014. A 3D biomimetic model of tissue stiffness interface for cancer drug testing. *Molecular Pharmaceutics*, 11, 2016-21.

Lamouille, S., Xu, J. & Derynck, R. 2014. Molecular mechanisms of epithelial-mesenchymal transition. *Nature Reviews Molecular Cell Biology*, 15, 178-96.

Landini, G. 2021. *ImageJ plugins* [Online]. Available: https://blog.bham.ac.uk/intellimic/g-landini-software/ [Accessed 1 March 2022].

Landini, G. & Rippin, J. W. 1993. Fractal dimensions of the epithelial-connective tissue interfaces in premalignant and malignant epithelial lesions of the floor of the mouth. *Analytical and Quantitative Cytology and Histology*, 15, 144-9.

Landini, G. & Rippin, J. W. 1996. How important is tumour shape? Quantification of the epithelial-connective tissue interface in oral lesions using local connected fractal dimension analysis. *Journal of Pathology*, 179, 210-7.

Lebman, D. A. & Spiegel, S. 2008. Cross-talk at the crossroads of sphingosine-1-phosphate, growth factors, and cytokine signaling. *Journal of Lipid Research*, 49, 1388-94.

Lepley, D., Paik, J. H., Hla, T. & Ferrer, F. 2005. The G protein–coupled receptor S1P2 regulates Rho/Rho kinase pathway to inhibit tumor cell migration. *Cancer Research*, 65, 3788-95.

Li, C. H. & Lee, C. K. 1993. Minimum cross entropy thresholding. *Pattern Recognition*, 26, 617-25.

Li, J., Liu, H., Hu, J., Liu, S., Yin, J., Du, F., Yuan, J. & Lv, B. 2015. New tumor regression grade for rectal cancer after neoadjuvant therapy and radical surgery. *Oncotarget*, 6, 42222-31.

Li, S., Wang, Q., Wang, Y., Chen, X. & Wang, Z. 2009. PLC-γ1 and Rac1 coregulate EGF-induced cytoskeleton remodeling and cell migration. *Molecular Endocrinology*, 23, 901-13.

Liang, C. C., Park, A. Y. & Guan, J. L. 2007. In vitro scratch assay: a convenient and inexpensive method for analysis of cell migration in vitro. *Nature Protocols*, 2, 329-33.

Liang, J., Oyang, L., Rao, S., Han, Y., Luo, X., Yi, P., Lin, J., Xia, L., Hu, J., Tan, S., Tang, L., Pan, Q., Tang, Y., Zhou, Y. & Liao, Q. 2021. Rac1, a potential target for tumor therapy. *Frontiers in Oncology*, 11, 674426-42.

Lim, G., Kang, S.-J. & Lee, J. Y. 2020. Novel invasion indices quantify the feed-forward facilitation of tumor invasion by macrophages. *Scientific Reports*, 10, 718-27.

Liu, H., Lu, T., Kremers, G.-J., Seynhaeve, A. & ten Hagen, T. 2020. A microcarrier-based spheroid 3D invasion assay to monitor dynamic cell movement in extracellular matrix. *Biological Procedures Online*, 22, 3-14.

Liu, R., Li, X., Qiang, X., Luo, L., Hylemon, P. B., Jiang, Z., Zhang, L. & Zhou, H. 2015. Taurocholate induces cyclooxygenase-2 expression via the sphingosine 1-phosphate receptor 2 in a human cholangiocarcinoma cell line. *Journal of Biological Chemistry*, 290, 30988-1002.

Liu, Y., Zhi, Y., Song, H., Zong, M., Yi, J., Mao, G., Chen, L. & Huang, G. 2019. S1PR1 promotes proliferation and inhibits apoptosis of esophageal squamous cell carcinoma through activating STAT3 pathway. *Journal of Experimental and Clinical Cancer Research*, 38, 369-83.

Long, J. S., Fujiwara, Y., Edwards, J., Tannahill, C. L., Tigyi, G., Pyne, S. & Pyne, N. J. 2010. Sphingosine 1-phosphate receptor 4 uses HER2 (ERBB2) to regulate extracellular signal regulated kinase-1/2 in MDA-MB-453 breast cancer cells *Journal of Biological Chemistry*, 285, 35957-66.

Lu, Z., Jiang, G., Blume-Jensen, P. & Hunter, T. 2001. Epidermal growth factor-induced tumor cell invasion and metastasis initiated by dephosphorylation and downregulation of focal adhesion kinase. *Molecular and Cellular Biology*, 21, 4016-31.

Malchinkhuu, E., Sato, K., Maehama, T., Mogi, C., Tomura, H., Ishiuchi, S., Yoshimoto, Y., Kurose, H. & Okajima, F. 2008. S1P2 receptors mediate inhibition of glioma cell migration through Rho signaling pathways independent of PTEN. *Biochemical and Biophysical Research Communications*, 366, 963-8.

Malet-Engra, G., Yu, W., Oldani, A., Rey-Barroso, J., Gov, Nir S., Scita, G. & Dupré, L. 2015. Collective cell motility promotes chemotactic prowess and resistance to chemorepulsion. *Current Biology*, 25, 242-50.

Mandelbrot, B. 1967. How long is the coast of britain? Statistical self-similarity and fractional dimension. *Science*, 156, 636-8.

Marei, H. & Malliri, A. 2017. GEFs: dual regulation of Rac1 signaling. *Small GTPases*, 8, 90-9.

Matte, B. F., Kumar, A., Placone, J. K., Zanella, V. G., Martins, M. D., Engler, A. J. & Lamers, M. L. 2019. Matrix stiffness mechanically conditions EMT and migratory behavior of oral squamous cell carcinoma. *Journal of Cell Science*, 132, 224360-9.

Mead, T. J. & Lefebvre, V. 2014. Proliferation assays (BrdU and EdU) on skeletal tissue sections. *Methods in Molecular Biology*, 1130, 233-43.

Medlin, M. D., Staus, D. P., Dubash, A. D., Taylor, J. M. & Mack, C. P. 2010. Sphingosine 1-phosphate receptor 2 signals through leukemia-associated RhoGEF (LARG), to promote smooth muscle cell differentiation. *Arteriosclerosis, Thrombosis, and Vascular Biology*, 30, 1779-86.

Miki, H., Yamaguchi, H., Suetsugu, S. & Takenawa, T. 2000. IRSp53 is an essential intermediate between Rac and WAVE in the regulation of membrane ruffling. *Nature*, 408, 732-5.

Miller, A. V., Alvarez, S. E., Spiegel, S. & Lebman, D. A. 2008. Sphingosine kinases and sphingosine-1-phosphate are critical for transforming growth factor β-induced extracellular signal-regulated kinase 1 and 2 activation and promotion of migration and invasion of esophageal cancer cells. *Molecular and Cellular Biology*, 28, 4142-51.

Miller, E., Yang, J., DeRan, M., Wu, C., Su, Andrew I., Bonamy, Ghislain M. C., Liu, J., Peters, Eric C. & Wu, X. 2012. Identification of serum-derived sphingosine-1-phosphate as a small molecule regulator of YAP. *Chemistry and Biology*, 19, 955-62.

Montero, P. H. & Patel, S. G. 2015. Cancer of the oral cavity. *Surgical Oncology Clinics of North America*, 24, 491-508.

Mullins, R. D., Heuser, J. A. & Pollard, T. D. 1998. The interaction of Arp2/3 complex with actin: nucleation, high affinity pointed end capping, and formation of branching networks of filaments. *Proceedings of the National Academy of Sciences of the United States of America*, 95, 6181-6.

Murali, A. & Rajalingam, K. 2014. Small Rho GTPases in the control of cell shape and mobility. *Cellular and Molecular Life Sciences*, 71, 1703-21.

Nanci, A., *Ten Cate's Oral Histology*, 9th Ed., Elsevier Health Sciences, 2017. Ch4, Intercellular junctions. p119-26.

Negahdari, B., Shahosseini, Z. & Baniasadi, V. 2016. Production of human epidermal growth factor using adenoviral based system. *Research in Pharmaceutical Sciences*, 11, 43-8.

Nema, R., Vishwakarma, S., Agarwal, R., Panday, R. & Kumar, A. 2016. Emerging role of sphingosine-1-phosphate signaling in head and neck squamous cell carcinoma. *OncoTargets and Therapy*, 9, 3269-80.

Newton, J., Lima, S., Maceyka, M. & Spiegel, S. 2015. Revisiting the sphingolipid rheostat: evolving concepts in cancer therapy. *Experimental Cell Research*, 333, 195-200.

Obenauf, A. C. & Massagué, J. 2015. Surviving at a distance: organ-specific metastasis. *Trends in cancer*, 1, 76-91.

Ohnishi, Y., Yasui, H., Kakudo, K. & Nozaki, M. 2017. Regulation of cell migration via the EGFR signaling pathway in oral squamous cell carcinoma cells. *Oncology Letters*, 13, 930-6.

Oliveira, S., van Bergen en Henegouwen, P. M., Storm, G. & Schiffelers, R. M. 2006. Molecular biology of epidermal growth factor receptor inhibition for cancer therapy. *Expert Opinion on Biological Therapy*, 6, 605-17.

Olivera, A., Kohama, T., Edsall, L., Nava, V., Cuvillier, O., Poulton, S. & Spiegel, S. 1999. Sphingosine kinase expression increases intracellular sphingosine-1-phosphate and promotes cell growth and survival. *Journal of Cell Biology*, 147, 545-58.

Osada, M., Yatomi, Y., Ohmori, T., Ikeda, H. & Ozaki, Y. 2002. Enhancement of sphingosine 1-phosphate-induced migration of vascular endothelial cells and smooth muscle cells by an EDG-5 antagonist. *Biochemical and Biophysical Research Communications*, 299, 483-7.

Paladini, R. D., Takahashi, K., Bravo, N. S. & Coulombe, P. A. 1996. Onset of re-epithelialization after skin injury correlates with a reorganization of keratin filaments in wound edge keratinocytes: defining a potential role for keratin 16. *Journal of Cell Biology*, 132, 381-97.

Palleria, C., Di Paolo, A., Giofrè, C., Caglioti, C., Leuzzi, G., Siniscalchi, A., De Sarro, G. & Gallelli, L. 2013. Pharmacokinetic drug-drug interaction and their implication in clinical management. *Journal of Research in Medical Sciences*, 18, 601-10.

Pang, M., Li, C., Zheng, D., Wang, Y., Wang, J., Zhang, W., Li, F. & Jing, H. 2020. S1PR2 knockdown promotes migration and invasion in multiple myeloma cells via NF-κB activation. *Cancer Management and Research*, 12, 7857-65.

Parri, M. & Chiarugi, P. 2010. Rac and Rho GTPases in cancer cell motility control. *Cell Communication and Signaling*, 8, 23-36.

Patel, V., Rosenfeldt, H., Lyons, R., Servitja, J.-M., Bustelo, X., Siroff, M. & Gutkind, J. S. 2007. Persistent activation of Rac1 in squamous carcinomas of the head and neck: evidence for an EGFR/Vav2 signaling axis involved in cell invasion. *Carcinogenesis*, 28, 1145-52.

Patmanathan, S. N., Johnson, S. P., Lai, S. L., Panja Bernam, S., Lopes, V., Wei, W., Ibrahim, M. H., Torta, F., Narayanaswamy, P., Wenk, M. R., Herr, D. R., Murray, P. G., Yap, L. F. & Paterson, I. C. 2016. Aberrant expression of the S1P regulating enzymes, SPHK1 and SGPL1, contributes to a migratory phenotype in OSCC mediated through S1PR2. *Scientific Reports*, 6, 25650-62.

Pentenero, M., Gandolfo, S. & Carrozzo, M. 2005. Importance of tumor thickness and depth of invasion in nodal involvement and prognosis of oral squamous cell carcinoma: a review of the literature. *Head and Neck*, 27, 1080-91.

Petti, L., Rizzo, G., Rubbino, F., Elangovan, S., Colombo, P., Restelli, S., Piontini, A., Arena, V., Carvello, M., Romano, B., Cavalleri, T., Anselmo, A., Ungaro, F., D'Alessio, S., Spinelli, A., Stifter, S., Grizzi, F., Sgambato, A., Danese, S., Laghi, L., Malesci, A. & Vetrano, S. 2020. Unveiling role of sphingosine-1-phosphate receptor 2 as a brake of epithelial stem cell proliferation and a tumor suppressor in colorectal cancer. *Journal of Experimental and Clinical Cancer Research*, 39, 253-66.

Pijuan, J., Barceló, C., Moreno, D. F., Maiques, O., Sisó, P., Marti, R. M., Macià, A. & Panosa, A. 2019. In vitro cell migration, invasion, and adhesion assays: from cell imaging to data analysis. *Frontiers in Cell and Developmental Biology*, 7, 107-22.

Pitson, S. M., Moretti, P. A., Zebol, J. R., Lynn, H. E., Xia, P., Vadas, M. A. & Wattenberg, B. W. 2003. Activation of sphingosine kinase 1 by ERK1/2-mediated phosphorylation. *EMBO Journal*, 22, 5491-500.

Pitson, S. M., Xia, P., Leclercq, T. M., Moretti, P. A., Zebol, J. R., Lynn, H. E., Wattenberg, B. W. & Vadas, M. A. 2005. Phosphorylation-dependent translocation of sphingosine kinase to the plasma membrane drives its oncogenic signalling. *Journal of Experimental Medicine*, 201, 49-54.

Price, S. T., Beckham, T. H., Cheng, J. C., Lu, P., Liu, X. & Norris, J. S. 2015. Sphingosine 1-phosphate receptor 2 regulates the migration, proliferation, and differentiation of mesenchymal stem cells. *International Journal of Stem Cell Research and Therapy*, 2, 14-32.

Prime, S. S., Eveson, J. W., Stone, A. M., Huntley, S. P., Davies, M., Paterson, I. C. & Robinson, C. M. 2004. Metastatic dissemination of human malignant oral keratinocyte cell lines following orthotopic transplantation reflects response to TGF-beta 1. *Journal of Pathology*, 203, 927-32.

Prime, S. S., Game, S. M., Matthews, J. B., Stone, A., Donnelly, M. J., Yeudall, W. A., Patel, V., Sposto, R., Silverthorne, A. & Scully, C. 1994. Epidermal growth factor and transforming growth factor alpha characteristics of human oral carcinoma cell lines. *British Journal of Cancer*, 69, 8-15.

Puls, T. J., Tan, X., Husain, M., Whittington, C. F., Fishel, M. L. & Voytik-Harbin, S. L. 2018. Development of a novel 3D tumor-tissue invasion model for high-throughput, high-content phenotypic drug screening. *Scientific Reports*, 8, 13039-52.

Quint, P., Ruan, M., Pederson, L., Kassem, M., Westendorf, J. J., Khosla, S. & Oursler, M. J. 2013. Sphingosine 1-phosphate (S1P) receptors 1 and 2 coordinately induce mesenchymal cell migration through S1P activation of complementary kinase pathways. *Journal of Biological Chemistry*, 288, 5398-406.

Rasband, W. S. 1997. ImageJ. U. S. National Institutes of Health, Bethesda, Maryland, USA.

Ribeiro, F. A., Noguti, J., Oshima, C. T. & Ribeiro, D. A. 2014. Effective targeting of the epidermal growth factor receptor (EGFR) for treating oral cancer: a promising approach. *Anticancer Research*, 34, 1547-52.

Rice, A. J., Cortes, E., Lachowski, D., Cheung, B. C. H., Karim, S. A., Morton, J. P. & del Río Hernández, A. 2017. Matrix stiffness induces epithelial-mesenchymal transition and promotes chemoresistance in pancreatic cancer cells. *Oncogenesis*, 6, e352-60.

Ross, D.W., *Introduction to Oncogenes and Molecular Cancer Medicine*, Springer New York, 1998. Ch3, Oncogenes: control of cell growth and senescence. p32.

Ruiz, M., Okada, H. & Dahlbäck, B. 2017. HDL-associated ApoM is anti-apoptotic by delivering sphingosine 1-phosphate to S1P1 & S1P3 receptors on vascular endothelium. *Lipids in Health and Disease*, 16, 36-47.

Russ J.C. & Dehoff R.T., *Practical Stereology*, 2nd Ed., Kluwer Academic, 2000. Ch4, Classical Stereological Measures. p56.

Salomone, S., Potts, E. M., Tyndall, S., Ip, P. C., Chun, J., Brinkmann, V. & Waeber, C. 2008. Analysis of sphingosine 1-phosphate receptors involved in constriction of isolated cerebral arteries with receptor null mice and pharmacological tools. *British Journal of Pharmacology*, 153, 140-7.

Salomone, S. & Waeber, C. 2011. Selectivity and specificity of sphingosine-1-phosphate receptor ligands: caveats and critical thinking in characterizing receptor-mediated effects. *Frontiers in Pharmacology*, 2, 9-16.

Sanchez, T., Skoura, A., Wu, M. T., Casserly, B., Harrington, E. O. & Hla, T. 2007. Induction of vascular permeability by the sphingosine-1-phosphate receptor–2 (S1P2R) and its downstream effectors ROCK and PTEN. *Arteriosclerosis, Thrombosis, and Vascular Biology*, 27, 1312-8.

Sant, S. & Johnston, P. A. 2017. The production of 3D tumor spheroids for cancer drug discovery. *Drug Discovery Today: Technologies*, 23, 27-36.

Satelli, A. & Li, S. 2011. Vimentin in cancer and its potential as a molecular target for cancer therapy. *Cellular and Molecular Life Sciences*, 68, 3033-46.

Schüppel, M., Kürschner, U., Kleuser, U., Schäfer-Korting, M. & Kleuser, B. 2008. Sphingosine 1-phosphate restrains insulin-mediated keratinocyte proliferation via inhibition of Akt through the S1P2 receptor subtype. *Journal of Investigative Dermatology*, 128, 1747-56.

Seoane-Romero, J. M., Vázquez-Mahía, I., Seoane, J., Varela-Centelles, P., Tomás, I. & López-Cedrún, J. L. 2012. Factors related to late stage diagnosis of oral squamous cell carcinoma. *Medicina Oral Patologia Oral Y Cirugia Bucal*, 17, e35-40.

Shu, X., Wu, W., Mosteller, R. D. & Broek, D. 2002. Sphingosine kinase mediates vascular endothelial growth factor-induced activation of ras and mitogen-activated protein kinases. *Molecular and Cellular Biology*, 22, 7758-68.

Slattum, G. M. & Rosenblatt, J. 2014. Tumour cell invasion: an emerging role for basal epithelial cell extrusion. *Nature Reviews Cancer*, 14, 495-501.

Smith-Zagone, M. J. & Schwartz, M. R. 2005. Frozen section of skin specimens. *Archives of Pathology and Laboratory Medicine*, 129, 1536-43.

Staneva, R., Burla, F., Koenderink, G. H., Descroix, S., Vignjevic, D. M., Attieh, Y. & Verhulsel, M. 2018. A new biomimetic assay reveals the temporal role of matrix stiffening in cancer cell invasion. *Molecular Biology of the Cell*, 29, 2979-88.

Suh, Y. J., Pandey, M., Segall, J. E. & Wu, M. 2022. Tumor spheroid invasion in epidermal growth factor gradients revealed by a 3D microfluidic device. *Physical Biology*, 19, 36002-11.

Sukocheva, O., Wadham, C., Holmes, A., Albanese, N., Verrier, E., Feng, F., Bernal, A., Derian, C. K., Ullrich, A., Vadas, M. A. & Xia, P. 2006. Estrogen transactivates EGFR via the sphingosine 1-phosphate receptor Edg-3: the role of sphingosine kinase-1. *Journal of Cell Biology*, 173, 301-10.

Szczepaniak, W. S., Pitt, B. R. & McVerry, B. J. 2010. S1P2 receptor-dependent Rho-kinase activation mediates vasoconstriction in the murine pulmonary circulation induced by sphingosine 1-phosphate. *American Journal of Physiology-Lung Cellular and Molecular Physiology*, 299, L137-45.

Takashima, S., Sugimoto, N., Takuwa, N., Okamoto, Y., Yoshioka, K., Takamura, M., Takata, S., Kaneko, S. & Takuwa, Y. 2008. G12/13 and Gq mediate S1P2-induced inhibition of Rac and migration in vascular smooth muscle in a manner dependent on Rho but not Rho kinase. *Cardiovascular Research*, 79, 689-97.

Takuwa, N., Du, W., Kaneko, E., Okamoto, Y., Yoshioka, K. & Takuwa, Y. 2011. Tumor-suppressive sphingosine-1-phosphate receptor-2 counteracting tumor-promoting

sphingosine-1-phosphate receptor-1 and sphingosine kinase 1 - Jekyll Hidden behind Hyde. *American Journal of Cancer Research*, 1, 460-81.

Tamashiro, P. M., Furuya, H., Shimizu, Y. & Kawamori, T. 2014. Sphingosine kinase 1 mediates head & neck squamous cell carcinoma invasion through sphingosine 1-phosphate receptor 1. *Cancer Cell International*, 14, 76-84.

Tanaka, S., Kawano, S., Hattori, T., Matsubara, R., Sakamoto, T., Hashiguchi, Y., Kaneko, N., Mikami, Y., Morioka, M., Maruse, Y., Kitamura, R., Hamada, E., Hiwatashi, M., Oobu, K., Kiyoshima, T. & Nakamura, S. 2020. Cytokeratin 19 as a biomarker of highly invasive oral squamous cell carcinoma with metastatic potential. *Journal of Oral and Maxillofacial Surgery, Medicine, and Pathology*, 32, 1-7.

Tanimoto, T., Lungu, A. O. & Berk, B. C. 2004. Sphingosine 1-phosphate transactivates the platelet-derived growth factor β receptor and epidermal growth factor receptor in vascular smooth muscle cells. *Circulation Research*, 94, 1050-8.

Theveneau, E. & Mayor, R. 2013. Collective cell migration of epithelial and mesenchymal cells. *Cellular and Molecular Life Sciences*, 70, 3481-92.

Tilghman, R. W., Cowan, C. R., Mih, J. D., Koryakina, Y., Gioeli, D., Slack-Davis, J. K., Blackman, B. R., Tschumperlin, D. J. & Parsons, J. T. 2010. Matrix rigidity regulates cancer cell growth and cellular phenotype. *PLOS One*, 5, e12905-17.

Tojkander, S., Gateva, G. & Lappalainen, P. 2012. Actin stress fibers – assembly, dynamics and biological roles. *Journal of Cell Science*, 125, 1855-64.

Tumur, Z., Katebzadeh, S., Guerra, C., Bhushan, L., Alkam, T. & Henson, B. S. 2015. RhoC mediates epidermal growth factor-stimulated migration and invasion in head and neck squamous cell carcinoma. *Neoplasia*, 17, 141-51.

Uhlenbrock, K., Eberth, A., Herbrand, U., Daryab, N., Stege, P., Meier, F., Friedl, P., Collard, J. G. & Ahmadian, M. R. 2004. The RacGEF Tiam1 inhibits migration and invasion of

metastatic melanoma via a novel adhesive mechanism. *Journal of Cell Science*, 117, 863-71.

van Meer, G., Gumbiner, B. & Simons, K. 1986. The tight junction does not allow lipid molecules to diffuse from one epithelial cell to the next. *Nature*, 322, 639-41.

Veiseh, O., Kievit, F. M., Ellenbogen, R. G. & Zhang, M. 2011. Cancer cell invasion: treatment and monitoring opportunities in nanomedicine. *Advanced Drug Delivery Reviews*, 63, 582-96.

Vicente-Manzanares, M., Ma, X., Adelstein, R. S. & Horwitz, A. R. 2009. Non-muscle myosin II takes centre stage in cell adhesion and migration. *Nature Reviews Molecular Cell Biology*, 10, 778-90.

Vinci, M., Box, C. & Eccles, S. A. 2015. Three-dimensional (3D) tumor spheroid invasion assay. *Journal of Visualized Experiments*, e52686-94.

Voldborg, B. R., Damstrup, L., Spang-Thomsen, M. & Poulsen, H. S. 1997. Epidermal growth factor receptor (EGFR) and EGFR mutations, function and possible role in clinical trials. *Annals of Oncology*, 8, 1197-206.

Vrzalikova, K., Ibrahim, M., Vockerodt, M., Perry, T., Margielewska, S., Lupino, L., Nagy, E., Soilleux, E., Liebelt, D., Hollows, R., Last, A., Reynolds, G., Abdullah, M., Curley, H., Care, M., Krappmann, D., Tooze, R., Allegood, J., Spiegel, S., Wei, W., Woodman, C. B. J. & Murray, P. G. 2018. S1PR1 drives a feedforward signalling loop to regulate BATF3 and the transcriptional programme of Hodgkin lymphoma cells. *Leukemia*, 32, 214-23.

Wagner, V. P., Webber, L. P., Curra, M., Klein, I. P., Meurer, L., Carrad, V. C. & Martins, M. D. 2017. Bryne's grading system predicts poor disease-specific survival of oral squamous cell carcinoma: a comparative study among different histologic grading

systems. *Oral Surgery, Oral Medicine, Oral Pathology, and Oral Radiology*, 123, 688-96.

Walker, S., Worst, T. & Vrana, K. 2002. Semiquantitative real-time PCR for analysis of mRNA levels. *In:* WANG, J. (ed.) *Drugs of Abuse.* Humana Press Inc.

Walko, G., Castañón, M. J. & Wiche, G. 2015. Molecular architecture and function of the hemidesmosome. *Cell and Tissue Research*, 360, 363-78.

Wang, P., Henning, S. M. & Heber, D. 2010. Limitations of MTT and MTS-based assays for measurement of antiproliferative activity of green tea polyphenols. *PLOS One*, 5, e10202-11.

Wee, P. & Wang, Z. 2017. Epidermal growth factor receptor cell proliferation signaling pathways. *Cancers*, 9, 52-96.

Wieduwilt, M. J. & Moasser, M. M. 2008. The epidermal growth factor receptor family: biology driving targeted therapeutics. *Cellular and Molecular Life Sciences*, 65, 1566-84.

Windoffer, R., Beil, M., Magin, T. M. & Leube, R. E. 2011. Cytoskeleton in motion: the dynamics of keratin intermediate filaments in epithelia. *Journal of Cell Biology*, 194, 669-78.

World cancer research fund international. 2022. *Mouth and oral cancer statistics* [Online]. Available: https://www.wcrf.org/cancer-trends/mouth-and-oral-cancer-statistics/ [Accessed 22 December 2022].

Wu, R., Coniglio, S. J., Chan, A., Symons, M. H. & Steinberg, B. M. 2007. Up-regulation of Rac1 by epidermal growth factor mediates COX-2 expression in recurrent respiratory papillomas. *Molecular Medicine*, 13, 143-50.

Wullkopf, L., West, A. V., Leijnse, N., Cox, T. R., Madsen, C. D., Oddershede, L. B. & Erler, J. T. 2018. Cancer cells' ability to mechanically adjust to extracellular matrix stiffness correlates with their invasive potential. *Molecular Biology of the Cell*, 29, 2378-85.

Xie, H., Ma, Y., Li, J., Chen, H., Xie, Y., Chen, M., Zhao, X., Tang, S., Zhao, S., Zhang, Y., Du, J., Zhang, F. & Gu, L. 2020. WNT7A promotes EGF-induced migration of oral squamous cell carcinoma cells by activating β-catenin/MMP9-mediated signaling. *Frontiers in Pharmacology*, 11, 98-113.

Xu, N., Lao, Y., Zhang, Y. & Gillespie, D. A. 2012. Akt: a double-edged sword in cell proliferation and genome stability. *Journal of Oncology*, 2012, 951724-38.

Xu, Q., Zhang, Q., Ishida, Y., Hajjar, S., Tang, X., Shi, H., Dang, C. & Le, A. 2016. EGF induces epithelial-mesenchymal transition and cancer stem-like cell properties in human oral cancer cells via promoting Warburg effect. *Oncotarget*, 8, 9557-71.

Yamamoto, S., Yako, Y., Fujioka, Y., Kajita, M., Kameyama, T., Kon, S., Ishikawa, S., Ohba, Y., Ohno, Y., Kihara, A. & Fujita, Y. 2015. A role of the sphingosine-1-phosphate (S1P)- S1P receptor 2 pathway in epithelial defense against cancer (EDAC). *Molecular Biology of the Cell*, 27, 491-9.

Yang, L., Han, Z., Tian, L., Mai, P., Zhang, Y., Wang, L. & Li, L. 2015. Sphingosine 1-phosphate receptor 2 and 3 mediate bone marrow-derived monocyte/Macrophage motility in cholestatic liver injury in mice. *Scientific Reports,* 5**,** 13423-35.

Yoon, S. & Leube, R. E. 2019. Keratin intermediate filaments: intermediaries of epithelial cell migration. *Essays in Biochemistry*, 63, 521-33.

Young, N. & Van Brocklyn, J. R. 2007. Roles of sphingosine-1-phosphate (S1P) receptors in malignant behavior of glioma cells. Differential effects of S1P2 on cell migration and invasiveness. *Experimental Cell Research*, 313, 1615-27.

Yu, F. X., Zhao, B., Panupinthu, N., Jewell, J. L., Lian, I., Wang, L. H., Zhao, J., Yuan, H., Tumaneng, K., Li, H., Fu, X. D., Mills, G. B. & Guan, K. L. 2012. Regulation of the Hippo-YAP pathway by G-protein-coupled receptor signaling. *Cell*, 150, 780-91.

Zanoni, M., Piccinini, F., Arienti, C., Zamagni, A., Santi, S., Polico, R., Bevilacqua, A. & Tesei, A. 2016. 3D tumor spheroid models for in vitro therapeutic screening: a systematic approach to enhance the biological relevance of data obtained. *Scientific Reports*, 6, 19103-13.

Zegers, M. M. & Friedl, P. 2014. Rho GTPases in collective cell migration. *Small GTPases*, 5, e28997-9006.

Zihni, C., Mills, C., Matter, K. & Balda, M. S. 2016. Tight junctions: from simple barriers to multifunctional molecular gates. *Nature Reviews Molecular Cell Biology*, 17, 564-80.